UHP metamorphic rocks of the Eastern Rhodope Massif, NE Greece: new constraints from petrology, geochemistry and zircon ages

Dissertation

zur Erlangung des Grades

“Doktor der Naturwissenschaften“

im Promotionsfach Geologie-Paläontologie

am Fachbereich Chemie, Pharmazie und Geowissenschaften

der Johannes Gutenberg-Universität Mainz

Nina Kaarina Cornelius

geb. in Kiel

Mainz, 2008

Erklärung

Ich versichere hiermit, die vorliegende Arbeit selbständig und nur unter Verwendung der angegebenen Quellen und Hilfsmittel verfasst zu haben.

Mainz, Juli 2008

Abstract

In this PhD thesis, a multidisciplinary study has been carried out on metagranitoids and paragneisses from the Eastern Rhodope Massif, northern Greece, to decipher the pre-Alpine magmatic and geodynamic evolution of the Rhodope Massif and to correlate the eastern part with the western/central parts of the orogen. The Rhodope Massif, which occupies the major part of NE Greece and S Bulgaria, represents the easternmost part of the Internal Hellenides. It is regarded as a nappe stack of high-grade units, which is classically subdivided into an upper unit and a lower unit, separated by a SSE-NNW trending thrust plane, the Nestos thrust. Recent research in the central Greek Rhodope Massif revealed that the two units correspond to two distinct terranes of different age, the Permo-Carboniferous Thracia Terrane, which was overthrusted by the Late Jurassic/Early Cretaceous Rhodope Terrane. These terranes are separated by the Nestos suture, a composite zone comprising metapelites, metabasites, metagranitoids and marbles, which record high-pressure and even ultrahigh-pressure metamorphism in places.

Similar characteristic rock associations were investigated during this study along several well-constrained cross sections in vincity to the Ada, Sidiro and Kimi villages in the Greek Eastern Rhodope Massif. Field evidence revealed that the contact zone of the two terranes in the Eastern Rhodope Massif is characterized by a mélange of metapelites, migmatitic amphibolites/eclogites, strongly sheared orthogneisses and marbles. The systematical occurrence of this characteristic rock association between the terranes implies that the Nestos suture is a continuous belt throughout the Greek Rhodope Massif.

In this study, a new UHP locality could be established and for the first time in the Greek Rhodope, metamorphic microdiamonds were identified in situ in their host zircons using Laser-Raman spectroscopy. The presence of the diamonds as well as element distribution patterns of the zircons, obtained by TOF-SIMS, indicate metamorphic conditions of $T > 1000$ °C and $P > 4$ GPa. The high-pressure and ultrahigh-pressure rocks of the mélange zone are considered to have formed during the subduction of the Nestos Ocean in Jurassic times at ~150 Ma. Melting of metapelitic rocks at UHP conditions facilitated the exhumation to lower crustal levels.

To identify major crust forming events, basement granitoids were dated by LA-SF-ICPMS and SHRIMP-II U-Pb analyses of zircons. The geochronological results revealed that the Eastern Rhodope Massif consists of two crustal units, a structurally lower Permo-Carboniferous unit

corresponding to the Thracia Terrane and a structurally upper Late Jurassic/Early Cretaceous unit corresponding to the Rhodope Terrane, like it was documented for the Central Rhodope Massif. Inherited zircons in the orthogneisses from the Thracia Terrane of the Eastern Rhodope Massif indicate the presence of a pre-existing Neoproterozoic and Ordovician-Silurian basement in this region. Triassic magmatism is witnessed by the zircons of few orthogneisses from the easternmost Rhodope Massif and is interpreted to be related to rifting processes.

Whole-rock major and trace element analyses indicate that the metagranitoids from both terranes originated in a subduction-related magmatic-arc environment. The Sr-Nd isotope data for both terranes of the Eastern and Central Rhodope Massif suggest a mixed crust-mantle source with variable contributions of older crustal material as already indicated by the presence of inherited zircons.

Geochemical and isotopic similarity of the basement of the Thracia Terrane and the Pelagonian Zone implies that the Thracia Terrane is a fragment of a formerly unique Permo-Carboniferous basement, separated by rifting and opening of the Meliata-Maliac ocean system in Triassic times. A branch of the Meliata-Maliac ocean system, the Nestos Ocean, subducted northwards in Late Jurassic times leading to the formation of the Late Jurassic/Early Cretaceous Rhodope magmatic arc on remnants of the Thracia Terrane as suggested by inherited Permo-Carboniferous zircons. The ~150 Ma zircon ages of the orthogneisses from the Rhodope Terrane indicate that subduction-related magmatism and HP/UHP metamorphism occurred during the same subduction phase. Subduction ceased due to the closure of the Nestos Ocean in the Late Jurassic/Early Cretaceous. The post-Jurassic evolution of the Rhodope Massif is characterized by the exhumation of the Rhodope core complex in the course of extensional tectonics associated with late granite intrusions in Eocene to Miocene times.

Zusammenfassung

Im Rahmen dieser Dissertation wurden Metagranitoide und Paragneise aus dem östlichen Rhodope Massiv in Nordgriechenland interdisziplinär untersucht, um ihre prä-alpine magmatische und geodynamische Entwicklung zu entschlüsseln und den östlichen Teil des Gebirges mit dem westlichen/zentralen Teil zu korrelieren. Das Rhodope Massiv stellt den nordöstlichsten Teil der Internen Helleniden dar und nimmt den größten Teil Nordost-Griechenlands und Süd-Bulgariens ein. Es ist aus hochgradig metamorphen Decken aufgebaut und wird im klassischen Sinne in eine untere und obere lithologische Einheit unterteilt, die durch eine SSE-NNW verlaufende Überschiebung, die Nestos Überschiebung, voneinander abgegrenzt sind. Neueren Forschungsergebnissen im zentralen Teil des griechischen Rhodope Massivs zufolge sind diese beiden Einheiten zwei verschiedenen Krustenblöcken verschiedenen Alters zuzuordnen. Das permo-karbonische Thracia Terrane wurde vom spät-jurassischen/früh-kretazischen Rhodope Terrane überschoben. Die Nestos Sutur, welche die Terranes voneinander abgrenzt, setzt sich aus einer Vielzahl von verschiedenen Gesteinstypen zusammen, insbesondere aus Metapeliten, Metabasiten, Metagranitoiden und Marmoren. Diese Gesteine haben eine Hochdruck-Metamorphose (HP) erfahren und in seltenen Fällen sind Indikatoren für eine Ultrahochdruck-Metamorphose (UHP) erhalten.

Für die vorliegende Dissertation wurden mehrere Geländeprofile untersucht, die eine ähnliche Gesteinsparagenese zeigen. Diese Profile liegen in der Nähe der Orte Ada, Sidiro und Kimi im östlichen Rhodope Massiv Griechenlands. Die Geländebeobachtungen belegen, daß die Kontaktzone der beiden Terranes stets durch eine charakteristische Gesteinsassoziation aus Metapeliten, migmatitischen Amphiboliten/Eklogiten, stark gescherten Orthogneisen und Marmoren besteht. Das systematische Vorkommen dieser charakteristischen Gesteinsassoziation deutet darauf hin, daß die Nestos Sutur ein durchgehender Gürtel durch das Rhodope Massiv ist.

Mittels Ramanspektroskopie konnten metamorphe Mikrodiamanten in situ in Zirkonen zweier Metapelitproben nachgewiesen und somit eine neue UHP-Lokalität im griechischen Rhodope Massiv etabliert werden. Die Diamanteinschlüsse in den Zirkonen sowie TOF-SIMS Elementverteilungsbilder selbiger Zirkone deuten auf Temperaturen von $T > 1000$ °C and Drücke von $P > 4$ GPa hin. Die HP- und UHP-Metamorphose der Metapelite erfolgte während der Subduktion des Nestos Ozeans im Jura um ca. 150 Ma. Schmelzprozesse der metapelitischen

Gesteine im UHP-metamorphen Bereich ermöglichten eine Exhumierung der Gesteine bis in die untere Kruste.

Durch LA-SF-ICPMS und SHRIMP-II U-Pb Datierungen von Zirkonen wurden zwei magmatische, krustenbildende Hauptereignisse identifiziert, wie es schon für den zentralen Teil des griechischen Rhodope Massivs nachgewiesen werden konnte. Die strukturell untere Einheit ist permo-karbonischen Alters und entspricht dem Thracia Terrane, während die strukturell obere Einheit spät-jurassischen/früh-kretazischen Alters ist und dem Rhodope Terrane entspricht.

Ererbte Zirkone in den Orthogneisen des Thracia Terranes lassen darauf schließen, daß eine präexistierende neoproterozoische und ordovizisch-silurische Kruste in der Region vorhanden war. Die Zirkone einiger Orthogneise aus dem östlichsten Rhodope Massiv deuten auf ein Rifting-Ereignis in der Trias und damit verbundenen Magmatismus hin.

Die Edukte der Orthogneise beider Terranes konnten durch Haupt- und Spurenelementgeochemie als subduktionsbezogene vulkanische-Bogen-Granitoide klassifiziert werden. Untersuchungen zur Sr und Nd Gesamtgesteinsisotopie dieser Orthogneise ergaben, daß die Magmenquelle einen Mischcharakter aus Mantel und Kruste hatte und in unterschiedlichem Maß von einer älteren Krustenkomponente beeinflußt wurde. Diese ältere Krustenkomponente wird auch durch die ererbten Zirkone belegt.

Aus der geochemischen und isotopischen Ähnlichkeit des Thracia Terranes und der Pelagonischen Zone wird abgeleitet, daß beide Fragmente eines ehemals ganzheitlichen permo-karbonischen Grundgebirges darstellen, welches durch die Öffnung des Meliata-Meliac Ozean Systems in der Trias geteilt wurde. Ein Zweig dieses Meliata-Maliac Ozean Systems, der Nestos Ozean, wurde im Jura nordwärts subduziert, wodurch subduktionsbezogener Magmatismus zur Bildung des spät-jurassischen/früh-kretazischen Rhodope vulkanischen Inselbogens auf einem Thracia Fragment führte. Dies wird auch durch ererbte permo-karbonische Zirkone in den Jurassischen Orthogneisen belegt.

Das Alter der Zirkone der Orthogneise des Rhodope Terranes beträgt ca. 150 Ma und deutet darauf hin, daß der subduktionsbedingte Magmatismus und die HP- /UHP-Metamorphose ihren Ursprung in der gleichen Subduktionsphase haben. Die Subduktion endete mit der Schließung des Nestos Ozeans im späten Jura/ in der frühen Kreide. Die post-jurassische Entwicklung des Rhodope Massivs wird durch die Exhumierung des Kernkomplexes durch Extensionstektonik bestimmt. Damit verbunden ist die Intrusion von Graniten zwischen Eozän und Miozän.

Table of Contents

1. Introduction

Since the discovery of coesite in a pyrope-quartzite from Dora Maira in the Western Alps (Chopin 1984) and in an eclogite from the Western Gneiss Region in Norway (Smith 1984) the limits of metamorphism of crustal rocks and the corresponding geodynamic processes had to be reconsidered. The formation of the ultrahigh-pressure (UHP) mineral coesite in felsic rocks provided evidence for the subduction of crustal rocks to depths in excess of 90 km into the earth´s mantle and their exhumation back to the surface. The term ultrahigh-pressure metamorphism refers to conditions of at least 600°C and 27 kbar, which mark the experimentally determined transition of quartz to its polymorph coesite (e.g. Massonne 2005 and references therein). Sobolev and Shatsky (1990) observed the in situ occurrence of diamonds in felsic gneisses and marbles from the Kokchetav Massif in northern Kazakhstan, implying that these rocks experienced even higher pressures of ca. 40 kbar. In the following years such coesite and/or diamond-bearing rocks were found in more collisional orogens, e.g. Dabie Shan and Sulu in China and the Saxonian Erzgebirge in Germany. These studies also revealed new UHP indicators like clinopyroxene-, rutile- and apatite exsolutions in garnets from eclogites of the Sulu Mountains in China (Ye et al. 2000). A summery of the established and potential UHP localities worldwide is given in Figure 1.1.

First evidence for UHP metamorphism in Greece was reported by Kostopoulos et al. (2000) from graphitized diamonds in metamorphic mafic and sedimentary rocks of the eastern Vardar Zone, the Circum-Rhodope Belt and the western Serbo-Macedonian Massif in Central Macedonia. One year later, UHP indicators, namely microdiamonds, exsolutions of rutile-, quartz- and apatite within garnet and pseudomorphs after coesite, were discovered in garnet-kyanite gneisses of the Greek Rhodope Massif (Mposkos and Kostopoulos 2001).

The Rhodope Massif is regarded as a nappe stack of high-grade units (e.g. Burg et al. 1996), which is classically subdivided into an upper unit and a lower unit, separated by a SSE-NNW striking thrust plane, the Nestos thrust (Papanikolaou and Panagopoulos 1981). According to Reischmann and Kostopoulos (2007) and Turpaud and Reischmann (submitted), in the Central Rhodope Massif the two units correspond to two distinct terranes of different age, the Permo-Carboniferous Thracia Terrane, which was overthrusted by the Late Jurassic/Early Cretaceous Rhodope Terrane. The terranes are separated by the Nestos suture, a composite zone comprising

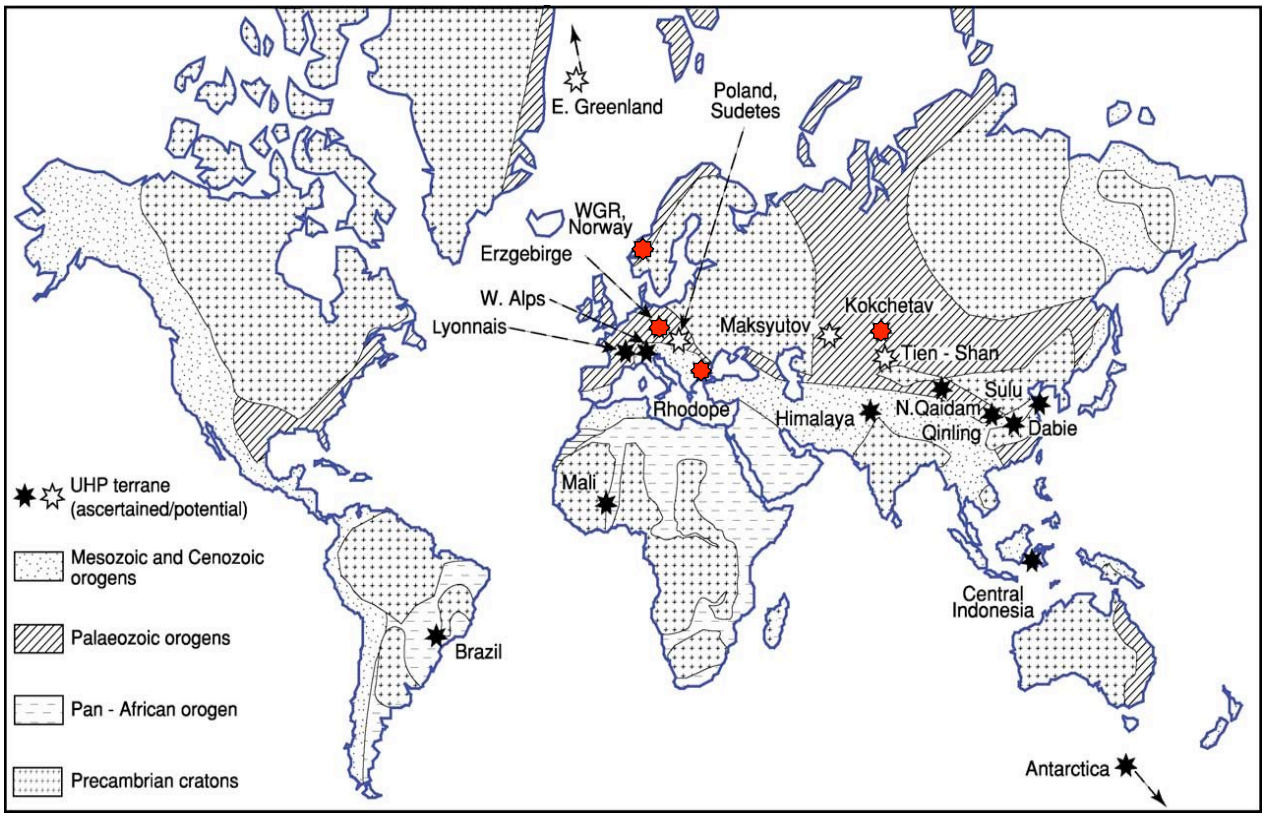

Fig. 1.1: Occurrences of UHP rocks worldwide modified after Massone (2005) and references therein. Red stars indicate the UHP occurrences, where microdiamonds were discovered in metapelitic rocks.

a variety of lithologies like metapelitic gneisses, amphibolites/eclogites with oceanic affinities (e.g. Barr et al. 1999), marbles, orthogneisses and migmatites. The metapelitic and mafic rocks of this mélange zone record a former HP and locally UHP metamorphism overprinted by a retrograde amphibolite-facies metamorphism (e.g. Liati 1986, Liati and Seidel 1996, Mposkos and Kostopoulos 2001).

This thesis focuses on the eastern part of the Rhodope Massif, northeastern Greece, where microdiamonds, indicative of UHP metamorphism, were reported from garnet-kyanite gneisses close to the Kimi and Sidiro villages (Mposkos and Kostopoulos 2001, Perraki et al. 2006). Since this discovery, several structural, petrological and geochronological studies have been carried out on the Rhodope Massif, but often concentrating on the local areas around the rocks bearing the UHP relicts. A common feature of all these localities is a variable state of retrogression of the

rocks, generally an amphibolite-facies overprint (e.g. Liati 1986), which erases the UHP history of the rocks. Therefore, tracing UHP metamorphism is a matter of microscale investigation.

The following study constitutes a combined petrological, geochemical and geochronological approach on both metapelites and orthogneisses of the Eastern Rhodope Massif to find out if the HP/UHP bearing intermediate zone is a belt throughout the Greek Rhodope Massif and if this zone is restricted to the Nestos suture. Therefore, the contact zone of the two terranes was studied along several well-constrained cross sections close to the Ada, Kimi and Sidiro villages in the Eastern Rhodope. Inclusions in zircons from metapelites were classically investigated in situ with Raman Spectroscopy and elemental distributions in zircons were studied for the first time with time-of-flight-secondary-ion mass spectrometry (TOF-SIMS) to constrain more precisely the processes and the environment of the diamond formation. Raman spectroscopy has proven to be a valuable, non-destructive tool to detect/confirm in situ diamond or coesite inclusions within other minerals like garnet or zircon, especially if these inclusions are under the surface of the host mineral. Zircon is a mineral that is chemically very resistant and stable over a wide pressure-temperature range. For these reasons it is considered to be the best host for UHP minerals (e.g. Sobolev and Shatsky 1990; Chopin and Sobolev 1995; Tabata et al. 1998).

Furthermore, zircons from felsic orthogneisses of the eastern part of the Greek Rhodope were dated by laser-ablation magnetic sector-field inductively-coupled plasma mass spectrometry (LA-SF-ICPMS) and sensitive-high-resolution microprobe (SHRIMP-II) to test the applicability of the two terrane-model of the Central Rhodope Massif (Reischmann and Kostopoulos 2007, Turpaud and Reischmann submitted) there. Another aim of this study is to decipher the pre-Alpine magmatic evolution of the Rhodope Massif and find out possible correlations to one of the other zones of the Internal Hellenides, e.g. to the Pelagonian Zone, which is similar in age and geochemistry to the structurally lower unit of the Rhodope Massif. Therefore, this thesis also presents the first Sr and Nd isotopic data of orthogneisses from both units of the Greek Central and Eastern Rhodope Massif.

2. Geological framework of the Rhodope Massif

The Hellenides formed from Cretaceous to Mid-Tertiary times as a result of terrane accretion and finally plate convergence and collision of Africa and Europe. The Hellenic orogen is traditionally divided into NNW-SSE-trending tectonostratigraphic zones (e.g. Jacobshagen 1986), starting in the east with the most internal part of the Hellenides, the Rhodope Massif, followed by the Serbo-Macedonian Massif, the Vardar Zone and the Pelagonian Zone, then followed by the External Hellenides to the west (Fig. 2.1).

Pelagonian Zone

The Pelagonian Zone is the westernmost unit of the Internal Hellenides. It comprises mainly Permo-Carboniferous igneous basement rocks of continental magmatic-arc tectonic setting (Anders et al. 2007) and Mesozoic metasedimentary rocks overlain by Tertiary to recent sediments. The Pelagonian is interpreted as a drifted Eurasian fragment, that was rifted off in the Early Mesozoic from the Eurasian margin as a result of the opening of the Meliata back-arc basin (e.g. Vavassis et al. 2000). In the northwestern part of the Pelagonian Zone Anders et al. (2006) reported the occurrence of Precambrian basement rocks, namely the Neoproterozoic Florina Terrane. The latter is interpreted as a remnant of a Gondwana-derived terrane and is assumed to be the basement on which the Pelagonian magmatic arc formed, before both units were incorporated in the Hellenides during the Eohellenic event (Jacobshagen 1986).

Vardar Zone

The Vardar Zone is located between the Pelagonian Zone to the west and the Serbo-Macedonian Massif to the east. It comprises granites, gneisses, volcanic rocks and it is characterized by numerous ophiolites. These ophiolites outline a subduction zone along the easternmost border of the Vardar Ocean. Three sub-units are distinguished in the Greek part of the Vardar Zone. The Peonias sub-zone in the east is followed by the Paikon- and the Almopias sub-zones to the west (Mercier 1966). The origin of the Paikon sub-zone is still under debate. After Brown and Robertson (2004) the Paikon arc is assumed to have formed in Mid- to Late Jurassic times as a result of the subduction of the Almopias sub-zone underneath the Serbo-Macedonian Massif.

Ricou et al. (1998) interpreted the Paikon sub-zone as a tectonic window. Felsic rocks with volcanic-arc affinity of the south-eastern part of the Peonias sub-zone were studied by Anders et al. (2005), yielding igneous formation ages between 155 and 164 Ma. Zachariadis (2007) suggested that the ophiolites of the Vardar Zone formed between 170-155 Ma in the back-arc region of an intra-oceanic subduction zone at the eastern border of the Vardar Ocean.

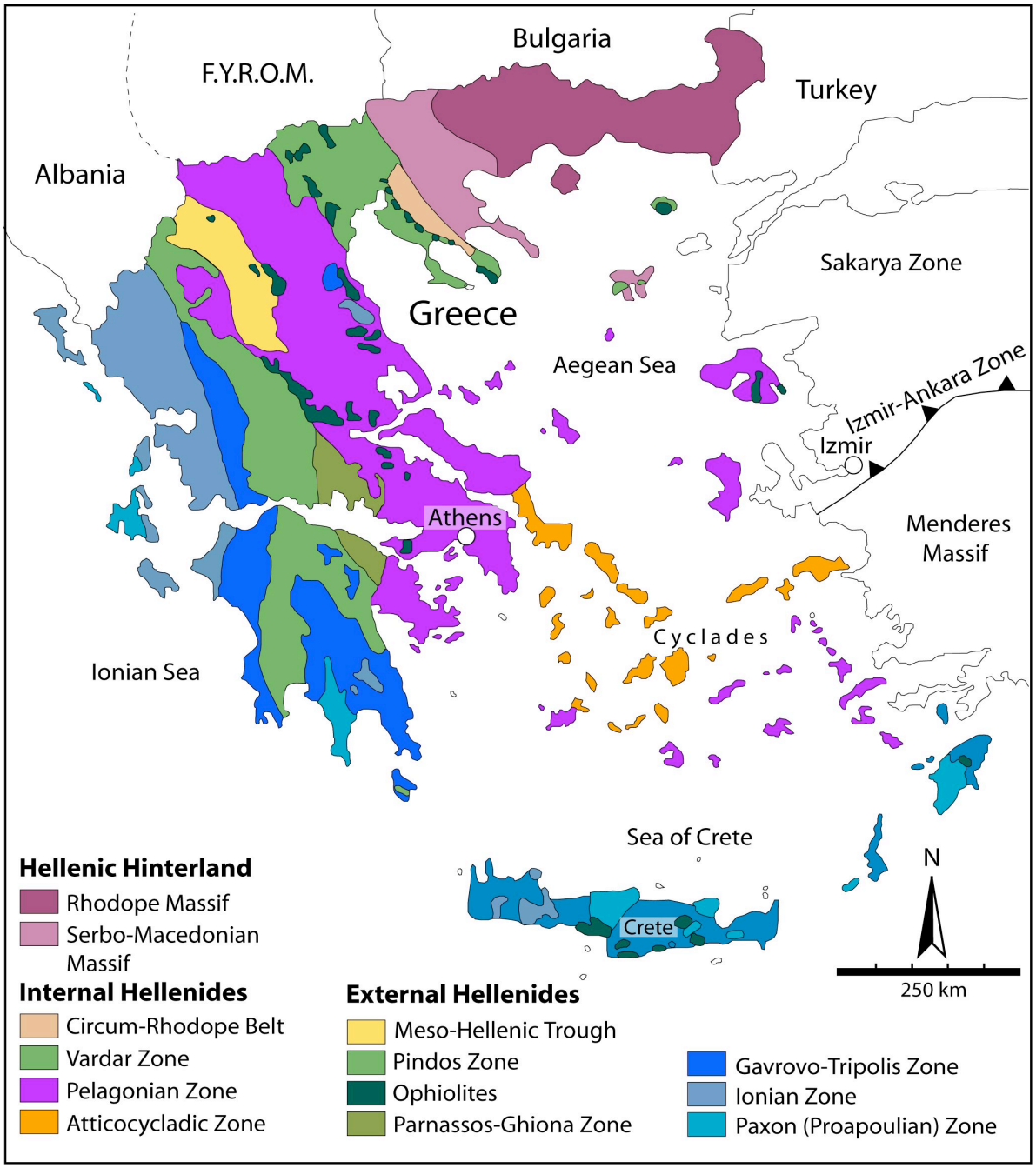

Fig. 2.1: Simplified geological map of Greece modified after Zachariadis (2007 and references therein) showing the tectonostratigraphic units of the Hellenides.

Serbo-Macedonian Massif

The Serbo-Macedonian Massif is sandwiched between the Vardar Zone to the west and the Rhodope Massif to the east. Formerly it was subdivided into two major units, the Vertiskos Unit in the northwest and the Kerdillion Unit in the east by Kockel et al. (1971). The recent work of Himmerkus et al. (2006a) complemented this subdivision by a third unit, the Late Precambrian Pirgadikia Unit, an exotic terrane located in the central-eastern Part of the Chalkidiki Peninsula. The Vertiskos Unit is characterized by Silurian, arc-related orthogneisses intruded by the granites of the Arnea suite in Triassic times (Himmerkus et al. 2006a). The Kerdillion experienced three magmatic pulses, one in the Permo-Carboniferous, one in the Late Jurassic and Early Tertiary, respectively. Geochronology, isotope chemistry and structural features are similar to the adjacent Rhodope Massif and therefore Himmerkus et al. (2006b) assumed that the Kerdillion Unit is the western promontory of the Rhodope Massif. The Vertiskos Unit and the Kerdillion Unit are separated by a crustal-scale shear zone, the Athos-Volvi Zone, comprising mafic und ultramafic rocks as well as metasediments. This is interpreted as a major ophiolite-decorated suture zone by Himmerkus et al. (2005).

Rhodope Massif

This study focuses on the easternmost part of the Hellenides, the Rhodope Massif, which occupies the major part of NE Greece and S Bulgaria. It is located between the Balkan Belt, a N-NE vergent thrust belt, to the north and the Dinarides-Hellenides to the S-SW. To the west, the Rhodope is separated from the adjacent Serbo-Macedonian Massif by a Tertiary detachment, the Strymon valley detachment (e.g. Dinter and Royden 1993). Some authors regarded the Serbo-Macedonian Massif as part of the Rhodope (e.g. Ricou et al. 1998). Controversy existed about the tectonic history of the Rhodope. For a long time, the Rhodope was regarded as a stable continental block of Precambrian or Hercynian age (e.g. Boncev 1971). More recently, the structure of the Rhodope is considered as synmetamorphic nappes, resulting from terrane accretion during the closure of a Tethys ocean (e.g. Ricou et al. 1998). Deformation and metamorphism of the Rhodope are considered to belong to events of the Alpine orogeny (e.g. Papanikolaou and Panagopoulos 1981; Burg et al. 1996). Simplified, the Rhodope Massif can be subdivided into two units as proposed by several authors (e.g. Papanikolaou and Panagopoulos

1981; Mposkos 1989). Different nomenclatures for these units were introduced in different areas/countries. A summary of the previous subdivisions of the Rhodope Massif by various authors was adapted from Turpaud (2006) and is shown in Fig. 2.2.

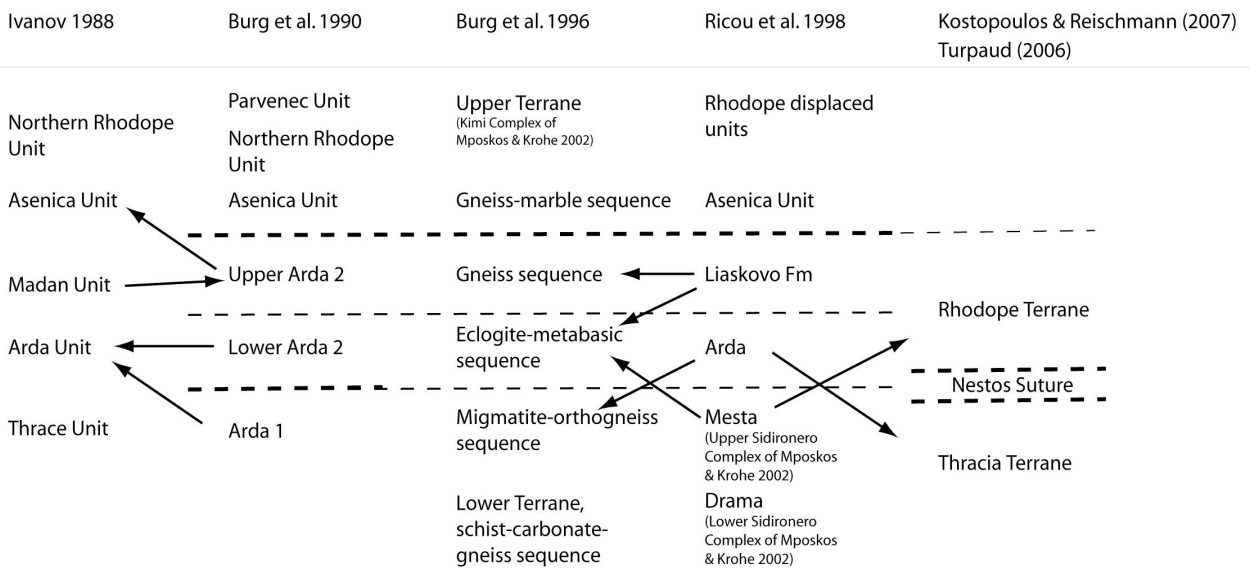

Fig. 2.2: Nomenclature for the subdivisions of the Rhodope Massif by various authors modified after Turpaud (2006).

In the Greek part, a structurally lower and a structurally upper unit are distinguished, separated by a NNW-SSE trending thrust fault, the Nestos thrust of Papanikolaou and Panagopoulos (1981). A similar subdivision was suggested by Mposkos (1989) based on the difference in metamorphic grade of the two units. According to Reischmann and Kostopoulos (2007) and Turpaud and Reischmann (submitted) these two units correspond to two distinct terranes, the Permo-Carboniferous Thracia Terrane, which was overthrusted by the Late Jurassic/Early Cretaceous Rhodope Terrane. Formerly, the tectonic units were considered to consist of metamorphic rocks of oceanic and continental origin, such as orthogneisses (some migmatitic), metapelitic gneisses, amphibolites (some „eclogitic“) and marbles, intruded and overlain by post-metamorphic volcanic and plutonic rocks (e.g. Mposkos 1989). Recent research revealed that most of the metapelites, amphibolites and marbles are part of a suture zone, which is located inbetween the two terranes (Reischmann and Kostopoulos 2007, Turpaud and Reischmann submitted). The origin of the amphibolites of the suture zone are tholeiitic basalts with either oceanic or volcanic-arc affinities (e.g. Kolcheva et al. 1986; Liati 1986; Barr et al. 1999).

Both terranes show widespread amphibolite-facies metamorphism and metamorphic conditions for the structurally lower Thracia Terrane are in the range of 550-600 °C and 14-16 kbar (garnet-chloritoid±staurolite in pelitic schists, Mposkos 1989; Mposkos and Liati 1993). Metamorphic conditions of the structurally upper Rhodope Terrane in Central Rhodope were considered to be of high-pressure metamorphism as recorded by garnet-biotite±kyanite gneisses (Mposkos and Liati 1993) and high-temperature granulite-facies conditions as suggested by a kyanite eclogite near Thermes (Liati and Seidel 1996). But following the two-terrane model of Turpaud and Reischmann (submitted) these high pressure and temperature conditions refer to rocks of the suture zone. Therefore precise P-T estimations for the structurally upper unit are not available.

A recent study of Bauer et al. (2007) on an eclogite and one metapelite of the Kimi area, which belong to the suture zone, suggests conditions of 700 °C and > 17.5 kbar for the high-pressure stage of the eclogite, followed by a high-temperature overprint (820 °C; 15.5 – 17.5 kbar). Granulite-facies metamorphism is proposed for the metapelite because of melt- and mineral inclusions trapped in zircon during formation.

The same metapelitic sample from the Kimi area is considered to have experienced even higher metamorphic conditions, since Mposkos and Kostopoulos (2001) reported the discovery of microdiamonds, multicrystalline polygonal quartz inclusions and mineral exsolutions within garnet, which are indicative of ultrahigh-pressure metamorphism. The same authors describe similar UHP indicators within garnet-biotite±kyanite gneisses from localities close to Xanthi and Sidiro in Central- and Eastern Rhodope, respectively. Pressure and temperature estimations indicate $P > 7$ GPa and $T \approx 1100$ °C for these metapelitic gneisses from the Greek Rhodope Massif (Mposkos and Kostopoulos 2001).

Timing of the metamorphic events

The ages of metamorphism of the Rhodope Massif are still under debate. A compilation of the important metamorphic ages is given in Fig. 2.3. For the Central Greek Rhodope, a SHRIMP U-Pb age of 42.2±0.9 Ma, measured on zircons of an eclogite close to Thermes, is interpreted to represent the high pressure metamorphism (Liati and Gebauer 1999). Metamorphic rims of zircons of the surrounding orthogneiss countryrock yielded almost the same age, 42.0±1.1 Ma. Therefore, the authors suggested that both, the eclogite and the orthogneiss experienced maximum pressures around 42 Ma. Further, Liati and Gebauer (1999) presented an U-Pb age of

40.0±1.0 Ma for the temperature peak, dated on zircons from a leucosome of a migmatite in the Thermes area. Metamorphic rims of zircons from a garnet-kyanite gneiss of the Central Rhodope, dated at 148.8±2.2 Ma, show Pb-loss at 40 Ma, while metamorphic domains from an amphibolitized eclogite of the West Rhodope are 51±1.0 Ma old (Liati 2005).

Because the rare earth element (REE) patterns of the metamorphic domains of the zircons from both rocks show no Eu-anomaly and the HREE patterns are flat, indicating garnet growth during zircon formation, Liati (2005) concluded that the zircons of both rocks had grown close to high-pressure conditions. Magmatic and metamorphic zircon domains from a garnet-bearing mafic rock of the Eastern Rhodope gave an U-Pb age of 117.4±3.4 Ma (protolith crystallization) and 73.5±3.4 Ma ((U)HP event), respectively (Liati et al. 2002). The latter age was also interpreted as the age of the high-pressure stage. Therefore, Liati (2005) suggested that four high-pressure metamorphic events can be distinguished and the Rhodope consists of different microcontinents, accreted during multiple Alpine subduction and collision events.

For the Kimi area in the Eastern Rhodope, Wawrzenitz and Mposkos (1997) determined an Early Cretaceous age of 119±3.5 Ma for the high-pressure metamorphism using Sm-Nd whole-rock and garnet and clinopyroxene isochrons of a garnet-pyroxenite. The same authors reported a Rb-Sr isochron age of 65.4±0.7 Ma for muscovite and feldspar cores of an cross-cutting pegmatite. Liati et al. (2002) obtained an U-Pb age of 61.9±1.9 Ma for a pegmatoid cross-cutting the garnet-bearing mafic rock in the same area. Also for the Kimi area, high-temperature peak metamorphism of an eclogite and diamondiferous metapelite was dated at 170 to 160 Ma by Bauer et al. (2007), while the retrograde amphibolite facies overprint of the eclogite occurred at 79±3 Ma.

Reischmann and Kostopoulos (2002) dated a diamondiferous garnet-kyanite gneiss from the Central Rhodope close to Xanthi. The Sm-Nd garnet-whole-rock age of 140±4 Ma is interpreted as a cooling age after UHP metamorphism. Monazite ages of the same sample, which could represent the UHP event, range between 185 and 146 Ma. Rb/Sr mica/whole rock ages of the same sample yielded ages of 37 (muscovite) and 34 (biotite) Ma and document Eocene exhumation (Reischmann and Kostopoulos 2002).

Similar K-Ar ages on micas, ranging between 35 and 50 Ma, were interpreted as Eocene cooling ages (Liati 1986; Lips et al. 2000). Liati (2005) emphasized that the youngest ages (around 35 Ma) are the closest to the metamorphic event and could be correlated to the 36.1±1.2 Ma

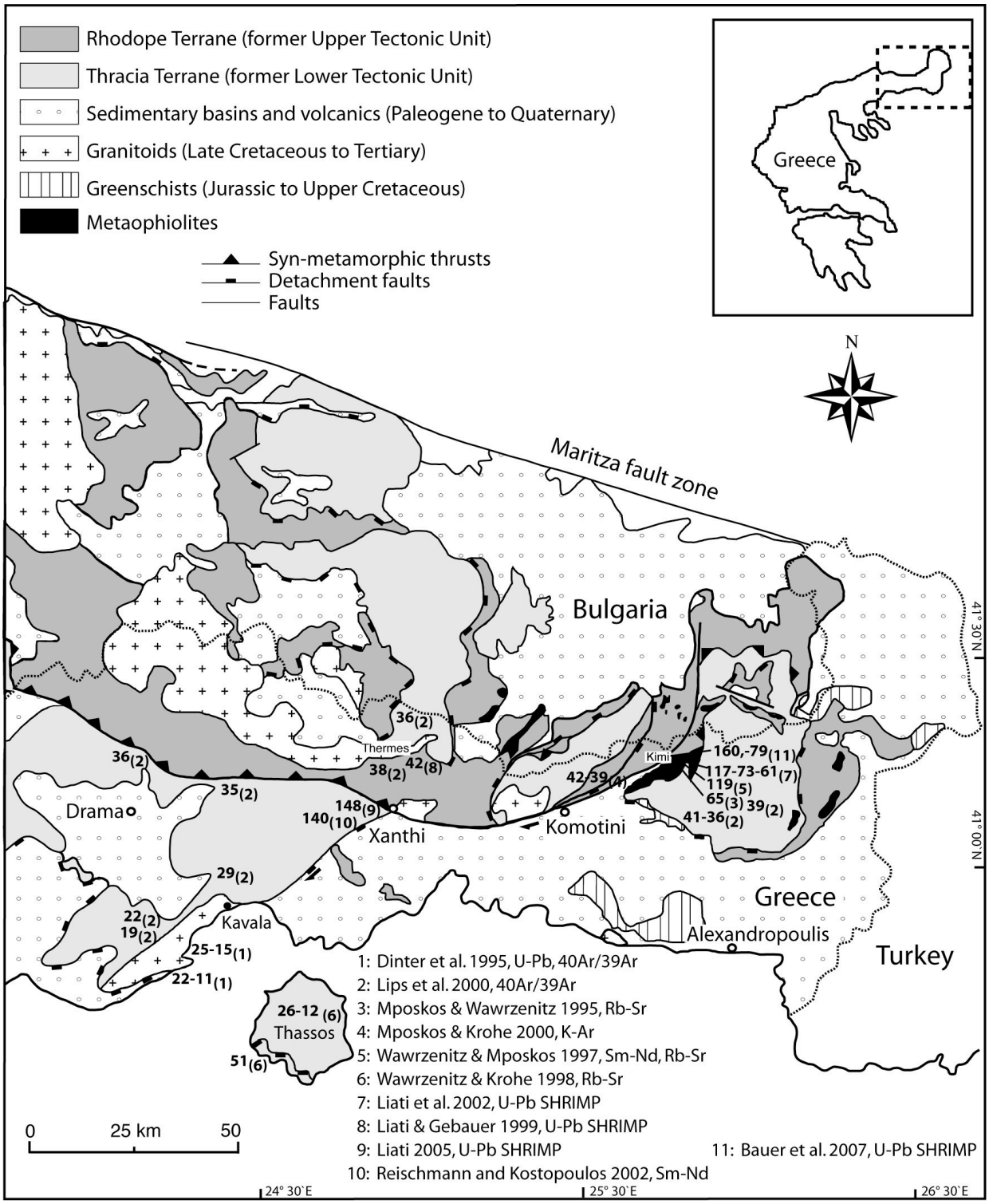

Fig. 2.3: Simplified map of the Rhodope Massif modified after Bonev et al. (2006) showing the main tectonic units and locations of dated metamorphic events interpreted as metamorphic cooling ages of various authors.

SHRIMP age of a late pegmatite in the Sminthi area, representing late stage fluids. Similar cooling ages are reported from Bulgaria (Ar-Ar 35.5±0.4 Ma; Rb-Sr 35.3±0.4 Ma, both on biotite, Rohrmeier et al. 2002; Ovtcharova et al. 2003). Ar-Ar ages decrease to 15 Ma in the structurally lower unit near the eastern margin of the Strymon valley (Lips et al. 2000).

In the Bulgarian Rhodope, U-Pb monazite ages of migmatites of the upper unit range between 35 and 37 Ma and date the high-temperature overprint (Peytcheva et al. 2004, Ovtcharova et al. 2004). From the lower unit, including also migmatic gneisses, Ovtcharova et al. (2004) reported monazite ages between 47 and 52 Ma, and interpreted the age difference as a result of different exhumation of the two units.

Protolith intrusion ages

In the Rhodope Massif two main protolith intrusion age groups can be distinguished. Permo-Carboniferous ages are restricted to the structurally lower Thracia Terrane, whereas the structurally upper Rhodope Terrane comprises Late Jurassic and Early Cretaceous ages (Fig. 2.4).

Thracia Terrane: Wawrzenitz (1997) dated orthogneisses from Thassos island by the conventional U-Pb method and obtained an age of 285±3 Ma on monazite and ca. 260 Ma on zircon. From the Central and Eastern Bulgarian Rhodope, Peytcheva and von Quadt (1995), Ovtcharova et al. (2002) and Peytcheva et al. (2004) reported U-Pb ages of 300±5.5, 310.7±4.6 and 319±9 Ma for various metagranitoids. Furthermore, SHRIMP U-Pb ages of 294±8 Ma and 313.9±2.1 Ma were reported for orthogneisses in the Central and Eastern Rhodope, respectively (Liati and Gebauer 1999, Liati and Fanning 2005).

Rhodope Terrane: Gebauer and Liati (1997) dated a biotite-metagranitoid from Central Rhodope at 151±4 Ma via SHRIMP. Similar ages (149.0±0.66 Ma, 151.9±2.2 Ma) are reported from Bulgaria (Ovtcharova et al. 2004). Recently, Turpaud (2006) and Turpaud and Reischmann (submitted) dated orthogneisses from the Central Rhodope using single-zircon Pb-Pb evaporation and U-Pb SHRIMP dating. The results supported the data mentioned above and contributed significantly to distinguish the two major units by their protolith intrusion ages, being a Permo-Carboniferous lower terrane overthrusted by a Late Jurassic/Early Cretaceous upper terrane. Based on geochronological and geochemical data of the orthogneisses, the units were interpreted

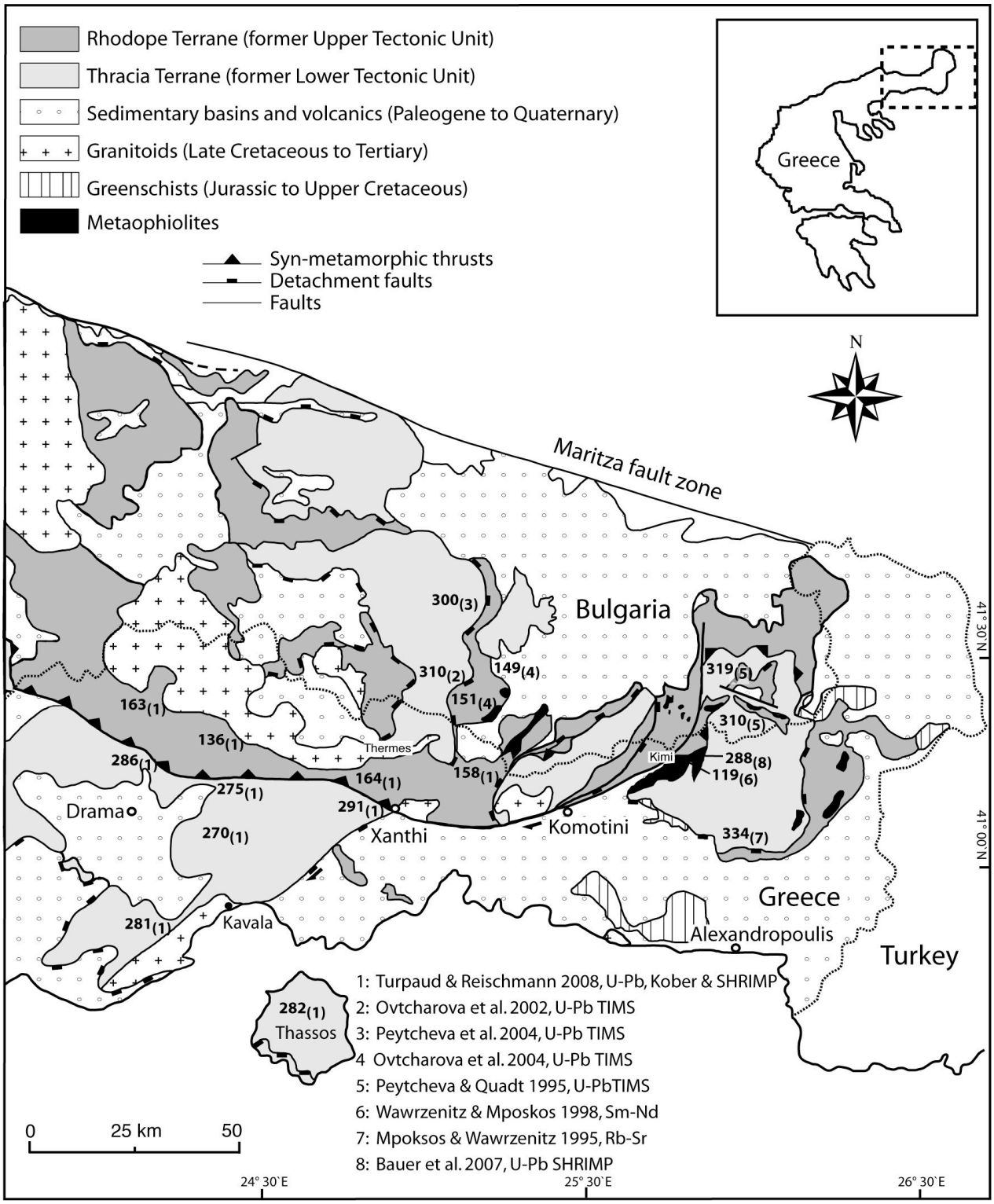

Fig. 2.4: Simplified map of the Rhodope Massif modified after Bonev et al. (2006) showing the main tectonic units and locations of protolith age dating of various authors.

by Reischmann and Kostopoulos (2007) and Turpaud and Reischmann (submitted) as two distinct terranes, separated by a suture. The latter can be seen as a strongly sheared melange zone, comprising mylonites, migmatites, amphibolites/eclogites, metapelites and marbles, where the mafic and pelitic rocks show evidence for HP and locally UHP metamorphism (Mposkos and Kostopoulos 2001, Perraki et al. 2006).

Protolith intrusion ages for the mafic rocks of the suture zone are rare. U-Pb SHRIMP dating of a garnet-rich mafic rock from the Kimi area gave an age of 117.4±3.4 Ma (Liati et al. 2002). A similar rock was dated by Wawrzenitz and Mposkos (1997) at 119±3.5 Ma and interpreted as the age of high-pressure metamorphism. Bauer et al. (2007) suggest a Permian crystallization age for the gabbroic protolith of an eclogite from the Kimi area.

3. Study Area

The study area comprises several well-constrained cross sections in the Greek part of the Eastern Rhodope Massif, close to the Ada, Kimi and Sidiro villages (Figs. 3.1, 3.5). In the following these sections are referred to as the „Paterma-Ada section“, the „Drania-Organi-Kimi section“ as well as the „Mega Derio-Sidiro section“. These areas were chosen because of the opportunity to investigate both tectonic units, the Thracia and the Rhodope Terrane, as well as the intermediate mélange unit lying in between. Additionally, to constrain more precisely the extent of the different units, orthogneisses were sampled also from within the two terranes. Sample localities and geographic coordinates are given in Appendix A.

The Paterma-Ada section

This SSW-NNE trending, 7.5 km long section starts north of Paterma within the intermediate mélange zone (Fig. 3.1). The major foliation of the different lithologies of this section dips ca. 45° to the southeast. Simplified cross sections are shown in Fig. 3.2a, b.

Near Paterma, a massif horizon of migmatitic amphibolites, locally garnet-bearing, crops out. In some places, the leucosomes contain cm-sized garnet. Further to the north, the amphibolites are followed by a sequence of orthogneisses. Three varieties of gneiss alternate in this sequence: Medium-greyish augengneiss with mostly stretched augen up to 3 cm (Fig. 3.3a), medium to coarse-grained biotite-muscovite-gneiss without significant augen-texture and leucocratic, fine-grained gneiss with predominantly muscovite. A m-sized horizon of marble is embedded within the gneiss sequence. The section continues with predominantly amphibolites, mainly fine- to medium-grained, without visible garnet, but where leucosomes are present, garnets can reach up to several mm across. The lithology merges into a zone with dm-scale intercalations of amphibolites, highly sheared orthogneisses, garnet-kyanite micaschists (e.g. F157, Fig. 3.3b) and garnet-bearing amphibolites/garnet-amphibole-bearing gneisses (e.g. F166, Fig. 3.3c). This zone is interpreted here as a highly sheared mélange zone and has a width of approximately 350 m. The mélange zone is followed by a horizon of massive amphibolites, which overlay strongly deformed augengneisses further to the north, belonging to the structurally lower Thracia Terrane. The end of the section is marked by a weak to virtually undeformed, porphyritic, granitic gneiss close to Mitikas village in the structurally lower Thracia Terrane (Fig. 3.3d).

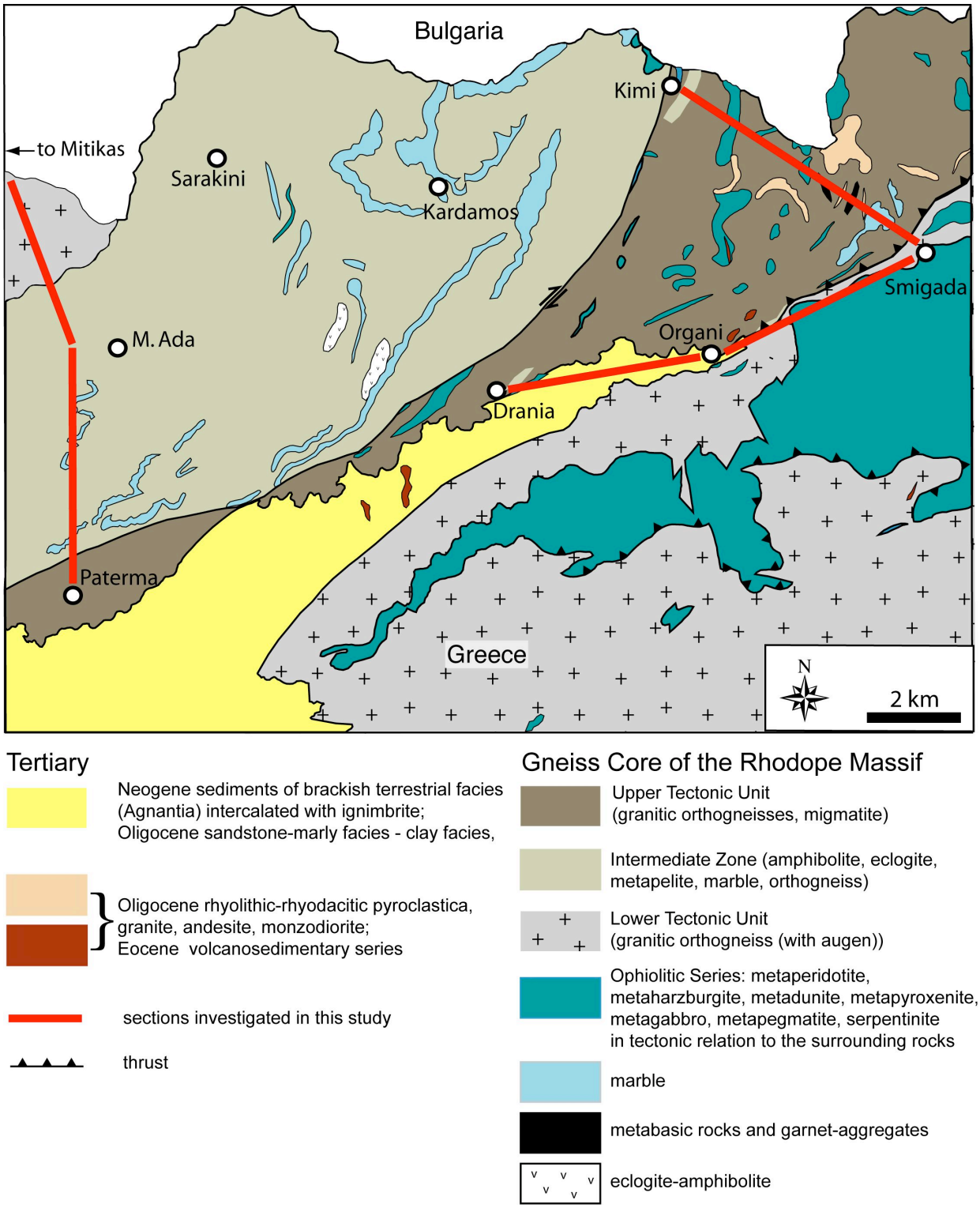

Fig. 3.1: Geological map of the study area Paterma-Ada-Organi-Kimi based on unpulished IGME work, courtesy of Dr. Papadopoulos, Xanthi branch, 2004, and own field observations. Red lines mark the cross sections investigated during this study.

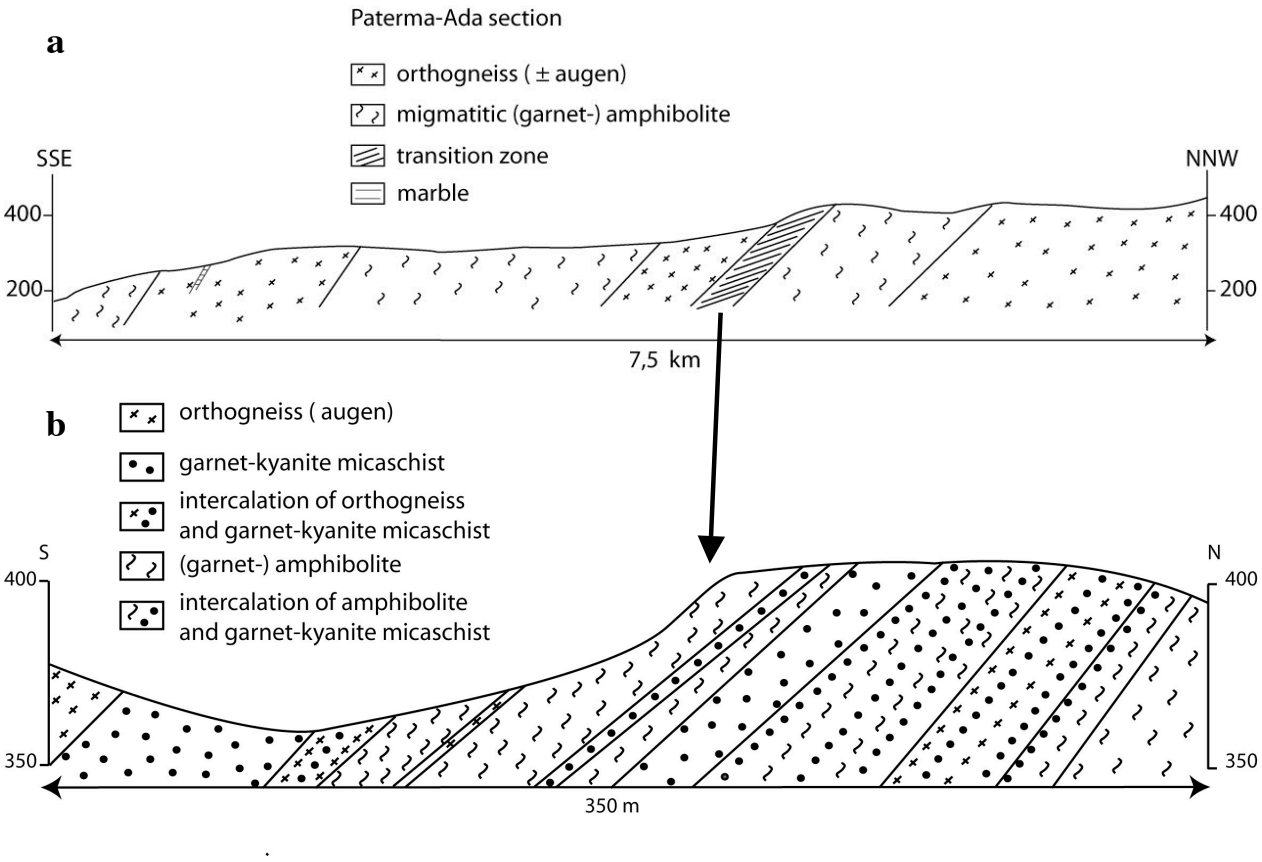

Fig. 3.2a, b: a) Simplified cross section NNW of Paterma, 5 x vertical exaggeration. The location of the section is shown in Fig. 3.1. b) Simplified cross section of the transition zone NNW of Paterma, 6.5 x horizontal exaggeration.

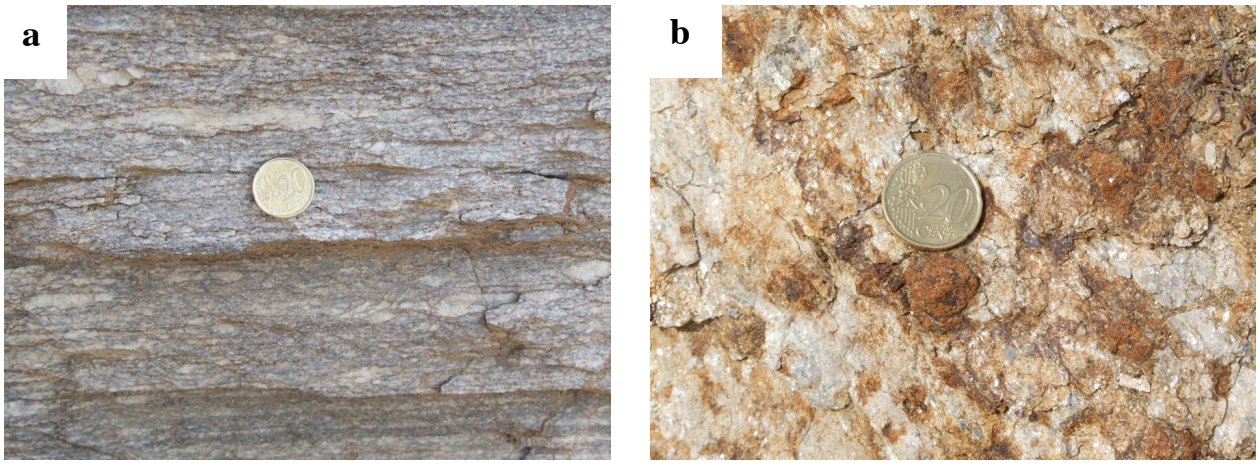

Fig. 3.3a, b: Photographs from the Ada-section; a) Medium-greyish orthogneiss with stretched augen (e.g. RH345); b) Garnet-kyanite gneiss; garnet size can reach up to 2 cm (F157).

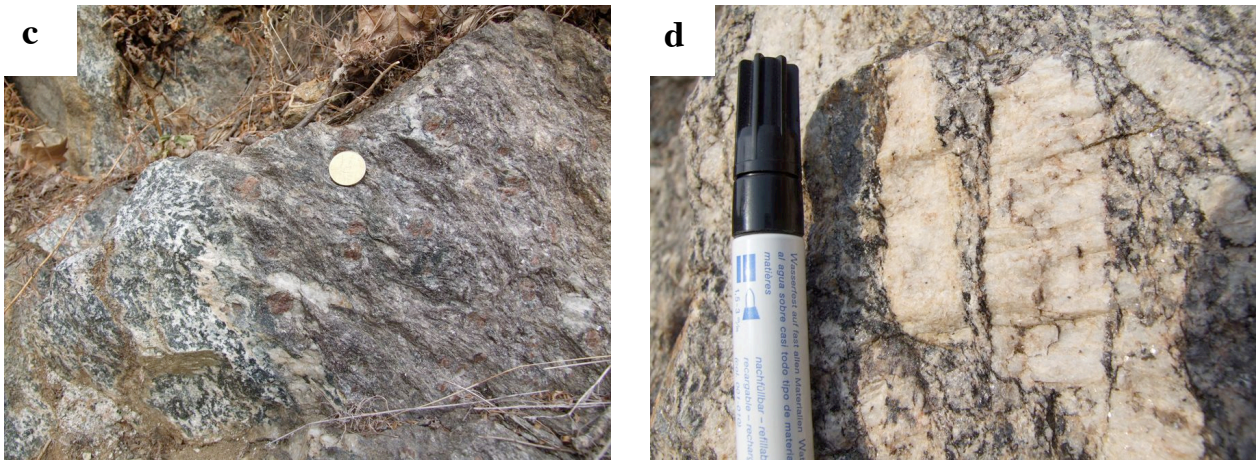

Fig. 3.3c, d: Photographs from the Paterma-Ada-section; c) Contact of amphibolite (left) and garnet-kyanite-gneiss (F166, right) showing signs of partial melting; d) Weakly deformed, porphyritic orthogneiss close to Mitikas (RH361).

The Drania-Organi-Kimi section

The Kimi area comprises more than one profile. Outcrops were studied along the roads from Drania to Organi, from Organi to Smigada and from Smigada to Kimi (Fig. 3.1). The SW-NE trending Drania-Organi-Smigada section is ca. 13 km long and the major foliation of the different lithologies dips to the northwest, with angles of ca. 65° between Drania and Organi and ca. 44° between Organia and Smigada. The section is parallel to the contact zone of the Thracia and the Rhodope Terrane (Fig. 3.1). The SE-NW trending Smigada-Kimi section has a length of ca. 7 km and the major foliation of the rocks dips ca. 56° to the southeast. Simplified cross sections are shown in Fig. 3.4a, b.

East of the village Drania, a garnet-micaschist crops out (RH412), enclosing lenses of garnet-amphibolite with 20 cm up to 40 cm in diameter, followed by a horizon of migmatitic amphibolite, locally intercalated with sheared biotite-gneisses. These rocks belong to the Intermediate Unit and are overlain by Tertiary sediments (sandstones) until the village Organi (Fig. 3.1, 3.4a). East of Organi a leucocratic, fine-grained to mylonitic gneiss crops out (RH413), where only in few parts the augen-texture is preserved.

Fig. 3.4a, b (page 18): a) Simplified cross section NE of Drania, 2.9 x vertical exaggeration. b) Simplified cross section SE of Smigada, 2.9 x vertical exaggeration. The location of the sections is shown in Fig. 3.1.

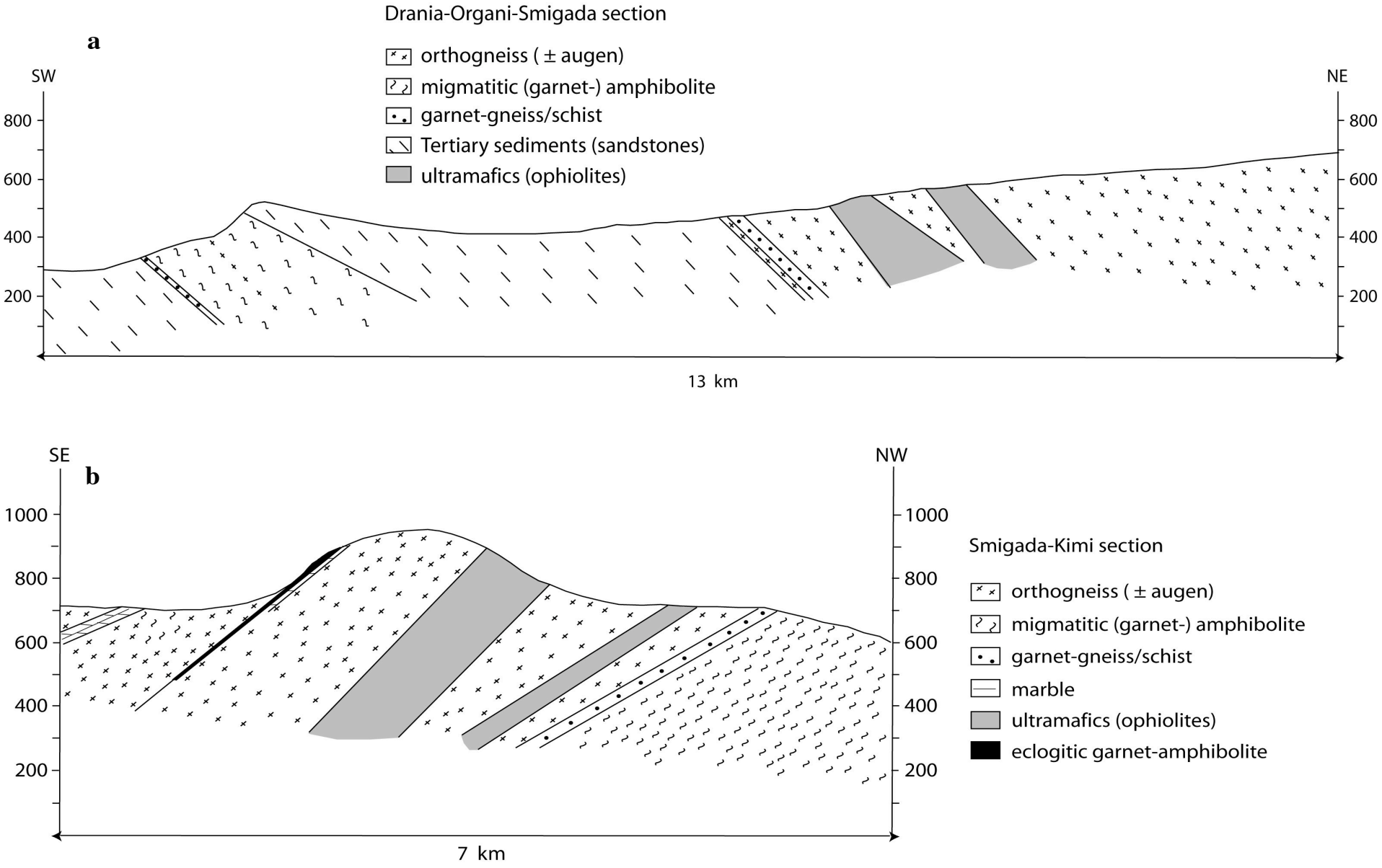
a
Drania-Organi-Smigada section
orthogneiss (± augen)
migmatitic (garnet-) amphibolite
garnet-gneiss/schist
Tertiary sediments (sandstones)
ultramafics (ophiolites)
SW
NE
800
600
400
200
13 km
b
SE
NW
1000
800
600
400
200
7 km
Smigada-Kimi section
orthogneiss (± augen)
migmatitic (garnet-) amphibolite
garnet-gneiss/schist
marble
ultramafics (ophiolites)
eclogitic garnet-amphibolite

Further northeast the section continues with a 100 m-sized horizon of garnet-micaschist (RH414) followed by medium to fine-grained augengneisses intercalated with leucocratic muscovite-gneisses. The rest of the section along the road towards Smigada is characterized by a complex alternation of augengneisses (e.g. RH429), belonging to the Thracia Terrane, and ultramafic rocks. The latter belong to ophiolitic bodies, which are abundant in this area (Fig. 3.1).
The cross section Smigada-Kimi displays the typical rock assemblage of the mélange zone, comprising garnet-gneisses, amphibolites, eclogites, orthogneisses (locally migmatitic) and marbles (Fig. 3.4b). It starts northwest of Smigada with a medium-grained, weakly deformed, medium-grained biotite-gneiss (RH423) followed by a 200 m-sized horizon of marble. The section continues with strongly deformed, locally mylonitic biotite-gneiss, which is in some places intercalated with migmatitic amphibolites and/or leucocratic muscovite-gneisses. A massive coarse-grained layered garnet-amphibolite block of about 35 meters in diameter is embedded in this gneiss sequence. This rock contains layers of predominantly garnet in cm-scale and is surrounded by a medium-grained amphibolite without visible garnet, crosscut by numerous leucosomes. The section continues with a ca. 100 m-sized marble horizon. Further northwest the section is characterized by intercalations of mainly biotite-gneisses and amphibolites, which are followed by ophiolitic ultramafic rocks. Near the village Kimi a horizon of completely disintegrated garnet-gneiss/schist is followed by migmatitic amphibolites until the village.

The Sidiro section

The W-E-trending profile starts east of Mega Derio on a road towards Sidiro village in orthogneisses belonging to the Thracia Terrane (Fig. 3.5). The section is 8 km long and the major foliation of the different lithologies dips to the northeast, with angles of approx. 50°. A simplified cross section is shown in Fig. 3.6. The orthogneisses are predominantly highly sheared, leucocratic muscovite-gneisses (e.g. RH387), in few places, biotite-muscovite-gneisses with small augen (up to 4 mm) occur, but were not sampled because of the advanced stage of weathering. Therefore, similar samples were taken on a parallel road, several hundred meters to the south (RH389, RH390). After 3 km, the sheared orthogneisses are followed by a ca. 100 m broad horizon of garnet-gneiss with garnets up to 1 cm in size (RH388, Fig. 3.7a) in the central

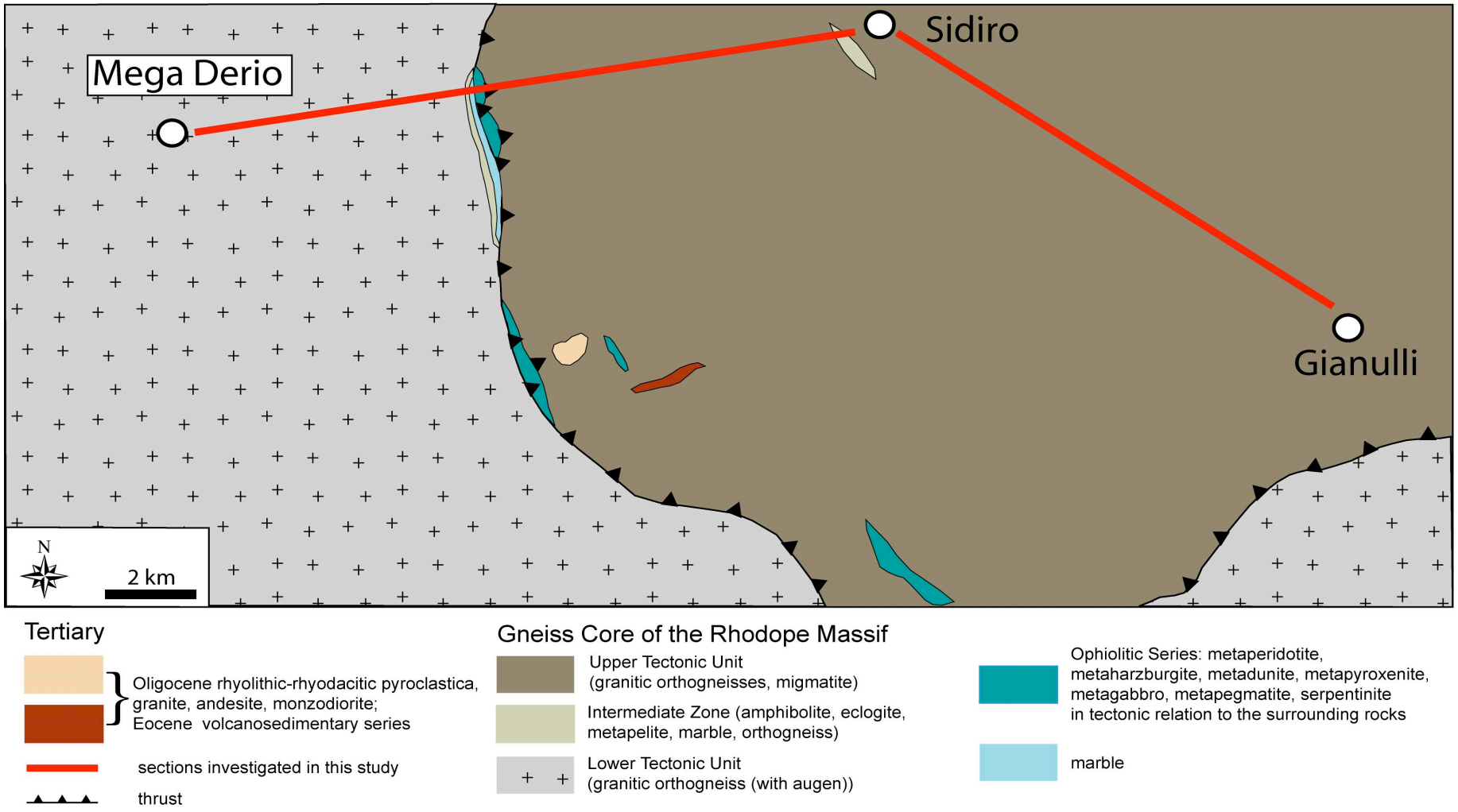

Fig. 3.5: Geological map of the study area Mega Derio-Sidiro-Gianulli based on unpulished IGME work, courtesy of Dr. Papadopoulos, Xanthi branch, 2004, and own field observations. Red lines mark the cross sections investigated during this study.

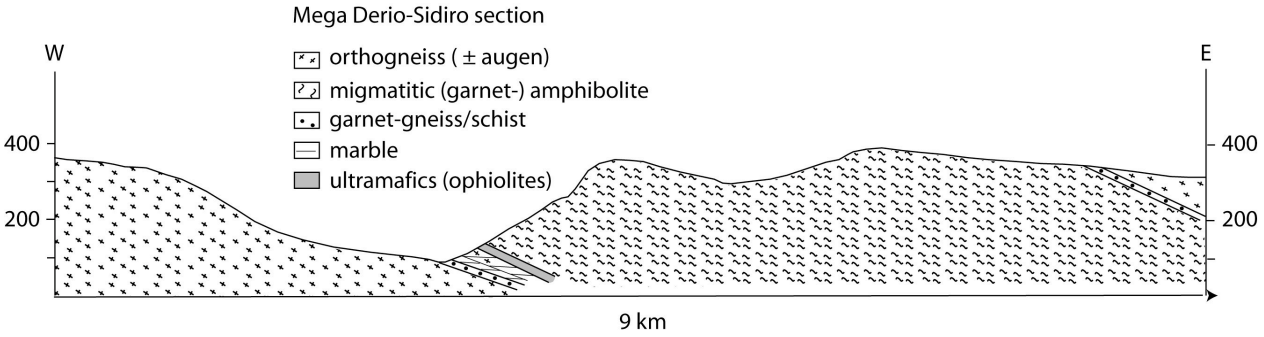

Fig. 3.6: Simplified cross section W of Mega Derio, 2.9 x vertical exaggeration. Location of the section is shown in Fig. 3.5.

part of the metapelite horizon and decreasing garnet size to the outer parts. Boudinaged amphibolite lenses of around 15 x 20 cm in size and eclogitic texture are intercalated in this garnet-gneiss (Fig. 3.7b). Macroscopically, these medium-grained rocks show small garnets surrounded by plagioclase-coronas in a matrix of amphibole. The cross section continues with two alternations of highly sheared muscovite-gneiss and marble. The marble layers are ca. 3–5 m thick. Further to the east, the second marble horizon is followed by ophiolitic, ultramafic rocks and then by a horizon of garnet-amphibolite with eclogitic texture. The amphibolite is characterized by cm-sized muscovite flakes. The remaining profile is dominated by migmatitic amphibolites until Sidiro village. East of Sidiro, a disintegrated horizon of garnet-gneiss is followed by migmatic, leucocratic muscovite-gneisses of the Rhodope Terrane (RH447, RH455).

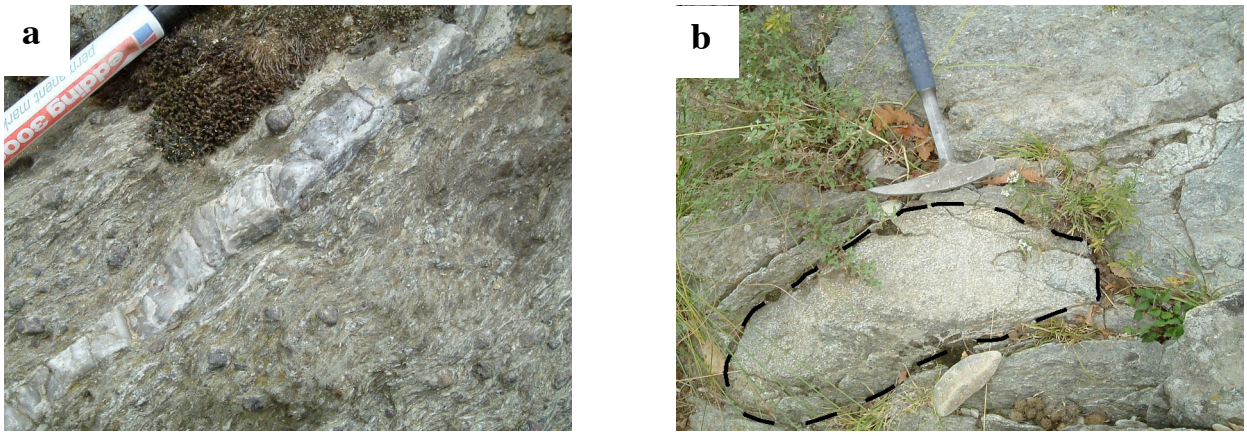

Fig. 3.7a, b: a) Garnet-gneiss (RH388) with garnet size up to one cm from the Sidiro-section; b) Amphibolite lens in garnet-gneiss (RH388), the “whitish” colour results from plagioclase coronas around garnet.

4. Metapelites

4.1 Petrography of the metapelites

The metapelites investigated in this study were sampled from the intermediate mélange zone between the Thracia and Rhodope Terrane which is exposed in the cross sections described in chapter 3. They belong to the Upper Tectonic Unit in the sense of Mposkos and Liati (1993). Typically the metapelites, namely garnet±kyanite micaschists or gneisses, are intercalated with quartzofeldspatic rocks, amphibolites (presumably former eclogites) and marbles. The mineral assemblage includes garnet, ± kyanite, ± staurolite, muscovite, ± paragonite (only F157), biotite, ± amphibole, plagioclase, ± K-feldspar, and quartz and accessory minerals like rutile, turmaline, apatite and zircon. The mineralogy of the investigated samples is given in *Table 4.1.1*. In the Ada section two varieties of garnet-kyanite gneisses can be observed. One variety contains only biotite and muscovite, the other is biotite-dominated and additionally contains amphibole.

Table 4.1.1: Mineralogy of the metapelites of the Eastern Rhodope Massif (abbreviations are explained in Appendix C)

sample	location	qtz	kfs	pl	grt	amph	bt	ms	par	chl	ky	st	ep	zoi	ru	tur
RH350	Ada	x	±	x	x	-	-	x	-	x	-	-	-	-	-	-
RH352	Ada	x	±	x	x	-	x	x	x	x	x	x	x_{ep}	-	x	-
F157	Ada	x	x	x	x	-	x	x	x	x	x	x	x_{ep}	-	x	-
F162	Ada	x	x	x	x	x	x	x	-	x	-	-	x_{ep}	x_{zoi}	x	-
F163	Ada	x	x	x	x	-	x	x	-	x	x	-	x_{ep}	-	x	-
RH362	Ada	x	x	x	x	x	x	-	-	x	x	-	-	-	x	-
RH363	Ada	x	±	x	x	x	x	-	-	x	x	-	-	x_{zoi}	x	-
RH364	Ada	x	±	x	x	-	x	x	-	x	x	-	x_{ep}	-	x	-
F166	Ada	x	±	x	x	x	x	x	-	x	x	-	x_{ep}	-	x	-
RH388	Mega Derio-Sidiro	x	±	x	x	-	x	x	-	x	-	-	-	-	-	x
RH391	Mega Derio-Sidiro	x	±	x	x	-	x	x	-	x	-	-	-	-	-	x
RH412	Drania-Organi	x	±	x	x	-	x	x	-	x	x	-	-	-	-	-
RH414	Organi-Smidaga	x	x	x	x	-	-	x	-	-	-	-	-	-	x	x
RH422	Smigada-Mirtiski	x	±	x	x	-	-	x	-	-	-	-	-	-	x	x
RH433	Kissari	x	±	x	x	-	x	x	-	x	-	-	-	-	x	x

The size of the **garnet** porphyroblasts ranges from a few millimetres (RH412) up to ca. two centimetres (F157) and the grains are typically partly resorbed and replaced by plagioclase and biotite and/or muscovite. Inclusions in the garnet are abundant and comprise quartz, rutile, white mica, biotite, amphibole (RH363), plagioclase, epidote/zoisite, apatite, zircon and ore minerals (magnetite, ilmenite, Fe-sulfides). Furthermore, samples RH352 and F157 exhibit paragonite,

staurolite and rarely kyanite inclusions in the garnet, which indicate prograde growth in the stability fields of these minerals (Figs. 4.1.1a-c). All garnets show evidence for deformation because they are cracked, sheared and often torn apart (e.g. F157, RH412) or rotated (RH388); the latter is indicated by the s-shaped inclusion pattern. Some samples contain skeletons of garnets which form a network around rectangular quartz-inclusions. A peculiarity of the garnet in sample RH388 is the growth of a second garnet generation forming a rim with less inclusions around the older rotated core (Fig. 4.1.1d). The cracks in garnet are filled either by biotite and plagioclase, sometimes K-feldspar or late stage chlorite. **Kyanite** occurs generally as prismatic porphyroblasts in the matrix of the samples (Fig. 4.1.1e). In the samples RH352 and F157 kyanite occurs also as inclusions in garnet. The grains can locally reach up to 5 mm in size (F157) but are usually much smaller around half a millimetre and they are partly replaced by biotite and plagioclase or muscovite. Similar to the garnet they are deformed and sheared, showing undulose extinction and are often torn apart. Because all other minerals lack this intensive deformation, it is clear that garnet and kyanite were formed before the pervasive deformation took place. Additionally to kyanite, the mineralogy of the matrix of these metapelites comprises quartz, plagioclase, biotite, muscovite, chlorite, amphibole, epidote, (clino-) zoisite, rutile and sometimes turmaline. K-feldspar is rare and only observed in a few samples. **Muscovite** either occurs as inclusions in garnet, as large flakes together with quartz defining the foliation or as small flakes in embayments of garnet or kyanite. In the large muscovite flakes, which form layers together with quartz, rutile aggregates are common inclusions. **Biotite** is usually associated with plagioclase, except for rare biotite inclusions in garnet porphyroblasts (e.g. F157) and except for biotite and quartz growing in pressure shadows of garnet (F157). Biotite and plagioclase partly replace garnet and kyanite porphyroblasts, but apart from this, the two minerals form layers in the foliation of the rocks. In contrast to the other samples, in RH412 matrix biotite grows in no preferred orientation. In many samples biotite is strongly chloritized (e.g. RH412) and locally it shows pleochroitic halos around zircon inclusions. It is likely that much of the **chlorite** is derived from biotite, which is indicated by partly chloritized biotite grains or sagenitic rutile within the chlorite flakes that point to a former Ti-rich phase. Chlorite also replaces amphibole and represents the last stage of metamorphism of the metapelitic rocks, which is greenschist-facies. Chlorite is present in the matrix as well as along cracks in garnet. The latter indicates that the greenschist-facies event represents the deformation event that caused the cracking of the garnet and the growth of chlorite on these cracks.

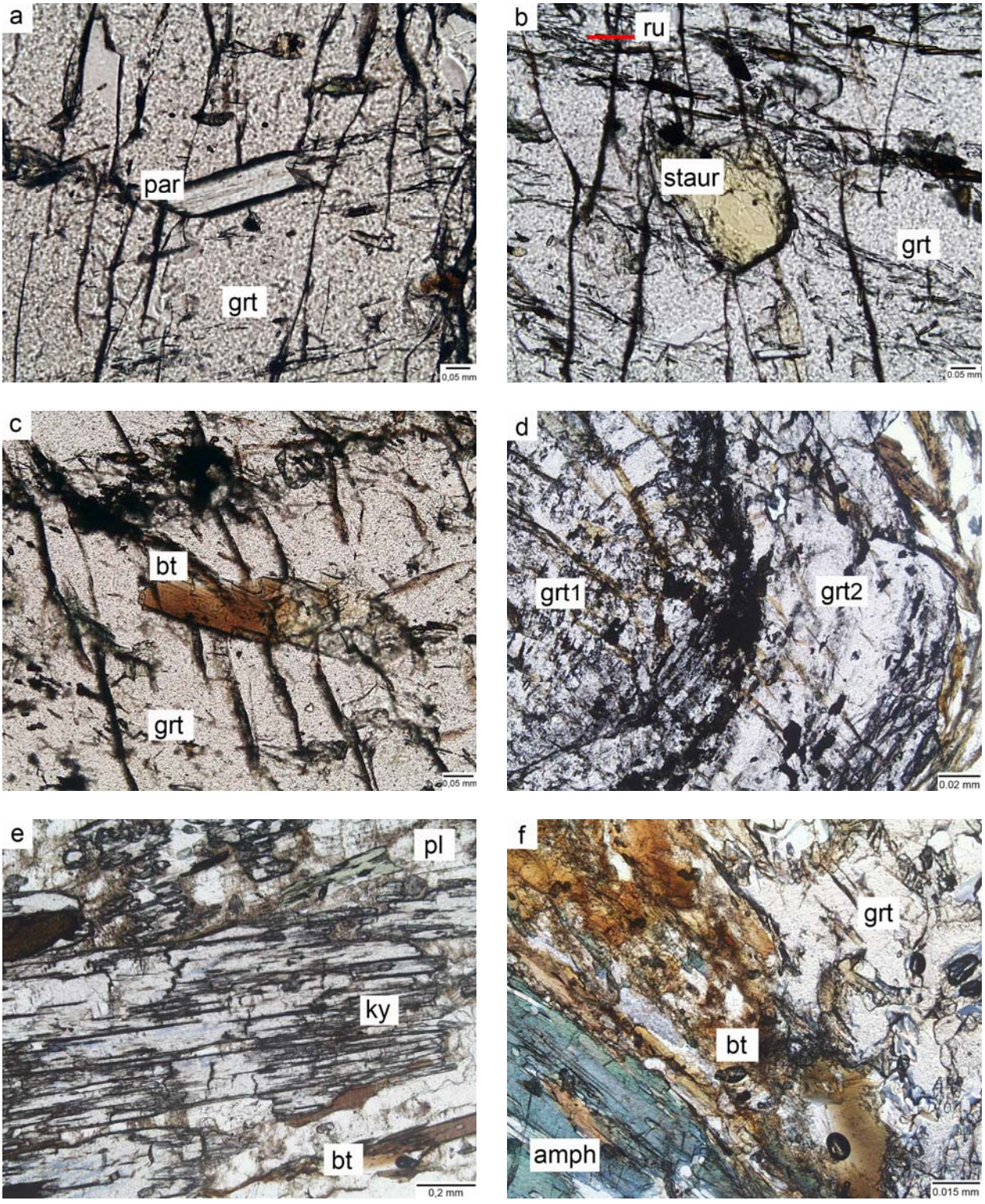

Figs. 4.1.1a-f: a) Paragonite inclusion in garnet in metapelite sample F157; b) Staurolite inclusion and rutile needles in garnet in F157; c) Biotite inclusion in garnet in F157; d) Two generations of garnet in sample RH388; e) Matrix kyanite in F157 surrounded by plagioclase and biotite; f) Biotite and amphibole growing retrograde at the expense of garnet in sample F166.

Some garnet-kyanite gneisses from the Ada section, which are derived from a more mafic source rock (see chapter 4.3), contain green **amphibole** in the matrix as well as inclusions in garnet. This amphibole forms layers in the foliation of the rock together with biotite (Fig. 4.1.1f). **Rutile** is an abundant mineral phase in most of the metapelites. It occurs as inclusion in most minerals and is also part of the matrix. Two types of textures of rutile can be observed. Rutile forms inclusions in garnet as roundish aggregates as well as bands or swarms of long prismatic needles (F157, Fig. 4.1.1b) whereas in the matrix only aggregates can be found. **Plagioclase** is part of multi-phase inclusions in garnet and is the dominant feldspar in the matrix of most samples. In most cases it shows well developed polysynthetic twinning but myrmekites occur as well (F166). Plagioclase also replaces **epidote and zoisite**, which form xenomorphic porphyroblasts in the matrix. **Quartz** is present in all metapelitic samples. It occurs as inclusion in garnet and as layers together with muscovite. Matrix quartz is always recrystallized. In the case of RH388 quartz and fine-grained muscovite define the mylonitic texture of the rock.

4.2 Mineral chemistry of the metapelites

The major element analyses of garnet, staurolite, muscovite/paragonite, biotite, chlorite, amphibole, kyanite and plagioclase were obtained by using the Jeol 8900 RL electron microprobe of the University of Mainz. Four metapelitic samples were chosen for investigation: The samples F157 and F166 from the Ada section, RH388 from the Sidiro section and RH412 from the Kimi section. Representative analyses of the minerals described in the following are compiled in the *Tables 4.2.2, 4.2.3* and *4.2.4*. Analytical procedures and analyses are given in Appendix B and C.

Garnet

The garnets are all almandines with X_{fe} (Fe/(Fe+Mg) ranging from 0.63 to 0.95, of which RH412 has the lowest X_{fe} (0.63–0.72) and the highest X_{mg} (0.24–0.30). The grossular content (X_{grs}=Ca/(Fe+Mg+Mn+Ca)) varies between 0.11 and 0.29 and the spessartine component between 0.01 and 0.08. Before measuring profiles on the garnet, element maps have been proceeded on the grains to test if concentric zoning occurs (Figs. 4.2.1a-d). It is apparent that in the case of F157 the core, which is indicated best by the Mn distribution map, is not in the center of the garnet grain (Fig. 4.2.1a). This explains the rather unsymmetric pattern of the profile measured on this garnet.

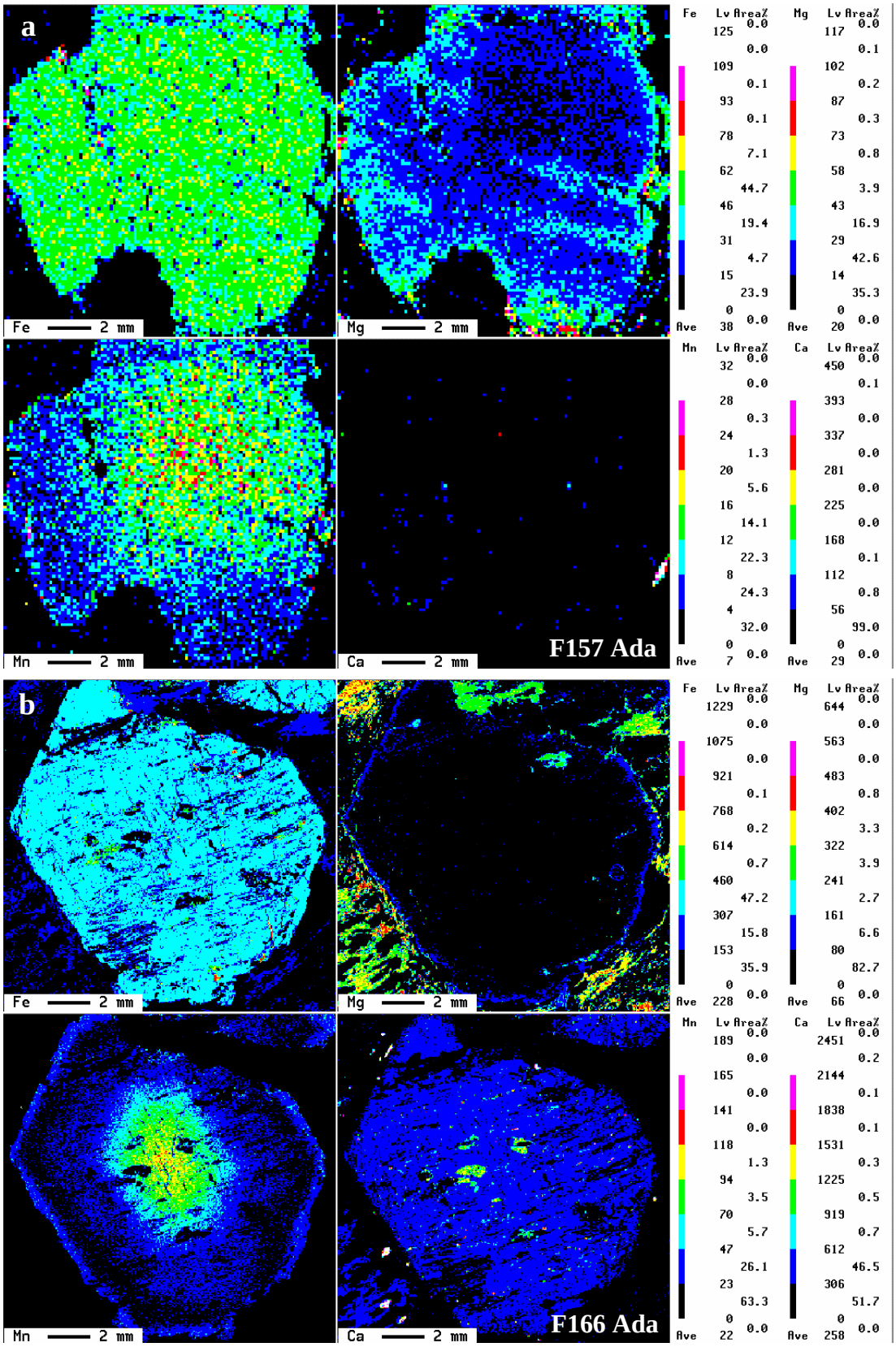

Figs. 4.2.1a-b: Element distribution maps for Fe, Mg, Mn and Ca of garnets from the metapelite samples; a) F157, b) F166.

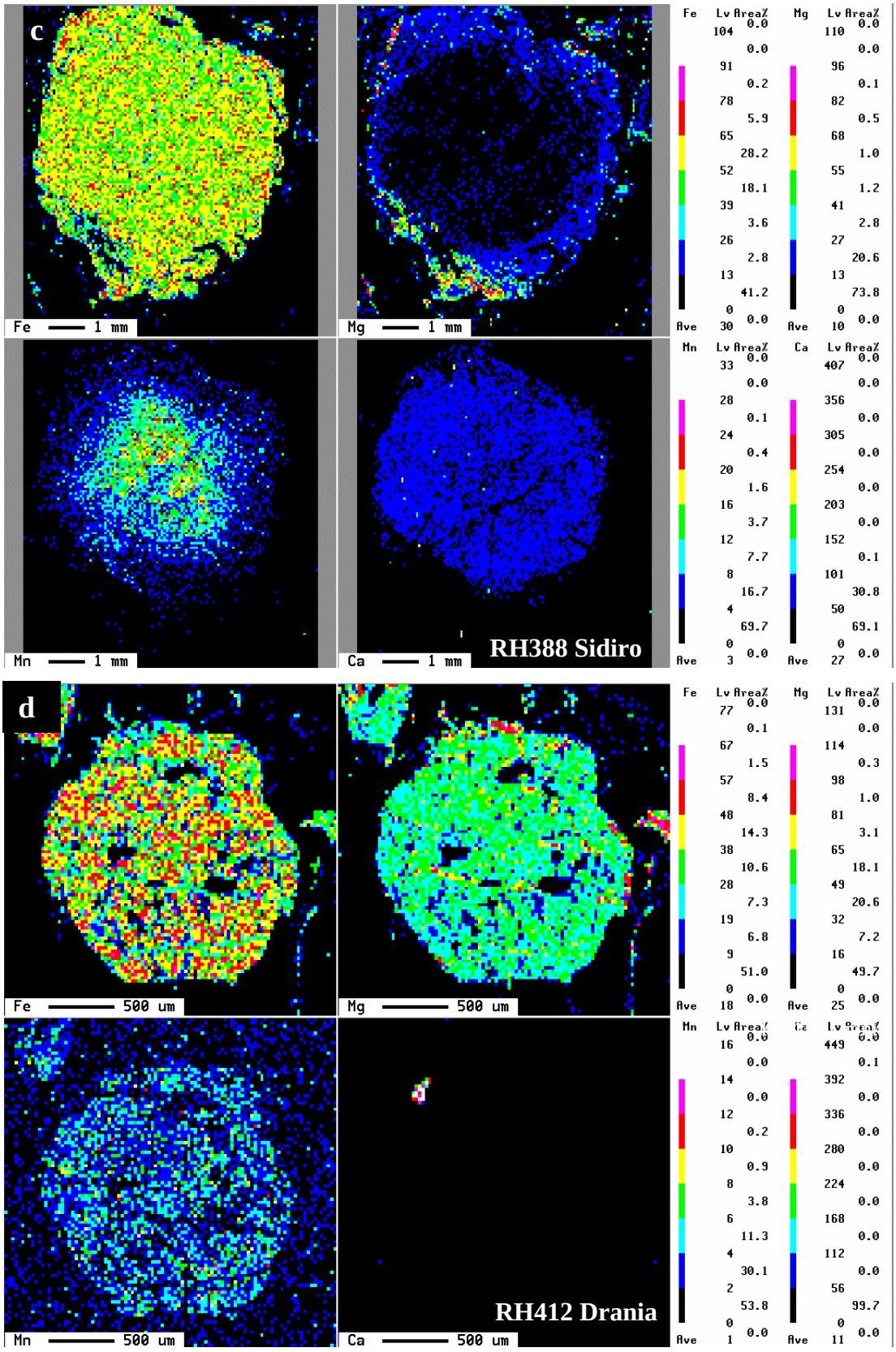

Figs. 4.2.1c-d: Element distribution maps for Fe, Mg, Mn and Ca of garnets from the metapelite samples; c) RH388 and d) RH412.

In the maps of F157, F166 and RH388 Mg shows a zoning parallel to the rim of the garnet and in F157 additionally on cracks. Nevertheless, the cores of the garnets of these samples are rather flat, except where inclusions intersect the garnet profile (Figs. 4.2.2a-c). The Mn-profiles display a slight bell-shape which is typical of garnets from amphibolite-facies pelitic schists (e.g. Hickmott and Spear 1991). The garnets of those samples are characterized by a continuous heating event towards the rim, which is represented by the decreasing X_{fe}, X_{alm},X_{grs} and X_{sps} and the increasing X_{prp} component in the profiles. This kind of zoning is interpreted as growth zoning during prograde metamorphism. In contrast to the other three samples, RH412 shows only retrograde zoning towards the rim with increasing X_{fe}, X_{alm},X_{grs} and decreasing X_{prp} (Fig. 4.2.2d). It is worth mentioning that the very outermost rims of the garnets of F157 and F166 might record a final, small cooling event which is indicated by the abrupt decrease of X_{prp} in sample F157 and the increase of X_{sps} in sample F166, respectively. This event is only visible in these two components at the outermost rims whereas the three other components of the garnets show continuous heating to the rim. The question is, which process or reaction influenced only these specific elements.

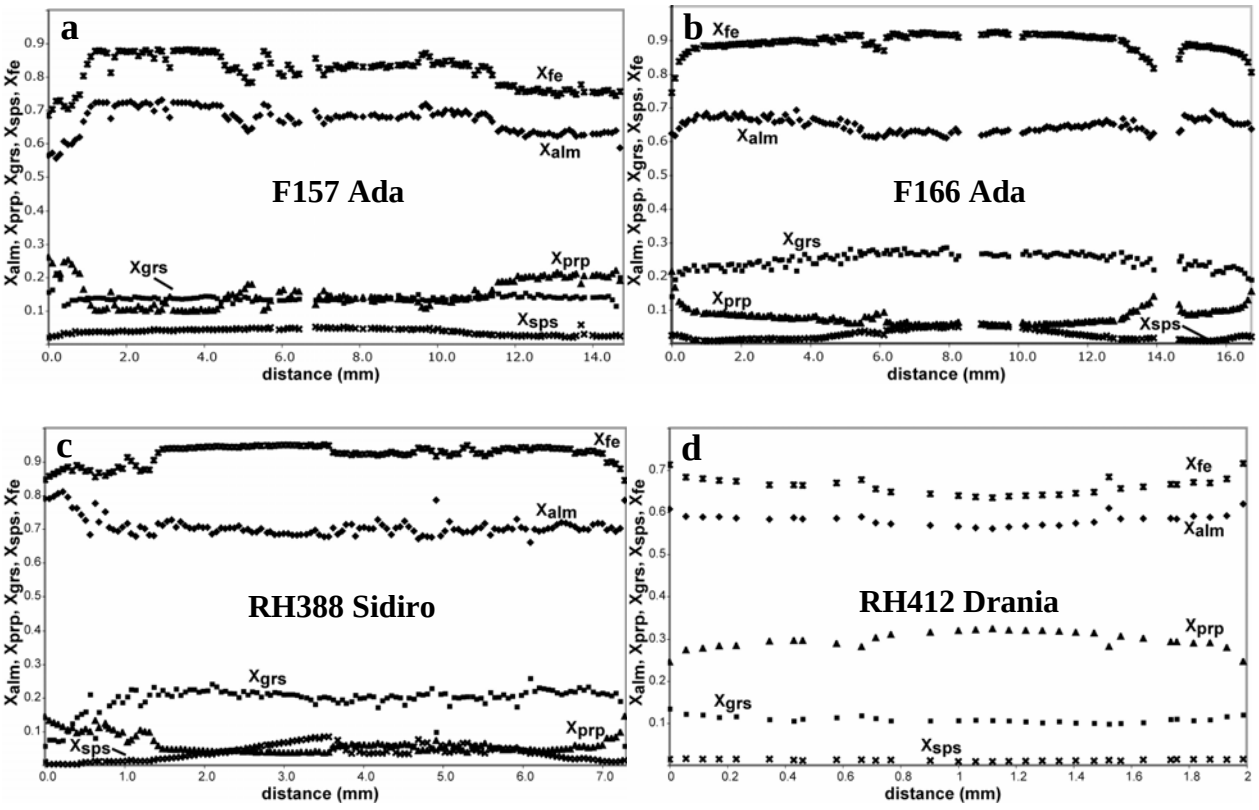

Figs. 4.2.2a-d: Representative zoning profiles of garnets from the samples F157, F166, RH388 and RH412.

The diffusion of Fe, Mg, Mn and Ca in garnet is different for these four elements because of the non-ideal behaviour of the ions, namely the charge and ionic radius. Furthermore the diffusion of these elements is dependent on the composition of the host garnet (Chakraborty and Ganguly 1991). Generally, Ca is more difficult to mobilize than Fe, Mg and Mn. According to Robinson (1991) a net-transfer reaction could be the reason for the increase of Mn in the rim of the garnet. While the garnet is resorbed in order to form e.g. biotite or chlorite, the liberated Mn equilibrates with the new garnet rim because the affinity of Mn for garnet is stronger than for other Fe-Mg minerals. To homogenize garnet by volume diffusion, temperatures exceeding 650°C are needed (Tracy 1982). This can be demonstrated by solving the following two equations from Spear (1993) and calculating the diffusivity coefficient (D) of Mg and the time (t in Ma) that Mg needs to diffuse over a certain distance (h) at a temperature (T). R is the universal gas law constant.

$$D = 9.8 * 10^{-9} (m^2 * \sec^{-1}) * \exp(\frac{-239[kJ * mol^{-1}]}{R * T[^\circ K]}$$ Diffusivity of Mg in garnet for T

$$h = \sqrt{D * t} \quad \Rightarrow \quad t = \frac{h^2}{D}$$ Diffusion-time needed for distance h

It is evident that the diffusion of Mg at 600 °C is to slow to homogenize a several mm-sized garnet within a reasonable geological time scale (*Table 4.2.1*). In contrast, at temperatures of 800 °C Mg diffuses a distance of 5000 μm within ~ 35 Ma in a garnet.

Table 4.2.1: Time (t in Ma) that Mg needs to diffuse the distances 100 to 5000 μm in garnet in the temperature range from 600 to 800°C

T °C	100μm	200μm	500μm	1000μm	5000μm
600	6.454	25.815	161.344	645.374	16134.355
700	0.219	0.875	5.471	21.885	547.125
800	0.014	0.056	0.349	1.394	34.862
900	0.001	0.006	0.036	0.142	3.552

Staurolite

Staurolite occurs only in samples F157 and RH352 as inclusions in garnet and therefore belongs to the prograde minerals in these rocks. The staurolites are characterized by X_{fe} =0.70 – 0.97 (*Table 4.2.2*). Figs. 4.2.3a, b shows an element distribution map for Fe and Mg of a staurolite inclusion in garnet. In the outermost rim at the contact to the garnet the X_{fe} of the staurolite

increases slightly. Depending on where the inclusion is situated in the garnet, the X_{fe} of the staurolite is higher or lower than the X_{fe} of garnet (Figs. 4.2.4a, b). Generally, inclusions in the garnet cores have higher X_{fe} than those in the garnet rims.

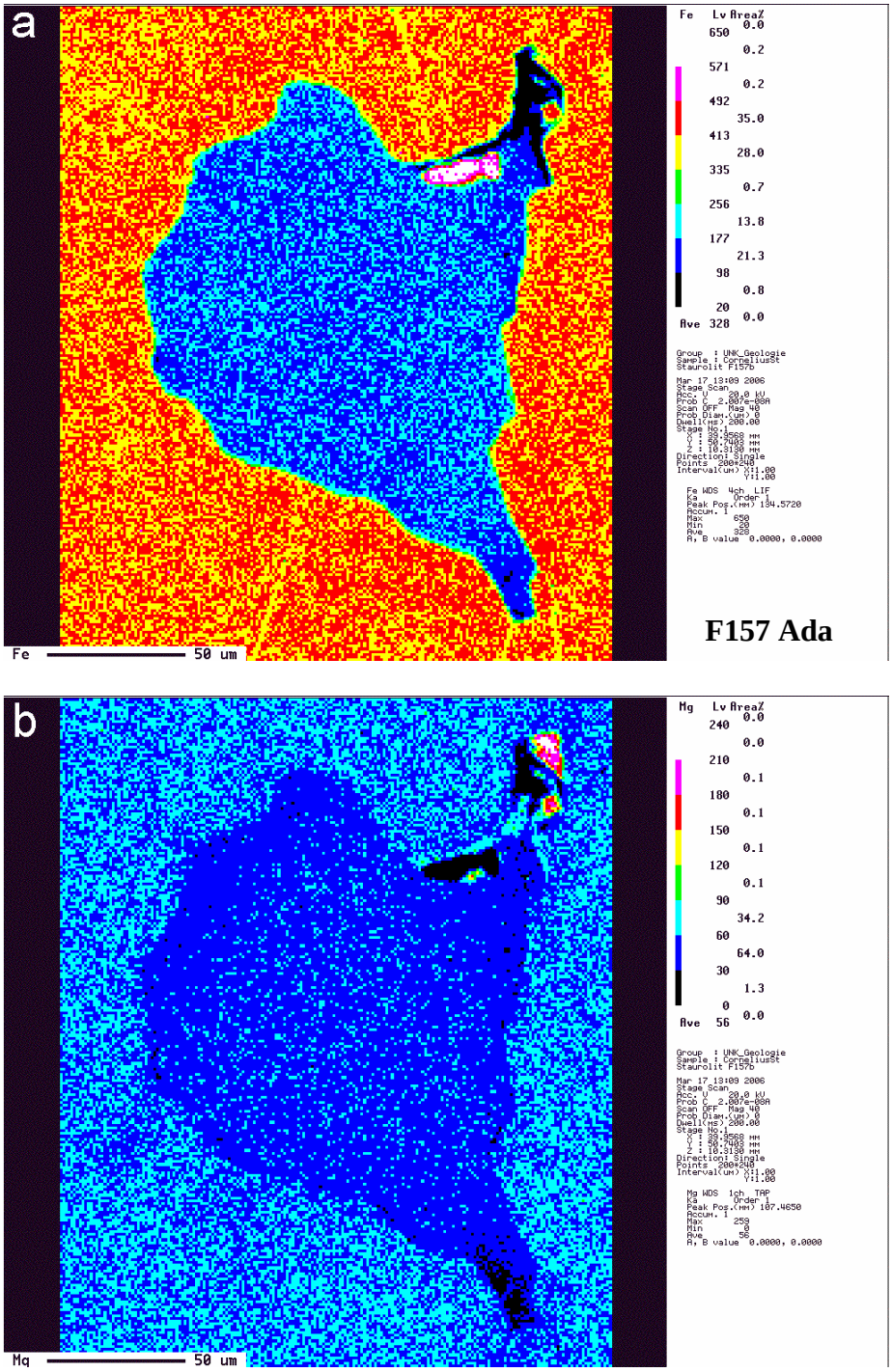

Figs. 4.2.3a, b: Element distribution maps for Fe (Fig. a) and Mg (Fig. b) of a staurolite inclusion in garnet (sample F157).

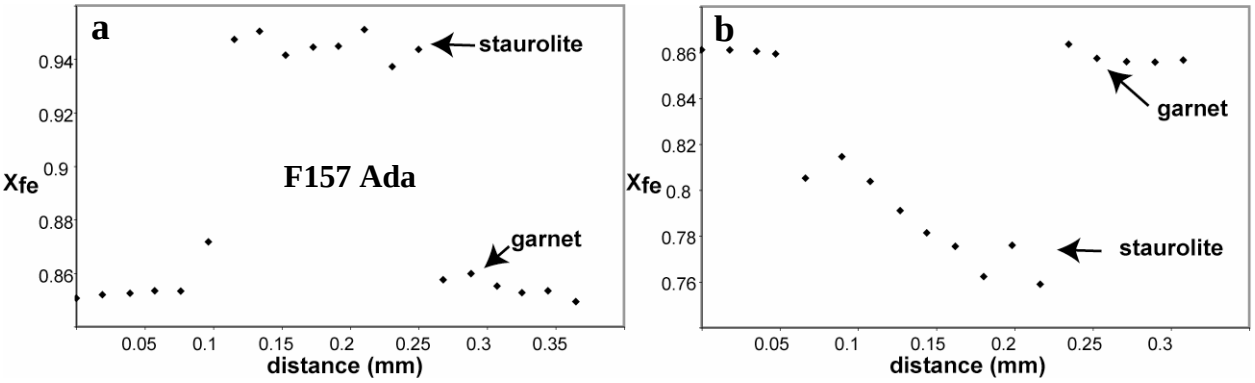

Figs. 4.2.4a, b: X_{fe} profiles of Staurolite inclusions in garnet, sample F157.

Paragonite/muscovite

Paragonitic white mica was observed only as inclusions within garnet in the samples F157 and RH352, but in these samples the paragonite inclusions are quite abundant and occur in both, core and rim of the garnet. The Na_2O content of the paragonite inclusions varies between 4.28 and 7.11 wt% (*Table 4.2.3*). Muscovite inclusions in the same garnet of the same samples contain between 2.12 and 2.41 wt% Na_2O. Generally, the matrix muscovite of all the investigated metapelites is rather poor in celadonite component, but the values for Si per formular unit (p.f.u.) scatter between 3.0 and 3.3 (Fig. 4.2.5a; *Table 4.2.3*). Muscovites in the samples RH412 and F166 are the most homogeneous in composition, while the muscovites of sample RH388 show the largest variation in Si. The highest measured Si was 3.34 p.f.u. in a muscovite flake close to garnet in sample RH388 (*Table 4.2.3*). The Na_2O content of the matrix muscovite varies between 0.53 and 1.48 wt%.

Biotite/Chlorite

Several different textural types of biotite can be distinguished in the four samples. In the samples F157, F166 and RH388 biotite rarely occurs as prograde inclusion in garnet porphyroblasts. The identification of such inclusions has to be made carefully because most of the biotite within garnet is restricted to cracks, pointing to the resorption of garnet by biotite and plagioclase. The X_{fe} of such a presumably prograde biotite inclusion in sample F157 ranges between 0.38 and 0.41 (*Table 4.2.3*) and is therefore within the range of matrix biotites of the same sample (X_{fe} = 0.37 –

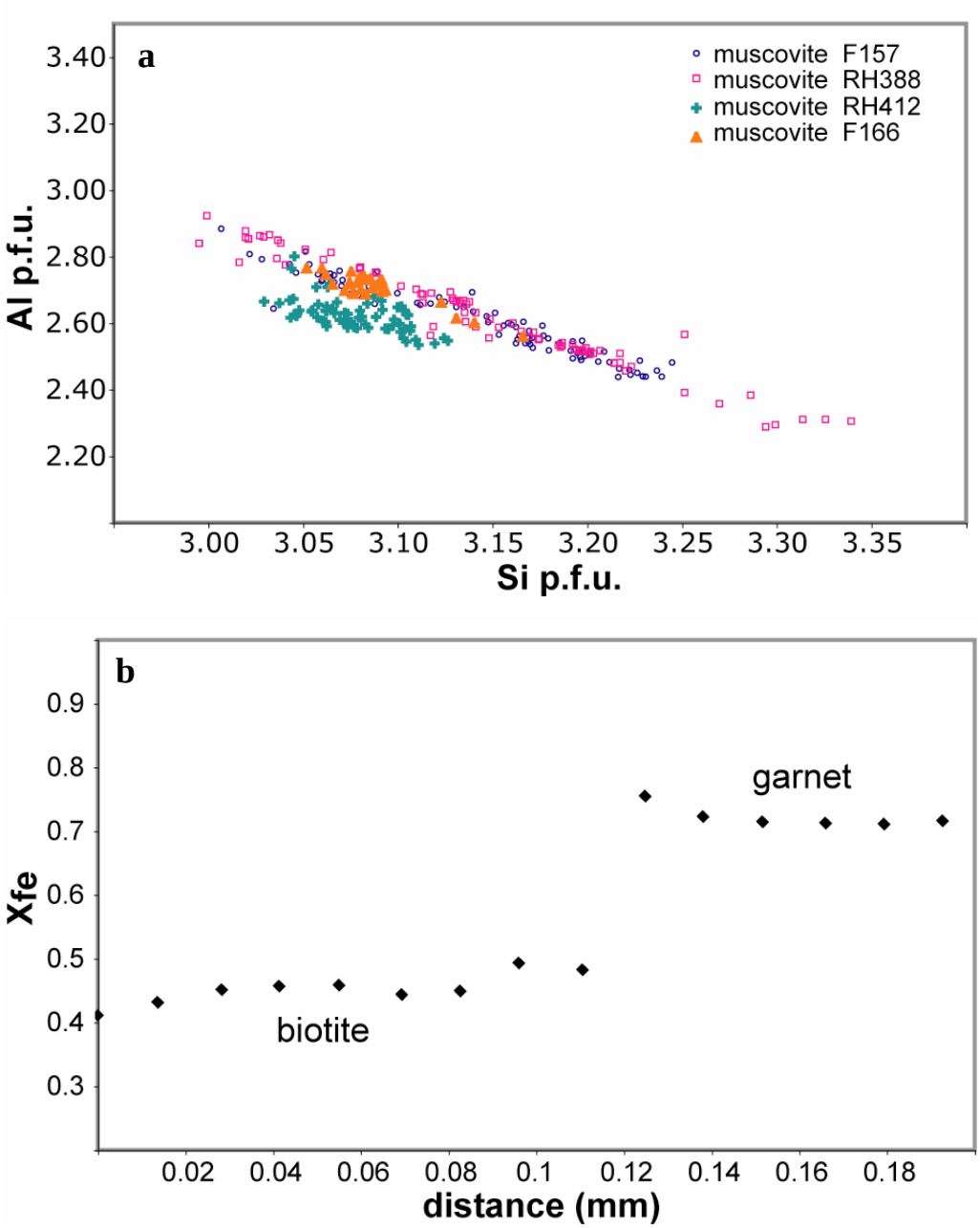

Figs. 4.2.5a, b: a) Al p.f.u. versus Si p.f.u. diagram for muscovites of the samples F157, F166, RH388 and RH412; b) Profile of X_{fe} at the contact of biotite and garnet (F166).

0.41). Biotite replacing kyanite is also of similar composition (X_{fe} = 0.38 – 0.40). The highest X_{fe} = 0.48 was measured at the very contact of biotite, formed during retrogression, and garnet (Fig. 4.2.5b). The TiO_2 content of the biotites ranges between 1.25 and 2.21 wt%. Matrix biotite of the other three samples is in the range of X_{fe} = 0.32 – 0.50 with corresponding TiO_2 contents between 1.35 and 2.3. In all samples biotite shows an increasing degree of chloritization, indicated by the

decreasing K_2O content. Biotites showing evidence for chloritization often have higher X_{fe} values. All kinds of transitional stages can be found. Pure chlorite is characterized by X_{fe} = 0.44 – 0.66.

Amphibole

Amphibole associated with biotite forms part of the matrix in the garnet-kyanite gneiss F166. X_{fe} values are between 0.32 and 0.39. With Na_2O = 1.08 – 1.55 and K_2O = 0.31 – 0.55 the amphibole can be classified as tschermakite.

Plagioclase/K-feldspar

Plagioclase is the dominant feldspar in the studied metapelites and it is generally more albitic in composition. Depending on its textural position the composition of the plagioclase grains is slightly different in the sample F157. Plagioclase inclusions in garnet of F157 have an albite content of X_{ab} = 0.64 – 0.72 with a corresponding anorthite content of X_{an} = 0.28 – 0.36 (*Table 4.2.4*). Plagioclase inclusions in the same garnet of the same sample associated with Fe-sulfides or ilmenite are in the same range but more homogeneous in composition (X_{ab} = 0.69 – 0.71). Matrix plagioclase is generally slightly more albitic (X_{ab} = 0.72 – 0.76), in one case a very weakly zoned grain was measured in the matrix with more sodium in the core (X_{ab} = 0.81). K-feldspar occurs rarely as inclusion in garnet (X_{kfs} = 0.98) or on cracks in garnet (X_{kfs} = 0.94 – 0.96, X_{ab} = 0.04 – 0.06).

The albite content of matrix plagioclase in the other samples ranges between X_{ab} = 0.65 and 0.78, but some large grains in sample RH388 can reach very high albite contents up to X_{ab} = 0.93 – 0.98. In F166 plagioclase in contact with garnet shows slightly lower sodium values (X_{ab} = 0.70 – 0.74) than the grains in the matrix (X_{ab} = 0.77 – 0.78).

Table 4.2.2: Representative electron-microprobe analyses of garnet, staurolite and kyanite

	F157 grt core	F157 grt rim	F166 grt core	F166 grt rim	RH388 grt core	RH388 grt rim	RH412 grt core	RH412 grt rim	F157 st in grt	F157 st in grt	F157 st in grt	F157 ky matrix
Spot No.	75	148	228	307	270	334	348	365	30	93	155	74
SiO2	37.50	37.21	37.26	37.72	37.60	38.15	38.46	38.07	28.24	27.84	27.91	37.25
TiO2	0.05	0.04	0.26	0.07	0.14	0.05	0.02	0.03	0.68	0.69	0.69	0.01
Al2O3	21.89	22.15	21.44	21.77	20.94	21.60	22.24	21.93	53.40	53.80	54.13	62.15
Cr2O3	0.05	0.06	0.64	0.05	0.07	0.04	0.03	0.06	0.07	0.13	0.06	0.07
FeO	31.03	27.15	28.93	29.92	30.71	35.60	26.55	28.83	13.25	12.22	12.99	0.70
MgO	3.47	4.96	1.59	3.31	1.41	3.67	8.40	6.43	1.36	0.76	0.84	0.01
MnO	2.11	1.12	2.21	1.05	3.28	0.63	0.40	0.66	0.41	0.54	0.44	0.01
ZnO	-	-	-	-	-	-	-	-	1.78	2.55	1.39	-
NiO	-	-	-	-	-	-	-	-	0.05	0.00	0.02	-
CoO	-	-	-	-	-	-	-	-	0.04	0.01	0.02	-
Na2O	-	-	-	-	-	-	-	-	0.02	0.08	0.04	0.00
CaO	4.77	7.36	9.19	6.93	6.49	2.00	3.88	4.36	0.02	0.01	0.01	0.02
K2O	-	-	-	-	-	-	-	-	0.01	0.00	0.00	0.00
V2O3	-	-	-	-	-	-	-	-	0.03	0.03	0.00	-
Total	100.87	100.05	100.36	100.38	100.64	101.78	99.98	100.36	99.33	98.65	98.54	100.22
structural formula based on no. of oxygens:						grt: 12			st: 24	24	24	ky: 5
Si	2.96	2.93	2.97	2.97	3.01	3.00	2.97	2.97	4.06	4.03	4.03	1.00
Ti	0.00	0.00	0.02	0.00	0.01	0.00	0.00	0.00	0.07	0.07	0.07	0.00
Al	2.04	2.05	2.01	2.02	1.97	2.01	2.02	2.02	9.05	9.18	9.21	1.98
Cr	0.00	0.00	0.00	0.00	0.00	0.00	0.00	0.00	0.01	0.01	0.01	0.00
Fe	2.05	1.79	1.89	1.97	2.05	2.43	1.71	1.88	1.59	1.48	1.57	0.02
Mg	0.41	0.58	0.19	0.39	0.17	0.43	0.79	0.75	0.29	0.16	0.18	0.00
Mn	0.14	0.07	0.15	0.07	0.22	0.04	0.03	0.04	0.05	0.07	0.05	0.00
Zn	-	-	-	-	-	-	-	-	0.19	0.27	0.15	-
Ni	-	-	-	-	-	-	-	-	0.01	0.00	0.00	-
Co	-	-	-	-	-	-	-	-	0.00	0.00	0.00	-
Na	-	-	-	-	-	-	-	-	0.00	0.02	0.01	0.00
Ca	0.40	0.62	0.78	0.58	0.56	0.17	0.32	0.36	0.00	0.00	0.00	0.00
K	-	-	-	-	-	-	-	-	0.00	0.00	0.00	0.00
V	-	-	-	-	-	-	-	-	0.00	0.00	0.00	-
Total	8.01	8.04	8.01	8.01	7.99	7.99	8.02	8.02	15.34	15.31	15.29	3.00
X_{fe}	0.83	0.75	0.91	0.84	0.92	0.84	0.64	0.72	0.85	0.90	0.77	-
X_{Alm}	0.68	0.58	0.63	0.65	0.68	0.78	0.57	0.62	-	-	-	-
X_{Prp}	0.14	0.19	0.06	0.13	0.06	0.14	0.32	0.25	-	-	-	-
X_{Grs}	0.13	0.20	0.26	0.19	0.19	0.06	0.11	0.12	-	-	-	
X_{Sps}	0.05	0.02	0.05	0.02	0.07	0.01	0.01	0.01	-	-	-	-

X_{fe} = Fe/(Fe+Mg); X_{Alm} = Fe/(Fe+Mg+Ca+Mn); X_{Prp} = Mg/(Fe+Mg+Ca+Mn); X_{Grs} = Ca/(Fe+Mg+Ca+Mn); X_{Sps} = Mn/(Fe+Mg+Ca+Mn)

Table 4.2.3: Representative electron-microprobe analyses of paragonite, muscovite, biotite, amphibole and chlorite

	F157 par in grt	F157 ms matrix	F166 ms matrix	RH388 ms matrix	RH412 ms matrix	F157 bt in grt	F157 bt near grt	F166 bt matrix	RH388 bt matrix	RH412 bt matrix	F166 amph matrix	F157 chl near grt
Spot No.	59.00	93	174	105	205	70	194	156	223	200	217	87
SiO2	45.68	48.51	46.41	49.68	45.35	35.91	35.85	36.99	36.50	38.96	45.41	24.85
Al2O3	39.19	31.10	35.00	29.12	33.77	17.98	19.51	18.69	18.44	22.73	13.84	21.27
TiO2	0.16	0.29	0.20	0.39	1.46	1.61	1.11	1.89	1.64	2.30	0.40	0.07
FeO	1.76	2.52	1.43	1.78	2.49	15.36	17.64	13.77	17.90	11.32	12.31	28.20
MgO	0.12	2.36	1.27	2.56	1.17	13.55	10.59	14.98	10.37	9.09	13.04	12.74
MnO	0.00	0.04	0.00	0.01	0.03	0.00	0.50	0.09	0.06	0.11	0.08	0.89
Cr2O3	0.08	0.01	0.08	0.09	0.03	0.08	0.05	0.15	0.02	0.00	0.00	0.04
CaO	0.66	0.00	0.00	0.01	0.00	0.00	0.02	0.00	0.14	0.03	11.55	0.03
Na2O	5.49	0.73	0.76	0.62	0.99	0.30	0.20	0.23	0.21	0.34	1.34	0.00
K2O	2.72	9.74	10.25	9.47	9.55	8.96	9.33	9.41	8.11	8.14	0.44	0.00
BaO	0.00	0.34	0.45	0.14	0.74	0.40	0.34	0.14	0.38	0.02	0.04	0.00
Cl	0.21	0.00	0.00	0.01	0.00	2.45	0.52	0.02	0.01	0.19	0.00	0.01
F	0.00	0.13	0.13	0.40	0.00	0.00	0.10	0.06	0.03	0.19	0.08	0.00
Total	96.07	95.78	95.99	94.29	95.59	96.61	95.77	96.42	93.81	93.41	98.53	88.10
structural formular based on no. of oxygens:				mica: 22								chl: 28
Si	5.90	6.46	6.16	6.68	6.09	5.44	5.44	5.42	5.57	5.70	6.26	5.32
Al (IV)	2.10	1.54	1.84	1.32	1.91	2.56	2.56	2.58	2.43	2.30	1.74	2.68
Al (VI)	3.86	3.34	3.64	3.29	3.43	0.65	0.92	0.64	0.89	1.63	0.50	2.68
Ti	0.02	0.03	0.02	0.04	0.15	0.18	0.13	0.21	0.19	0.25	0.04	0.01
Fe (tot)	0.19	0.28	0.16	0.20	0.28	1.95	2.24	1.69	2.29	1.39	1.42	5.05
Mg	0.02	0.47	0.25	0.51	0.23	3.06	2.39	3.27	2.36	1.98	2.68	4.06
Mn	0.00	0.00	0.00	0.00	0.00	0.00	0.06	0.01	0.01	0.01	0.01	0.16
Cr	0.01	0.00	0.01	0.01	0.00	0.01	0.01	0.02	0.00	0.00	0.00	0.01
Ca	0.09	0.00	0.00	0.00	0.26	0.00	0.00	0.00	0.02	0.10	1.71	0.01
Na	1.38	0.19	0.19	0.16	0.00	0.09	0.06	0.06	0.06	0.00	0.36	0.00
K	0.45	1.66	1.74	1.62	1.64	1.73	1.81	1.76	1.58	1.52	0.08	0.00
Ba	0.00	0.02	0.02	0.06	0.04	0.19	0.16	0.01	0.19	0.09	0.00	0.00
Cl	0.05	0.00	0.00	0.00	0.00	0.63	0.13	0.00	0.00	0.00	0.00	0.00
F	0.00	0.06	0.05	0.02	0.00	0.00	0.01	0.03	0.00	0.01	0.03	0.00
Total	14.06	14.05	14.09	13.93	14.04	16.50	15.92	15.70	15.59	14.98	14.83	19.99
Si p.f.u.	-	3.23	3.08	3.34	3.05	-	-	-	-	-	-	-
X_{fe}	-	-	-	-	-	0.39	0.48	0.34	0.49	0.41	0.35	0.55

p.f.u. = per formula unit; X_{fe} = Fe/(Fe+Mg)

Table 4.2.4: Representative electron-microprobe analyses of feldspar

	F157 pl in grt+ilm	F157 pl in grt	F157 kfs in grt	F157 pl matrix	F166 pl near grt	F166 pl matrix	RH388 pl matrix	RH388 pl matrix	RH412 pl matrix
Spot No.	34	48	71	223	174	149	127	113	154
SiO2	58.95	61.49	64.37	61.89	61.49	62.44	66.03	67.80	60.77
Al2O3	24.77	24.03	17.93	22.12	23.93	23.30	21.09	19.35	23.99
TiO2	0.00	0.00	0.17	0.06	0.03	0.00	0.00	0.00	0.00
FeO	0.43	0.34	0.90	0.52	0.05	0.00	0.07	0.03	0.02
MgO	0.00	0.00	0.00	0.02	0.01	0.00	0.02	0.00	0.01
MnO	0.05	0.02	0.03	0.00	0.02	0.00	0.00	0.03	0.02
Cr2O3	0.01	0.00	0.03	0.06	0.06	0.04	0.00	0.04	0.01
CoO	0.03	-	-	-	-	-	-	-	-
NiO	0.00	-	-	-	-	-	-	-	-
ZnO	0.01	-	-	-	-	-	-	-	-
CaO	6.32	5.81	0.01	3.44	5.79	4.72	2.06	0.28	5.95
Na2O	8.10	8.03	0.17	8.99	8.60	9.33	10.40	11.43	8.32
K2O	0.10	0.12	16.18	0.27	0.13	0.24	0.10	0.08	0.12
V2O3	0.01	-	-	-	-	-	-	-	-
Total	98.78	99.84	99.78	97.36	100.10	100.07	99.77	99.04	99.21
structural formular based on no. of oxygens:					fsp: 8				
Si	2.67	4.10	2.99	2.81	2.73	2.77	2.91	2.99	2.72
Al	1.32	1.89	0.98	1.18	1.25	1.22	1.09	1.01	1.27
Ti	0.00	0.00	0.01	0.00	0.00	0.00	0.00	0.00	0.00
Fe	0.02	0.02	0.03	0.02	0.00	0.00	0.00	0.00	0.00
Mg	0.00	0.00	0.00	0.00	0.00	0.00	0.00	0.00	0.00
Mn	0.00	0.00	0.00	0.00	0.00	0.00	0.00	0.00	0.00
Cr	0.00	0.00	0.00	0.00	0.00	0.00	0.00	0.00	0.00
Ca	0.31	0.42	0.00	0.17	0.28	0.22	0.89	0.98	0.72
Na	0.71	1.04	0.02	0.79	0.74	0.80	0.10	0.01	0.29
K	0.01	0.01	0.96	0.02	0.01	0.01	0.01	0.00	0.01
Total	5.03	7.48	5.00	5.00	5.01	5.03	4.99	5.00	5.01
X_{ab}	0.69	0.71	0.02	0.81	0.72	0.77	0.90	0.98	0.71
X_{an}	0.30	0.28	0.00	0.17	0.27	0.22	0.10	0.01	0.28
X_{kf}	0.01	0.01	0.98	0.02	0.01	0.01	0.01	0.00	0.01

X_{ab} = Na/(Na+Ca+K); X_{an} = Ca/(Na+Ca+K); X_{kf} = K/(Na+Ca+K)

4.3 Whole-rock major and trace element geochemistry of the metapelites

Four metapelitic samples from the three sections were studied for their whole-rock geochemistry and trace elements. Representative garnet±kyanite micaschists/gneisses were chosen from each section: F157 and RH363 (amphibole-bearing) from the Ada section, RH388 from the Sidiro section and RH412 from the Kimi section. The whole-rock analyses of major and trace elements are given in *Table 4.3.1*.

Because the samples underwent a high-grade metamorphism their original geochemical composition might have been changed. Therefore, the use of classification diagrams for clastic sediments should be handled with care. Fig. 4.3.1 shows a classification diagram (Herron 1988) that is based on the logarithmic ratios of the major elements SiO_2/Al_2O_3 and Fe_2O_3/K_2O. The three garnet±kyanite micaschists/gneisses without amphibole plot at the boarder of the wacke-shale field, whereas the amphibole-bearing sample from the Ada section plots in the Fe-shale field indicating that this sample is derived from a more mafic source rock. This is in agreement with the lower SiO_2 and higher FeO, MgO and CaO values of RH363 in comparison to the other samples (*Table 4.3.1*). Fig. 4.3.2 shows a chondrite-normalized REE diagram for three of the garnet±kyanite micaschists/gneisses (without amphibole). The patterns are very similar. Light rare earth elements (LREE) are strongly enriched and all samples display a negative Eu-anomaly although not very pronounced. The HREE patterns are flat.

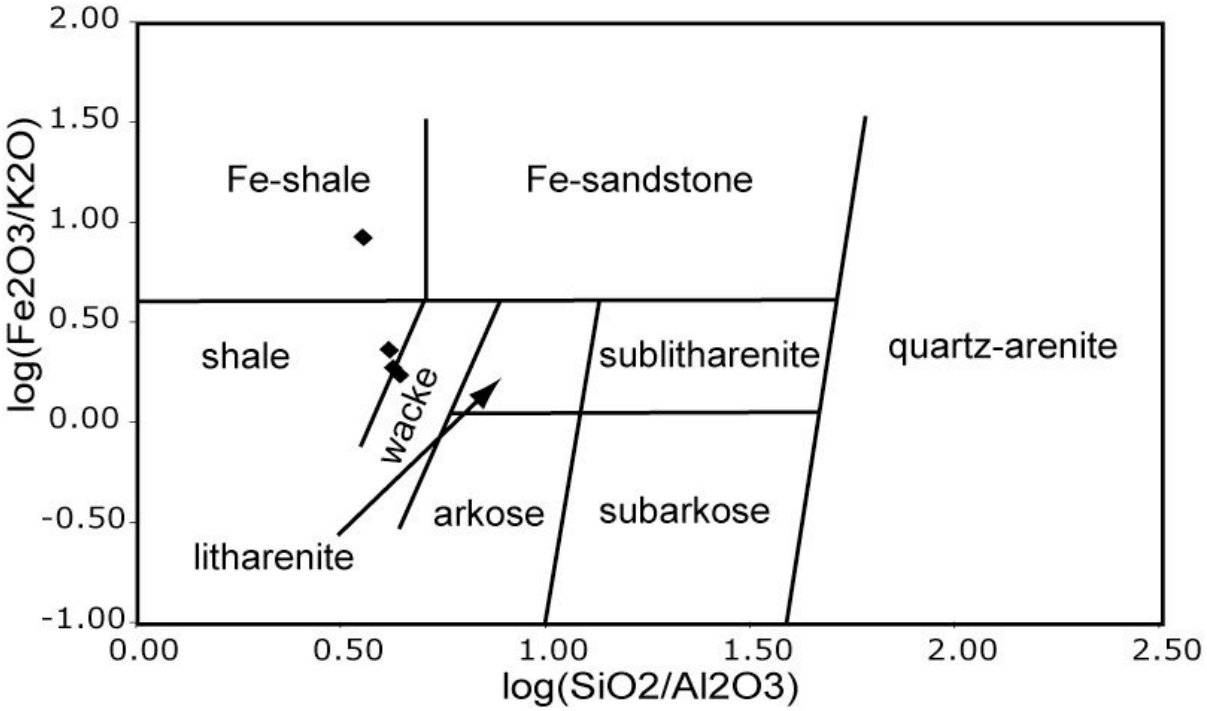

Fig. 4.3.1: Classification diagram for terrigenous clastic sediments after Herron (1988); garnet±kyanite micaschists plot at at the boarder of the wacke-shale field, amphibole-bearing sample RH363 from the Ada section plots in the Fe-shale field.

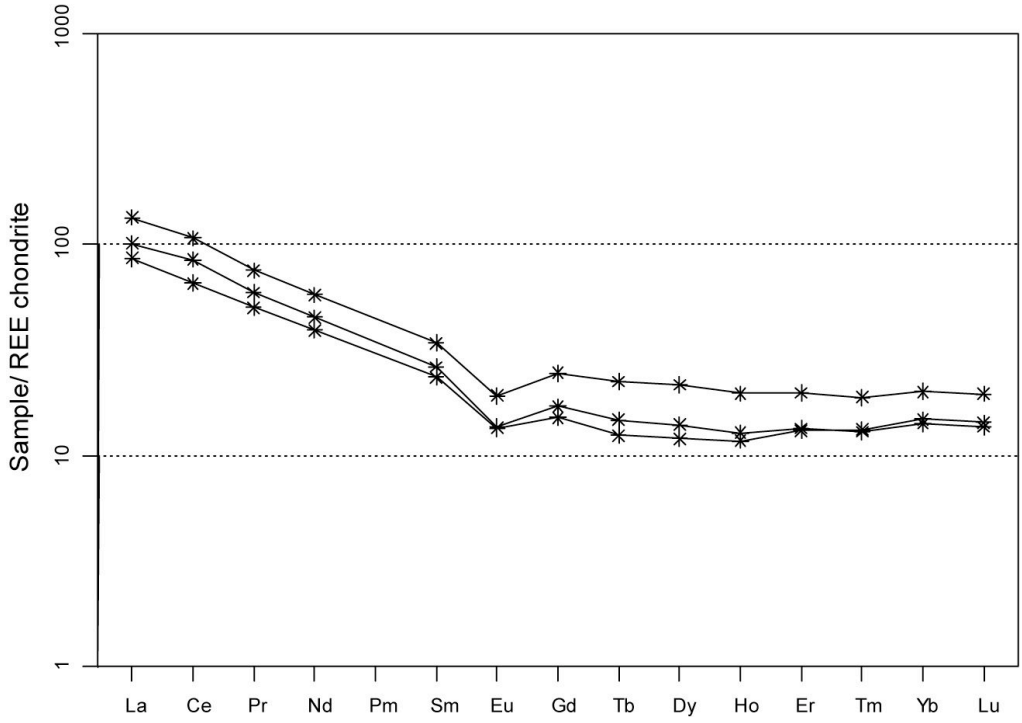

Fig. 4.3.2: Chondrite-normalized REE diagram for three garnet±kyanite micaschists/gneisses; normalizing values from Boynton et al. (1984).

Table 4.3.1: Whole-rock analyses of major and trace elements of the metapelites.

sample	F157	RH388	RH412	RH363
SiO2	66.13	68.64	65.4	58.85
TiO2	0.56	0.78	1.07	0.97
Al2O3	15.49	15.51	15.69	16.35
Fe2O3	5.46	6.06	6.8	9.7
MnO	0.21	0.07	0.09	0.34
MgO	1.8	1.52	2.27	5.1
CaO	1.48	0.85	0.71	4.79
Na2O	1.79	1.07	0.88	2.58
K2O	2.94	3.53	2.97	1.16
P2O5	0.15	0.12	0.05	0.07
LOI	1.76	2.21	2.46	0.6
Sum	97.76	100.38	98.4	100.51

sample	F157	RH388	RH412	RH363
Sc	11	13	n.d.	25
V	104	94	n.d.	179
Cr	105	77	n.d.	120
Co	14	16	n.d.	25
Ni	40	35	n.d.	104
Cu	36	20	n.d.	16
Zn	67	74	n.d.	61
Ga	20	19	n.d.	19
Rb	99	118	58	36
Sr	132	89	67	178
Y	24	26	39	25
Zr	282	241	382	102
Nb	10	14	24	8
Cs	3	3	1	n.d.
Ba	429	442	1525	157
La	27	31	42	11
Ce	53	69	87	25
Pr	6	7	9	2
Nd	23	27	35	11
Sm	5	5	7	2
Eu	1	1	1	n.d.
Gd	4	4	6	n.d.
Tb	1	1	1	n.d.
Dy	4	5	7	n.d.
Ho	1	1	1	n.d.
Er	3	3	4	n.d.
Tm	0	0	1	n.d.
Yb	3	3	4	n.d.
Lu	0	0	1	n.d.
Hf	7	6	10	n.d.
Ta	1	1	2	n.d.
Pb	9	6	2	9
Th	10	12	13	5
U	2	2	1	1

Major elements were obtained by X-ray fluorescence (XRF), trace elements by LA-ICPMS.

4.4 Zircon study and UHP indicators

Generally, zircons are common accessory minerals of metamorphic gneisses but they are also considered to be the best containers of UHP metamorphic minerals (e.g. Chopin and Sobolev 1995). In this regard, about two hundred zircons from two metapelitic gneisses (F157 and RH388) from the Ada and the Sidiro sections were separated, mounted in epoxy and investigated by Scanning-Electron Microscopy (SEM), Laser-Raman Spectroscopy and for the first time with Time-of-Flight Secondary-Ion Mass Spectrometry (TOF-SIMS). Zircon separation was carried out at the Max-Planck-Institut für Chemie in Mainz. Prof. D. Kostopoulos and Dr. E. Chatzitheodoris performanced the SEM-, Laser-Raman- and TOF-SIMS analyses. Laser-Raman analyses were carried out at the National Technical University of Athens using a Renishaw RM1000 spectrometer attached to a Leica DM microscope. TOF-SIMS ion mapping was performed at the University of Manchester using the Manchester instrument build in-house based on the BIOTOF design but with several modifications targeting to the study of inorganic samples for quantitative elemental and isotopic analysis. This chapter presents the first results of this study. Analytical procedures are given in Appendix B.

SEM and Laser-Raman study

Prior to the SEM and Laser-Raman analyses the zircons were studied optically. In several grains, especially from the sample F157, a zoning structure was observed, consisting of a rather inclusion-free detrital core surrounded by an inclusion-rich rim of metamorphic origin (Figs. 4.4.1a-c). It is worth notifying that the majority of the inclusions of the zoned zircons are located close to the interface of core and rim (best seen in Figs. 4.4.1a-b). Most zircons of sample RH388 are virtually unzoned (Fig. 4.4.1d).

The detailed Laser-Raman study revealed mineral- as well as fluid inclusions in situ in the host zircon. In the detrital core domains of zoned zircons from sample F157 quartz and monazite inclusions were found. The rims of the zircons contain a variety of inclusions comprising albite, plagioclase, K-feldspar, white mica, kyanite, rutile, hematite, monazite, apatite, xenotime, CO_2 gas inclusions and diamond. The presence of diamond indicates that the rims of the zircons grew at ultra-high-pressures exceeding 4 GPa. Nevertheless, in the virtually unzoned zircons (Fig. 4.4.1d) diamond inclusions were detected as well, indicating that the grains experienced the same pressure conditions.

Figures 4.4.2a, b show SEM images of the zoned zircon Z1 (F157, Figure 4.4.1a) with its exposed inclusions. The mineral chemistry of these inclusions was confirmed by energy dispersive analyses (EDS) and the locations of selected measurements are shown in Figure 4.4.2b. Representative EDS spectra of the inclusions are shown in Figures 4.4.2c-h. The zircon Z1 (F157, Fig. 4.4.1a) exhibits kyanite, zoisite, monazite and xenotime inclusions (Fig. 4.4.2a). Furthermore, it contains three diamonds, which are located also in the interface area between core and rim. Laser-Raman-spectra of the diamonds are shown in Figures 4.4.3a-c. Figures 4.4.3a and b show the spectra of the large exposed diamonds (see SEM images, Figures 4.4.2a-b), whereas Figure 4.4.3c shows the spectrum of a dual inclusion of monazite and diamond completely enclosed by the host zircon (therefore not visible in the SEM image Fig. 4.4.2a).

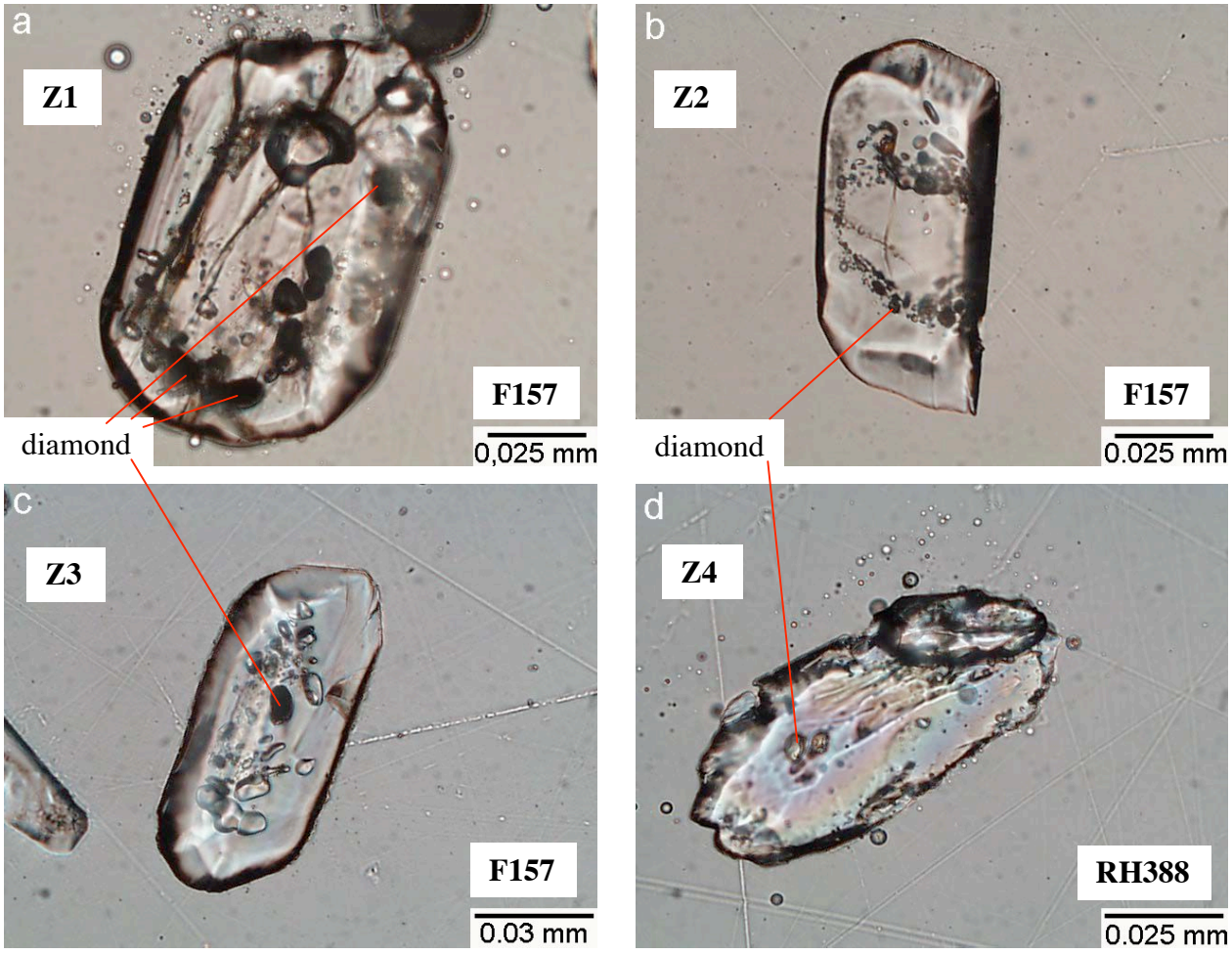

Fig. 4.4.1a-d: Selected photographs of zircons from metapelite samples F157 and RH388 studied by Laser-Raman Spectroscopy and TOF-SIMS, note the zoned structure of detrital core and rim of the grains on the photos a and b.

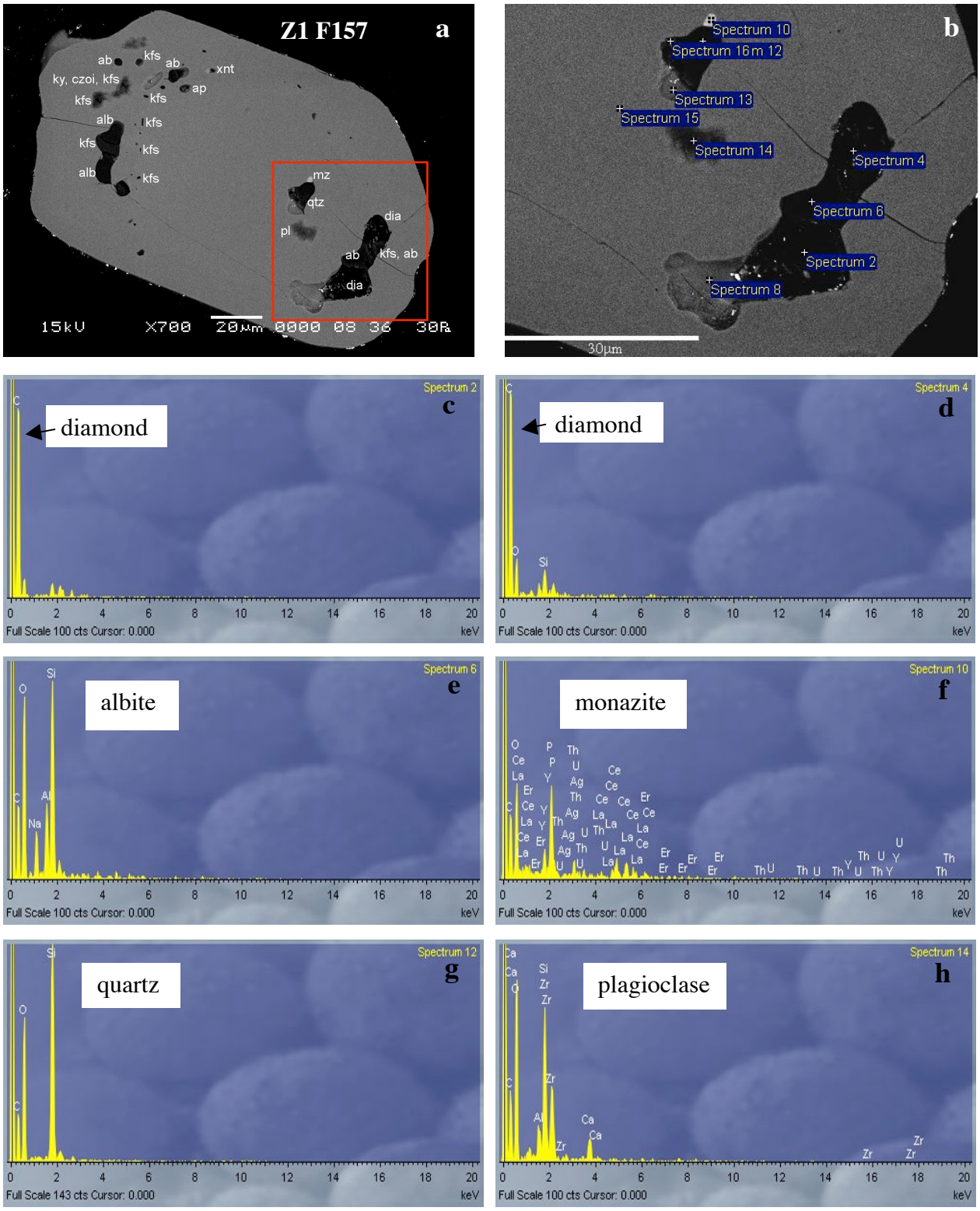

Fig. 4.4.2: a) SEM image of the zircon Z1 shown in Figure 4.4.1a (sample F157); b) Detailed SEM image of the right part (red box) of the same zircon showing the exposed inclusions; c-h: Selected EDS-spectra of the inclusions within this zircon: c) Carbon (diamond); d) Carbon (diamond); e) Albite; f) Monazite; g) Quartz; h) Plagioclase.

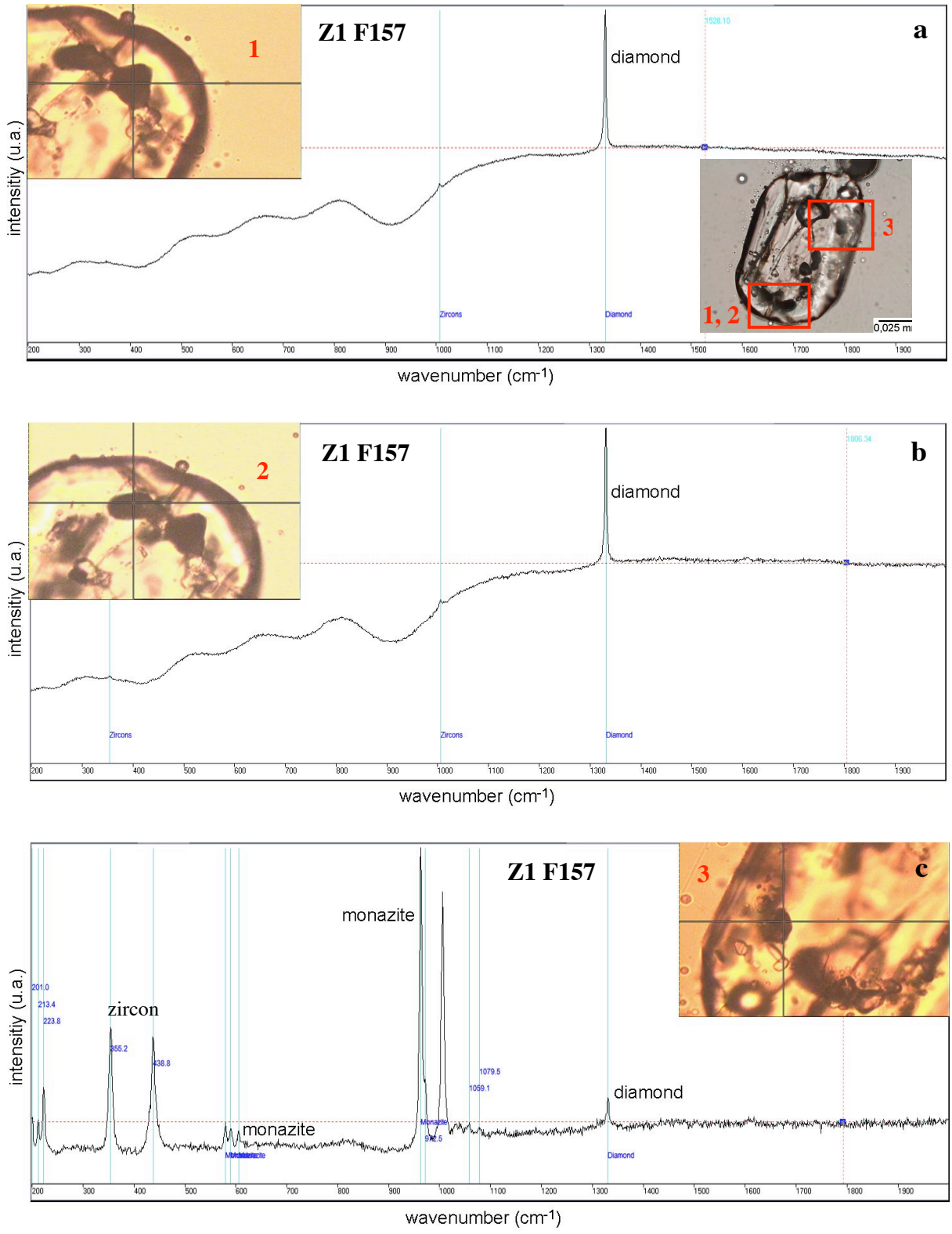

Figs. 4.4.3a-c: Selected Laser-Raman-Spectra of two single diamond inclusions and a dual monazite-diamond inclusion occurring in the zircon Z1 shown in Fig. 4.4.1a; inlets show photographs of the inclusion analysed by Laser-Raman Spectroscopy.

EDS spectra obtained from the exposed diamonds exhibit an extraordinary strong carbon peak (Fig. 4.4.2c, d). Many inclusions consist of albite and K-feldspar. Morphology and mineralogy of multiphase inclusions of albite and diamond (Fig. 4.4.2a) and/or albite and white mica (not shown here) in the vicinity of diamond indicate that these minerals have precipitated from a granitic melt at ultra-high pressures.

The inclusion paragenesis of the second zircon grain Z2 (sample F157), shown in Fig. 4.4.1b, exhibits two diamonds, hematite, CO_2 gas and white mica (Fig. 4.4.4a-c). The presence of hematite inclusions right next to diamond and CO_2 gas inclusions within the same zircon domain raises the question if redox reactions could be involved during diamond formation. The precipitation of diamond from CO_2 or supercritical C-O-H fluids has been studied by experiments (e.g. Akaishi et al. 2000, Dobrzhinetskaya et al. 2003). It is likely that the diamonds formed at the expense of CO_2, probably due to a dissociation of CO_2. The residual carbon is transformed to diamond, whereas oxygen is liberated and forms hematite together with iron which is coming from a fluid or melt phase (redox reaction indicated by inclusions: $CO_2 \rightarrow C^{4+} + 2O^{2-}$; $3O^{2-} + 2Fe^{3+} \rightarrow Fe_2O_3$). Diamonds can also be grown from alkaline-carbonate melts (Shatsky et al. 2001) and carbonates are known to be diamond-forming solvent-catalysts at high pressures (Sato et al. 1999). Therefore, the original source of the CO_2 might be sought in the marble horizons, which were found in all localities in vincity of the metapelites from which the diamond-bearing zircons were extracted.

TOF-SIMS study

A detailed TOF-SIMS study was carried out on the zircons that show a pronounced detrital core and rim domain. With this method a set of elemental distribution maps of the zircon grains was generated (Chatzitheodoridis et al. 2005). Ion maps of major elements and their combination allow drawing conclusions about the main mineralogy. Selected ion maps of major elements are presented in Figs. 4.4.5a-d. The ion maps of Al and Ca together with a combined map of Na, K and Si indicate the location of feldspar inclusions, which were confirmed before by EDS and Laser-Raman analyses. The carbon ion map (Fig. 4.4.5d) demonstrates the position of two large diamond inclusions within the zircon (confirmed by Laser-Raman analyses, see also Fig. 4.4.3a, b).

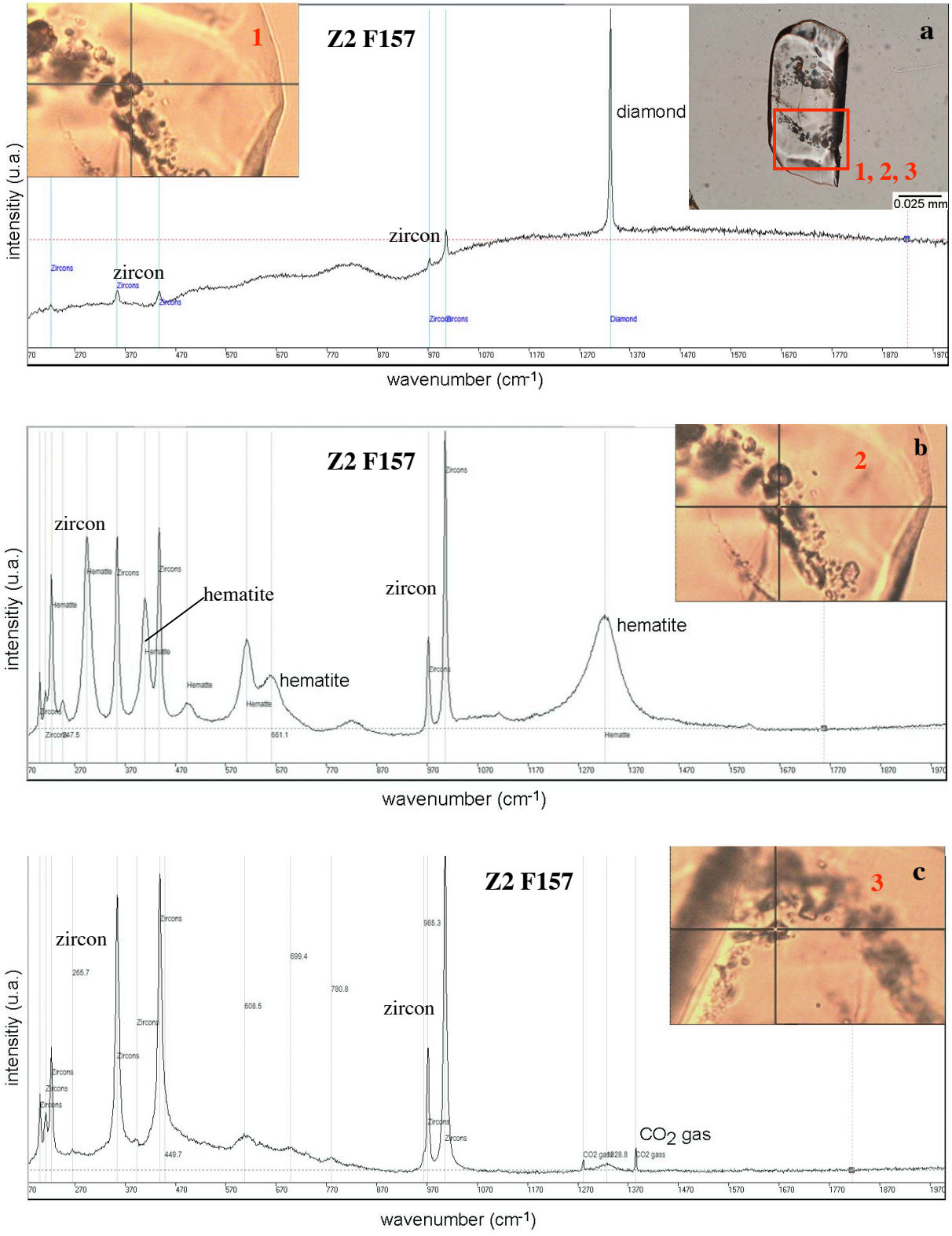

Figs. 4.4.4a-c: Selected Laser-Raman-Spectra of a diamond, hematite and CO_2 gas inclusion occurring in the zircon Z2 shown in Fig. 4.4.1b; inlets show photographs of the inclusion analysed by the Laser-Raman Spectroscopy.

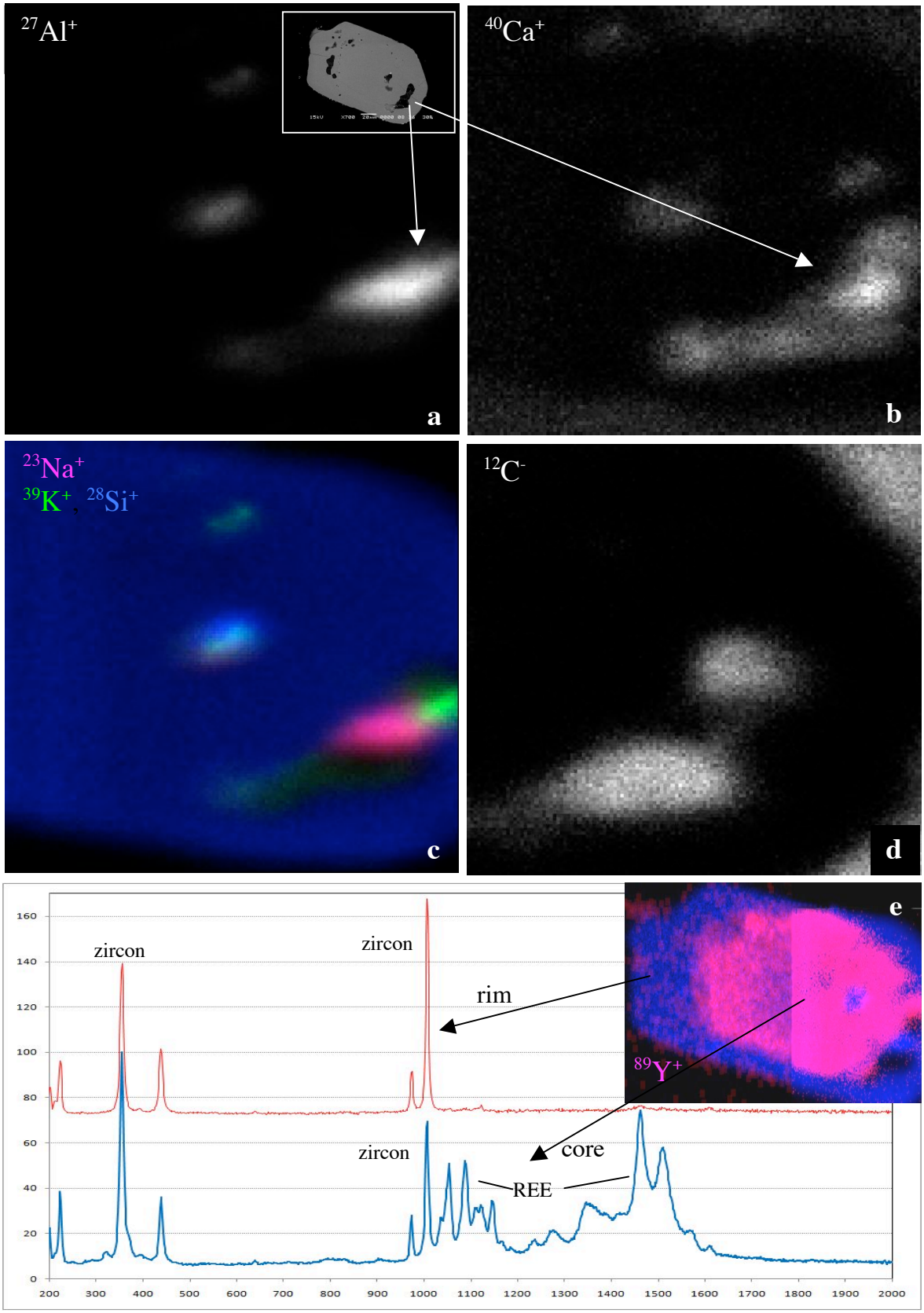

For explanation see next page.

Fig. 4.4.5: a-d: Selected TOF-SIMS ion maps of major elements; Note: Figure c is a combination of $^{23}Na^+$, $^{39}K^+$, and $^{28}Si^+$ distribution maps; e) Raman-analyses with a green laser showing a REE-poor rim (red line) and a REE-rich core (blue line), inlet shows enrichment of ^{89}Y (pink area) in the zircon core.

Outstanding results were obtained by trace element mapping. The trace element maps produced with TOF-SIMS have proven to be a very good method to distinguish the two zircon domains which were already visible under the microscope. The inlet in Fig. 4.4.6e shows the outline of a zircon (the grain in Fig. 4.4.2a) in blue colour, which corresponds to the Si distribution, whereas the pink coloured area is defined by the distribution map of ^{89}Y. Thus, it is evident that this rare earth element (REE) is concentrated in the detrital core of the grain while the UHP-metamorphic rim containing the diamond shows no significant amounts of ^{89}Y (see also Fig. 4.4.6b). This feature can also be observed using Laser-Raman Spectroscopy with a green laser (514.5 nm) (Fig. 4.4.5e). Analyses of the core (blue line) clearly shows a concentration of rare earth elements whereas the rim area of the grain (red line) shows no significant REE amounts. A similar behaviour although less pronounced can be observed for example in the ^{174}Yb ion map (Fig. 4.4.6a). The fact that ^{89}Y and ^{174}Yb are enriched in the detrital core but almost not present in the rim of the zircon can be explained by a partition of these REE elements into garnet. According to Rubatto and Hermann (2007), the zircon/garnet partition coefficients of HREE decrease with increasing temperature. A calculation based on their experimental results reveals that ultra-high temperatures of 1070°C at 20 kbar are necessary for Y to partition into garnet instead of zircon, that is a partition coefficient of Y between garnet and zircon above unity in the presence of a melt phase at very high temperatures.

In contrast to this, Li shows a reverse distribution pattern in the TOF-SIMS ion map (Fig. 4.4.6c-d). Although less pronounced Li is enriched in the rim of the zircons. Figure 4.4.6c shows the sum ion map of the two Li isotopes $^6Li^+$ und $^7Li^+$ and Figure 4.4.6d shows the Li concentration in pink colour on blue background (Si distribution) to show more precise the area of Li enrichment. Taking into account the diamond inclusions and the HREE-impoverishment of the rim area, the resulting metamorphic conditions, that are pressures above 4GPa and temperatures above 1000 °C, are melting conditions for metapelitic lithologies. Phengite is an important phase in subducted crustal rocks being stable up to pressures of 10 kbar and it can host significant amounts of Li. The breakdown of phengite due to dehydration melting of the mineral occurs at temperatures in excess of 1000°C (Schmidt et al. 2004).

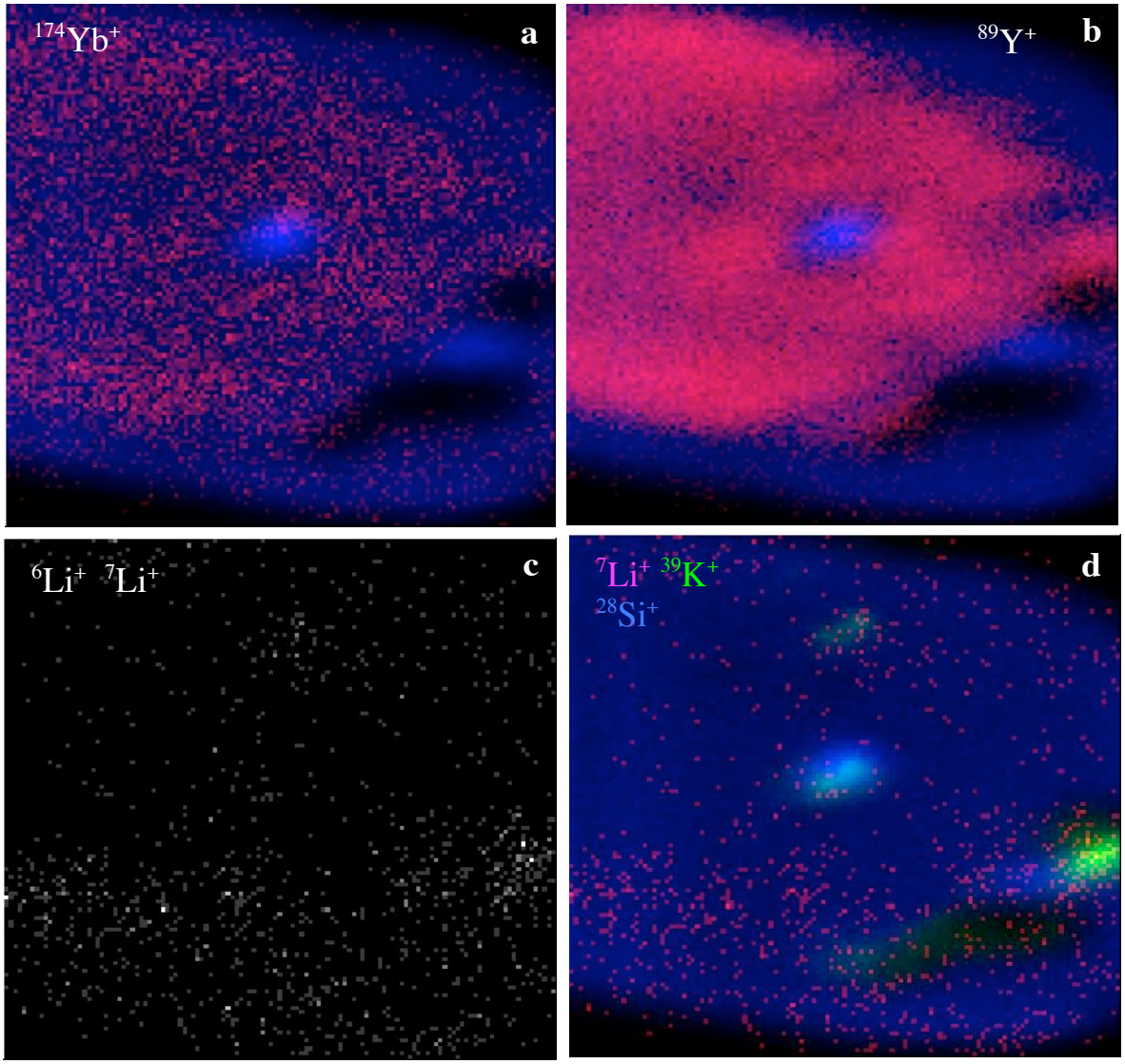

Fig. 4.4.6: a) Combined TOF-SIMS ion map: ^{174}Yb = red, $^{28}Si^+$= blue; b) ^{89}Y = red, $^{28}Si^+$= blue; c-d: $^6Li^+$ / $^7Li^+$ ion maps; Note: Figure d is combination of $^7Li^+$, $^{39}K^+$, and $^{28}Si^+$ distribution maps.

Thus, dehydration melting of phengite can give a significant input of Li in depths greater than 100 km and is the favoured explanation for the Li-enriched zircons rims observed in this study.

The zircons were also investigated for some negative secondary ions with the TOF-SIMS method. Ion maps of sulphur, chlorine and hydrogen show higher concentrations in the area of the two exposed diamonds (Figs. 4.4.7a-c), whereas the phosphorous ion map shows no significant amount of $^{31}P^-$ except for a monazite grain (small pink area) in the left part of Figure 4.4.7d. The presence of sulphur, chlorine and hydrogen in the diamond inclusion area implies a diamond precipitation from C-O-H-S-Cl-fluids.

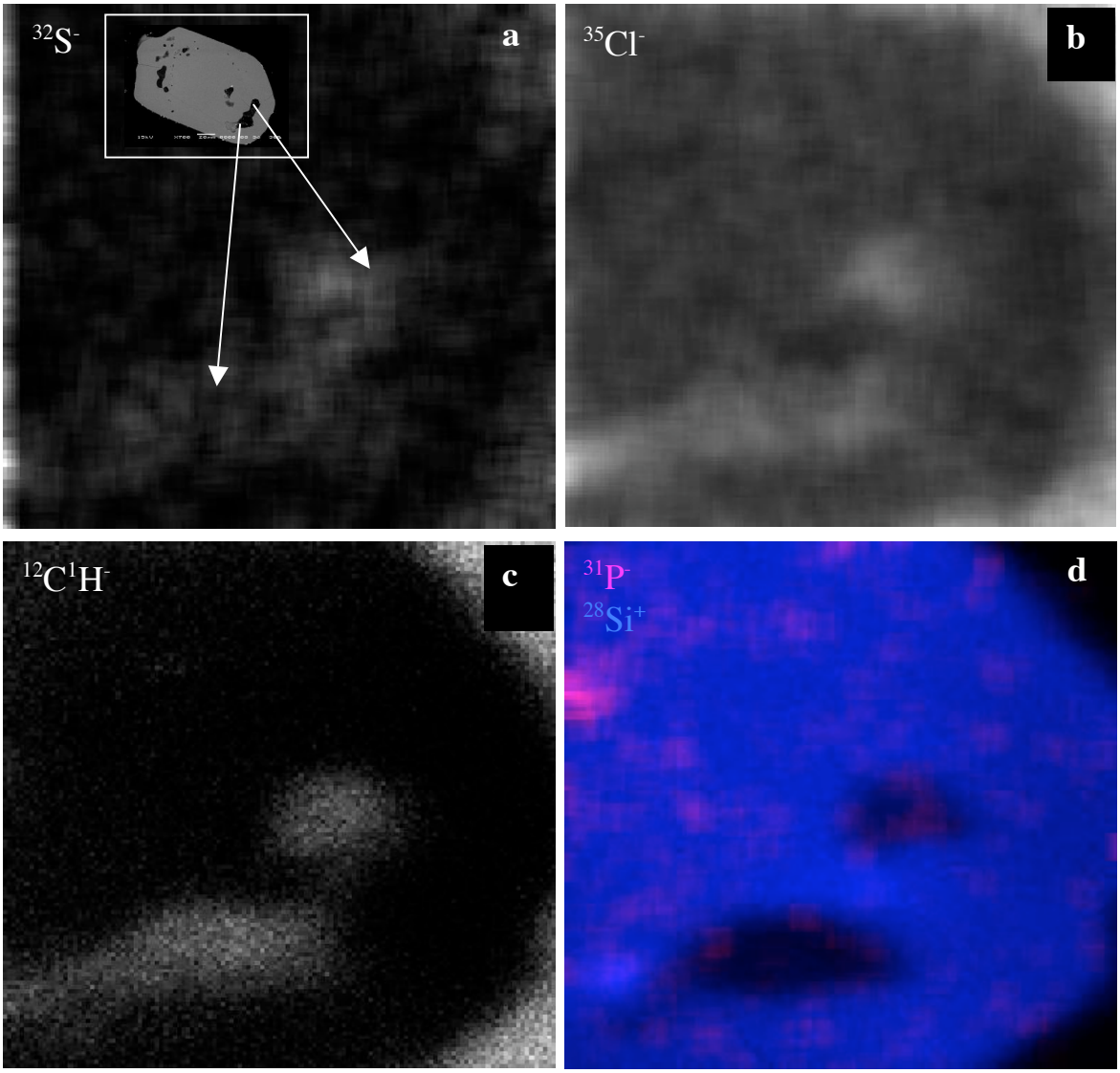

Fig. 4.4.7: TOF-SIMS ion maps of secondary negative ions: a) $^{32}S^-$, b) $^{35}Cl^-$, c) $^{12}C^1H^-$, d) Combined ion map: $^{31}P^-$= red, $^{28}Si^+$ =blue.

P-T conditions

The minimum peak metamorphic conditions of the metapelite samples F157 and RH388 can be estimated from their zircon inclusion mineralogy and the element mapping of the zircons with TOF-SIMS.

Minimum peak pressures of 4 GPa are indicated by the presence of diamond in metamorphic rims of the zircons. Ultra-high temperatures of 1070 °C at 20 kbar are indicated by the absence of Y in the metamorphic rims of the zircons and by the enrichment of Li in the same zircon domain,

which points to phengite dehydration melting during subduction. Fig. 4.4.8 shows a P-T diagram and the suggested P-T path for the metapelites of the Eastern Rhodope investigated during this study. Prograde mineral assemblages in the metapelites are only preserved as inclusions in garnet porphyroblasts. Therefore, a prograde path through the staurolite into the kyanite stability field is assumed. Minimum peak-metamorphic conditions (P > 4 GPa, T ~ 1100°C) of the metapelites of the Eastern Rhodope Massif are indicated by the black star. Cross-hatched areas indicate the two possibilities for phengite dehydration melting. Melting may occur either by crossing the phengite dissolution solidus with 2 wt% H_2O (Schmidt et al. 2004; here extended to lower pressures and temperatures) or, where the PT-path crosses the dehydration solidus. Retrograde P-T conditions are indicated by the grey ellipse and were calculated using mineral equilibria (e.g. garnet-biotite thermometre and the garnet-plagioclase-kyanite-quartz barometre for metapelites) of metapelites and amphibolites close to Xanthi, Thermes and north of Drama in the Central Rhodope (Kostopoulos et al. 2003, Kostopoulos et al. 2007). The diagram includes peak-metamorphic P-T data (~ 7 GPa, ~ 1100 °C) of UHP-metapelites of the Central Rhodope in Greece and southern Bulgaria (Mposkos and Kostopoulos 2001, Kostopoulos et al. 2003) indicated by the grey star (Fig. 4.4.8).

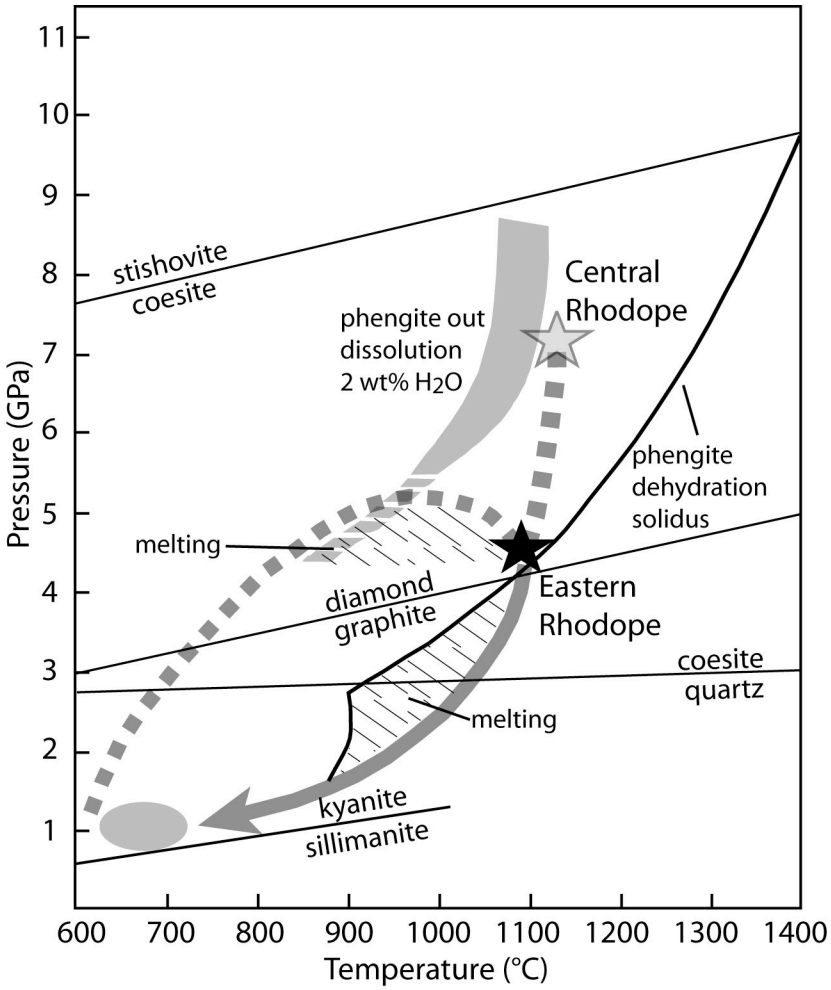

Fig. 4.4.8: P-T diagram and the suggested P-T path for the metapelites investigated during this study. Phengite dissolution and dehydration solidus are from Schmidt et al. (2004); the diamond-graphite transition was calculated with thermodynamic data from Chatterjee et al. (1998); the quartz-coesite transition is from Hemingway et al. (1998); coesite-stishovite transition is from Zhang et al. (1996); sillimanite-kyanite transition after Bohlen et al. (1991), grey star indicates peak-metamorphic conditions of metapelites of the Central Rhodope of Greece and southern Bulgaria (Mposkos and Kostopoulos 2001, Kostopoulos et al. 2003).

4.5 Dating of UHP sample F157

Prior to the zircon study with Laser-Raman Spectroscopy and TOF-SIMS, 40 zircons from the metapelitic garnet-kyanite gneiss F157 from the Ada section were mounted in epoxy and dated by LA-SF-ICPMS to constrain better the age of this sample and to provide some information about the provenance of this rock, although a detailed provenance study is not the purpose of this thesis. Information about the method as well as ages and analyses are given in Appendix B and E. All ages mentioned in the following text refer to $^{206}Pb/^{238}U$ ages unless stated otherwise and errors are given at 2 sigma-level. The Geological Time Scale (GTS) of Gradstein et al. (2004) was used for age interpretation.

Optically, the zircons are characterized by an oval to elongated shape and rounded edges. The length of the grains ranges between 110 and 200 µm and they are mostly colourless. Several grains show evidence for a zoning structure, consisting of an inclusion-free detrital core surrounded by an inclusion-rich rim. The majority of the inclusions of the zoned zircons are located close to the interface of core and rim (see previous chapter). CL-images show that all zircons contain detrital cores (Figs. 4.5.1a-f), which are partly rounded in shape, but several grains still exhibit crystal faces with minor rounded edges (Figs. 4.5.1d, e) indicating only little

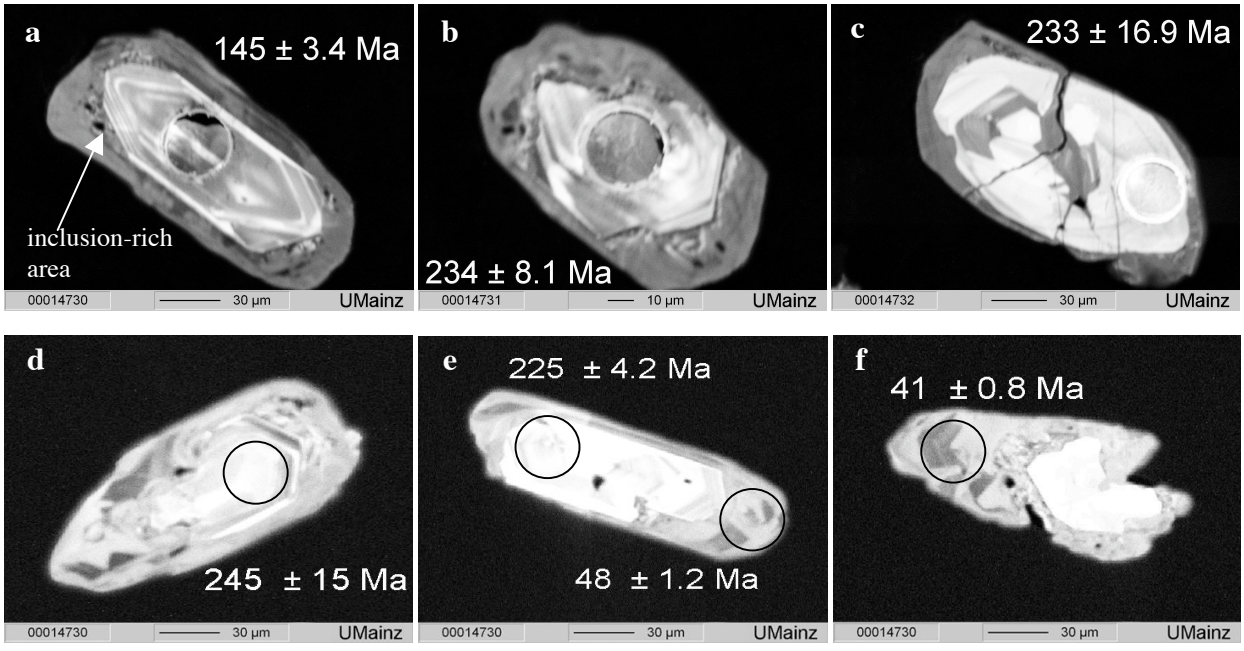

Figs. 4.5.1a-f: Selected CL-images of zircons from the metapelitic sample F157 of the Ada section; black circles in Figs. c-d indicate the location of LA-SF-ICPMS analyses.

sedimentary transport. The simple morphology of the detrital crystals is characteristic of volcanic rocks (the 101-bipyramid dominates over the 211-bipyramid, as does the 100-prism over the 110-prism, see Pupin 1980). Some of these cores indicate that they were of magmatic origin because oscillatory zoning is preserved (Figs. 4.5.1a, b), but the majority consists of rather homogeneous, unzoned crystals (Figs. 4.5.1c-f). Most of the detrital zircons are surrounded by a complex rim showing features of recrystallization and convolute zoning (Figs. 4.5.1a, b, d, f). Three different events can be distinguished from the CL-images. Several detrital cores are surrounded by a heterogeneous "chaotic" zone, which contains simultaneously U-rich (CL-dark) and U-poor (CL-bright) domains (Figs. 4.5.1 a, b, f). This heterogeneous zone equates to the inclusion-rich interface area already visible under the microscope. It is followed by a CL-medium-grey, U-poor band (Fig. 4.5.1a, b, c). In some cases, the heterogeneous inclusion-rich domain is not present and the detrital cores are surrounded by CL-medium-grey, U-poor rims (Fig. 4.5.1e). Some grains show evidence for new magmatic growth at the tips of the zircons (Fig. 4.5.1 f).

Thirty-eight LA-SF-ICPMS analyses were carried out on cores and rims of the zircon grains. Analyses of detrital cores are characterized by low U-contents (5–215 ppm), whereas analyses of the rims show higher U-contents (225–449 ppm). The corresponding Th/U ratios range between 0.18 – 3.59 (cores) and 0.03 – 0.82 (rims), respectively.

Twenty-six analyses on cores yielded ages between 113 and 280 Ma (Fig. 4.5.2a, b). Eleven of those are discordant and their $^{206}Pb/^{207}Pb$-ages indicate Permo-Carboniferous to Palaeoproterozoic sources (*Table 4.5.1*). From the remaining fifteen analyses, a prominent cluster of seven concordant ages occurs in the range between 204 to 245 Ma. For these analyses $^{206}Pb/^{207}Pb$-ages point to Late Permian and Carboniferous ages. Their Th/U ratios of 0.89 to 2.52 suggest a magmatic origin. Another five concordant ages between 126 and 165 Ma were also measured only on cores. $^{206}Pb/^{207}Pb$-ages of these analyses indicate Triassic to Carboniferous ages. Their Th/U ratios range between 0.31 and 2.24 and point to an igneous origin as well.

Twelve analyses were processed on the zircon rims ranging between 115 and 41 Ma and seven of those analyses yielded concordant ages. Three of them cluster around 100 Ma, one analysis gives an age of 73 Ma and one yields 60 Ma (Fig. 4.5.2a, b). The youngest concordant ages are obtained from two measurements on rims of the zircons (Fig. 4.5.1e, f) with ages of 48 and 41 Ma, respectively. Four of these seven rim analyses have Th/U ratios less than 0.1 indicating a metamorphic event. The Th/U ratios of the ages of 107 Ma, 60 Ma and 48 Ma are 0.20, 0.75 and 0.11 respectively, suggesting magmatic character.

The correlation of the ages obtained from rims with a geologically meaningful event is difficult, since the complex structure of the zircon rims and the limited spatial resolution of the laser beam led to mixed analyses of the different rim domains. The youngest event is probably dated best by the age of 41 ±1 Ma measured on the tip of a zircon grain (Fig. 4.5.1f). In the Rhodope Massif this age is usually correlated with granite intrusions and a migmatization event in basement rocks (Jones et al. 1992, Liati 2005).

Conclusively it can be said that inherited cores provide evidence that predominantly Permo-Triassic to Carboniferous igneous rocks but also Silurian to Palaeoproterozoic rocks were present in the source area during deposition of this sediment. In the Internal Hellenides, Triassic ages are related to rifting processes like in the Serbo-Macedonian Massif, where A-type granitoids of the Arnea suite intruded into the Siluarian basement. The age of sedimentation of this metapelitic sample F157 remains unclear, but assuming that the zircons with $^{206}Pb/^{207}Pb$-ages in the range of 200 – 233 Ma are the youngest detrital input (although a better statistic is needed here), the age of this sediment is probably younger than 200 Ma.

CL-images reveal that the zircons experienced three different magmatic/metamorphic events. The age of these events is still ambiguous, but the youngest event is indicated by the new growth of zircon at the tips probably around 41 Ma. The age of the heterogeneous inclusion-rich domain can be estimated only relatively. It is younger than the youngest detrital input of ~ 200 Ma but older than 41 Ma.

Table 4.5.1: Selected LA-SF-ICPMS analyses of detrital zircon cores from metapelite sample F157

sample	no.	ratios									ages								
		207Pb	Ua	Pba	Thc	207Pbe	2 s	206Pbe	2 s	rho	207Pbe	2 s	207Pb	2 s	206Pb	2 s	207Pb	2 s	Conc
		(cps)	(ppm)	(ppm)	U	235U	%	238U	%		206Pb	%	235U	(Ma)	238U	(Ma)	206Pb	(Ma)	(%)
F157	z33	1442	64	2	0.78	0.1944	5.9	0.0240	3.6	0.61	0.0588	4.7	180	11	153	6	558	51	85
F157	z37	2330	64	4	3.21	0.3135	5.0	0.0394	3.1	0.61	0.0578	3.9	277	14	249	8	520	43	90
F157	z41	4196	68	5	1.87	0.5916	41.1	0.0444	6.6	0.16	0.0967	40.6	472	194	280	19	1561	381	59
F157	z49	4742	61	3	1.88	0.1986	4.7	0.0272	3.4	0.73	0.0530	3.2	184	9	173	6	327	37	94
F157	z50	5155	344	6	0.31	0.1391	6.3	0.0177	2.1	0.33	0.0570	6.0	132	8	113	2	490	66	86
F157	z60	2571	179	4	0.42	0.1412	5.0	0.0194	2.1	0.41	0.0528	4.6	134	7	124	3	321	52	92
F157	z66	1359	43	1	0.98	0.2102	6.0	0.0270	2.8	0.46	0.0564	5.4	194	12	172	5	469	59	89
F157	z73	4202	215	8	1.09	0.2220	3.6	0.0299	2.0	0.56	0.0539	3.0	204	7	190	4	367	34	93
F157	z78	2493	180	5	0.56	0.1771	4.5	0.0244	2.8	0.62	0.0526	3.5	166	7	156	4	310	40	94
F157	z80	1212	20	1	1.89	0.3360	6.0	0.0440	3.8	0.63	0.0554	4.6	294	18	278	10	427	52	94
F157	z86	2628	152	5	0.50	0.2442	4.5	0.0314	2.7	0.61	0.0565	3.6	222	10	199	5	471	39	90

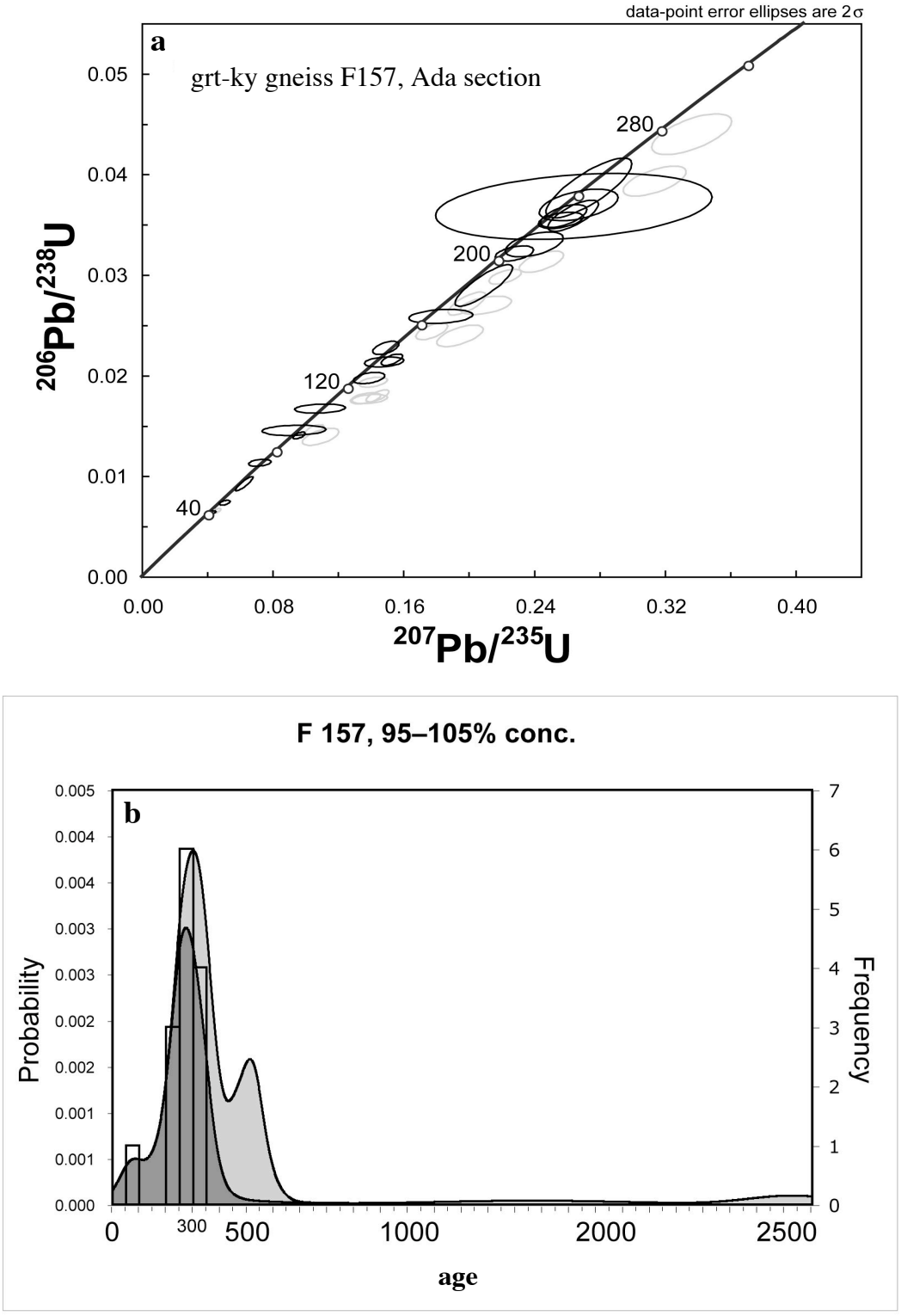

Fig. 4.5.2a, b: a) Concordia diagram ($^{206}Pb/^{238}U$) of the garnet-kyanite gneiss F157 from the Ada section; black ellipses mark the concordant ages; b) Combined probability density and histogram plots for $^{206}Pb/^{207}Pb$-ages of sample F157; n = 38; dark shaded areas correspond to concordant ages, light-grey shaded areas correspond to discordant ages.

4.6 Summary metapelites

The metapelites investigated in this study are garnet±kyanite-bearing micaschists/gneisses, which were sampled from the intermediate mélange zone. The latter crops out between the Jurassic Rhodope Terrane and the Permo-Carboniferous Thracia Terrane and can be identified in the field by its characteristic rock association of migmatitic amphibolites, garnet-bearing micaschists/gneisses, marbles and intercalated orthogneisses. Such characteristic rock associations were found in the Ada-, Sidiro-, and Kimi sections in the study area.

The size of the **garnet** porphyroblasts of the metapelites ranges between a few millimetres up to about two centimetres and they are all almandines with X_{fe} = 0.63-0.95. Profiles and element distribution maps suggest a prograde growth zoning except for garnets from sample RH412 from the Kimi section. **Kyanite** occurs as prismatic porphyroblasts in many samples and locally it can reach a size up to several millimetres. Kyanite and garnet show evidence for a strong deformation. **Staurolite** occurs along with kyanite and paragonite as inclusions in the garnet of sample F157 from the Ada section indicating a prograde garnet growth in the stability-fields of these minerals. Matrix **muscovite** is generally poor in celadonite component with Si p.f.u. values ranging from 3.0 to 3.3. The highest Si p.f.u. of 3.34 was measured in matrix muscovites of the sample RH388.

Whole-rock geochemistry suggests that the source rocks of the garnet±kyanite-bearing micaschists/gneisses are wackes or shales. Amphibole-bearing garnet-gneisses are derived from more mafic sources. REE patterns indicate a derivation from old upper continental crust and/or young differentiated arc material.

A **SEM-, Laser-Raman- and TOF-SIMS** study of zircons from sample F157 revealed a simple zoning structure for the zircon grains. A rather inclusion-free, detrital core is surrounded by an inclusion-rich rim of metamorphic origin. The rims of the zircons contain inclusions comprising albite/plagioclase, K-feldspar, white mica, kyanite, rutile, hematite, monazite, apatite, xenotime, CO_2 gas inclusions and diamond. The diamond inclusions indicate pressures in excess of 4 GPa. TOF-SIMS element distribution maps display a concentration of HREE in the detrital core and an enrichment of Li in the metamorphic rim. Experimental results of Rubatto and Hermann (2007) suggest temperatures around 1070 °C at 20 kbar for a partition coefficient of Y between garnet and zircon above unity. Significant input of Li at depths greater than 100 km can be explained by

dehydration melting of phengite and is the favoured explanation for the Li-enriched zircons rims observed in this study.

LA-SF-ICPMS dating of detrital zircons from the metapelitic sample F157 indicate that Permo-Triassic to Carboniferous igneous rocks but also Silurian to Palaeoproterozoic rocks were present in the source area during deposition of this sediment. The age of sedimentation of this metapelitic sample F157 is probably younger than 200 Ma. CL-images reveal that the zircons experienced three different magmatic/metamorphic events. The age of these events is still ambiguous due to mixed analyses, but the youngest event is indicated by the new growth of zircon at the tips related to a thermal overprint at probably around 41 Ma. The age of the heterogeneous inclusion-rich domain can be estimated only relatively. It is younger than the youngest detrital input of ~ 200 Ma but older than 41 Ma.

5. Orthogneisses

5.1 Petrography of the orthogneisses

The orthogneisses investigated in this study were sampled along the cross sections close to Paterma-Ada, Drania-Smigada-Kimi and Mega Derio-Sidiro (see chapter 3) and, to constrain more precisely the extent of the different terranes, orthogneisses were sampled also from other localities within the units. The mineralogy of the orthogneisses is given in *Table 5.1.1*, GPS-coordinates are listed in Appendix A.

The Thracia Terrane of the Eastern Rhodope Massif comprises different types of orthogneisses. The most frequent orthogneiss-variety of the Thracia Terrane is a medium-greyish augengneiss with a foliation defined by micas (Fig. 5.1.1a). The augen mostly form σ-clasts, and their size can reach from few millimetres up to one centimetre. Most gneisses contain biotite and muscovite, but in some places a leucocratic muscovite-gneiss variety occurs (e.g. RH387), which is highly sheared (Fig. 5.1.1b) and sometimes displays mylonitic textures. A third variety of orthogneisses was observed in the Paterma-Ada section, where the gneisses show slightly different textures. Most of these rocks are more sheared and show only small (~ 1mm) or stretched K-feldspar porphyoclasts (see previous chapter Fig. 3.3a), but they contain also both, muscovite and biotite.

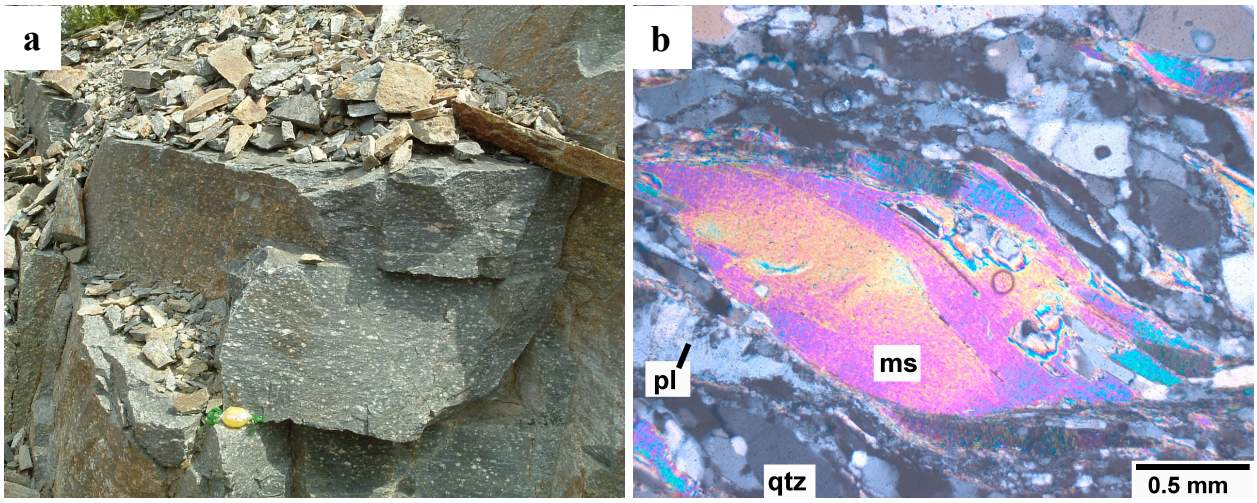

Fig. 5.1.1a, b: a) Photograph of a typical augengneiss of the Thracia Terrane from the Eastern Rhodope Massif; scale: sweet, 2cm length; b) Mica-fish (muscovite) from highly sheared leucocratic muscovite-gneiss (RH387), surrounded by a matrix of plagioclase, quartz and white mica, polarized light.

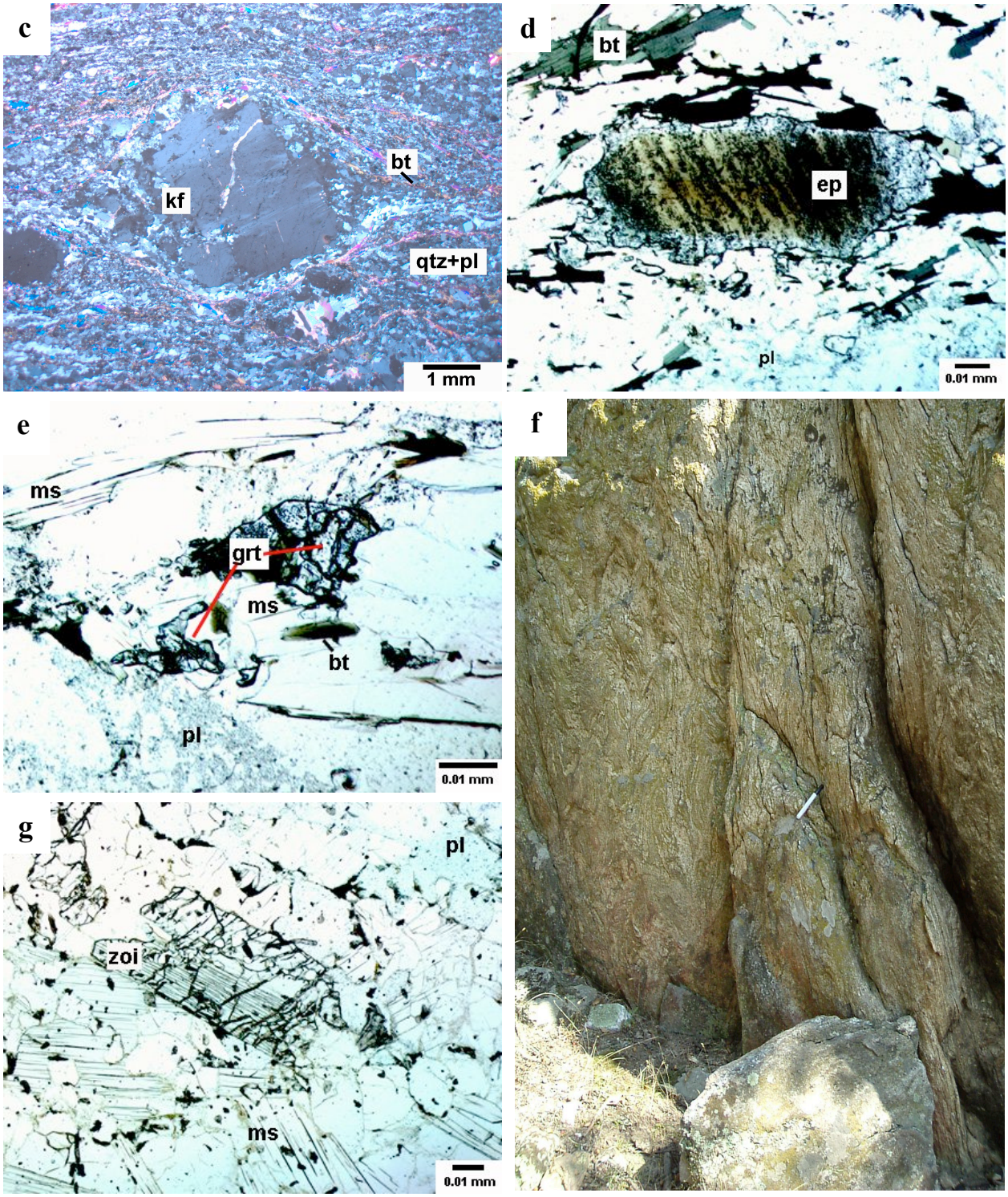

Fig. 5.1.1c-g: c) Deformed K-feldspar porphyroclast in a fine-grained matrix of plagioclase, quartz, biotite and muscovite (typical augengneiss), polarized light; d) Epidote with an old brownish core surrounded by a second generation of colourless to light-greenish epidote (RH369), transmitted light; e) Garnet relicts are replaced by muscovite, plagioclase and minor biotite (RH371), transmitted light; f) Outcrop of sample RH477: folded, migmatic, leucocratic gneiss occurring between Sidiro and Gianulli; g) Zoisite surrounded by muscovite und minor plagioclase (RH477), transmitted light.

The fourth orthogneiss variety is marked by a weakly deformed, porphyritic, granitic gneiss at the end of the Paterma-Ada section (see previous chapter Fig. 3.3d).

In thin section the augengneisses show typically K-feldspar porphyroclasts (Fig. 5.1.1c), partly recrystallized and often with myrmekites around them, in a fine- to medium-grained matrix of biotite, muscovite, K-feldspar, plagioclase and quartz. Biotite is often strongly chloritized, except in few orthogneisses from the Paterma-Ada section, where it is dark reddish brown in colour. Apatite is an abundant mineral in two of the Ada samples (RH345, RH346). Calcite is present along veins in two samples (RH358, RH434). In many orthogneisses, light-greenish epidote is an abundant matrix mineral in the mica-rich layers and sometimes epidotes with old, brownish cores and light-greenish rims can be observed (e.g. RH369, Fig. 5.1.1d).

Table 5.1.1: Mineralogy of the orthogneisses of the Eastern Rhodope Massif

sample	location	qtz	kfs	pl	bt	ms	chl	ep	zoi	grt	ap	ru/sph	cc
RH344	Ada	x	x	x	x	x	x	-	-	-	-	-	-
RH345	Ada	x	x	x	x	x	x	-	-	-	x	-	-
RH346	Ada	x	x	x	x	x	x	-	-	x	x	-	-
RH358	Ada	x	x	-	x	-	x	-	-	-	-	-	x
RH360	Ada	x	x	x	x	x	x	-	-	-	-	-	-
RH361	Ada	x	x	x	x	x	x	-	-	-	-	-	-
RH367	Ada	x	x	x	-	x	x	-	-	x	-	-	-
RH369	Dadia-Kotronia	x	x	x	x	-	x	-	x_{ep}	-	-	-	-
RH370	Dadia-Kotronia	x	x	x	x	-	x	-	-	-	-	-	-
RH371	Essimi-Leptokaria	x	x	x	x	x	x	-	-	x	-	-	-
RH373	Essimi-Leptokaria	x	x	x	x	x	x	-	x_{ep}	-	-	-	-
RH375	Leptokaria-Dadia	x	x	x	x	x	x	-	-	-	-	-	-
RH376	Leptokaria-Dadia	x	x	x	x	x	x	x_{zoi}	x_{ep}	-	-	x_{sph}	-
RH382	Dadia-Kotronia	x	x	x	x	x	x	-	-	-	-	-	-
RH383	Dadia-Kotronia	x	x	x	x	x	x	-	-	-	-	-	-
RH387	Mega Derio-Sidiro	x	x	x	-	x	-	-	-	-	-	-	-
RH389	Mega Derio-Sidiro	x	x	x	x	x	x	-	-	-	x	-	-
RH390	Mega Derio-Sidiro	x	x	x	x	x	x	x_{zoi}	x_{ep}	-	-	-	-
RH413	Drania-Organi	x	x	x	x	x	x	-	-	-	-	-	-
RH418	Organi-Smigada	x	x	x	x	x	-	-	-	-	-	-	-
RH423	Smigada-Kimi	x	x	x	x	x	x	-	x_{ep}	-	-	-	-
RH429	Smigada-Mirtiski	x	x	x	x	x	x	-	-	-	x	-	-
RH434	Leptokaria-N. Sanda	x	x	x	x	x	x	-	-	-	-	-	x
RH441	Nymphea	x	x	x	x	x	x	-	-	-	-	-	-
RH447	Sidiro-Gianulli	x	-	x	-	x	-	x_{zoi}	-	x	-	x_{ru}	-
RH455	Sidiro	x	-	x	-	-	x	-	-	-	-	-	-

Matrix-quartz-layers are much coarser than the feldspar-mica layers in some samples (RH373, RH382). Some of the gneisses show small relicts of garnet completely surrounded by plagioclase and/or micas (e.g. RH346, RH371, Fig. 5.1.1e).

The Rhodope Terrane of the Eastern Rhodope Massif is characterized by two different types of orthogneisses. The first type is represented by orthogneisses from the Smigada-Kimi section. The variably deformed, non-porphyritic biotite±muscovite gneisses from the Smigada-Kimi section (e.g RH423) correspond to the Central Rhodopian Terrane gneisses described by Turpaud (2006). Biotite is strongly chloritized in this sample and in contrast to the Thracian Terrane augengneisses, the dominant feldspar of sample RH423 is plagioclase. In the easternmost part of the Rhodope Massif between Sidiro and Gianulli, the Rhodope Terrane is characterized by strongly migmatitic, folded, leucocratic gneisses (RH477, RH455, Fig. 5.1.1f). In these two samples, plagioclase is the dominant feldspar as well. Zoisite growing in muscovite-rich layers is abundant in sample RH447 (Fig. 5.1.1g), which also contains relicts of garnet.

5.2 Geochronology of the orthogneisses

Zircons from sixteen orthogneiss samples from both terranes of the Eastern Rhodope Massif were dated by LA-SF-ICPMS, to constrain the timing of the emplacement of the orthogneisses protoliths. Usually, ten to thirty laser-spots were measured per sample. Two of the samples were additionally dated by sensitive high-resolution ion microprobe (SHRIMP II). SHRIMP-analyses were performed at the Centre of Isotopic Research (VSEGEI) in St. Petersburg, Russia, by Guido Meinhold. Ten spots on sample RH346 and five on sample RH373 were selected for SHRIMP-dating. In all cases, both domains, core and rim of the zircon grains were selected for dating. Locations of the dated samples are shown in Figure 5.2.1. GPS coordinates of the samples, the analytical procedure, ages and the corresponding analyses are given in Appendix A, B and E.

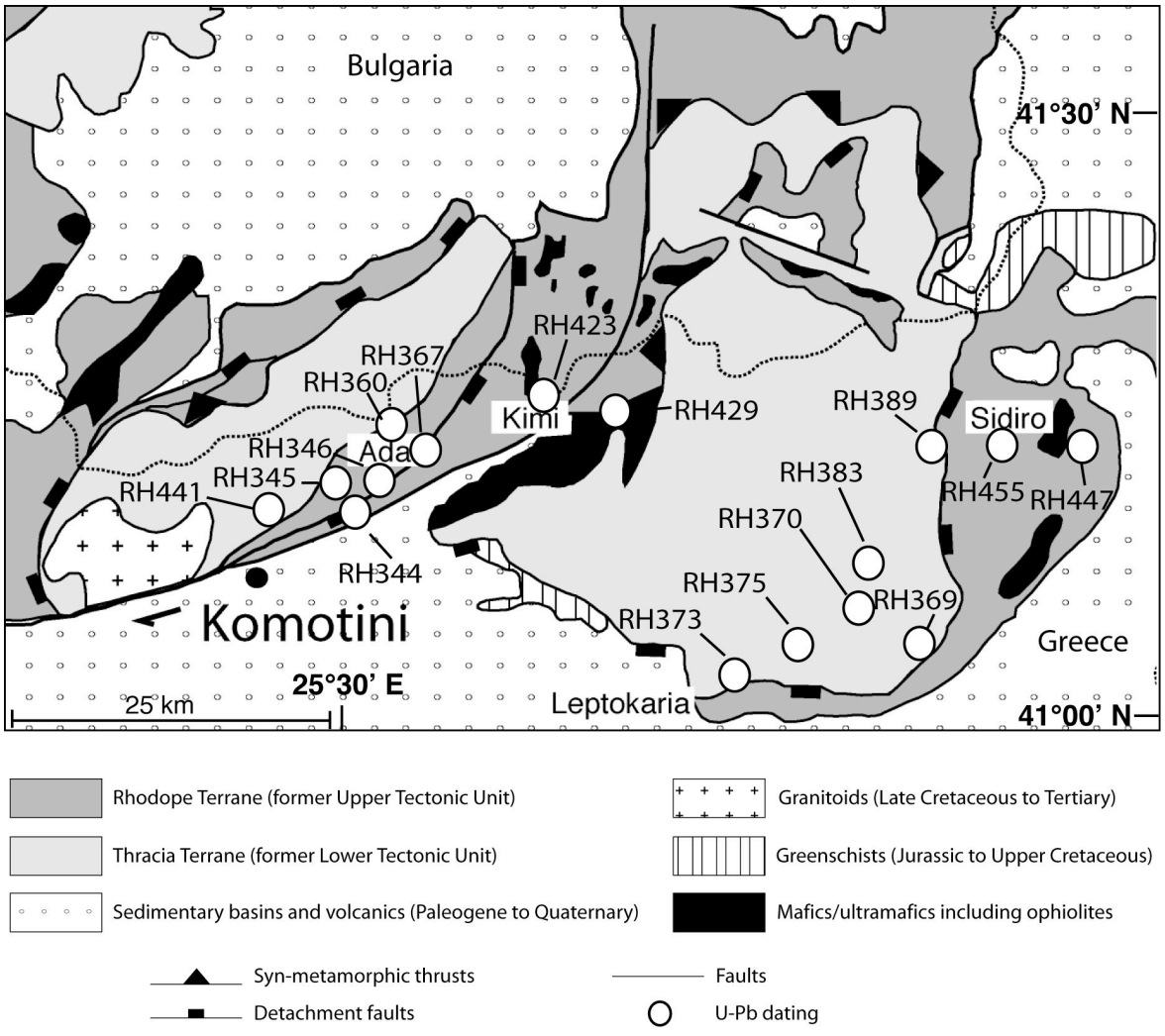

Fig. 5.2.1: Simplified geological map of the Eastern Rhodope Massif modified after Bonev et al. (2006) showing the Rhodope main tectonic units and the locations of the orthogneisses dated during this study.

Optical observations and cathodoluminescence imaging of the zircons

The zircons were investigated optically and with the cathodoluminescence (CL) technique of the Jeol JXA 8900 RL microprobe at the University of Mainz. The size of most zircons ranges between 60 and 150 μm, except few grains with up to ca. 250 μm. In most samples, the zircons are colourless or yellowish. Notably for samples from the Thracia Terrane the yellowish, bleary zircons are usually bigger then the colourless ones. Inclusions are present in most samples. They mostly consist of apatite and rutile, but also quartz and minor feldspar and micas were observed. In sample RH423 the amount of inclusions in the zircons is extremely high, whereas sample RH360 exhibits several inclusion-free grains. Crystal faces are not always well preserved. Nevertheless, some differences in typology could be distinguished. The zircon typology classification of Pupin (1980) is based on the development of the main zircon pyramid and prism faces. In some samples from the Eastern Rhodope the zircons show predominantly the bipyramidal 211-face (RH360, RH369, RH413, RH429), while in others the bipyramidal 101-face dominates over the 211-face (RH344, RH367, RH375, RH383, RH423, RH441). Some samples exhibit both crystal faces in varying size (RH345, RH346, RH370, RH373) (Fig. 5.2.2).
CL-images allow studying the internal structure of the zircon grains. This method gives important information for the interpretation of the age data, because the images display features like magmatic zoning, inherited cores or overgrowth of the grains. Four different groups of growth-textures of the zircons could be distinguished in this study. The first group is marked by zircons that show well-developed, continuous oscillatory zoning from core to rim (RH344, RH367, RH370, RH373, RH375, RH383, RH441, Fig. 5.2.3a, b, i, j, m – t, y, z), a feature indicative of a magmatic origin. Furthermore, RH383 exhibits some grains showing sector zoning (Fig. 5.2.3t). The second group consists of zircons, which often possess inherited, xenocryst cores of variable size (RH345, RH346, RH360, RH369, RH429, Fig. 5.2.3c, d, g, h, k, l, w, x). Primary growth zoning is preserved in these cores (Fig. 5.2.3e, f) and the contact to the rims is characterized by geometrically irregular surfaces generated by resorption. The cores are surrounded by a domain of oscillatory zoning, indicative of magmatic origin. Finally, the outer rim is marked by thin, newly grown metamorphic domains of rather homogeneous composition (Fig. 5.2.3a-d, α, β). The third group is represented by the zircons of sample RH423. The cores of the zircons are often highly metamict and are often crosscut by numerous cracks, while the rims show well-developed oscillatory zoning (Fig. 5.2.3α, β).

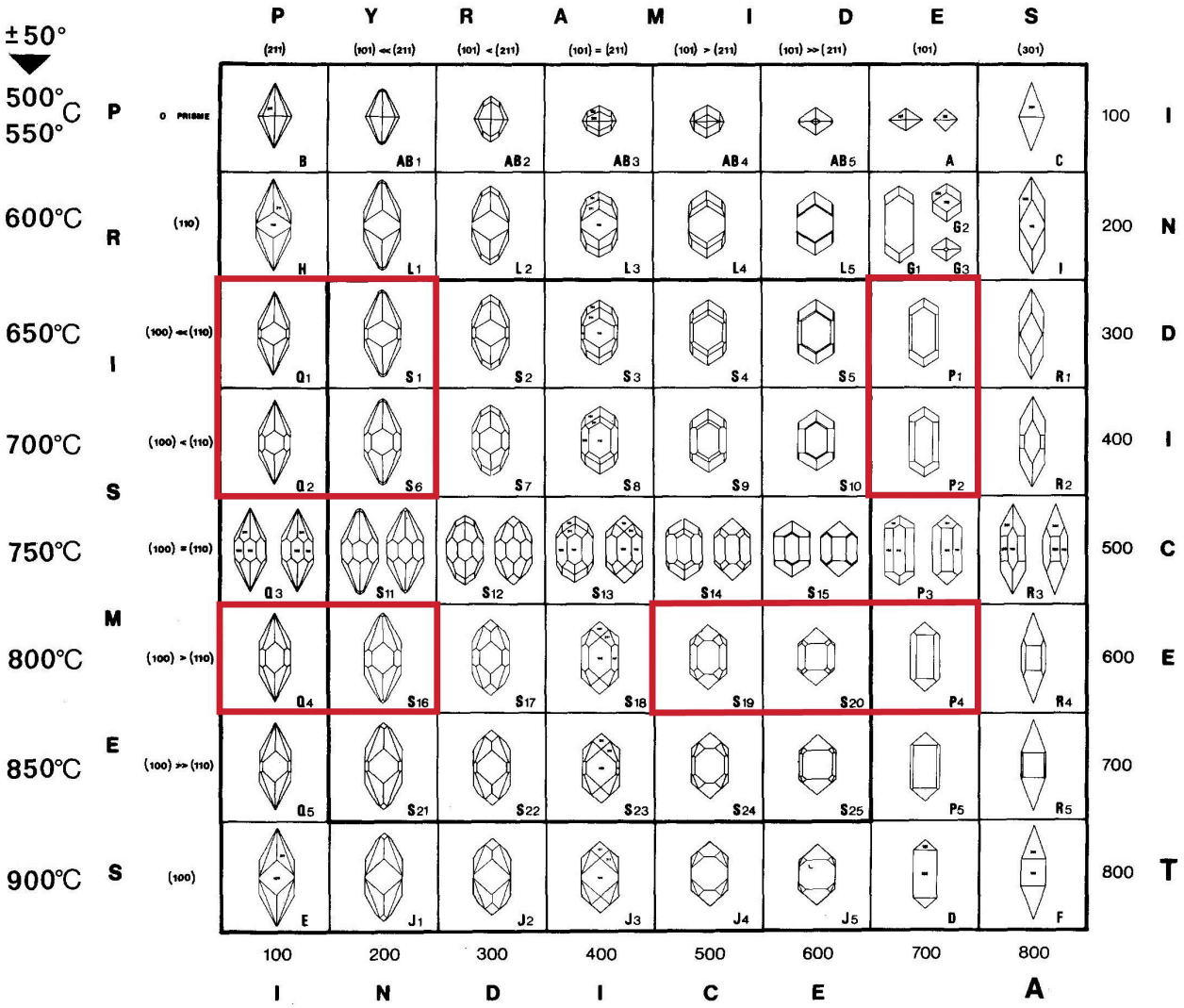

Fig. 5.2.2: Typologic classification of zircons and corresponding thermometric scale after Pupin and Turco (1972). Red boxes mark the main types of zircons observed in the orthogneisses from the Eastern Rhodope Massif in this study. Differences in zircon type do not allow to distinguish orthogneisses from different terranes or of different age.

Most of the zircons exhibit a thin, CL-bright rim of homogeneous composition (Fig. 5.2.3α, β). The zircons of the fourth group are characterized by convolute zoning (RH447, RH455, Fig. 5.2.3γ, ε). Recrystallization processes during late- and post-magmatic cooling cause the concentration of trace elements in convolute zones (Corfu et al. 2003).

Next page: Fig. 5.2.3a-p: Selected CL-images of magmatic zircons from the Thracia Terrane of the Eastern Rhodope Massif showing LA-ICPMS spots and corresponding U-Pb ages.

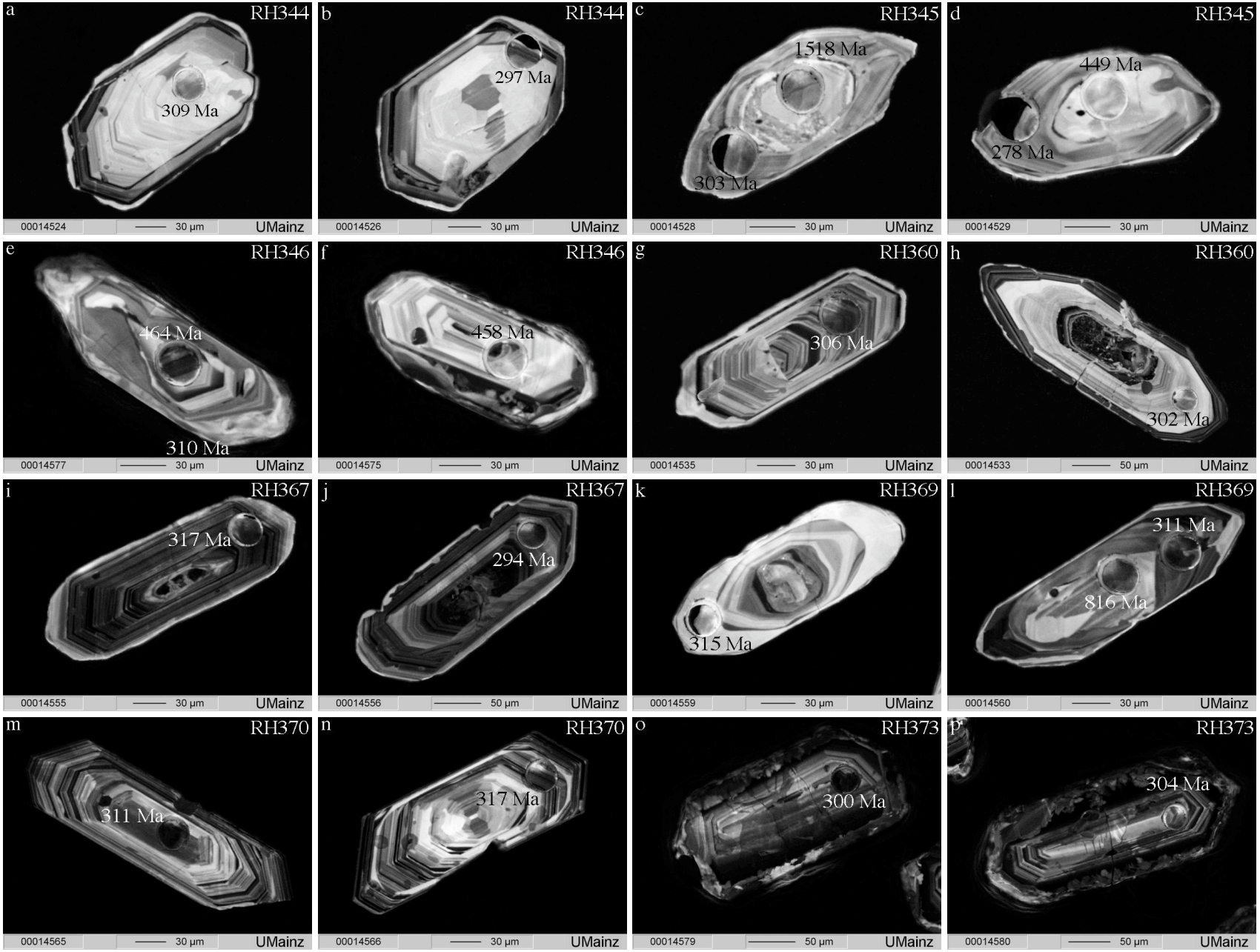

caption on page 64

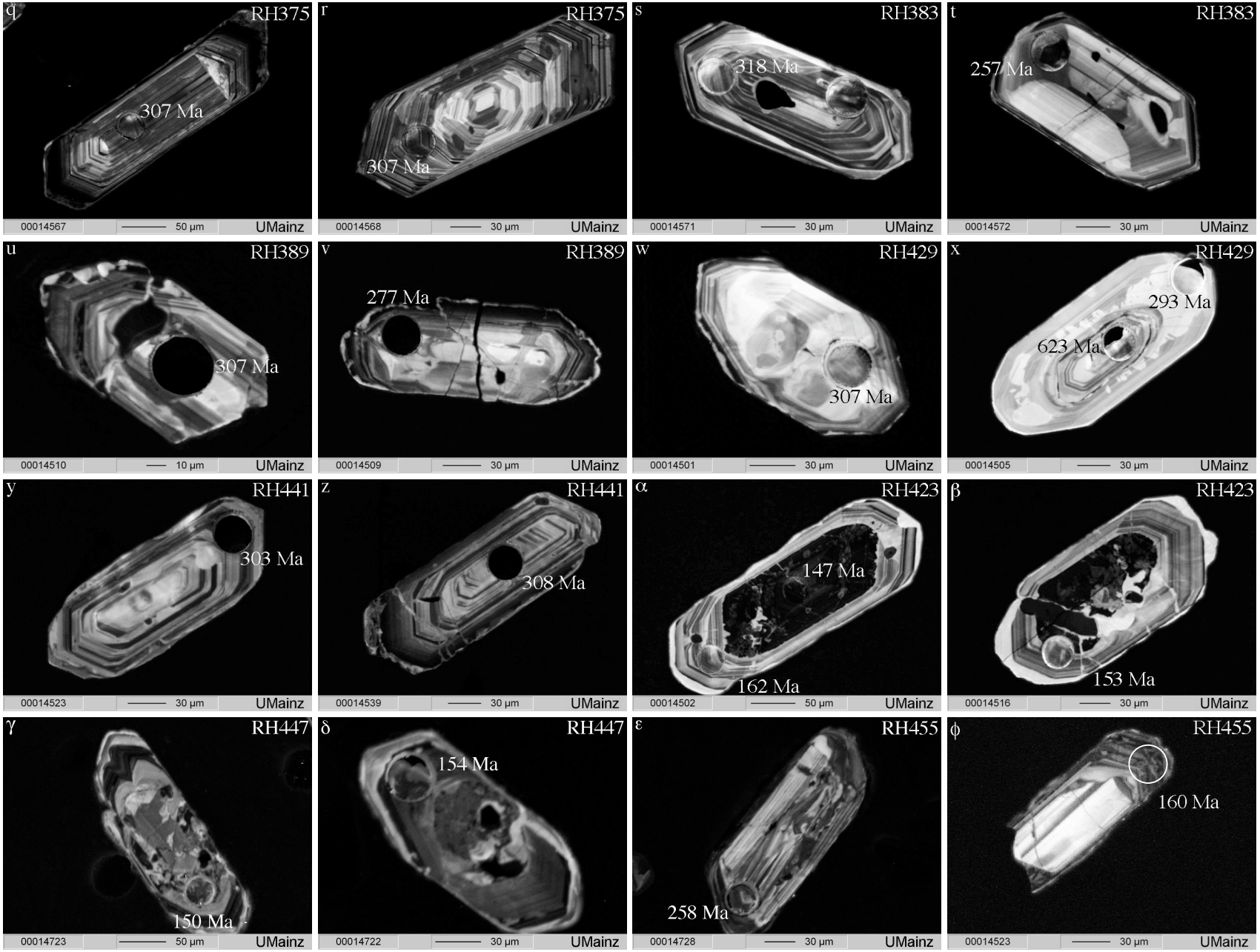

caption on page 67

Previous page: Fig. 5.2.3q-ϕ: Selected CL-images of magmatic zircons from the Eastern Rhodope Massif showing LA-ICPMS spots and corresponding U-Pb ages; (q-z) Thracia Terrane, note image t: sector zoned zircons from sample RH383; (α-ϕ) Rhodope Terrane.

Zircons from most of the felsic gneisses from the Eastern Rhodope exhibit detrital cores, which is clearly shown by CL-images. Figure 5.2.4 shows the age distribution of the inherited cores in a combined probability density and histogram plot. All ages were obtained using LA-SF-ICPMS and errors are given at 2-sigma-level. $^{206}Pb/^{238}U$-ages for these cores are often discordant and show much younger ages than the corresponding $^{206}Pb/^{207}Pb$-data. The oldest (discordant) $^{206}Pb/^{238}U$-age of a detrital core found in these samples is 2328 Ma (RH369). In a concordia plot the detrital core and the rim of this zircon grain indicate an upper intercept of 3088±31 Ma (in good agreement with the $^{206}Pb/^{207}Pb$-age of 3042 Ma) and a lower intercept of 324.6±7.8 Ma (Fig. 5.2.5). Three detrital cores of other grains show $^{206}Pb/^{238}U$-ages of 895, 1518 and 1918 Ma, respectively, but according to their $^{206}Pb/^{207}Pb$-ages, they are around 2 Ga-old (*Table 5.2.1*). The calculation of the upper intercept of the 1518 Ma-old core yields an age of 2172±74 Ma, which is again in good agreement with its $^{206}Pb/^{207}Pb$-age of 2099 Ma. Furthermore, $^{206}Pb/^{207}Pb$-ages of 1447 and 1744 Ma were observed, where corresponding $^{206}Pb/^{238}U$-ages give an age of 816 and 317 Ma (*Table 5.2.1*), respectively. Nevertheless, $^{206}Pb/^{207}Pb$-data should be treated carefully. The younger the ages of the zircons the smaller are the amounts of ^{207}Pb and the less precise are the $^{206}Pb/^{207}Pb$-ages. Therefore $^{206}Pb/^{207}Pb$-ages ages significantly younger than 1.2 Ga are less reliable. Twenty-one analyses yield $^{206}Pb/^{238}U$-ages between 510 and 654 Ma, while thirty measurements range between 410 and 485 Ma. Similar ages for inherited zircons of samples from the Rhodope Massif were reported by Liati (2005) for a garnet-kyanite-gneiss from the Xanthi-area and by Turpaud (2006) for two biotite-gneisses from the Central Rhodope. Ages in the range of 500–700 Ma and between 2 und 2.1 Ga point to a Gondwana provenance (e.g. Liati 2005, Meinhold et al. 2008).

Interestingly, the samples RH345 and RH346 from the Ada section show an accumulation of concordant ages between ca. 410 and 500 Ma, which is also the main peak in the histogram plot (Fig. 5.2.4). Many of the zircons show preserved oscillatory zoning and in some cases a Carboniferous overprinting event only at the outermost rims. Similar ages (400 – 500 Ma) were also found in some detrital zircon cores of the sample RH369, RH383 and RH455. It is worth notifying, that the sample RH429 from the section Smigada-Mirtiski shows even older

concordant ages clustering at 520 and 600 Ma (Fig. 5.2.3 CL-image x, Fig. 5.2.4 second highest peak).

Table 5.2.1: Selected LA-SF-ICPMS analyses of detrital zircon cores and some corresponding rims from orthogneisses of the Eastern Rhodope.

sample	no.						ratios						ages							
		core/	207Pb	Ua	Pba	Thc	207Pbe	1 s	206Pbe	1 s	rho	207Pbe	1 s	207Pb	2 s	206Pb	2 s	207Pb	2 s	Conc
		rim	(cps)	(ppm)	(ppm)	U	235U	%	238U	%		206Pb	%	235U	(Ma)	238U	(Ma)	206Pb	(Ma)	(%)
RH369	z46	c	82336	57	35	1.74	13.695	1.9	0.4349	1.7	0.88	0.2284	0.9	2729	104	2328	78	3041	15	85
RH369	z47	r	20743	494	24	0.09	0.378	1.5	0.0517	1.2	0.80	0.0530	0.9	325	10	325	8	330	20	100
RH369	z33	c	19586	109	16	0.46	1.694	3.0	0.1350	1.8	0.60	0.0910	2.4	1006	59	816	29	1447	45	81
RH369	z34	r	24244	612	29	0.29	0.361	2.0	0.0494	1.8	0.90	0.0531	0.9	313	12	311	11	331	19	99
RH345	z65	c	58124	184	52	0.48	4.762	2.8	0.2655	2.0	0.72	0.1301	1.9	1778	98	1518	61	2099	33	85
RH345	z66	r	14849	483	22	0.18	0.336	2.7	0.0465	2.1	0.79	0.0524	1.6	294	16	293	13	303	38	100
RH345	z46	c	8261	162	11	0.69	0.549	5.6	0.0622	3.7	0.65	0.0640	4.3	444	50	389	28	741	90	88
RH345	z68	c	15058	397	20	0.05	0.487	3.2	0.0515	1.4	0.45	0.0687	2.8	403	26	324	9	889	59	80
RH360	z38	c	49568	239	38	0.20	2.796	3.0	0.1490	1.6	0.53	0.1361	2.5	1355	81	895	28	2178	44	66
RH370	z07	c	27261	43	17	0.89	5.611	1.6	0.3309	1.3	0.83	0.1230	0.9	1918	62	1843	50	2000	16	96
RH383	z10	c	28197	192	36	0.63	1.664	1.8	0.1753	1.2	0.63	0.0688	1.4	995	37	1041	24	894	29	105
RH383	z26	c	6448	68	4	0.82	0.741	3.0	0.0503	1.6	0.53	0.1067	2.6	563	34	317	10	1744	47	56

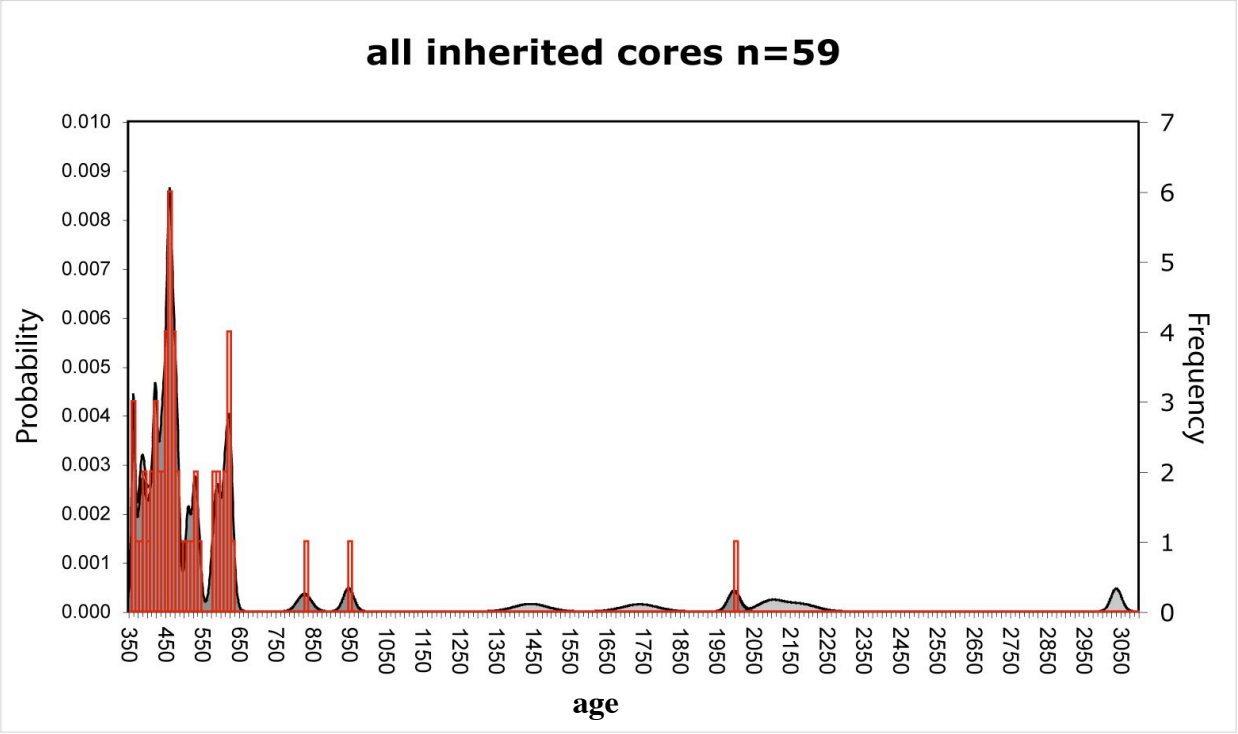

Fig. 5.2.4: Combined probability density and histogram plot for the 59 detrital cores observed in zircons from orthogneisses of the Eastern Rhodope. Dark grey-shaded fields mark concordant ages, whereas medium grey-shaded fields correspond to discordant ages. Ages older 1 Ga are $^{206}Pb/^{207}Pb$-data.

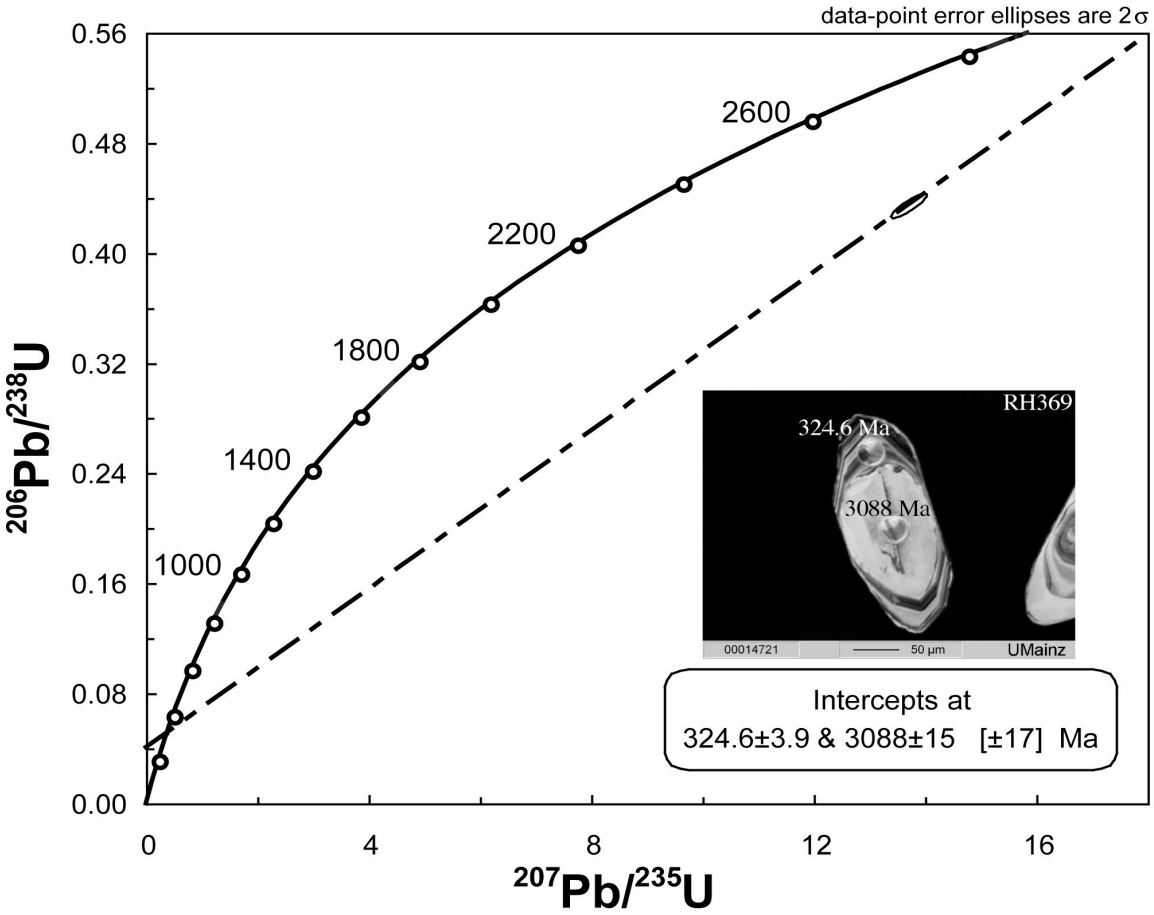

Fig. 5.2.5: Concordia plot of sample RH369 showing the upper und lower intercept of the oldest detrital zircon core observed in this study and the corresponding rim.

Protolith intrusion ages of orthogneisses from the Thracia Terrane

This group is represented by medium-greyish, biotite-muscovite-bearing augengneisses, which are typical rocks for the Thracia Terrane in the Eastern Rhodope. The zircons of these samples often exhibit inherited detrital zircon cores. Therefore, in order to determine the time of emplacement of the granitoids, the rims of the zircons, showing high-frequency oscillatory zoning, were measured and used for the calculation of concordia ages. Nevertheless, most samples do not show a completely homogeneous age distribution. Discordant ages impair the number of analyses that can be used for the calculation of concordia ages. The analyses selected for the age calculation were chosen carefully, but the possibility of mixed analysis of inherited cores and surrounding rims cannot be ruled out completely because of the limited spatial resolution of the laser beam. Also effects like partial resetting or a multistage overprint could be hidden within the analytical uncertainty (Janousek et al. 2006 and references therein). The ages

referred to in the text are $^{206}Pb/^{238}U$-ages unless stated otherwise and all errors are given at 2-sigma-level. Eleven samples yield Carboniferous concordia ages between 294 and 315 Ma (Figs. 5.2.6a-m). The corresponding Th/U-ratios range between 0.1 and 1.16 which is a typical range for magmatic zircons. In the concordia diagrams, the spots, which were used for the age calculation, are shown in red. Grey ellipses mark the spots excluded from the age calculation.

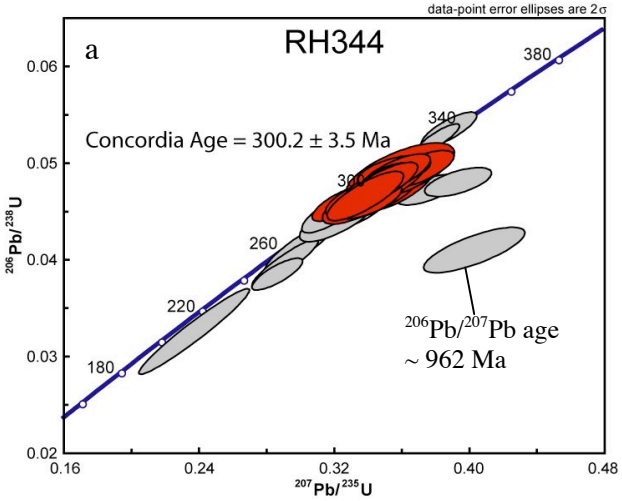

Fig. 5.2.6a: Concordia diagram, sample RH344.

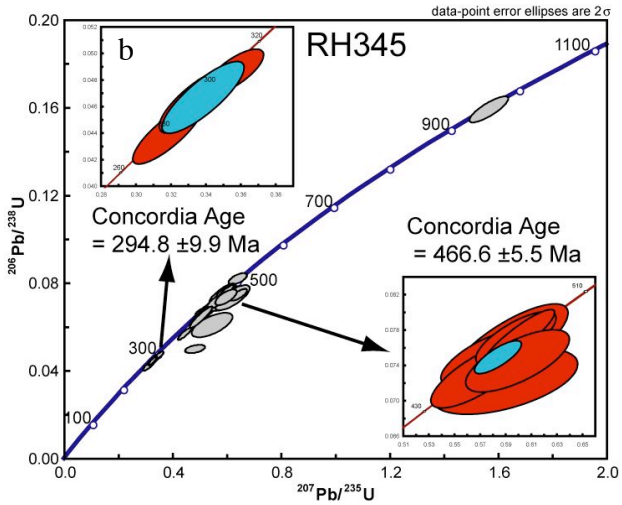

Fig. 5.2.6b: Concordia diagram, sample RH345

RH344–Ada

A concordia age of 300.2±3.5 Ma (2σ, MWSD = 10.5, 95 % confidence, Fig. 5.2.6a) is assumed to be the emplacement age of this biotite-gneiss. Two slightly older spots (336 and 330 Ma), which are perfectly concordant, are interpreted to point to an inherited component. Several analyses yield younger ages from 285 to 209 Ma interpreted as Pb-loss. The $^{206}Pb/^{207}Pb$ ages for these spots indicate older ages around 330 Ma. Three highly discordant spots were rejected from the age calculation.

RH345–Ada

This sample shows several clusters of concordant ages. The youngest event is Early Permian (concordia age of 294.8±9.9 Ma, 2σ, MWSD = 1.3, 95 % confidence, Fig. 5.2.6b) and recorded by only four spots measured on rims, whereas the majority of measurements yielded concordant Devonian to Ordovician ages (410 – 480 Ma). A concordia age of 466.6±5.5 Ma was calculated from 9 spots for the cores of the zircons. Six spots, which are concordant, but slightly younger (410 – 436 Ma) are not included in the age calculation. This sample shows also some older concordant ages of zircon cores (514, 951 Ma).

RH346–Ada

This sample was measured with both, LA-SF-ICPMS (grey ellipses) and SHRIMP II (green ellipses) (Fig. 5.2.6c). It shows a very heterogeneous age distribution with predominantly concordant ages ranging from

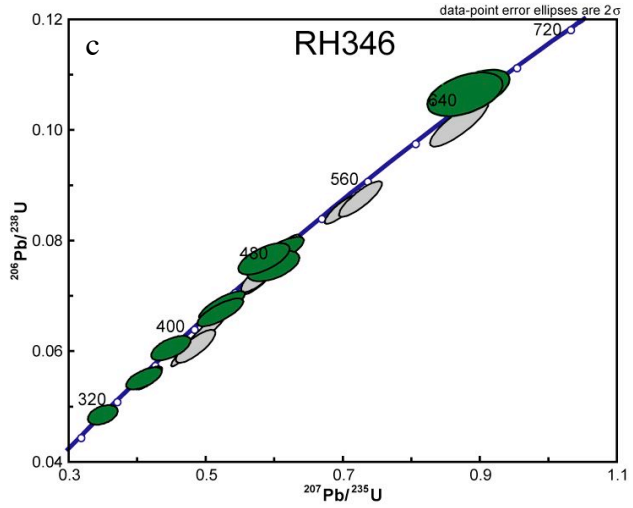

Fig. 5.2.6c: Concordia diagram, sample RH346

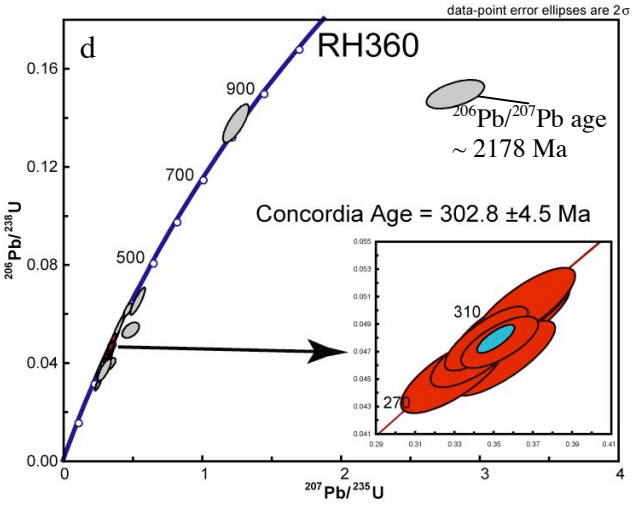

Fig. 5.2.6d: Concordia diagram, sample RH360

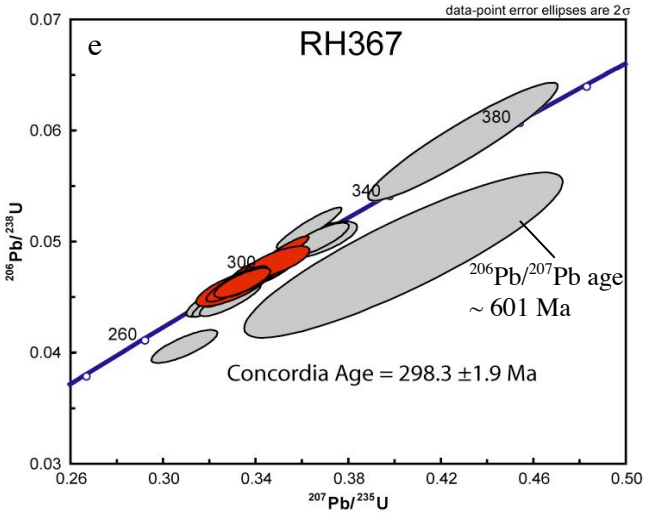

Fig. 5.2.6e: Concordia diagram, sample RH367

310 Ma to 654 Ma. The majority of the zircons shows evidence for older magmatic events because many of the inherited grains preserved their oscillatory zoning (Fig. 5.2.3e, f). The youngest age of 310 Ma was obtained from only one outermost rim and the low Th/U-ratio of 0.05 of this analysis points to a metamorphic (?) overprinting event at Carboniferous time (analysis RH346.7.1, Appendix E).

RH360–Ada

Twelve of twenty-nine laser spots on this sample resulted in a concordia age of 302.8± 4.5 Ma (2σ, MWSD = 10.8, 95 % confidence, Fig. 5.2.6d). Three spots measured on zircon cores are slightly older than the ones used for age calculation. They are interpreted to point at an inherited component. Another three spots on cores show clear evidence for an inherited component. Nine measurements on cores and rims show younger ages of 204 – 275 Ma. Most of them are discordant and their $^{206}Pb/^{207}Pb$ ages hint at Permo-Carboniferous to Neoproterzoic ages.

RH367–Ada

The concordia age of 298.3±1.9 Ma (2σ, MWSD = 0.42, 95 % confidence, Fig. 5.2.6e) was calculated from 14 spots. From the remaining eleven spots one analysis clearly records an inherited component of 369 Ma, whereas four analyses yield ages only slightly older than the ones used for the concordia age (analyses 64, 76, 78, 80, Appendix E). While spot 64 was located on a core, the analysis 76, 78 and 80 were measured on the inner rims of zircons showing nicely developed oscillatory zoning from core to rim. The CL-images do no show an obvious inherited core. Spot 78 shows a younger $^{206}Pb/^{207}Pb$ age (Appendix E), indicating some disturbance. Spots 76 and 80 are interpreted to be magmatic. Few analysis show younger ages caused by Pb-loss.

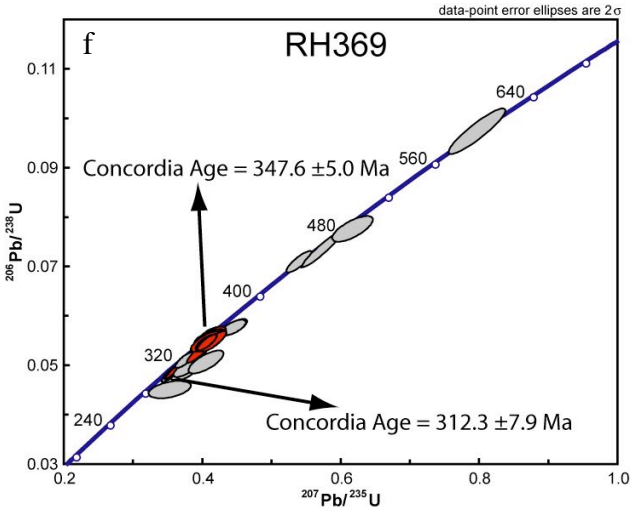

Fig. 5.2.6f: Concordia diagram, sample RH369

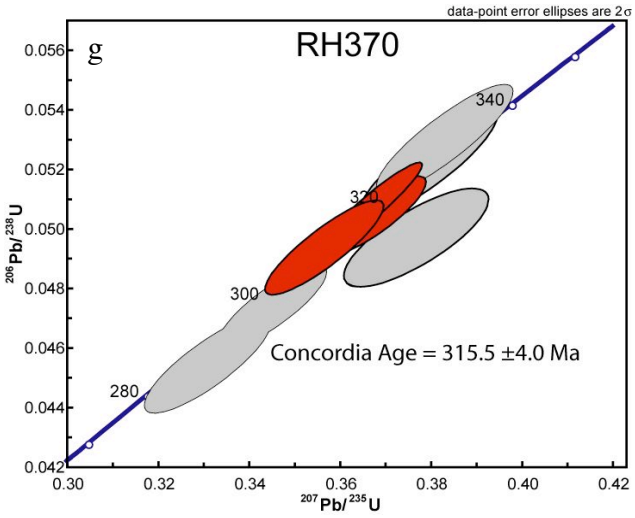

Fig. 5.2.6g: Concordia diagram, sample RH370

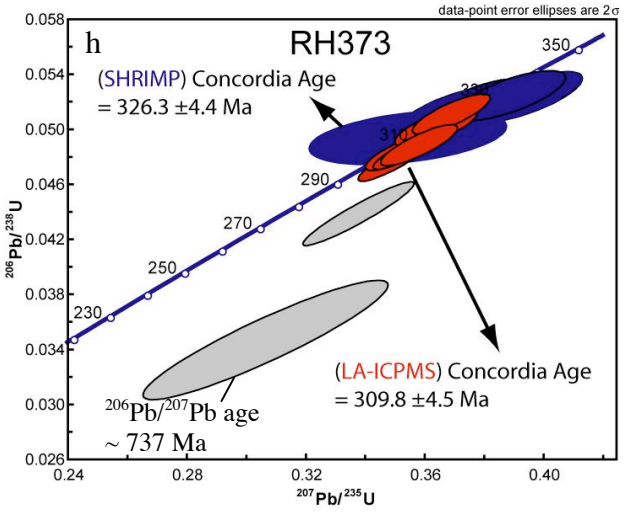

Fig. 5.2.6h: Concordia diagram, sample RH373

RH369–Dadia-Kotronia

For this sample the precise calculation of the intrusion age is problematic because measurements on rims range between 310 and 347 Ma. Nevertheless they indicate a Carboniferous age. CL-images show a complex structure for several grains. Inherited zircons in the cores are separated by a recrystallized, homogeneous inner rim from the outermost rims, which show mostly magmatic zoning. Two spots measured on outermost rims yield a concordia age of 312± 7.9 Ma. Ages obtained from inner rims or cores cluster around 347 Ma (Fig. 5.2.6f). This sample shows also concordant Ordovician and Neoproterozoic ages for zircon cores.

RH370– Dadia-Kotronia

Ten laser spots were measured on the zircons of this sample. The analyses cluster between 287 and 333 Ma and imply clearly a Carboniferous age. The concordia age of this sample is 315.5±4.0 Ma (n=3, 2σ, MWSD = 0.98, 95 % confidence, Fig. 5.2.6g). Two spots, although measured on rims, yield slightly older $^{206}Pb/^{238}U$ ages probably indicating an inherited component. Another two spots show slightly younger ages, one of them with a very low Th/U ratio of 0.06. They were sorted out from the age calculation.

RH373–Essimi-Leptokaria

This sample was dated with both methods, LA-SF-ICPMS and SHRIMP II. Ten spots were carried out with LA-SF-ICPMS and five by SHRIMP II. The zircons show a very homogeneous Carboniferous age distribution clustering between 300 and 329 Ma. Nevertheless the Concordia ages estimated by the two methods differ by ca. 13 Ma. The concordia age calculated from LA–SF–ICPMS measurements for this sample is 309.8±4.5 Ma (n=7, 2σ, MWSD = 7.5, 95 % confidence**,** Fig. 5.2.6h red ellipses). The spread of the ages into two groups can be

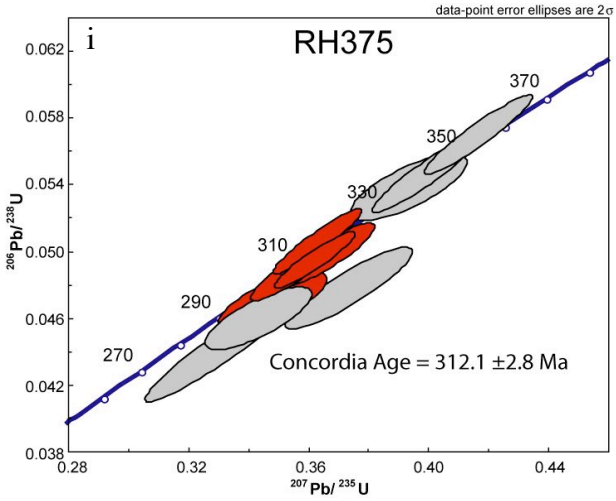

Fig. 5.2.6i: Concordia diagram, sample RH375

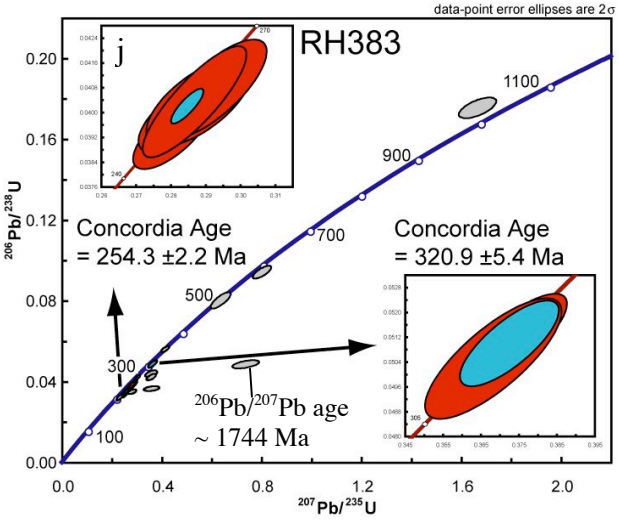

Fig. 5.2.6j: Concordia diagram, sample RH383

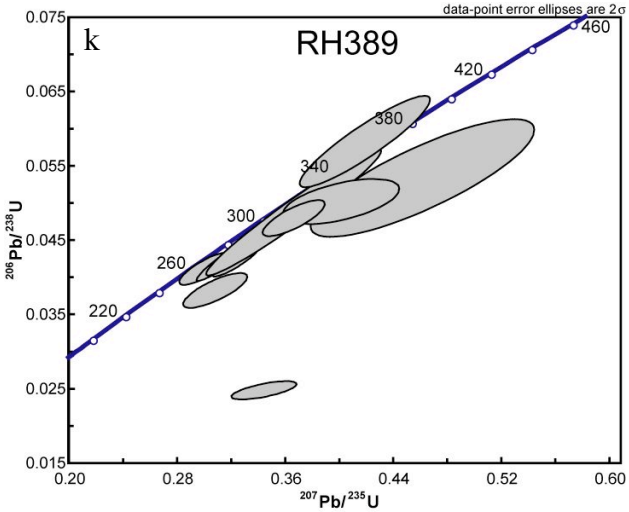

Fig. 5.2.6k: Concordia diagram, sample RH389

explained by different spot localities (inner rims are slightly older than outer rims) and probably by mixed analyses due to deeper penetration into the zircon by the laser-beam if compared to the SHRIMP-technique. The concordia age calculated from SHRIMP II spots is 326.3±4.4 (n=4, 2σ, MWSD = 0.68, 95 % confidence, blue ellipses). Two discordant spots were rejected from the age calculation.

RH375–Leptokaria-Dadia

This sample shows a homogeneous age distribution and is clearly of Carboniferous age. Nineteen of 28 spots on this sample yield a concordia age of 312.1±2.5 Ma (2σ, MWSD = 3.0, 95 % confidence, Fig. 5.2.6i). Seven spots yield older ages and were rejected from the age calculation. These measurements were carried out on inner rims or grains which show cracks or slightly metamict cores and hence could be disturbed. Three younger spots seem to have suffered Pb-loss; their ^{206}Pb/^{207}Pb ages indicate Devonian ages.

RH383–Dadia-Kotronia

Two groups of zircons were observed in this sample (see Fig. 5.2.3 s, t) and each group seems to represent a different age. Two concordant Carboniferous ages were analysed on zircons showing magmatic zoning like the one in Fig. 5.2.3 s whereas the majority of analyses yields Permo-Triassic ages obtained from grains showing sector zoning (Fig. 5.2.3 t). For the latter a Late Permian concordia age of 254±2.2 Ma was calculated from eight spots (Fig. 5.2.6j). This sample shows also evidence for concordant Cambrian and Neoproterozoic ages.

RH389–Mega Derio-Sidiro

The zircons of this sample are often crosscut by numerous cracks (Fig. 5.2.3v) and it was difficult to find a fracture-free part to fit a laser spot. It is likely that these cracks worked as channels for fluids leaching radiogenic Pb

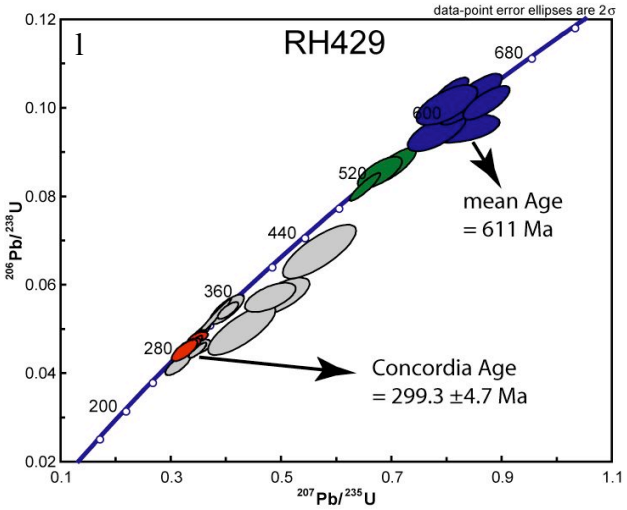

Fig. 5.2.6l: Concordia diagram, sample RH429

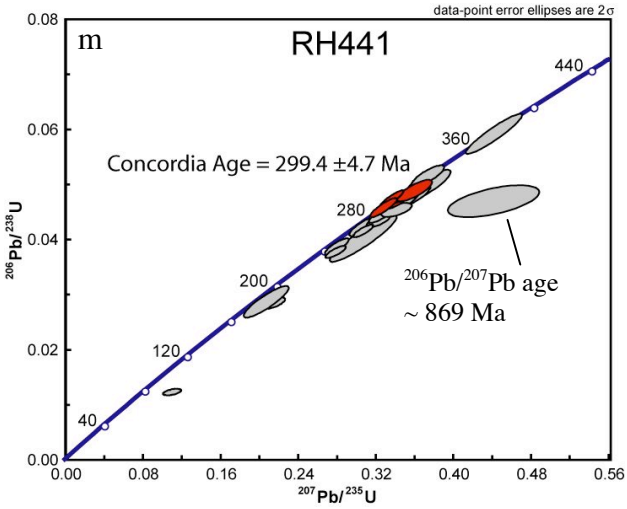

Fig. 5.2.6m: Concordia diagram, sample RH441

as well as trace elements from the grains. Nevertheless, ten spots were analysed on cores and rims of the zircon grains of this sample. Four of them are concordant but not sufficient for a calculation of a concordia age. The ages range between 262 and 365 Ma (Fig. 5.2.6k). Nevertheless the age cluster in the concordia diagram indicates that this sample could be of Carboniferous age (~ 290 Ma), although better statistics are needed here.

RH429–Smigada-Mirtiski

Thirty analyses have been carried out on the zircon grains of this rock. Seven of those gave a concordia age of 299.3±4.7 Ma (2σ, MWSD = 1.9, 95 % confidence, Fig 5.2.6l). It is worth mentioning that these latest Carboniferous ages were obtained only from parts of the zircons that show variable amounts of recrystallization (see Fig. 5.2.3w, x), probably due to metamorphic overgrowth. Twelve analysis on cores and those parts of the grains, where growth zoning is preserved, yield concordant Cambrian to Neoproterozoic ages (green and blue ellipses). Six analysis measured on cores with ages ranging between 317 and 362 Ma are discordant. Two younger spots indicate Pb-loss.

RH441–Nymphea

The ages obtained by the 29 measurements on this sample range between 83 and 371 Ma. Six analysis located on the parts of the grains, that show nicely developed growth zoning, yield a concordia age of 299.4±4.7 Ma (2σ, MWSD = 0.062, 95 % confidence, Fig 5.2.6 m). Three older ages were obtained from cores and contribute to an inherited component. Several younger ages indicate that the zircons suffered Pb-loss, which is also supported by the $^{206}Pb/^{207}Pb$ ages, which propose generally older ages for these analyses.

Protolith intrusion ages of orthogneisses from the Rhodope Terrane

This group is represented by three samples. RH423 was collected along the cross section from Smigada to Kimi and is a weak- to medium deformed biotite-gneiss without augen-texture. RH447 was sampled between Sidiro and Gianuli, several hundred metres south of the main road. RH455 was sampled at the western entrance of the village Sidiro. Both, RH447 and RH455, are leucocratic, folded, migmatized gneisses. The zircons of these three samples show a more complex internal structure than the ones from the Thracia Terrane gneisses (see Fig. 5.2.3 α-ϕ).

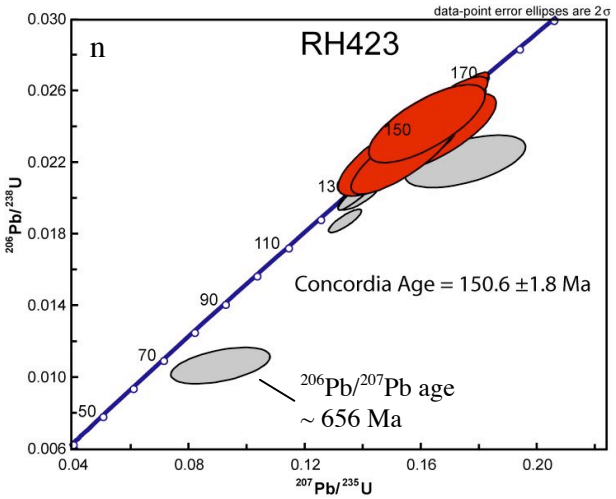

Fig. 5.2.6n: Concordia diagram, sample RH423

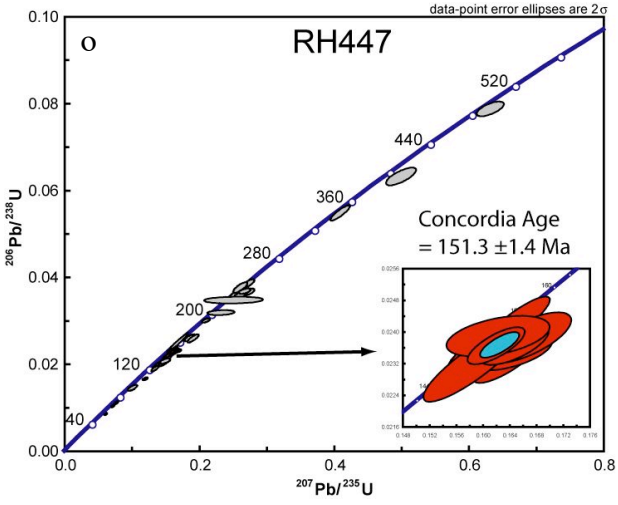

Fig. 5.2.6o: Concordia diagram, sample RH447

RH423–Smigada-Kimi

The zircons of this sample are characterized by highly metamict, crack-bearing cores surrounded by rims showing oscillatory zoning. Most zircons exhibit a bright, narrow outermost overgrowth–rim of homogeneous composition (Fig. 5.2.3α, β). Nine measurements on the cores gave ages between 104 and 156 Ma, with a main cluster around 120 – 130 Ma, which is in some cases younger than the corresponding rim and a result of the metamictization. Eighteen analysis result in a concordia age of 150.6±1.8 Ma (2σ, MWSD = 0.1, 95 % confidence, Fig 5.2.6n) and thus this sample is clearly of Jurassic age. In one single case, the core of a zircon is still preserved. The core was dated concordantly at 290± 8Ma, while the rim was dated at 137± 4Ma.

RH447–Sidiro-Gianulli

Forty spots were measured on both zircon domains of this sample. The zircons of RH447 are variously affected by convolute zoning. The analyses show a heterogeneous distribution with ages ranging from 61 to 488 Ma. Two main age clusters can be observed. The first cluster points clearly to a Jurassic age and eight analyses result in a concordia age of 151.4±1.5 Ma (2σ, MWSD = 11.8, 95 % confidence, Fig 5.2.6o). The second age cluster is formed by measurements exclusively on zircon cores and indicates a Triassic event. Three analyses on cores show evidence for inherited Carboniferous, Devonian and Ordovician ages.

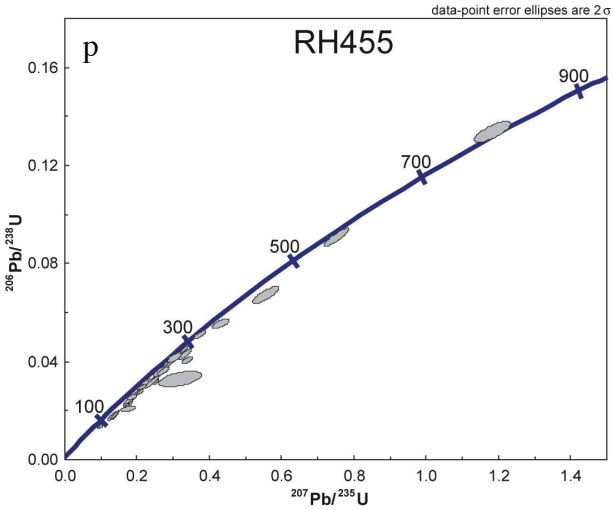

Fig. 5.2.6p: Concordia diagram, sample RH455

Interestingly, five spots measured on rims yield concordant ages ranging from 99 to 61 Ma with three ages around ca. 75 Ma. The Th/U ratios of the ages < 99 Ma are very low (0.01), thus indicating a metamorphic overprint in late Cretaceous times.

RH455–Sidiro

This sample shows a heterogeneous age distribution (Fig. 5.2.6p). Four different events can be distinguished from the CL-images. Detrital cores are surrounded or partly resorbed by a heterogeneous convolute zone, which is followed in some cases by a CL-medium-bright magmatic rim. The CL-medium-bright domain is followed by an U-rich, CL-dark rim showing magmatic zoning as well. Four measurements on cores yield concordant Neoproterozoic and Carboniferous ages. Several analyses on cores yield discordant ages and their $^{206}Pb/^{207}Pb$-ages indicate Carboniferous to Neoproterozoic sources as well. Three other age groups can be observed for the inner and outer rims: a Permian group, a Triassic group and a Jurassic group. Many of these ages are considered to be mixed analyses of the different rim domains, but two spots located on the CL-medium-bright domain point to a Late Permian-Early Triassic age. Jurassic ages measured on CL-dark outermost rims show very low Th/U ratios of 0.03 – 0.1 indicating a metamorphic event. The youngest age of a rim was measured concordantly at 93 Ma with a Th/U ratio of 0.23, thus indicating magmatic character.

5.3 Whole-rock major and trace element geochemistry of the orthogneisses

This chapter discusses the geochemical characteristics of orthogneisses from both, the Carboniferous Thracia and the Jurassic Rhodope Terrane of the Central- and Eastern Rhodope. Geochemical XRF- and LA-ICPMS-data of orthogneisses from the Greek Central Rhodope (Turpaud 2006 and this study), the Central Rhodopean Dome, Bulgaria (Peytcheva et al. 2004) and the Greek Pelagonian Zone (Anders 2005) are shown for comparison. Analytical procedures, XRF- and LA-ICPMS analyses are given in Appendix B and D. 21 representative samples of orthogneisses, including 16 augen-gneisses, one leucocratic, highly sheared muscovite-gneiss, two leucocratic, migmatized muscovite-gneisses and one weakly deformed biotite-gneiss from the Eastern Rhodope were analysed for their major- and trace element concentrations with XRF. Moreover, the rare earth elements of 29 orthogneisses, 11 from Central- and 18 from Eastern Rhodope, were obtained using LA-ICPMS. It is important to note that all rocks underwent at least amphibolite-facies metamorphism and experienced alteration processes that might have caused element mobilisation. Especially alkali and large-ion-lithophile (LIL) elements are known for mobility during metamorphism and alteration. The microscopic observation of the orthogneisses reveals that both, K-feldspar and plagioclase, are a little sericited. Biotite shows strong chloritization in many samples. Therefore, it is likely that the sodium and potassium values are not accurate. The degree of weathering can be expressed by the chemical index of alteration (CIA) after Nesbitt and Young (1982), which is the molecular ratio of $(Al_2O_3/(Al_2O_3+CaO_{inorg}+Na_2O+K_2O))*100$. The CIA value for the orthogneisses from the Eastern Rhodope Massif ranges between 50 and 55 with one exception of 62 (sample RH455). Orthogneisses from the Central Rhodope are in the range of 48 and 58 (calculated after XRF-values from Turpaud 2006). CaO was not corrected because apatite occurs only in few samples as an accessory mineral and the calcite-bearing samples are not included here. Because CIA values of 45 to 55 are characteristic for fresh granites (Nesbitt and Young 1982), most of the orthogneisses of the Central- and Eastern Rhodope can still be considered as fresh rocks. Figure 5.3.1 shows the ternary $(CaO + Na_2O)$ - Al_2O_3 - K_2O diagram after Nesbitt and Young (1984, 1989), which shows the trend of weathering (arrow). It is evident that the gneisses from the Rhodope Massif do not follow the weathering trend but instead form a group at quite constant Al_2O_3 values.

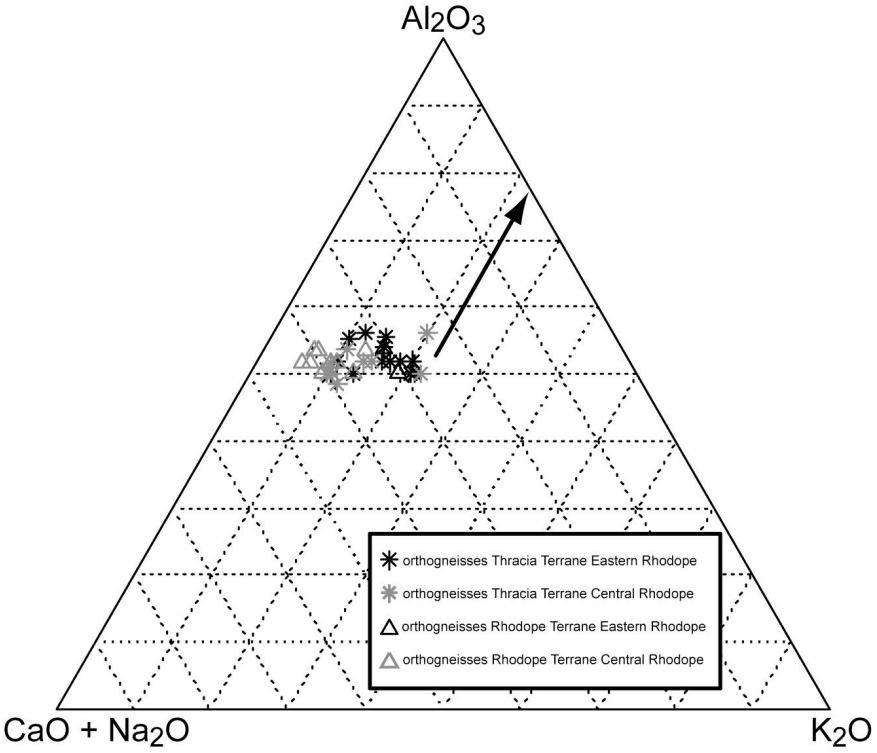

Fig. 5.3.1: Ternary ($CaO + Na_2O$) - Al_2O_3 - K_2O diagram after Nesbitt and Young (1984, 1989) showing orthogneisses from Central- and Eastern Rhodope Massif; the arrow shows the weathering trend; data for the Central Rhodope are from Turpaud (2006).

Major elements

In general, the orthogneisses of the Eastern Rhodope Massif (black symbols) are characterized by moderate to high silica contents (68–74 wt% SiO_2) with moderate alumina values (13–16 wt% Al_2O_3). The A/CNK ratio ranges between 1.05 and 1.62, respectively, thus indicating the peraluminous character of the orthogneisses (Fig. 5.3.2a). On the classification diagrams R1-R2 (De la Roche 1980) and the TAS diagram (Cox et al. 1979 after Le Bas et al. 1986) the majority of the samples from the Eastern Rhodope can be classified as granites and only few as granodiorites, whereas in the SiO_2 vs. Zr/TiO_2 diagram (Figs. 5.3.2b-d) they mostly plot in the field of granodiorites (Winchester and Floyd 1977). In contrast, Jurassic orthogneisses from the Rhodope Terrane of the Central Rhodope plot in the granodiorite, diorite and tonalite fields. Clear negative trends for most major elements like TiO_2, Al_2O_3, Fe_2O_3 and MgO can be seen in Harker diagrams (Figs. 5.3.3a-h). K_2O and Na_2O values scatter both between 2.5 and 5, but nevertheless a small positive trend can be anticipated for K_2O, while Na_2O shows no obvious correlation.

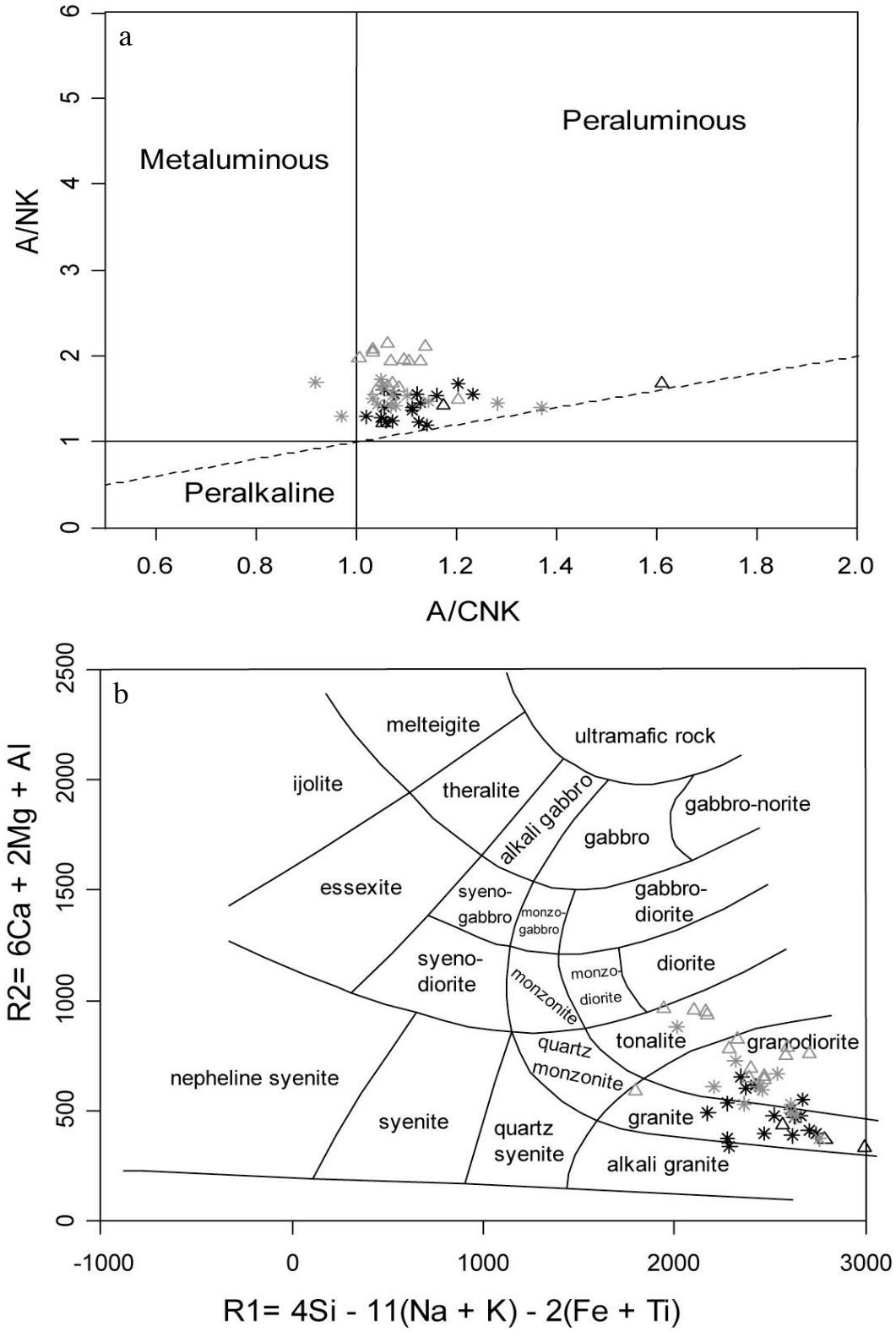

Figs. 5.3.2a-b: Geochemical discrimination diagrams for the orthogneisses of Central and Eastern Rhodope: a) Binary plot for the granitic protolith after Shand (1943); b) R1-R2 classification diagram after De la Roche et al. (1980), for legend see next page.

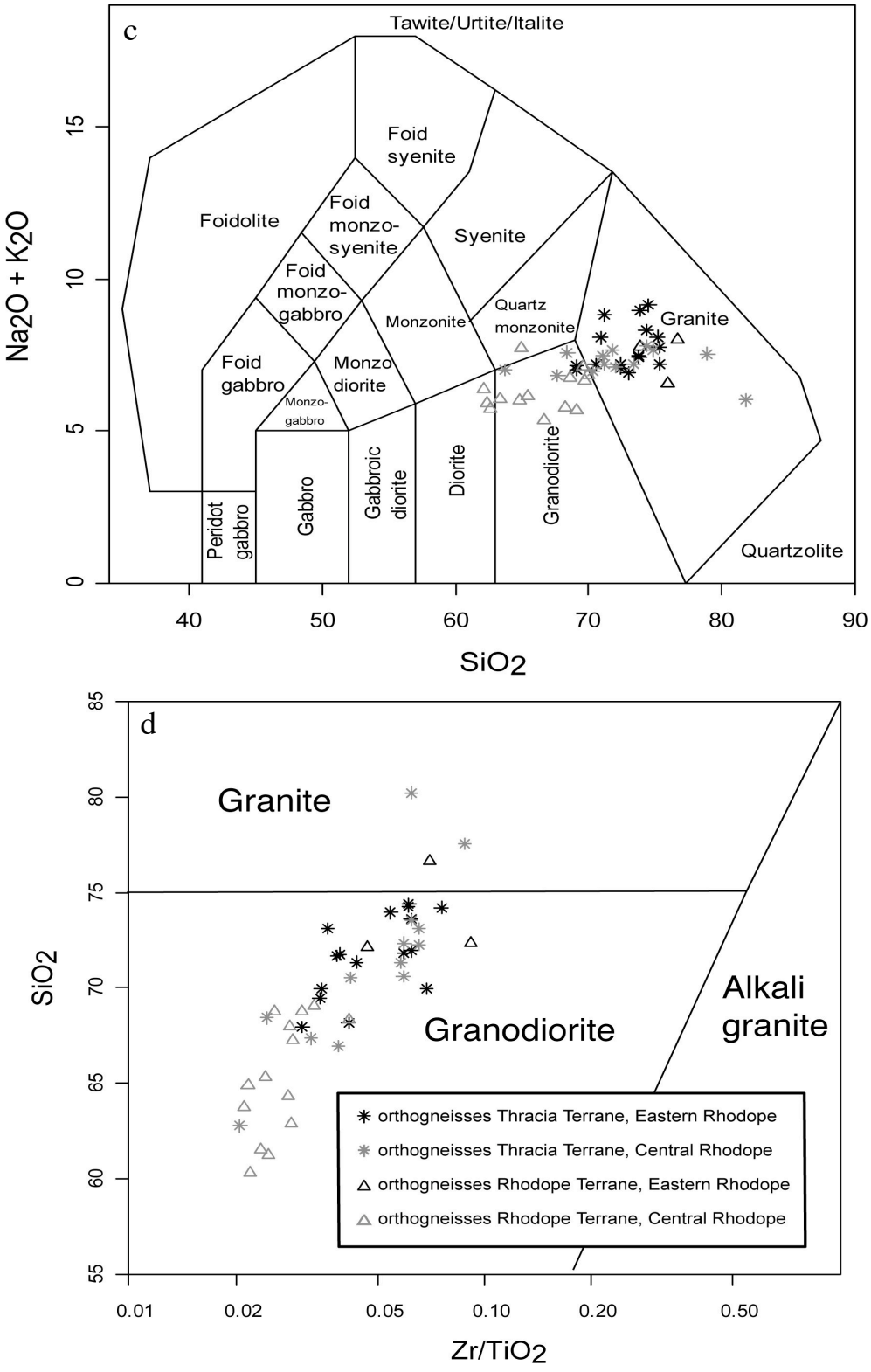

Figs. 5.3.2c-d: Geochemical discrimination diagrams for the orthogneisses of Central and Eastern Rhodope: c) TAS diagram of Cox et al. (1979) after Le Bas et al. (1986); d) SiO_2 vs. Zr/TiO_2 binary plot after Winchester and Floyd (1977); Data for the Central Rhodope are from Turpaud (2006).

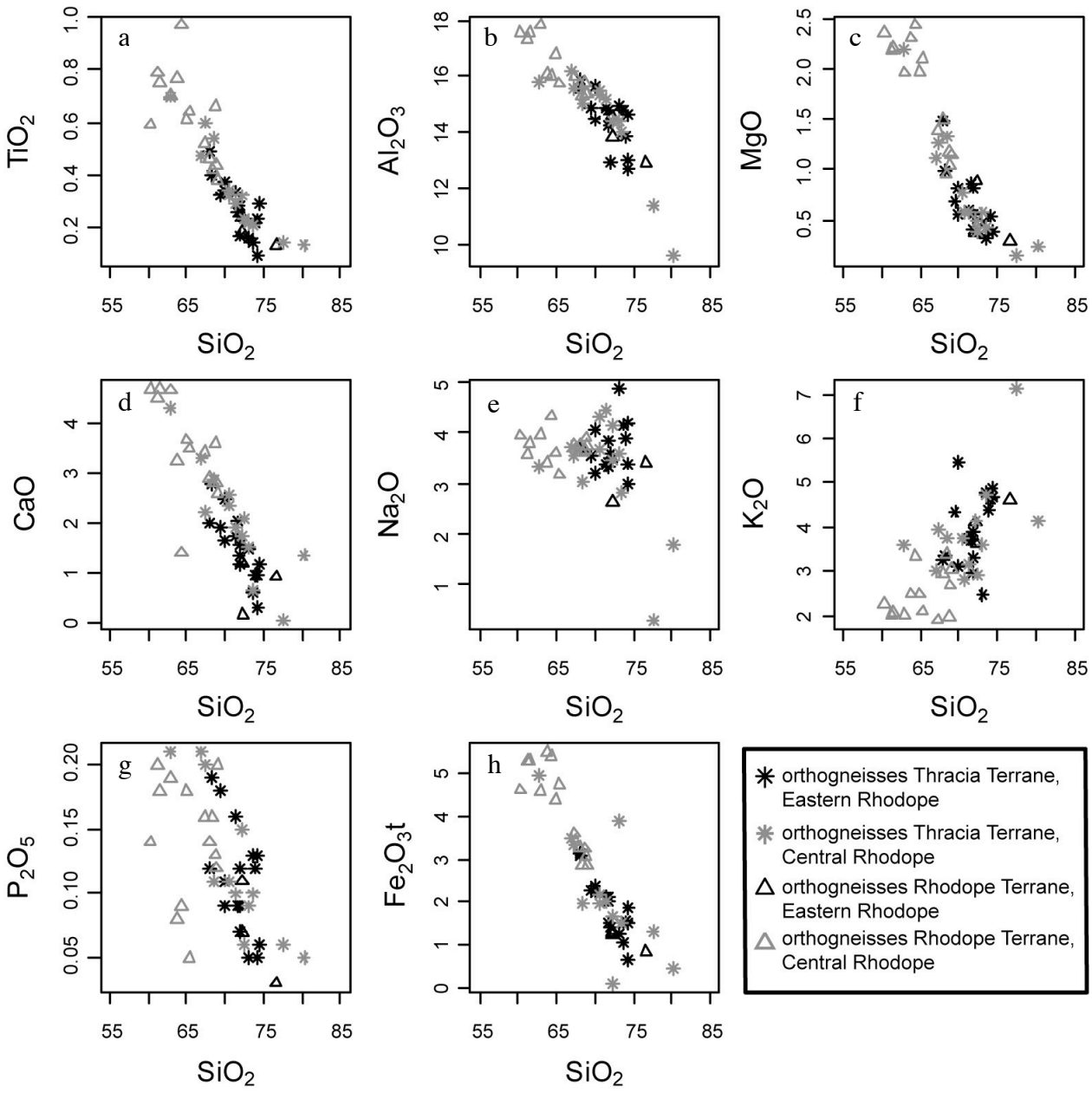

Figs. 5.3.3a-h: Harker major elements vs. SiO_2-diagrams for the orthogeneisses from the Thracia- and Rhodope Terrane of the Central- and Eastern Rhodope Massif; elements are given in wt%; note that the majority of the Jurassic orthogneisses from the Rhodope Terrane of the Central Rhodope form a distinct group in all diagrams.

It is evident that the Jurassic orthogneisses from the Rhodope Terrane of the Central Rhodope (grey triangles) are chemically different. They have lower SiO_2 and K_2O and higher Al_2O_3, MgO, TiO_2 and Fe_2O_3 contents, if compared to the orthogneisses from the Eastern Rhodope.

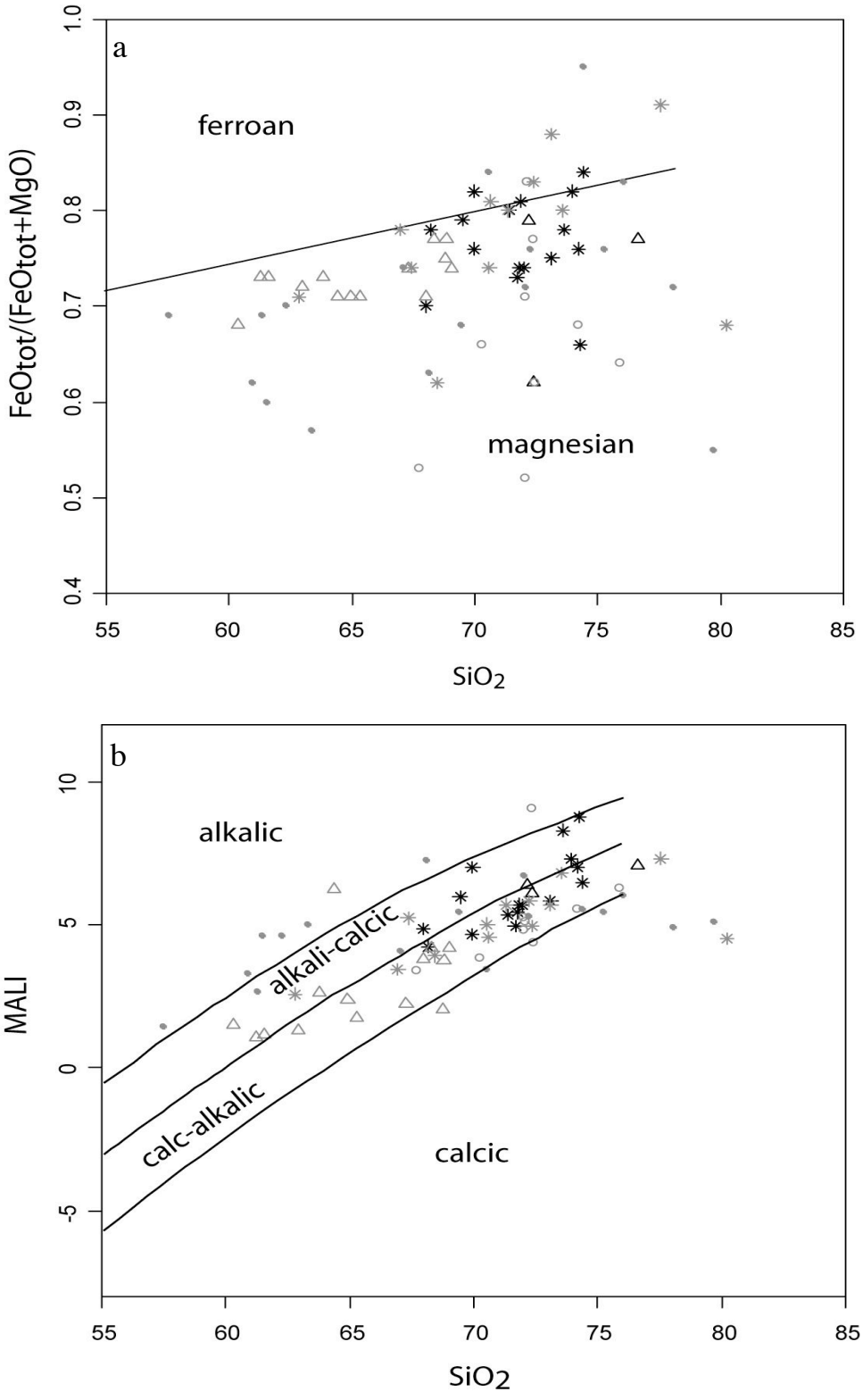

Figs. 5.3.4a-b: Geochemical classification diagrams based on major elements for the orthogneisses of Central and Eastern Rhodope after Frost et al. (2001): a) $FeO_{tot}/(FeO_{tot} + MgO)$ vs. SiO_2 plot; b) MALI vs. SiO_2 plot; for legend and explanation see next page.

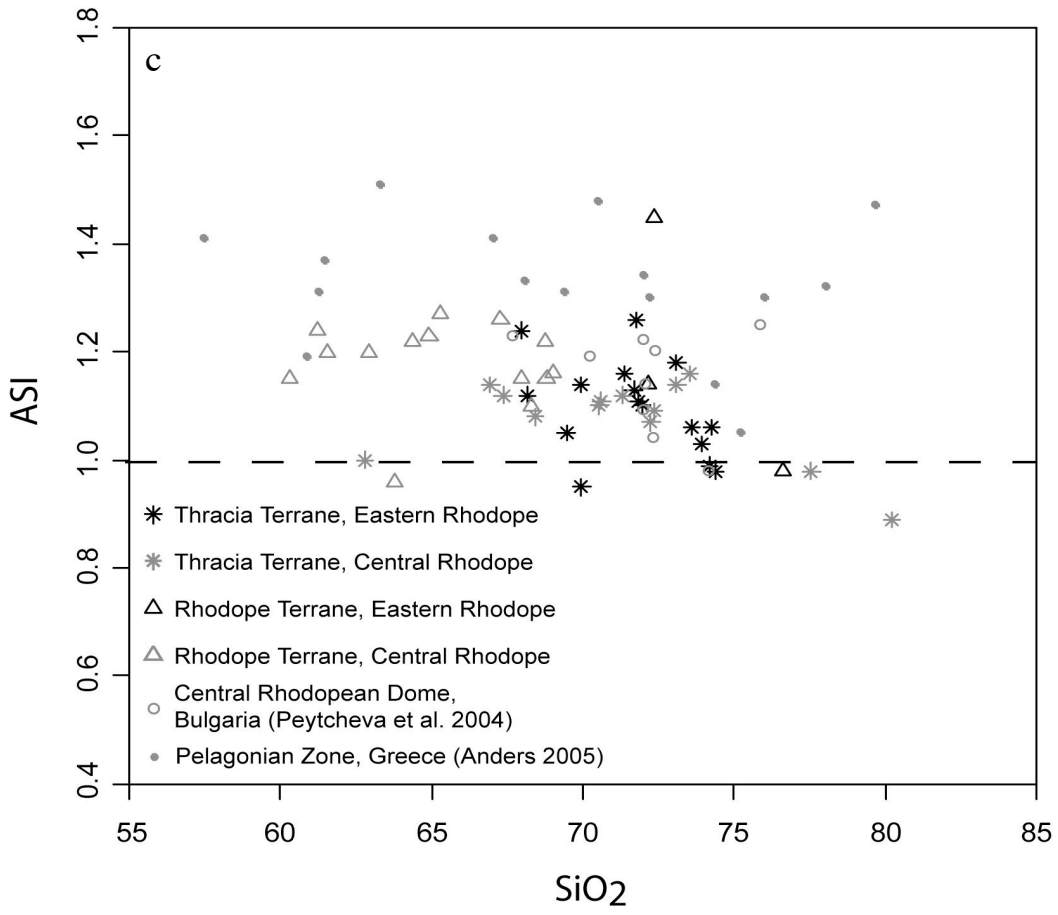

Fig. 5.3.4c: Geochemical ASI vs. SiO_2 classification diagram based on major elements for the orthogneisses of Central and Eastern Rhodope after Frost et al. (2001); the orthogneisses of Central and Eastern Rhodope can be classified as magnesian, calc-alkalic to alkali-calcic, peraluminous rocks; data for the Central Rhodope are from Turpaud (2006); data from the Central Rhodopean Dome of Bulgaria from Peytcheva et al. (2004); data from the Pelagonian Zone from Anders (2005).

A further non-genetic and non-tectonic classification scheme was suggested by Frost at al. (2001). The classification is based upon three parameters, the Fe*-number ($FeO_{tot}/(FeO_{tot}$ + MgO), the modified alkali-lime index (MALI = $Na_2O + K_2O$-CaO) and the aluminum saturation index (ASI, molecular ratio of Al/(Ca-1.67P + Na + K)). Figure 5.3.4a shows that most of the orthogneisses from the Rhodope Massif can be classified as magnesian and only few orthogneisses from the Thracia Terrane plot in the ferroan field.

In the MALI versus SiO_2-diagram the orthogneisses plot mostly in the calc-alkalic and but also in the alkali-calcic field (Fig. 5.3.4b). The ASI-value for most of the orthogneisses is > 1 indicating their peraluminous character (Fig. 5.3.4c), which is in agreement with the A/NK-A/CNK diagram

after Shand (1943) (see Fig. 5.3.2a). Data of orthogneisses from the Central Rhodopean Dome of Bulgaria (grey circles, Peytcheva et al. 2004) and selected data of orthogneisses from the Greek Pelagonian Zone (grey dots, Anders et al. 2005) are shown for comparison. It is evident that the Carboniferous orthogneisses from the Bulgarian Central Rhodopean Dome are chemically similar to orthogneisses from the Greek Thracia Terrane, especially on the MALI versus SiO_2-diagram and ASI versus SiO_2-diagram. Pelagonian Zone orthogneisses scatter more but can be classified as magnesian, calc-alkalic to alkali-calcic, peraluminous rocks as well. According to Frost et al. (2001), magnesian granitoids are probably related to island arc magmas, which follow relatively oxidizing differentiation trends. The alkali-lime index (MALI) can be influenced by both, the source or the differentiation of the magma. The crossing of the trend lines in Figure 5.3.4b by the orthogneisses from the Rhodope Massif can be explained by magma mixing or extreme differentiation of calcic tholeiitic magmas (Frost et al. 2001). According to the classification scheme of Frost et al. (2001), the orthogneisses of the Rhodope Massif can be chemically best related either to post-orogenic Caledonian-type granitoids or volcanic-arc Cordilleran-type granitoids. Caledonian-type granitoids with SiO_2 > 70 wt% are dominantly magnesian, calc-alkalic and peraluminous whereas Caledonian-type granitoids with SiO_2 < 70 wt% are magnesian as well and tend to be alkali-calcic (Frost et al. 2001). Cordilleran-type granitoids are predominantly magnesian and calcic to calc-alcalic. The magnesian, calc-alkalic to alkali-calcic, peraluminous orthogneisses of both terranes of the Central and Eastern Rhodope are therefore similar to granitoids, which have their origin in a subduction-related volcanic arc or collisional setting. A similar interpretation for orthogneisses of the Pelagonian Zone was made by Anders (2005), indicating a similarity of basement rocks of the Rhodope Massif and the Pelagonian Zone. The aluminum saturation index (ASI) provides information about the composition of the source and the melting process. Peraluminous magmas can be formed by either hydrous melting of mafic rocks (Ellis and Thompson 1986) or by melting of pelitic or semi-pelitic rocks (Holtz and Johannes 1991).

Trace and rare earth elements

On Harker diagrams, the majority of the trace elements of the Greek Rhodopean orthogneisses shows no clear correlation to SiO_2 (Figs. 5.3.5a-o), but weak negative trends can be anticipated for Sr, Sc, Nb, Zr, Zn, La and Ce. The values of Rb, Ba, Y and Ga show a relatively wide scatter

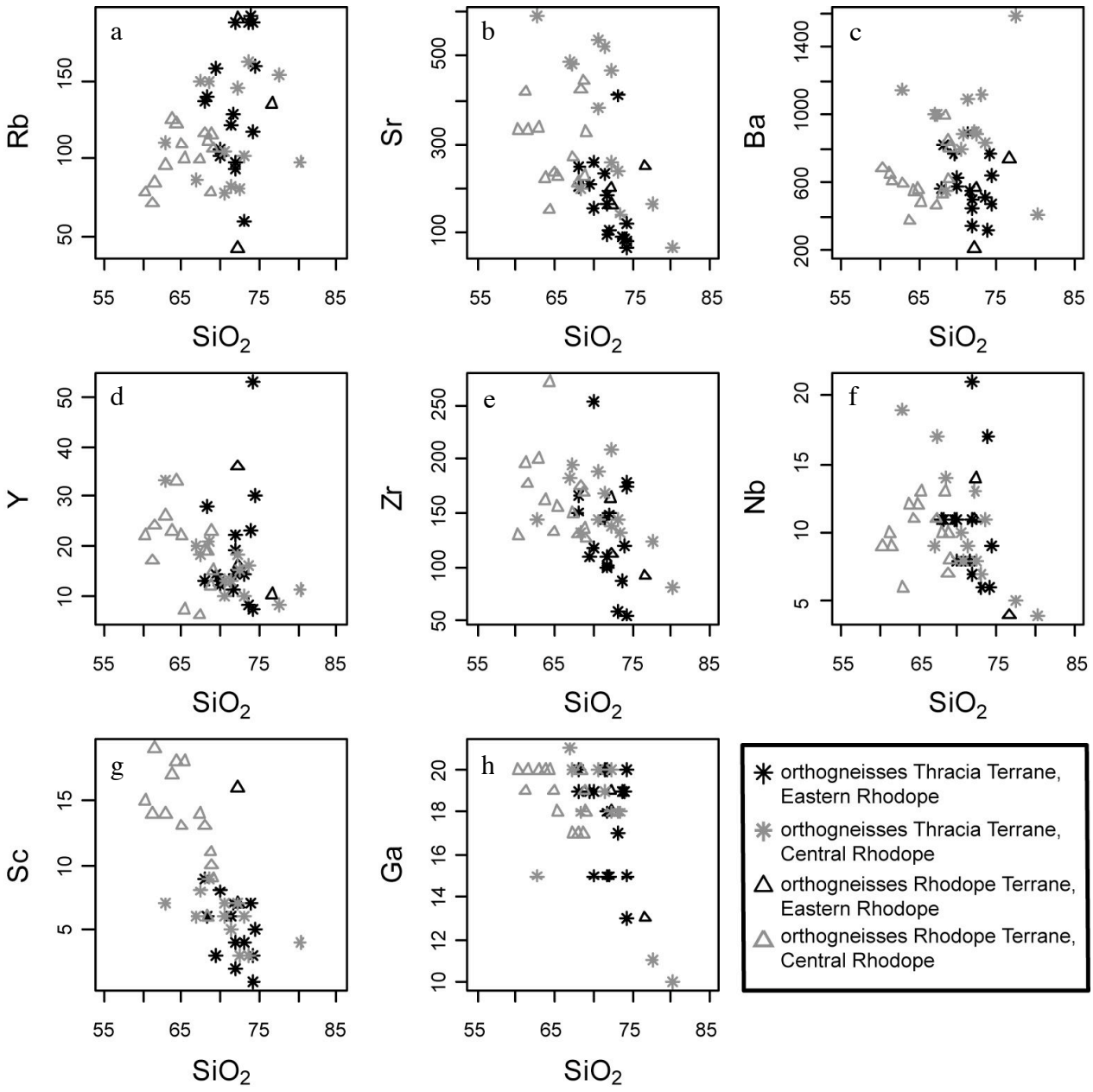

Fig. 5.3.5a-h: Harker trace-elements-vs-SiO_2-diagrams for the orthogeneisses from the Thracia- and Rhodope Terrane of Central- and Eastern Rhodope Massif; note that the majority of the Jurassic orthogneisses from the Rhodope Terrane of the Central Rhodope form a distinct group in all diagrams.

which might indicate metamorphic disturbance or alteration. Harker diagrams for Cr, Co, Ni and Cu show only small variation for these elements. The chemical difference of the Jurassic orthogneisses from the Rhodope Terrane of the Central Rhodope is evident, e.g. they are enriched in Sr, Sc, V, Cr, Co, Ni, Cu and Zn, if compared to the orthogneisses from the Eastern Rhodope.

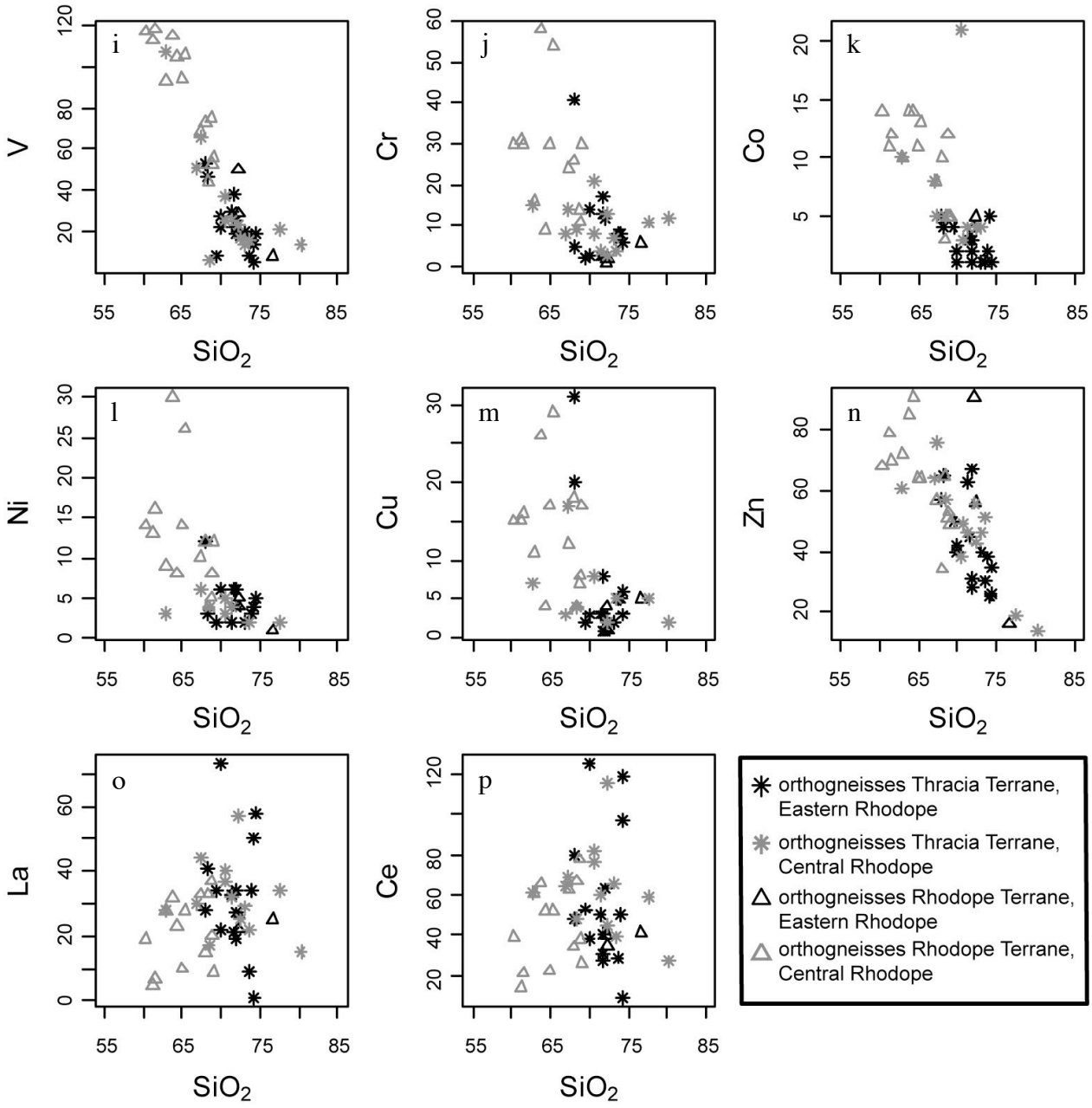

Fig. 5.3.5i-p: Harker trace-elements-vs-SiO_2-diagrams for the orthogeneisses from the Thracia- and Rhodope Terrane of Central- and Eastern Rhodope Massif; note that the majority of the Jurassic orthogneisses from the Rhodope Terrane of the Central Rhodope form a distinct group in all diagrams.

In the Y vs. Nb and Rb vs. (Y + Nb) discrimination diagram of Pearce et al. (1984), the protoliths of the orthogneisses of both terranes can be classified as granites of a volcanic arc or syn-collisional tectonic setting (Figs. 5.3.6a, b).

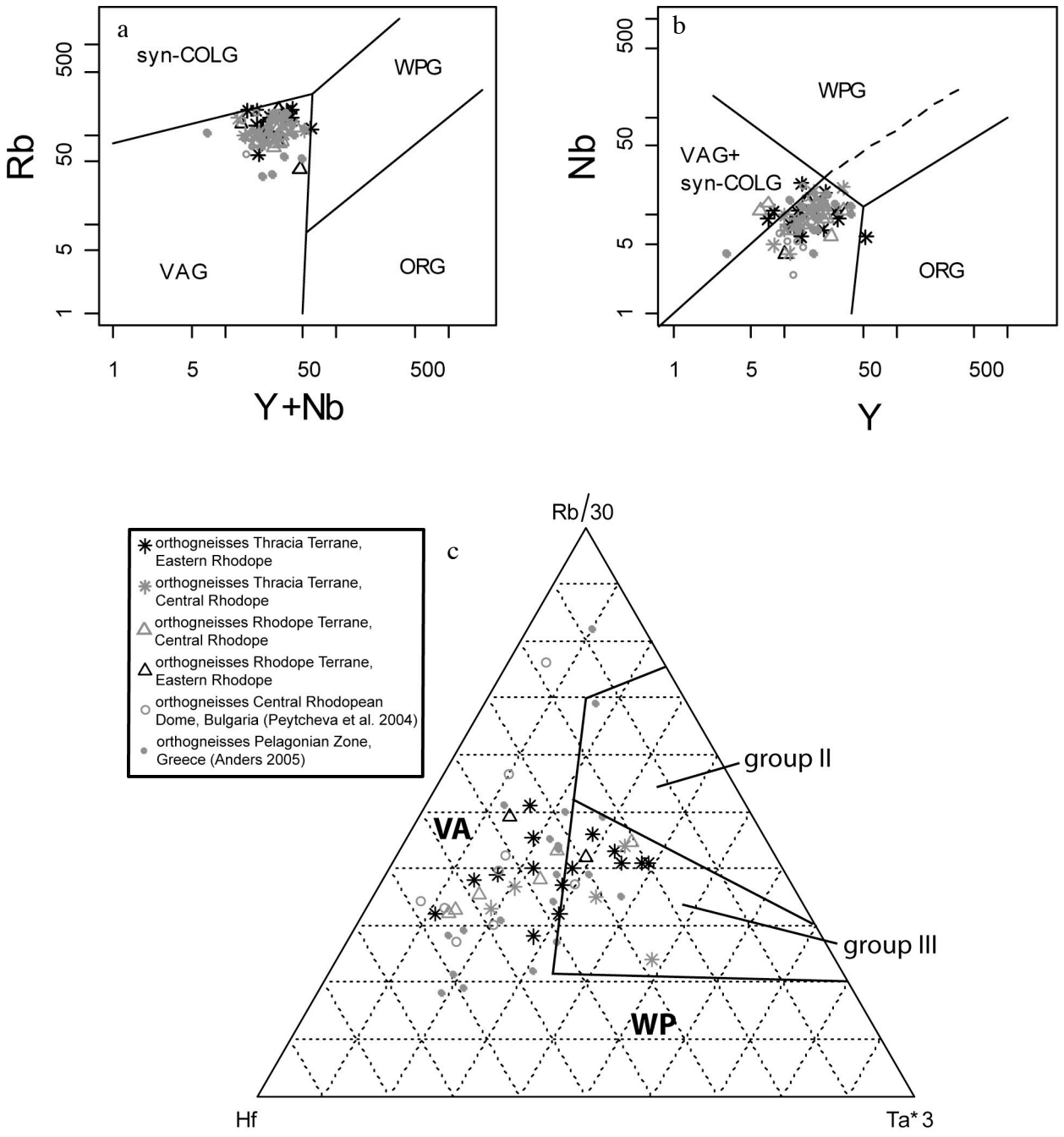

Figs. 5.3.6a-c: (a, b) Granite discrimination diagrams for the tectonic environment after Pearce et al. (1984); syn-COLG = syn-collisional granite, VAG = volcanic arc granite, WPG = within-plate granite, ORG = ocean-ridge granite; (c) after Harris et al. (1986); VA = volcanic-arc; WP = within-plate; group II = syn-collision; group III = post-collision; orthogneisses from the Eastern Rhodope Massif can be classified as VAG or syn-COLG after Pearce et al. (1984) or VA and group III after Harris et al. (1986) like the ones from Central Rhodope (Turpaud 2006), the Bulgarian Central Rhodopean Dome (Peytcheva et al. 2004) and the Pelagonian Zone (Anders 2005).

The feature that the orthogneisses plot in the upper right corner of the volcanic arc field (Fig. 5.3.6a) is indicative of a mixed or transitional character of the granitoids (Förster et al. 1997). Such granites are generated when an oceanic arc is located adjacent to a continental margin or in a mature volcanic arc environment (Förster et al. 1997).

Another discrimination diagram concerning the tectonic setting of granitoids, which is based on trace elements as well, is the Rb-Hf-Ta diagram of Harris et al. (1986) (Fig 5.3.6c). Figure 5.3.6c shows a discrimination of volcanic arc granites, (VA), within-plate granites (WP), syn-collisional granites (group II) and post-collisional granites (group III). The majority of the orthogneisses of both terranes of the Rhodope Massif plots in the volcanic arc field, but some samples plot in the field of post-collisional granitoids (group III). According to Harris et al. (1986), volcanic-arc and post-collisional granitoids show many geochemical similarities and therefore an overlap exists between volcanic arc intrusions from mature arcs and post-collisional intrusions.

29 samples of both terranes from the Greek Rhodope were investigated for their REE with LA-ICPMS (Figs. 5.3.7a, b). Sample preparation followed the method of Nehring et al. (2007). In general, the accuracy was better than 10% for the REE. In some cases less accurate concentrations for the low abundance REE Ho and especially Tm were obtained, which results in the positive anomalies in Figures 5.3.7a, b.

In the REE-diagrams normalized to chondrite (Boynton 1984) the majority of the orthogneisses from both terranes shows enrichment of the LREE, a negative Eu-anomaly between 0.29 and 0.92 and flat HREE patterns, which is characteristic for continental crust. A pronounced Eu-anomaly indicates that feldspar fractionation took place during magma genesis. Moreover, a pronounced Eu-anomaly is an indicator of reducing conditions, because Eu is preferably incorporated in feldspar in its divalent form Eu^{2+} (McKay 1989). The flat HREE patterns can be the result of the fractionation of accessory phases like epidote, monazite, allanite or apatite, which prefer LREE. The Carboniferous samples RH369, RH370, RH376 from the Eastern Rhodope and F34 from the Central Rhodope show no Eu-anomaly in Figure 5.3.7a and sample RH369 is furthermore the least enriched in REE. The lack of the Eu-anomaly indicates that either feldspar was not fractionated from the magma or that the magma generated under oxidizing conditions.

Multi-element diagrams normalized to Ocean Ridge Granite (ORG; Pearce et al. 1984) emphasize the strong enrichment in highly incompatible elements like K, Rb, Th and Ba as well as a depletion in elements like Zr and Y for most of the samples (Figs. 5.3.7c, d).

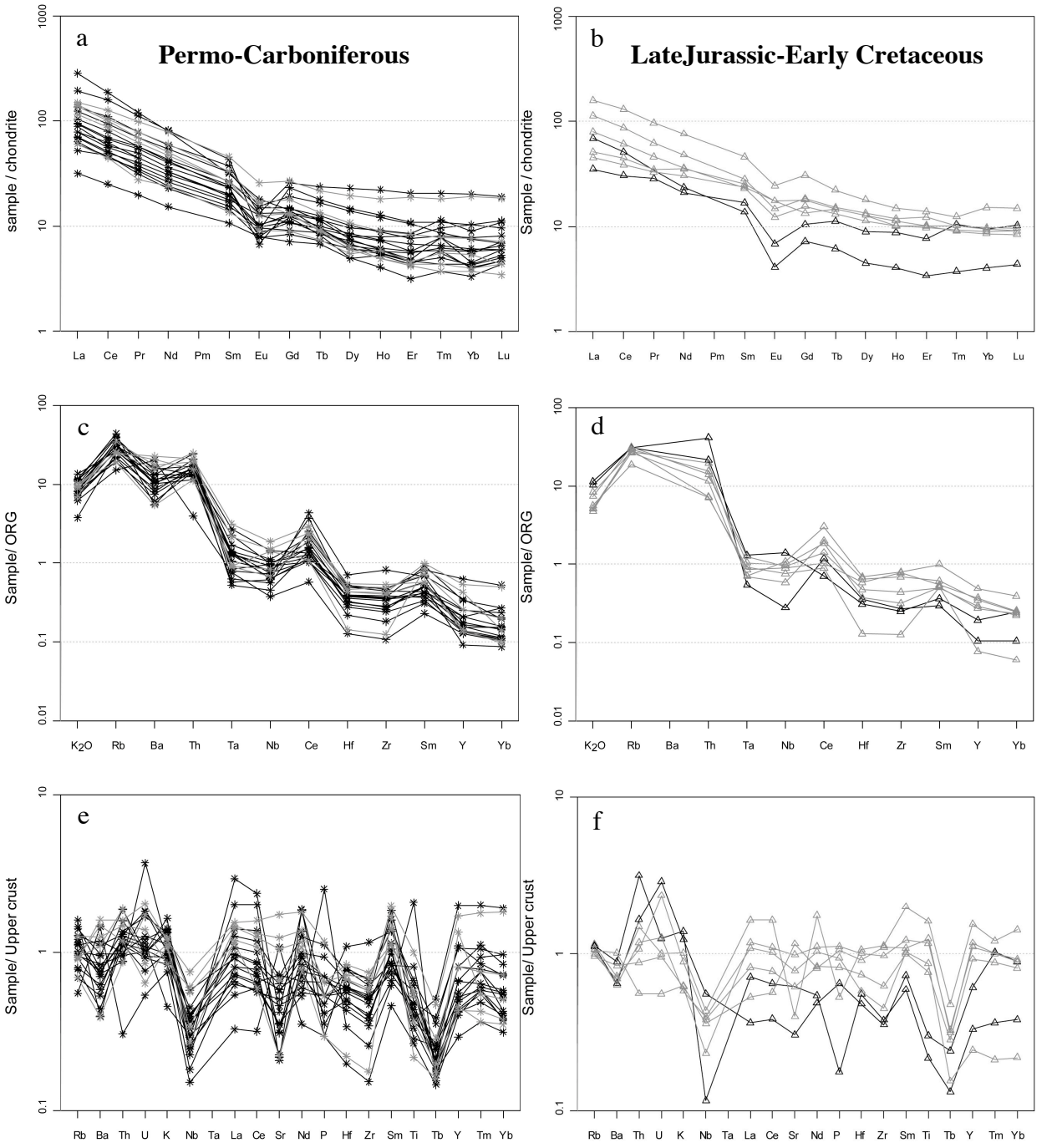

Figs. 5.3.7a-f: Normalized diagrams for the orthogneisses from the Thracia and Rhodope Terranes of Central and Eastern Rhodope Massif; (a, b) REE patterns for the orthogneisses from the Thracia (left) and Rhodope Terrane (right) normalized to chondrite after Boynton (1984); (c, d) Multi-element spider diagrams for the orthogneisses from the Thracia and Rhodope Terrane normalized to ORG after Pearce et al. (1984); (e, f) Multi-element spider diagrams for the orthogneisses from the Thracia and Rhodope Terrane normalized to upper crust after Taylor and McLennan. (1985), for the legend see Fig. 5.3.6c.

The patterns are very similar to those of volcanic-arc granites, but the orthogneisses from the Thracia Terrane may contain a collision zone granite component because of their Ba-anomaly, which is typical of COLG (Fig. 5.3.7c). In contrast, a Ba-anomaly is not present in the patterns of the Rhodope Terrane orthogneisses (Fig. 5.3.7.d).

The multi-element diagrams (Figs. 5.3.7e, f) normalized to upper crust after Taylor and McLennan (1985) show negative Nb- and Tb anomalies for the orthogneisses from both terranes of the Greek Rhodope. All orthogneisses are slightly more depleted than the avarage continental crust.

5.4 Sr- and Nd-Isotope geochemistry

The Sr- and Nd-isotopic composition was analysed of 26 orthogneiss samples from both terranes of the Central- and Eastern Greek Rhodope. The majority of the samples was dated using zircons (this study and Turpaud and Reischmann submitted). For the calculation of initial values, an intrusion age of 300 Ma was assumed for the remaining four samples RH358, RH413, RH418 and RH434 based on field relationships and petrography. Analytical procedures and data are given in Appendix B and F. Results of the Sr-isotopic analyses should be handled with care because the Rb-Sr system is more easily disturbed by metamorphism, alteration and weathering. Because isotopic ratios were measured over a time span of a year, all $^{143}Nd/^{144}/Nd$ ratios were corrected to a $^{143}Nd/^{144}/Nd$ ratio of 0.511850 for the La Jolla standard (Mahoney et al. 2003). Initial epsilon Nd values (εNd_i) for the Permo-Carboniferous orthogneisses of the Thracia Terrane from the Central- and Eastern Rhodope Massif range between –7.02 and –1.03. The spread of εNd_i for the samples from the Eastern and Central Rhodope Thracia Terrane is in the same range for both areas and no groups can be distinguished. The negative epsilon Nd values emphasize the crustal affinity of the orthogneisses from the Thracia Terrane and they imply that older continental crustal material was present in the source, from which the magmas originated. This is in agreement with the Nd depleted mantle model ages (T_{DM}) calculated for the Greek Thracia Terrane orthogneisses (after Liew and Hoffman 1988). The Nd depleted mantle model ages yield Mesoproterozoic ages between 1.1 and 1.6 Ga (Fig. 5.4.1a). By contrast, the inherited cores of the zircons from these samples infer Neo- and Palaeoproterozoic sources (see chapter 5.2). The range of T_{DM} for the Permo-Carboniferous orthogneisses from the Thracia Terrane is similar to T_{DM} (1.4 – 1.7 Ga) for middle European Variscan basement rocks (Liew and Hoffmann 1988). It is worth notifying that the initial epsilon Nd values and Nd depleted mantle model ages of orthogneisses from the Permo-Carboniferous Thracia Terrane are in good agreement with the corresponding values of Permo-Carboniferous orthogneisses from the Pelagonian Zone (Anders 2005).

The initial epsilon Nd values for the orthogneisses from the Late Jurassic-Early Cretaceous Rhodope Terrane of the Central and Eastern Rhodope Massif range between –1.8 and –6.5. Jurassic orthogneisses from the Eastern Rhodope Massif are scarce and represented by the samples RH423, RH447 and RH455. Their initial epsilon Nd values are -2.73, -3.87 and –5.4, respectively, whereas the ones of the Late Jurassic-Early Cretaceous orthogneisses from the

Central Rhodope range from –1.8 to –6.5. The corresponding Nd depleted mantle model ages for the Late Jurassic-Early Cretaceous Eastern Rhodopean orthogneisses are 1.1 Ga (RH423), 1.2 Ga (RH447) and 1.3 Ga (RH455) and for Central Rhodopean orthogneisses 1.1 to 1.4 Ga (Fig. 5.4.1b). The spread of the initial epsilon Nd values and Nd depleted mantle model ages for these gneisses is the same and does not allow the distinction of groups. Like the orthogneisses from the Thracia Terrane, the orthogneisses from the Late Jurassic-Early Cretaceous Rhodope Terrane have a crustal affinity and an older continental crust component in their magma source. In Fig. 5.4.1b the star symbols indicate εNd_i of the Permo-Carboniferous orthogneisses. It is evident that the source of the magma of the Late Jurassic-Early Cretaceous orthogneisses cannot be sought solely in the Permo-Carboniferous basement rocks of the Thracia Terrane. The magma of the Late Jurassic-Early Cretaceous orthogneisses is characterized by a stronger contribution of mantle material to the magma source.

The Sr-isotopic data give similar results. The $^{87}Sr/^{86}Sr_{initial}$ ratios of the Permo-Carboniferous samples from the Eastern Rhodope Massif range between 0.705 and 0.716. Only two samples of this group, RH345 and RH346 from the Ada section, show high initial $^{87}Sr/^{86}Sr$ ratios of > 0.710, which are characteristic for S-type granites. This is in agreement with the presence of many inherited Devonian-Ordovician cores in the zircons of these samples. The majority of the orthogneisses have ratios between 0.705 and 0.709. Lower values like 0.705 indicate more mantle derived sources, whereas higher values like 0.709 indicate that the source of these rocks contained significant amounts of crustal material. Similar $^{87}Sr/^{86}Sr_{initial}$ values were measured for the Permo-Carboniferous orthogneisses from the Central Rhodope Massif. The samples yield $^{87}Sr/^{86}Sr_{initial}$ ratios between 0.705 and 0.711. Two samples (RH11, F34) have values of > 0.710, which are characteristic for S-type granites. The $^{87}Sr/^{86}Sr_{initial}$ ratios of the Jurassic orthogneisses from the Eastern Rhodope are 0.707, 0.709 and 0.713, respectively. Late Jurassic-Early Cretaceous orthogneisses from the Central Rhodope are in the same range. One sample (F220) yields another high $^{87}Sr/^{86}Sr_{initial}$ ratio of 0.713, which indicates S-type character. The variations of the $^{87}Sr/^{86}Sr_{initial}$ ratios of orthogneisses from both Terranes of the Central and Eastern Rhodope Massif are continuous and no groups can be observed. In conclusion, it is not possible to distinguish the two terranes by their Sr isotopic composition.

The $^{87}Sr/^{86}Sr_{initial}$ of this study are in good agreement with Sr–data puplished by Peytcheva et al. (2004), who report $^{87}Sr/^{86}Sr_{initial}$ ratios in the range of 0.706 to 0.709 for the Carboniferous

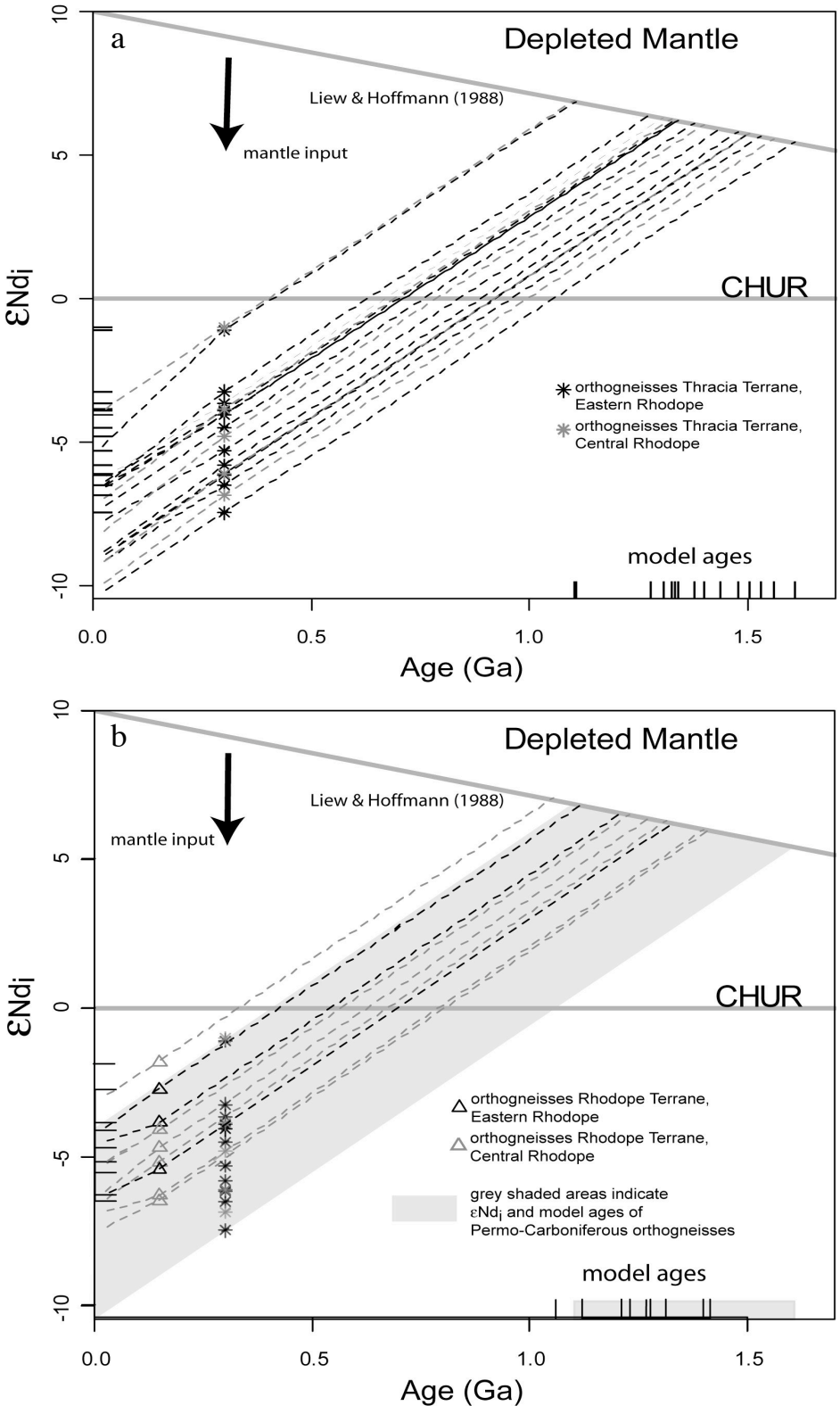

Figs. 5.4.1a, b: Two-stage Nd-isotope evolution diagrams (after Liew and Hoffmann 1988) showing εNd_i and T_{DM} for orthogneisses from the Central and Eastern Rhodope Massif. a) Permo-Carboniferous orthogneisses (Thracia Terrane), b) Late Jurassic-Early Cretaceous orthogneisses (Rhodope Terrane).

granitoids from the Central Rhodopean Dome in the Bulgarian part of the Rhodope Massif. These authors suggest a younger crustal source or a mixed crustal-mantle source for the magma of the granitoids, taking into account Hf-isotope zircon data as well (εHf = -2.58 to –5.52). Furthermore, the Sr- and Nd-isotopic data of the Permo-Carboniferous orthogneisses from the Rhodope Massif are in the range of basement rocks of the Pelgonian Zone (Anders 2005). Figure 5.4.2a shows the εNd_i and $^{87}Sr/^{86}Sr_{initial}$ data for granitoids of the Permo-Carboniferous Greek Rhodope Massif and the Pelagonian Zone (Anders 2005) as well as for the Cyclades (Engel 2006). Moreover, εNd_i and $^{87}Sr/^{86}Sr_{initial}$ data for sample Pl58 from the Precambrian Florina Terrane (Anders 2005), GLOSS (Plank and Langmuir 1998), metapelite sample F157 from the Eastern Rhodope Massif (this study) and the Depleted Mantle (isotopic ratio for N- MORB, Rb,

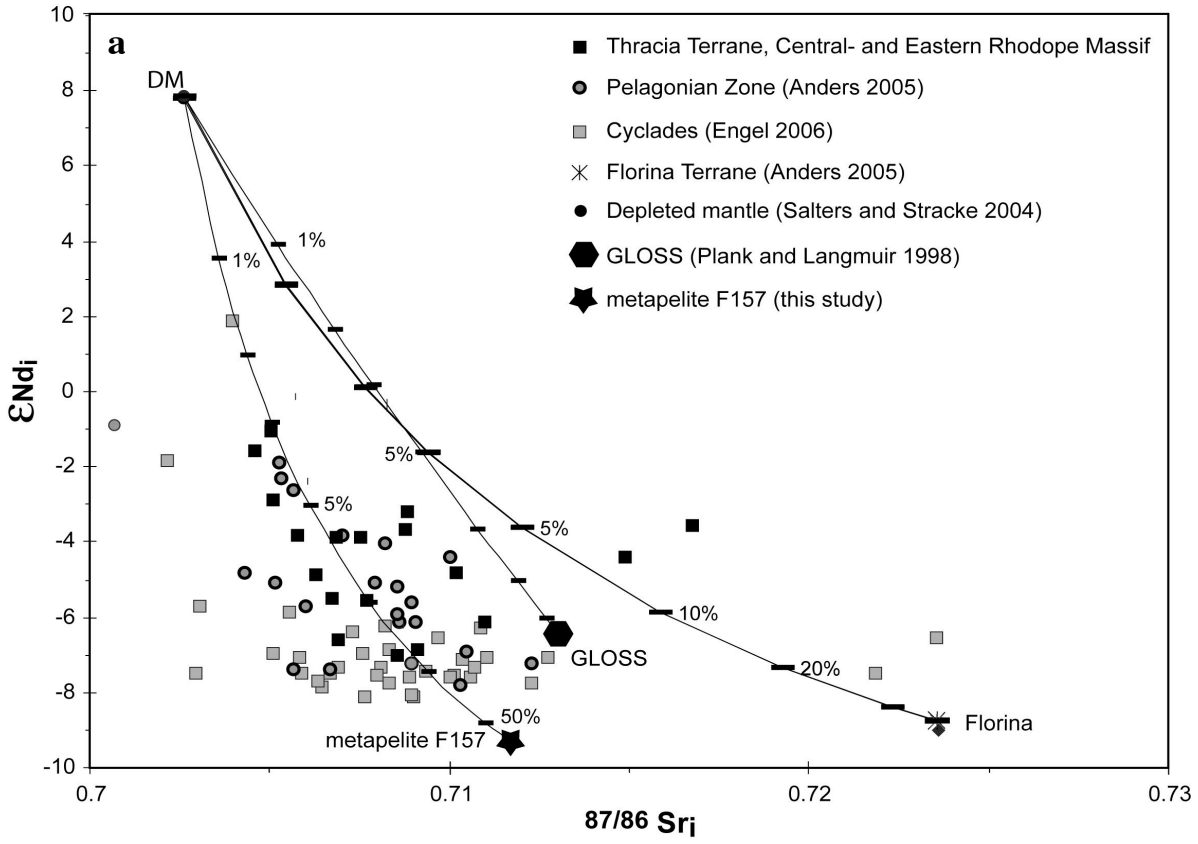

Fig. 5.4.2a: εNd_i vs. $^{87}Sr/^{86}Sr_{initial}$ data for Carboniferous basement rocks of the Greek Rhodope Massif, the Pelagonian Zone (Anders 2005), the Cyclades (Engel 2006) and the Florina Terrane (Anders 2005). Isotopic mixing lines were calculated for mixing of the Depleted Mantle (DM) (isotopic ratio for N-Morb, Rb, Sr, Sm, Nd values for the mantle from Salters and Stracke 2004) and sample Pl58 from the Florina Terrane, Depleted Mantle and GLOSS (Plank and Langmuir 1998) and Depleted Mantle and the metapelite F157 (this study).

Sr, Sm, Nd values for the mantle from Salters and Stracke 2004) were plotted in the diagram. All data were calculated to 300 Ma. Isotopic mixing lines were calculated for mixing between Depleted Mantle and sample Pl58 from the Florina Terrane, Depleted Mantle and GLOSS and Depleted Mantle and the metapelite F157.

It is evident that the mixing lines of the Depleted Mantle and sample Pl58 from the Florina Terrane and the mixing line of the Depleted Mantle and GLOSS are not suitable to explain the isotopic composition of the Thracian Terrane orthogneisses. Instead, to obtain the isotopic composition of the orthogneisses from the Thracia Terrane, a mixing of Depleted Mantle and an enriched component is required. Therefore, the isotopic compositions can be explained best by the input of 3 up to maximum 17 % of a crustal or sedimentary component (like the metapelitic sample F157) with a high Rb/Sr ratio. Based on Sr isotopes, orthogneisses from the Vertiskos Terrane could be a another possible source for such an enriched component. Their $^{87}Sr/^{86}Sr_{initial}$ ratios range between 0.705 and 0.723 (Himmerkus et al. 2006a). Moreover, Silurian ages like in the Vertiskos Terrane can be observed in some zircon cores from the orthogneisses of the Thracia Terrane.

To explain the isotopic composition of the Jurassic metagranitoids of the Rhodope Terrne, similar isotope mixing lines were calculated for the for mixing between Depleted Mantle and sample Pl58 from the Florina Terrane, Depleted Mantle and GLOSS and Depleted Mantle and the metapelite F157 (Fig. 5.4.2b). All data were calculated to 150 Ma. The isotopic compositions of the Jurassic metagranitoids can be explained by the input of 5 up to maximum 10 % of a sedimentary component with a high Rb/Sr ratio like the metapelitic sample F157.

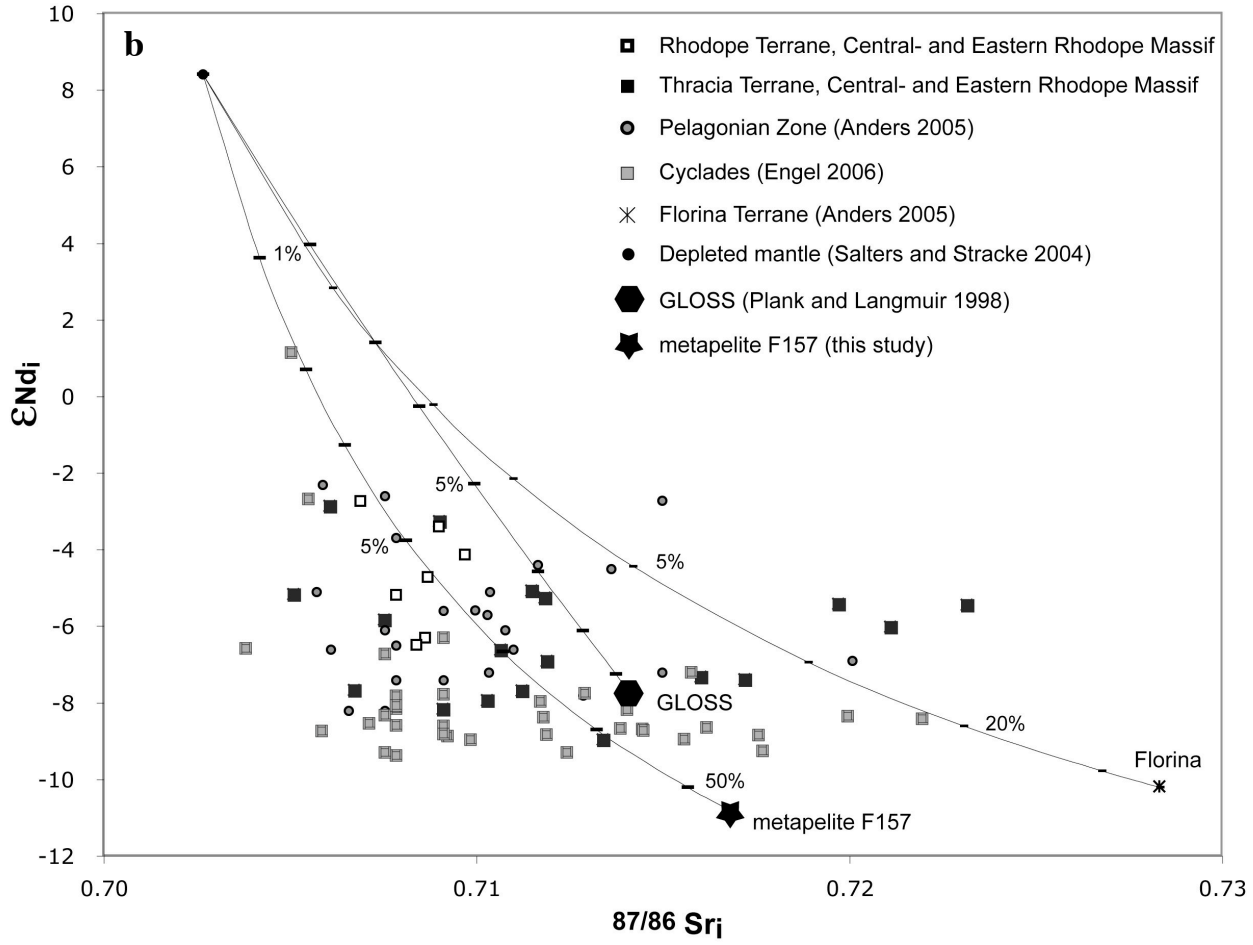

Fig. 5.4.2b: εNd_i vs. $^{87}Sr/^{86}Sr_{initial}$ data for Jurassic basement rocks of the Greek Rhodope Massif, the Pelagonian Zone (Anders 2005) and the Florina Terrane (Anders 2005). Isotopic mixing lines were calculated for mixing of the Depleted Mantle (DM) (isotopic ratio for N-Morb, Rb, Sr, Sm, Nd values for the mantle from Salters and Stracke 2004) and sample Pl58 from the Florina Terrane, Depleted Mantle and GLOSS (Plank and Langmuir 1998) and Depleted Mantle and the metapelite F157 (this study).

5.5 Summary orthogneisses

The orthogneisses investigated in this study were sampled from the Permo-Carboniferous Thracia Terrane and the Late Jurassic-Early Cretaceous Rhodope Terrane of the Eastern Rhodope Massif. The dominant orthogneisses of the Thracia Terrane of the Eastern Rhodope are medium-greyish augengneisses with a foliation defined by biotite and muscovite. The augen mostly form σ-clasts, and their size can reach from few millimetres up to one centimetre. Thin sections show that some of these samples contain abundant matrix-epidote. Within the augengneisses, in some places, leucocratic, strongly sheared muscovite-gneisses occur in the Thracia Terrane of the Eastern Rhodope Massif. Orthogneisses from the Rhodope Terrane of the Eastern Rhodope Massif are scarce. Sample RH423 from the Smigada-Kimi section, is a weak- to medium-deformed biotite-gneiss without augen-texture. Samples RH477 and RH455 from the Sidiro section are migmatitic, folded, leucocratic gneisses. In contrast to Thracian Terrane gneisses, plagioclase is the dominant feldspar in Rhodopean Terrane gneisses. Few samples from both terranes show garnet relicts completely surrounded by plagioclase and/or micas.

The size of most zircons, which were extracted from the orthogneisses, ranges between 60 and 150 μm, except few grains with up to ca. 250 μm. In most samples, the zircons are colourless or yellowish and often they contain inclusions. In the **CL-images**, four different types of growth-structures were observed. The first group is marked by zircons that show well-developed, continuous oscillatory zoning from core to rim, which indicates their magmatic character. In one case (RH383) these magmatic zircons are accompanied by zircons showing sector zoning. The second group consists of zircons which often possess inherited, xenocryst cores. Some of these cores preserved their primary growth zoning. The cores are surrounded by a domain of oscillatory zoning, indicative of magmatic origin. The outermost rim of these zircons is marked by thin, newly grown metamorphic domains of homogeneous composition. The third group is represented by the zircons of sample RH423. The cores of the zircons are highly metamict and are often crosscut by numerous cracks, while the rims show well-developed oscillatory zoning. The zircons of the fourth group belong to the sample RH447 and RH455 from the Rhodope Terrane of the Eastern Rhodope Massif and are characterized by complex structures and convolute zoning.

LA-SF-ICPMS and **SHRIMP II dating** revealed that ages from inherited cores range between ca. 3 Ga and 410 Ma. Especially, the samples RH345 and RH346 from the Ada section and sample RH429 from the Smigada-Mirtiski section show an accumulation of Devonian to

Ordovician or Cambrian to Neoproterozoic ages, respectively. Nevertheless, these samples were affected by a Carboniferous event, which is indicated by analyses of their outermost rims or recrystallized parts of the zircon grains. Zircons from eight orthogneisses show clear evidence for a Permo-Carboniferous intrusion age with concordia ages ranging between 326 (obtained by SHRIMP II) and 293 Ma (obtained by LA-SF-ICPMS). Some uncertainty remains for sample RH389, but the age cluster between 262 and 365 Ma indicates that this sample belongs to the Carboniferous age group. Sample RH383 shows two different types of zircons in the CL-images. Zircons showing oscillatory zoning are Carboniferous whereas zircons showing sector zoning are Permo-Triassic in age.

The **geochemical investigation** suggests that the orthogneisses from the Eastern Rhodope Massif were not too much affected by alteration or weathering because their CIA values (50 – 55) are in the range of fresh granites (Nesbitt and Young 1982). The orthogneisses of the Eastern Rhodope Massif are characterized by moderate to high silica contents (68–74 wt% SiO_2) with moderate alumina values (13–16 wt% Al_2O_3) and they can be classified as granites or granodiorites. The A/CNK ratio ranges between 1.05 and 1.62, thus indicating the peraluminous character of the orthogneisses. On Harker diagrams, most **major elements** like TiO_2, Al_2O_3, Fe_2O_3 and MgO show clear negative trends. It is evident, that Jurassic orthogneisses from the Rhodope Terrane of the Central Rhodope are chemically different. They have lower SiO_2 and K_2O and higher Al_2O_3, MgO, TiO_2 and Fe_2O_3 contents, if compared to the orthogneisses from the Eastern Rhodope. Jurassic orthogneisses from the Central Rhodope can be classified as granodiorites, diorites and tonalites. Following the classification scheme of Frost et al. (2001), most orthogneisses of both Terranes of the Central and Eastern Rhodope Massif can be classified as magnesian, calc-alkalic to alkali-calcic, peraluminous rocks. The orthogneisses of the Rhodope Massif can be best related either to post-orogenic Caledonian-type granitoids or volcanic-arc Cordilleran-type granitoids. Moreover they are chemically similar to orthogneiss samples from the Central Rhodopean Dome of Bulgaria (Peytcheva et al. 2004) and selected orthogneiss samples from the Greek Pelagonian Zone (Anders et al. 2005). On Harker diagrams, the majority of the **trace elements** of the Greek Rhodopean orthogneisses shows no clear correlation to SiO_2 but weak negative trends can be anticipated for Sr, Sc, Nb, Zr, Zn, La and Ce. Jurassic orthogneisses of the Central Rhodope are chemically different if compared to the orthogneisses from the Eastern Rhodope. They are enriched in Sr, Sc, V, Cr, Co, Ni, Cu and Zn. The protoliths of the orthogneisses of both terranes of the Rhodope Massif can be classified as granites of a mature volcanic arc or a syn-collisional

tectonic setting. In the **REE**-diagrams normalized to chondrite (after Boynton 1984) the majority of the orthogneisses from both Terranes shows enrichment of the LREE, a negative Eu-anomaly between 0.29 and 0.92 and flat HREE patterns, which are characteristic for continental crust. In **multi-element diagrams** normalized to Ocean Ridge Granite (ORG; Pearce et al. 1984), the orthogneisses from both Terranes of the Rhodope Massif show patterns which are very similar to those of volcanic-arc granites but the orthogneisses from the Thracia Terrane may contain a collision zone granite component because of their Ba-anomaly. The multi-element diagrams normalized to upper crust after Taylor and McLennan (1985) show that the orthogneisses from the Greek Rhodope are not related to a sedimentary source alone.

Initial epsilon Nd values (εNd_i) for the Permo-Carboniferous orthogneisses from the Central- and Eastern Rhodope Massif range between –7.02 and –1.03. The Nd depleted mantle model ages (after Liew and Hoffmann 1988) yield Mesoproterozoic ages between 1.1 and 1.6 Ga, which is in contrast to the inherited cores of the zircons from these samples, which infer Neo- and Paleoproterozoic sources. The initial epsilon Nd values for the orthogneisses from the Late Jurassic-Early Cretaceous Rhodope Terrane of the Central and Eastern Rhodope Massif range between –1.8 and –6.5. The corresponding Nd depleted mantle model ages for Late Jurassic-Early Cretaceous Rhodopean orthogneisses range from 1.1 to 1.4 Ga. The initial epsilon Nd values and Nd depleted mantle model ages emphasize the crustal character of the orthogneisses from the Thracia and Rhodope Terrane. They imply that older continental crustal material was present in the source, from which the magmas originated. The magma source of the the Late Jurassic-Early Cretaceous cannot be sought solely in the Permo-Carboniferous Thracia Terrane.

The **Sr-isotopic data** give similar results. The $^{87}Sr/^{86}Sr_{initial}$ ratios of the Permo-Carboniferous samples from the Eastern Rhodope Massif range between 0.705 and 0.716. Two samples (RH345, RH346) from the Ada section, show high initial $^{87}Sr/^{86}Sr_{initial}$ ratios of > 0.710, which are characteristic for S-type granites. This is in agreement with the presence of many inherited Devonian-Ordovician cores in the zircons of these samples. Lower values between 0.705 and 0.709 indicate a mixed crustal-mantle source. Similar results were obatined for the Permo-Carboniferous orthogneisses from the Central Rhodope Massif ($^{87}Sr/^{86}Sr_{initial}$ = 0.705 and 0.711). The $^{87}Sr/^{86}Sr_{initial}$ ratios of the Jurassic orthogneisses from the Easten Rhodope are 0.707 between 0.713. Late Jurassic-Early Cretaceous orthogneisses from the Central Rhodope are in the same range. Because the variations of the initial epsilon Nd values and $^{87}Sr/^{86}Sr_{initial}$ ratios of

orthogneisses from both Terranes of the Central and Eastern Rhodope Massif are in the same range, it is not possible to distinguish the two Terranes by their isotopic composition.
Moreover, Permo-Carboniferous orthogneisses from the Thracia Terrane are isotopically very similar to Permo-Carboniferous basement rocks of the Pelagonian Zone.

6. Discussion

6.1 Correlation of the cross sections of the Eastern and Central Rhodope Massif

A two-terrane model was proposed for the Central Rhodope Massif by Reischmann and Kostopoulos (2007) and Turpaud and Reischmann (submitted), where the lower Permo-Carboniferous Thracia Terrane was overthrusted by the Late Jurassic/Early Cretaceous Rhodope Terrane. These terranes are separated by the Nestos suture, an intermediate mélange zone comprising a variety of lithologies like metapelitic gneisses, amphibolites with oceanic affinities (mostly E-morb affinity, D. Kostopoulos, pers. communication), marbles, orthogneisses and migmatites. The metapelitic and mafic rocks of this mélange zone record a former HP and locally UHP metamorphism overprinted by a retrograde amphibolite- (locally granulite-) facies metamorphism (e.g. Liati 1986, Liati and Seidel 1996, Mposkos and Kostopoulos 2001). The formation of the HP und UHP rocks is explained by a single subduction event in Jurassic times as a result of the closure of a branch of the Meliata-Maliac ocean system (Reischmann and Kostopoulos 2007, Turpaud and Reischmann submitted).

Field evidence clearly reveals that the above-mentioned characteristic rock association of a mélange zone is present in the Eastern Rhodope Massif as well. Along the Ada, Sidiro and Kimi sections, where the contact of the two terranes is exposed, garnet±kyanite gneisses/micaschists occur together with amphibolites, marbles and orthogneisses squeezed between blocks of the two terranes. Nevertheless, a difference between Central and Eastern Rhodope can be observed. Turpaud (2006) describes the orthogneisses of the Late Jurassic/Early Cretaceous Rhodope Terrane of the Central Rhodope as exclusively non-porphyritic, dark biotite-orthogneisses, which can be migmatitic and locally contain amphibole. Petrography and geochemistry indicate an I-type affinity for these biotite-gneisses (Turpaud 2006 and chapter 5.3, this study). Despite the fact that orthogneisses from the Rhodope Terrane of the Eastern Rhodope Massif are not so frequent, it is evident that the orthogneisses of the easternmost part of the Rhodope Terrane represent a different rock type. They are migmatitic, leucocratic muscovite-gneisses similar to those occurring between Sidiro and Gianulli (RH447, RH455). Many inherited cores in the zircons and the isotopic composition of the samples indicate an S-type character for the Eastern Rhodopean Terrane samples. The variably deformed, non-pophyritic biotite±muscovite-gneisses from the Smigada-Kimi section (where RH423 was sampled) correspond more to the Central Rhodopean

Terrane gneisses described by Turpaud (2006). Despite the difference in rock type, LA-SF-ICPMS and SHRIMP II dating of zircons from the orthogneisses of the two terranes of the Eastern Rhodope Massif allow to distinguish two age groups as well: Orthogneisses from the structurally lower Thracia Terrane are Permo-Carboniferous and orthogneisses from the structurally upper Rhodope Terrane are Late Jurassic in age. The geochronological data are consistent with the structural observations made in the field and in agreement with the two-terrane model of Turpaud and Reischmann (submitted) for the Central Rhodope.

The Ada section starts north of Paterma village with amphibolites crosscut by numerous leucosomes, which are already part of the mélange zone. Further north, the amphibolites are followed by a sequence of alternating orthogneisses, amphibolites, metapelites and marbles, finally overlaying orthogneisses of the Thracia Terrane. The orthogneiss samples from the mélange zone and the underlying unit are all Permo-Carboniferous in age (RH344, RH345, RH346, RH360, RH367 and also RH441 west of Ada). Turpaud (2006) reported the occurrence of Permo-Carboniferous augengneiss slivers within a similar mélange zone north of Xanthi as well. This fact is explained by overthrusting parts of the structurally lower Thracia Terrane above the HP/UHP rocks of the mélange zone and incorporation of these augengneisses into the mélange zone. A similar explanation is conceivable for the Permo-Carboniferous augengneisses occurring within the mélange zone of the Ada section of the Eastern Rhodope Massif, thus there is the possibility that slices of the orthogneisses of the Thracia Terrane experienced UHP conditions as well. Orthogneisses of the Late Jurassic/Early Cretaceous Rhodope Terrane were not found in the Ada section so far.

In the adjacent Kimi section east of the Ada section, between the villages of Organi and Smigada, a strongly sheared augengneiss (RH429) sampled 2.2 km north-east of Organi in the structurally lower unit yielded a concordia age of 299.3 ± 4.7 Ma, thus representing the Permo-Carboniferous Thracia Terrane. Further north, in the structurally upper part between Smigada and Kimi, a medium-deformed biotite-gneiss gave a concordia age of 150.6 ± 1.8 Ma, characteristic of the Rhodope Terrane. In the contact zone between these two units, which crops out between Drania and Smigada, the typical mélange zone rock assemblage of garnet±kyanite gneisses/micaschists (RH412, RH414) intercalated within highly sheared orthogneisses and associated with migmatitic amphibolites can be found. Marbles are abundant at the contact of the two units along the Smigada–Kimi section. Moreover, microdiamonds, indicative for UHP metamorphism, were reported in garnet from garnet-kyanite-biotite schists/gneisses of the Kimi area (Mposkos and

Kostopoulos 2001, Perraki et al. 2006). Quartz, rutile and apatite exsolutions in garnet from the same rocks are interpreted to have exsolved from a former UHP high-Si and high-Ti garnet precursor (Mposkos and Kostopoulos 2001). The different ages of the orthogneisses as well as the characteristic sequence of rock types between them, which record HP and even UHP metamorphism, strongly suggest the same configuration of the two terranes as in the Central Rhodope Massif (Reischmann and Kostopoulos 2007, Turpaud and Reischmann submitted). This picture is further supported by the easternmost section investigated in this study, the Mega Derio–Sidiro section. Numerous augengneisses of the Thracia Terrane south-west of Mega Derio and one orthogneiss from between Mega Derio and Sidiro were dated by LA-SF-ICPMS and SHRIMP II (Fig. 6.1.1). All orthogneisses are Permo-Carboniferous in age (RH369, RH370, RH373, RH375, RH383, and RH389). In contrast, two orthogneiss samples from the Rhodope Terrane east of Sidiro yielded Jurassic ages (RH447, RH455).

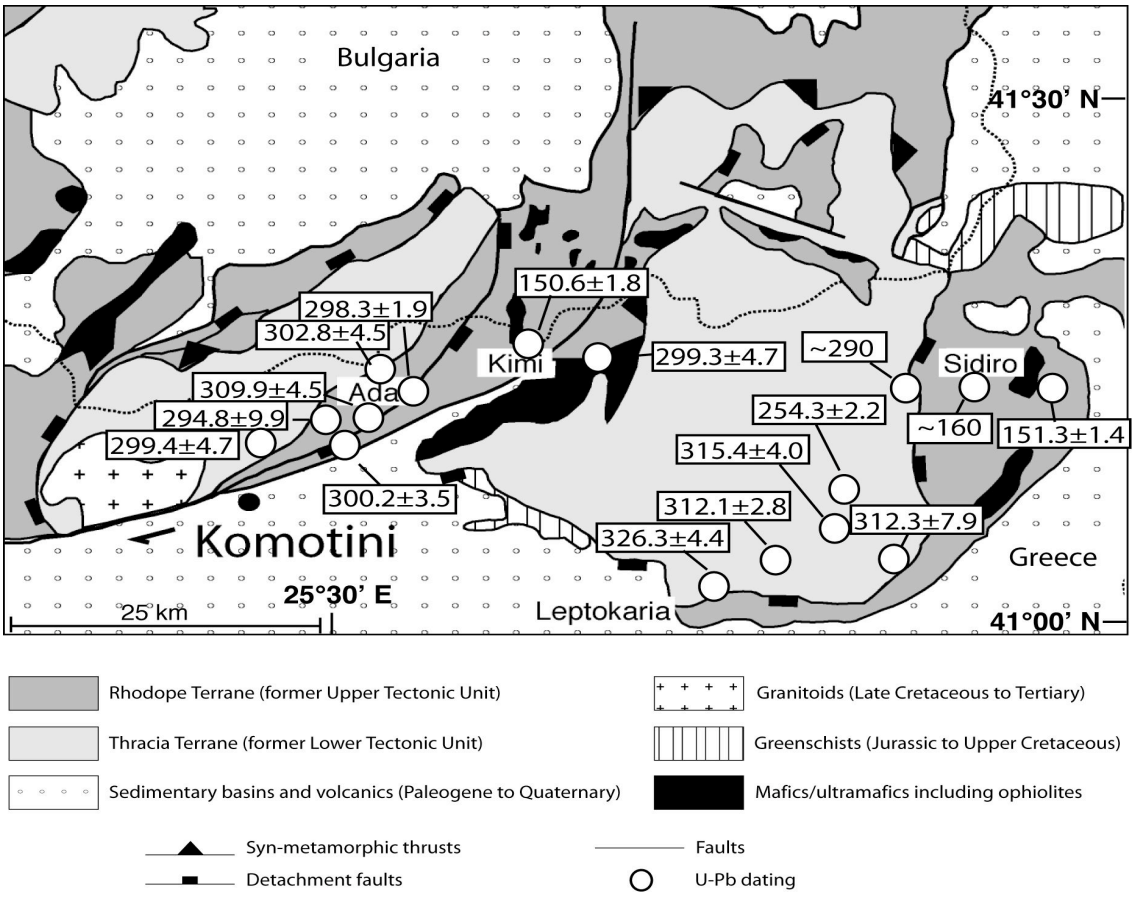

Fig. 6.1.1: Simplified geological map of the Eastern Rhodope Massif modified after Bonev et al. (2006) showing the Rhodope main tectonic units and the U-Pb zircon ages of the orthogneisses dated during this study.

At the contact between these two units, 4 km east of Mega Derio, garnet-micaschists (RH388) are intercalated with strongly sheared orthogneisses, accompanied by two m-sized marble horizons and migmatitic amphibolites.

The field evidence and geochronological results suggest that the sections from the Eastern Rhodope Massif are similar to those of the Central Rhodope described by Turpaud (2006). The systematic occurrence of garnet±kyanite gneisses/micaschists, marble, migmatitic amphibolites and strongly sheared orthogneisses at the contact between the two terranes implies that the Nestos suture of the Central Rhodope has an eastward continuation and that the HP/UHP mélange zone is a continuous belt throughout the Rhodope Massif.

6.2 Correlation of the UHP metapelites from Eastern and Central Rhodope Massif

To confirm the field evidence, a detailed Laser-Raman and TOF-SIMS study was carried out on about 200 zircons, which were separated from two metapelitic gneisses from the mélange zone of the Ada and Sidiro sections. These rocks were considered to be the best candidates for having experienced HP/UHP metamorphism because of their similar structural position with the Xanthi and Kimi UHP rocks.

In this study, metamorphic microdiamonds were identified in situ, for the first time in the Greek Rhodope, in their host zircons using Laser-Raman spectroscopy. The zircons consist of a rather inclusion-free detrital core followed by an inclusion-rich inner rim, characterized by patchy zoning in the CL-images, surrounded by a rather inclusion-free outer rim of metamorphic origin. The diamond inclusions are located in the inner rim, close to the core-rim interface. The presence of diamond indicates that this part of the rims of the zircons grew at ultra-high pressures exceeding 4 GPa. Striking similarities exist between the CL-images and inclusion mineralogy of the zircons investigated in this study and the ones from UHP metapelites of the Xanthi area described by Liati (2005) and of the Kimi area described by Bauer et al. (2007). Based on CL-images, Bauer et al. (2007) reported a three-fold division of the zircons from a garnet-kyanite-biotite gneiss from the Kimi area. Inherited cores are surrounded by an inclusion-rich inner rim with moderate to low CL-emission and patchy zoning, followed by a volumetrically dominant, inclusion-free, CL-bright outermost rim domain. The inclusions in the inner rim comprise carbonates, disordered graphite, CO_2 gas, rutile, anatase, biotite, kyanite and melt, which largely match the inclusions found in zircons in the garnet-kyanite gneiss F157 from the Ada section

(except for the diamonds). Moreover, zircons with a similar zoning structure were reported by Liati (2005) for a UHP-metamorphic garnet-kyanite-biotite gneiss from the Xanthi area in the Central Rhodope Massif. SHRIMP dating of the zircons from the Kimi garnet-kyanite-biotite gneiss yielded $^{206}Pb/^{207}Pb$-ages between 298 Ma and ca. 3 Ga for the inherited cores, whereas the inclusion-rich inner rims yielded a $^{206}Pb/^{238}U$-age of 171.0 ± 1 Ma and the outer rims 160.1 ± 1 Ma (Bauer et al. 2007). For the garnet-kyanite-biotite gneiss from the Xanthi area, Liati (2005) reported $^{206}Pb/^{238}U$-ages of 565 to 3234 Ma for the cores of the zircons, whereas the inner rims were dated at 148.8 ± 2.2 Ma and the outer ones between 148 and 83 Ma. The 171.0 ± 1 Ma age of Bauer et al. (2007) is interpreted either as zircon formation during prograde high-temperature metamorphism or decompression from UHP metamorphic conditions, whereas the 148.8±2.2 Ma age of Liati (2005) is interpreted as close to HP or UHP metamorphism. The $^{206}Pb/^{207}Pb$-ages between 250 Ma and 2.5 Ga of the inherited cores of the zircons of UHP sample F157 from the Ada section are in the range described Bauer et al. (2007) and Liati (2005 and references therein). Ages obtained for the rims of the zircons of sample F157 are less accurate due to the fact that the inclusion-rich inner rim domain but also the outer rim domain are too narrow to fit a laser spot. Rim analyses are therefore mostly mixed analyses of the two rim domains or mixed analyses of core and rim and yield $^{206}Pb/^{238}U$-ages between 115 and 41 Ma. Many of them are discordant and indicate Pb-loss during a subsequent metamorphic event probably around or after 41 Ma. This youngest concordant age was obtained from an outermost rim (at the tip) of a zircon grain of sample F157. Such Eocene ages were reported for different rock types from numerous localities of the Central Rhodope Massif. Interestingly, metamorphic rims of zircons from the garnet-kyanite-biotite gneiss close to Xanthi, dated at 148.8±2.2 Ma, show Pb-loss at ca. 40 Ma (Liati 2005). This age is in line with Rb-Sr dating of biotite and white mica from a similar sample by Reischmann and Kostopoulos (2002) yielding 37 Ma. For the Central Greek Rhodope, a SHRIMP U-Pb age of 42.2 ± 0.9 Ma, measured on zircons from an eclogite close to Thermes, is interpreted to represent the high pressure (eclogite) metamorphism (Liati and Gebauer 1999). Metamorphic rims of Hercynian zircons of the surrounding orthogneiss country rock yielded almost the same age, 42.0 ± 1.1 Ma. Therefore, these authors suggest that both, the eclogite and the orthogneiss experienced maximum pressures around 42 Ma. This Eocene HP event is highly questionable, since in the Rhodope Massif, Eocene to Oligocene ages are related to HT events like granite intrusions and extensive migmatization. Liati and Gebauer (1999) presented a U-Pb age of 40.0 ± 1.0 Ma for the temperature peak still at high pressure, by dating zircons from a

leucosome of a migmatite in the Thermes area. Large syntectonic granitoid plutons like the Skaloti-Oreon granite could be related to this migmatization event (Turpaud 2006). A late pegmatite crosscutting amphibolites of the Sminthi area is assumed to represent the late stages of metamorphism with a crystallization age of 36.1 ± 1.2 Ma (Liati and Gebauer 1999). Late Alpine (35–38 Ma) high-grade metamorphism and migmatization was reported from the Bulgarian Central Rhodopean Dome as well (Peytcheva et al. 2004 and references therein). Oligocene Rb-Sr ages of granitoid intrusions are known from the Eastern Rhodope Massif (Jones et al. 1992 and references therein). Therefore, it is likely that the garnet-kyanite gneiss from the Ada section experienced a thermal overprint around 40 Ma probably related to migmatization as well. Moreover, evidence for migmatization is provided by the large amounts of migmatitic amphibolites within the mélange zone.

For the Kimi area of the Eastern Rhodope Massif, an eclogite-facies metamorphic event, dated at ca. 74 Ma, was proposed by Liati et al. (2002). This event was reinterpreted by Bauer et al. (2007) as an amphibolite-facies (or even lower grade) metamorphic event at ca. 79 Ma. The UHP garnet-kyanite-biotite gneiss from the Kimi area investigated by Bauer et al. (2007) does not record the 79 Ma-event or any Tertiary HP/HT-metamorphism. Differences exist also in the compositions of the zircons from the garnet-kyanite-biotite gneisses. The inclusion-rich inner rim domain of zircons from the UHP paragneiss of the Kimi area shows high HREE contents (Bauer et al. 2007), whereas the same domain from the UHP paragneiss of the Xanthi area shows low HREE contents (Liati 2005). The latter is in agreement with the observations of the TOF-SIMS study of the UHP zircons of the paragneiss from the Ada section, which show low REE concentrations in the rim indicating zircon formation in the presence of garnet. The same was suggested by Liati (2005) for the Xanthi sample. The differences in age and REE patterns of the garnets gave rise to the question, if the rocks from the Central Rhodope Massif (Xanthi) represent different tectonic slices, which experienced HP/UHP at different times than the metapelites and amphibolites from Kimi (Liati 2005, Bauer et al. 2007). Taking into account the results of this study, multiple HP/UHP events are not likely. Instead, the HP/UHP rocks can be explained by a single event, the subduction of a branch of the Meliata-Maliac ocean system in Jurassic times like it was documented for the Central Rhodope by Turpaud and Reischmann (submitted). Jurassic subduction is inferred by palinspastic reconstruction models as well (e.g. Stampfli and Borel 2002) and moreoever, seismic tomography of the mantle of the Tethyan region corroborates this idea (Van Hinsbergen et al. 2005, Hafkenscheid et al. 2006). While the subduction of the Nestos

Ocean had already been ceased in the Jurassic, tomographic anomalies in the mantle of the Tethyan region, which are considered to represent the subducted Tethyan lithosphere, indicate that the subduction of Neo-Tethys started at ~ 140 Ma in the Arabian region (Hafkenscheid et al. 2006, based on palaeoreconstructions of Stampfli and Borel 2004).

6.3 Geodynamic evolution of the Rhodope

The petrographical, geochemical and geochronological results of the present study provide new insights into the geodynamic evolution of the Greek Rhodope Massif. Permo-Carboniferous magmatism is one of the most important crust-forming events not only in the Rhodope Massif but in the Internal Hellenides and it is most likely related to a volcanic-arc setting during the northward subduction of the Palaeotethys beneath the southern European continental margin (Fig. 6.3.1). Similar suggestions were made by Turpaud (2006) for the Central Rhodope and Reischmann et al. (2001) and Anders et al. (2007) for the Pelagonian Zone. Inherited cores of zircon grains in many Permo-Carboniferous samples of the Eastern Rhodope Massif record predominantly Devonian to Neoproterozoic and minor also Palaeoproterozoic and Archean ages. Notably orthogneiss RH429 from Organi/Smigada shows an accumulation of Cambrian and Neoproterozoic ages ranging between 510 and 632 Ma. Oscillatory zoning of these inherited cores indicates a magmatic origin. West of Organi/Smigada, the zircons of two orthogneisses from the Ada section (RH345, RH346) are all characterized by xenocrystic cores with predominantly Silurian and Ordovician ages. Because oscillatory zoning is often preserved in these cores they are considered to be of magmatic origin. Late Precambrian magmatism is a widespread phenomenon in the Mediterranean as it is known from the Pirgadikia Unit of the adjacent Serbo-Macedonian Massif (Himmerkus et al. 2006), from the Menderes Massif of southwestern Turkey (e.g. Hetzel and Reischmann 1996, Loos and Reischmann 1999), the Istanbul Zone of northwestern Turkey (Chen et al. 2002) and also from Bulgaria, for example, from the Kraiste region (Graf 2001) and the Sredna Gora Zone (Carrigan et al. 2006). Neoproterozoic (Cryogenian) rocks of the Florina Terrane were recently discovered in the Pelagonian Zone (Anders et al. 2006). Pan-African or Cadomian ages are generally linked to North Gondwana-derived terranes of the Avalonian-Cadomian belt (Nance and Murphy 1994). The inherited zircons from orthogneiss RH429 of the Eastern Rhodope Massif further support the

existence of such a pre-existing, Gondwana-derived Neoproterozoic basement on which the Permo-Carboniferous magmatic arc was built.

Ordovician basement rocks are rare in the Hellenides. Locally inherited zircon cores were reported from the Pelagonian Zone (Anders et al. 2006) or from the Vourinos ophiolite (Liati et al. 2004). Ordovician inherited zircons were also found in Variscan basement rocks of the Sredna Gora Zone in Bulgaria (Carrigan et al. 2005). An age of 462 Ma was obtained by Pb/Pb single evaporation of zircons from orthogneisses of the Biga Peninsula in northwestern Turkey (Özmen and Reischmann 1999). Ordovician and Silurian ages have been documented so far only from orthogneisses and paragneisses of the Vertiskos Terrane of the Serbo-Macedonian Massif (Himmerkus et al. 2006, Meinhold 2007). The orthogneisses of the Vertiskos Terrane originated in a magmatic-arc environment and were interpreted as a remnant of an active continental margin related to the eastern Hun superterrane (Himmerkus et al. 2006). The inherited Ordovician and Silurian zircons of the orthogneisses from the Ada section in the Eastern Rhodope Massif are therefore interpreted to be related to the Vertiskos Terrane. They document that fragments of the Vertiskos Unit or equivalent rocks, e.g. sediments with a Vertiskos age source, were also part of the pre-existing crust on which the Permo-Carboniferous magmatic arc formed. Moreover, basement rocks of Vertiskos-type with a high Rb/Sr-ratio could have influenced the isotopic signature of the Permo-Carboniferous magmatic arc granitoids. The first Sr-Nd isotope data for the Permo-Carboniferous basement of the Greek Central and Eastern Rhodope Massif suggest a mixed crust-mantle source with a variable contribution from older crustal material. These data further document the similarity of the Thracia Terrane and the basement rocks of the Pelagonian Zone, which are both of the same age and originated in a magmatic arc environment. The Sr-Nd isotopic similarity of the Thracia Terrane and the Pelagonian Zone implies that the Pelagonian could be an equivalent of the Thracia Terrane, which rifted off in Triassic times and moved northeastward during the formation of the intervening Maliac/Meliata oceans as suggested by Stampfli et al. (1998), Stampfli (2000), and Vavassis et al. (2000).

A similar process, although not related to the Pelagonian Zone, was suggested by Turpaud and Reischmann (submitted), who argue in favour of a Triassic rifting event, where the Permo-Carboniferous crust was separated by the opening of a marginal ocean, the Nestos Ocean, which belongs to the Meliata-Maliac ocean system (Fig. 6.3.1). According to Turpaud and Reischmann (submitted), the rifting process is followed by a northward subduction of the Nestos ocean below the southern European Margin in Late Jurassic times, which led to the formation of the Late

Jurassic/Early Cretaceous magmatic arc granitoids of the Rhodope Terrane on the remnants of the rifted Permo-Carboniferous crust. This interpretation is based on the observation that inherited zircons of Permo-Carboniferous age are present in the samples of the magmatic arc meta-granitoids of the Late Jurassic/Early Cretaceous Rhodope Terrane. Triassic rifting is known from other Terranes of the Internal Hellenides as well. The Silurian basement rocks of the adjacent Vertiskos Unit of the Serbo-Macedonian Massif were intruded by Triassic A-type granitoids of the Arnea suite in a within-plate rift setting (Himmerkus et al. 2008, submitted). Triassic rift-related magmatism is also known from the easternmost part of the Vardar Zone (Kockel et al. 1977, Dimitriadis and Asvesta 1993). Anders et al. (2007) reported magmatic Triassic zircon ages from a meta-rhyolite and a mylonitic orthogneiss from the Pelagonian zone, probably related to an extensional setting. In the Western Rhodope Massif, Late Permian/Early Triassic protolith crystallization ages were documented for amphibolitized eclogites (Liati 2005). These rocks were interpreted either as remnants of a Late Permian/Early Triassic ocean or related to underplating during a Permo-Triassic rifting event (Liati 2005). A similar rift-related protolith crystallization age of an eclogitic amphibolite is known from the Central Rhodope Massif (D. Kostopoulos, pers. communication).

Some orthogneisses from the Eastern Rhodope Massif could have been affected by a Late Permian to Early Triassic thermal overprint, which led to a partial reset of the U-Pb system. Notably orthogneiss RH383 from the Dadia-Kotronia area shows two different types of magmatic zircons, each representing a different age. Few zircons show well-developed oscillatory zoning from core to rim and are Carboniferous in age, whereas the majority of the zircons exhibit sector zoning and are Permo-Triassic in age. Further Permo-Triassic ages were obtained from inherited cores of the leucocratic, migmatitic orthogneisses RH447 and RH455 sampled between Sidiro and Gianulli in the easternmost Rhodope Terrane. Inherited zircons and the isotopic composition of the Late Jurassic/Early Cretaceous granitoids of the Rhodope Terrane of the Eastern Rhodope Massif suggest that they formed on continental crust. These data argue in favour of the Triassic rifting event proposed by Turpaud and Reischmann (submitted).

A possible candidate for the remnants of the rifted Permo-Carboniferous crust north of the Nestos Ocean can be sought in the Strandja Massif of northwestern Turkey and eastern Bulgaria, which comprises a Late Variscan basement unit (312±2 – 315±5 Ma, Sunal et al. 2006; Okay et al. 2001) similar to the Pelagonian Zone (Anders et al. 2007) and which is considered to have formed in a mature magmatic arc environment (Sunal et al. 2006).

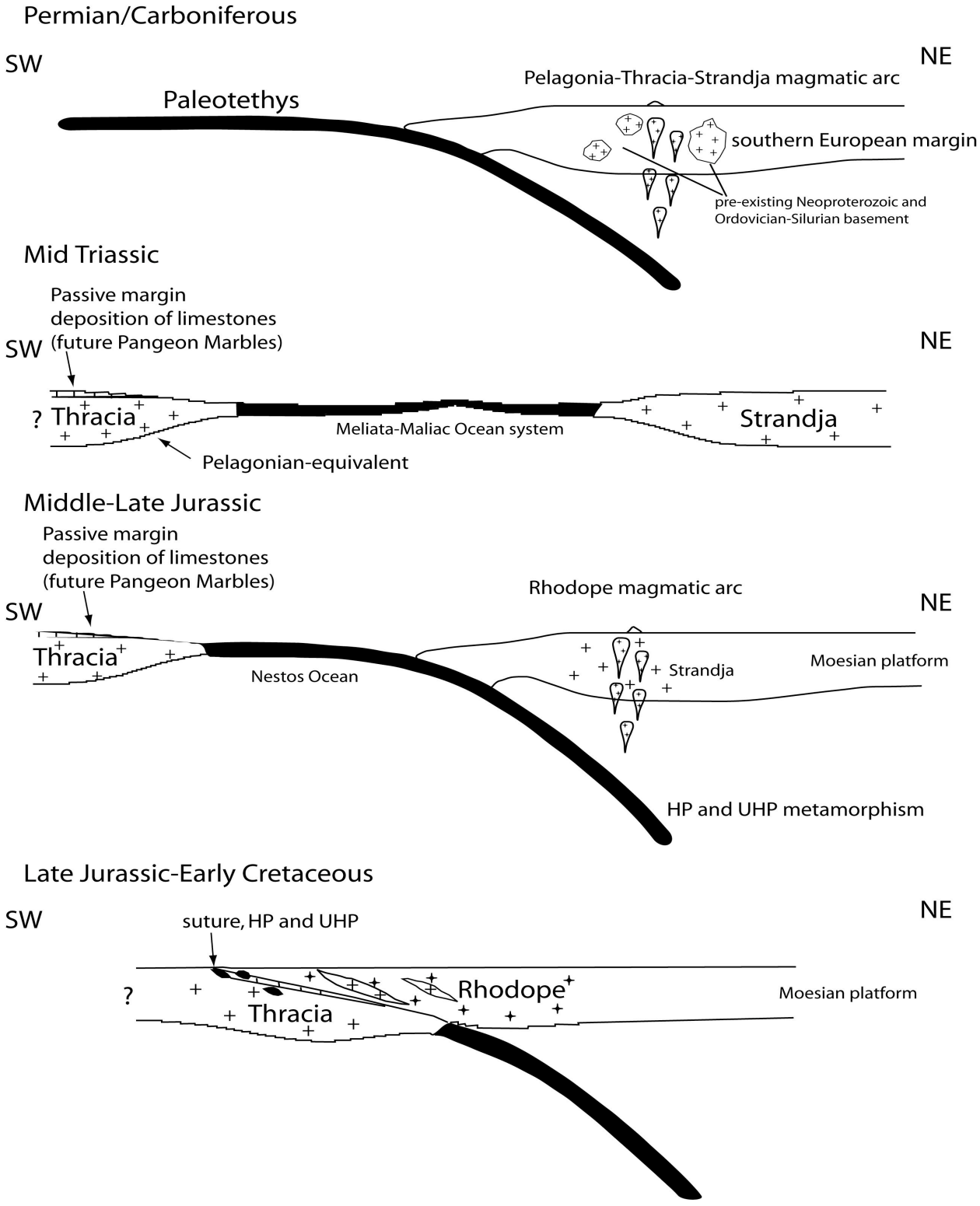

Fig. 6.3.1: Geodynamic evolution of the Rhodope Massif from Permo-Carboniferous to Late Jurassic/Early Cretaceous times modified after Turpaud (2006).

The following northward subduction of the intervening Nestos Ocean in Late Jurassic times is in agreement with the models of Ricou et al. (1998) and Van Hinsbergen et al. (2005). In the Late Jurassic/Early Cretaceous the Thracia Terrane and the Rhodope Terrane blocks collided (Burg et al. 1996, Van Hinsbergen et al. 2005), which led to their present-day configuration. The geodynamic evolution of the Rhodope Massif from Permo-Carboniferous to Early Cretaceous times is summarized in Figure 6.3.1.

6.4 Timing and conditions of UHP metamorphism and the exhumation of the UHP rocks

HP and UHP metamorphic rocks are considered to have formed during a single Jurassic subduction process (Turpaud and Reischmann submitted). This is in agreement with the U-Pb SHRIMP age of 148.8 ± 2.2 Ma of metamorphic zircon rims from the UHP metasediment of the Xanthi area (Liati 2005). Ages of metamorphic zircon rims between 171.0 ± 1 and 160.1 ± 1 Ma from the UHP metasediment of the Kimi area fit this range as well, although interpreted as the time of high-temperature metamorphism (Bauer et al. 2007). The age information from the UHP metapelite from Ada is too scarce to constrain the timing of UHP metamorphism precisely. Nevertheless, important information about the conditions of the UHP metamorphism of the metapelites of the Eastern Rhodope Massif stem from the Laser-Raman and TOF-SIMS studies (Fig. 6.4.1). The presence of diamond in the inner metamorphic rims was confirmed by laser-Raman spectroscopy and indicates that this part of the zircons grew at ultra-high pressures exceeding 4 GPa (Fig. 6.4.1). TOF-SIMS ion maps indicate diamond precipitation from C-O-H-S-Cl fluids. Elements like ^{89}Y and ^{174}Yb are concentrated in the detrital cores but are absent from the rims of the zircons. This can be explained by partitioning of these elements into garnet in the presence of a melt phase at very high temperatures. A calculation based on the experimental results of Rubatto and Hermann (2007) reveals that ultra-high temperatures of 1070°C at 20 kbar are necessary for Y to partition into garnet preferentially to zircon. In contrast, Li is enriched in the rim of the zircons, which suggests phengite melting during subduction, resulting in the liberation of Li, which was incorporated in the zircon rims. The breakdown of phengite due to dehydration melting was experimentally determined to occur at temperatures in excess of 1000°C (Schmidt et al. 2004).

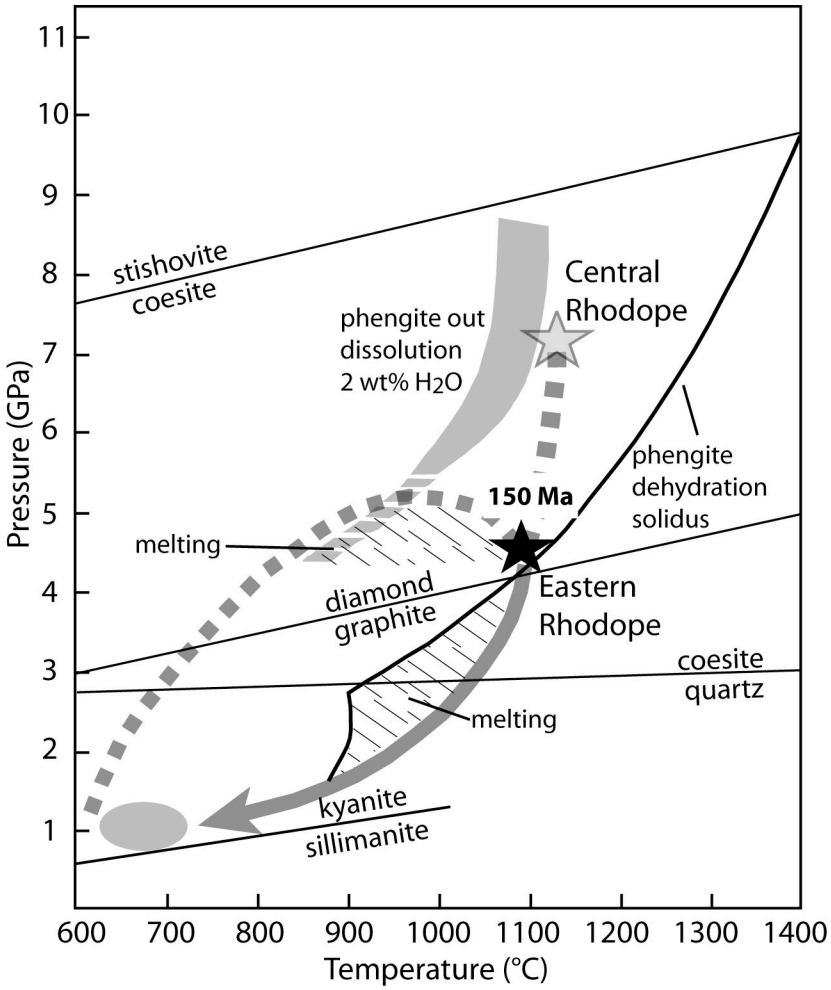

Fig. 6.4.1: P-T diagram and the suggested P-T path for the metapelites investigated during this study. Phengite dissolution and dehydration solidus are from Schmidt et al. (2004); the diamond-graphite transition was calculated with thermodynamic data from Chatterjee et al. (1998); the quartz-coesite transition is from Hemingway et al. (1998); coesite-stishovite transition is from Zhang et al. (1996); sillimanite-kyanite transition after Bohlen et al. (1991), grey star indicates peak-metamorphic conditions of metapelites of the Central Rhodope of Greece and southern Bulgaria (Mposkos and Kostopoulos 2001, Kostopoulos et al. 2003).

Such high temperatures are well in the range of melting conditions for metapelitic rocks, which gave rise to the question, if diamondiferous gneisses are related to melt processes (Kostopoulos et al. 2003, Massone 2003). Ultrahigh-pressure melting experiments on sedimentary compositions documented that melting can occur at around 1000°C if some water is in the system, e.g. stored in micas (Hermann and Green 2001). For the diamondiferous quartz-rich rocks of the Erzgebirge and Kokchetav Massifs, Massonne (2003) concluded that the minerals of these rocks have

crystallized from silicate melts, which originated by anatexis of deeply submerged metasediments. According to the UHP melting scenario of Massone (2003), only garnet survives the melting process as a restite and is the first to crystallize again during cooling. The UHP melting may also lead to resorption of zircons, which could be an explanation for the "chaotic" inner rims observed in zircons of the metapelites from Ada and Kimi. In UHP melts with S-type granitic composition, garnet crystallization is followed by the formation of kyanite and coesite during cooling of the melt (Huang and Wyllie 1981). Around 800°C and less, at lower-crustal levels, micas start to crystallize from the melt. The replacement of kyanite by coarse-grained muscovite in the UHP metasediments from the Erzgebirge is interpreted as evidence for this process (Massone 2003). Such textures are present in the garnet-kyanite gneisses of the Ada section as well. The order of crystallization of the minerals is in astonishingly good agreement with the petrographical observations of the garnet-kyanite gneisses of the Eastern Rhodope Massif. Garnet and kyanite seem to have formed earlier than the matrix minerals, since they show older deformation events not witnessed by the matrix minerals. Nevertheless, macroscopically the metapelites of the Eastern Rhodope Massif show no evidence of a magmatic texture; instead they are appear as metamorphic rocks, which experienced an intense amphibolite-facies overprint. Therefore, they might have lost most of their earlier magmatic memory due to the metamorphic overprint. A possibility to explain the prograde textures of garnet and kyanite in the metapelitic gneisses of the Eastern Rhodope Massif is a lower degree of melting of these UHP rocks. Since garnet porphyroblasts of sample F157 provide evidence for prograde staurolite and kyanite inclusions it is concievable that this metapelitic gneiss represents a partially molten rock. This model of a UHP restite-melt mush is the favoured explanation here for the preservation of prograde textures.

The evidence for melt can only be traced by microscale investigation. Hints for the presence of a melt can be found as melt inclusions. Multiple inclusions within garnet in the metapelites from the Erzgebirge consisting of microdiamond, quartz, feldspars and micas were interpreted as C-O-H-bearing silicate-rich fluids or melts trapped during UHP metamorphism (Stöckert et al. 2001). Multiphase melt inclusions were also reported by Georgieva et al. (2005) from garnet-kyanite schists from the Chepelare area, Central Rhodope, Bulgaria, for which UHP melting conditions have been postulated before by Kostopoulos et al. (2003). Melt inclusions were reported also from Bauer et al. (2007) from zircons of the UHP metapelite of the Kimi area, which is in

agreement with observations made in this study on the zircons of the UHP metapelite of the Ada area.

An interesting feature was described by Macheva et al. (2005) from the Ograzhden Mountains in southwestern Bulgaria, which are assigned to the Serbo-Macedonian Massif and where comparable kyanite-staurolite-garnet schists occur. These kyanite-staurolite-garnet schists, formerly considered as metamorphic rocks, show evidence of "ortho-character" based on field, petrological and geochemical data as well as zircon typology. The rocks were interpreted to have formed in a high-temperature deep crustal shear zone, which transformed granitoids into aluminous orthoschists (Macheva et al. 2005). The observations of Macheva et al. (2005) give rise to the question if such metapelitic rocks with an "ortho-affinity" could be another hint for (U)HP-derived melts.

Exhumation mechanisms for UHP rocks are considered to be driven by buoyancy forces (e.g. Ernst 2001) related to a density contrast of crust and mantle or by tectonic processes (e.g. Kurz and Froitzheim 2002). The evolving geometry of the subduction zone and the strength and density of the subducting crust and mantle lithosphere have an important influence on the exhumation mechanisms (buoyancy uplift, driven cavity flow and expulsion by a plunger) of UHP rocks (Warren et al. 2008).

The model of melt-derived UHP rocks (Kostopoulos et al. 2003, Massonne 2003) allows to explain the exhumation history of the Rhodope UHP rocks by a magmatic scenario. The first stages of exhumation are characterized by a quick rise of the magmas to lower-crustal levels (ca. 800°C and less) as a crystal-melt mush, where the crystallization of a mica phase from a peritectic reaction leads to the formation of more crystals and hampers further ascent (Massone 2003).

A two-stage exhumation model was introduced by Jolivet et al. (2003) for UHP rocks of the western Alps (Fig. 6.4.2). According to this model (Jolivet et al. 2003 and references therein), most of the material detaches from the subducting slab, before reaching greater depth but small amounts can be subducted to further depth. The low viscosity of the partially molten subducted material (e.g. metasediments) allows circulation in the subduction channel. A ductile extensional shear zone forms along the boundary of the subduction channel and the upper plate, which controls the upward flow of the exhumed material. In stage 1 (Fig. 6.4.2a) the orogen is single vergent and the subducted material is exhumed below a shear zone in the lower part of the accretionary complex.

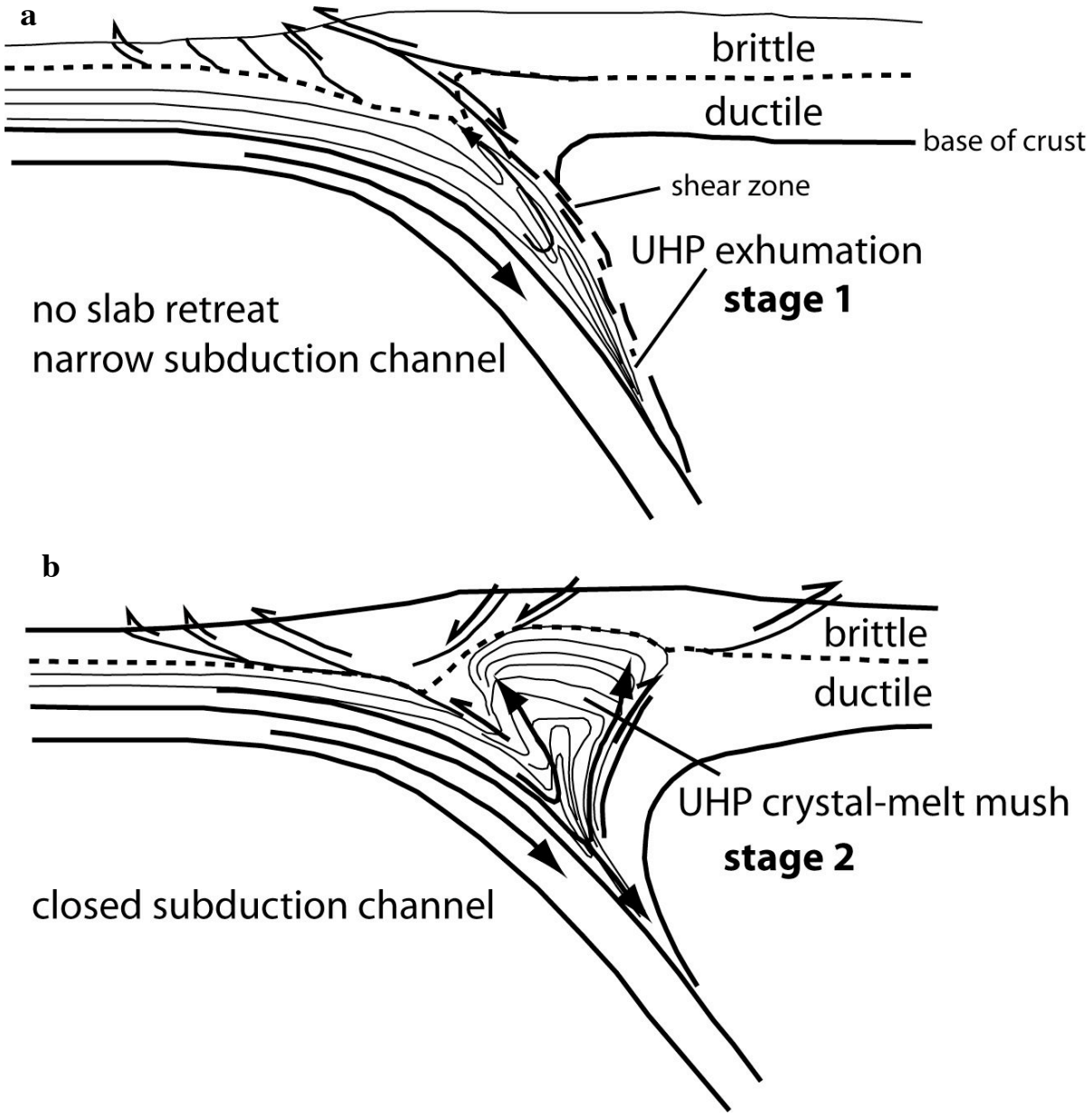

Figs: 6.4.2 a, b: Two-stage exhumation model for UHP rocks modified after Jolivet et al. (2003).

In stage 2 (Fig.6.4 .2b) the orogen becomes double vergent and the exhumation of the metamorphic domain (former UHP crystal-melt mush) leads to the formation of outward-dipping extensional shear zones, which have their roots in the brittle-ductile transition zone. Extension removes the overburden with the help of erosion (Jolivet et al. 2003).

7. Conclusions and implications for palaeogeographic reconstructions

The petrographical, geochemical and geochronological results of ortho- and paragneisses from the Greek Eastern Rhodope Massif presented in this study give new insights into the geodynamic evolution of the Rhodope Massif. Field evidence and geochronology revealed that the Eastern Rhodope Massif consists of two crustal units with a different magmatic and tectonic history, like it was documented for the Central Rhodope Massif (Reischmann and Kostopoulos 2007, Turpaud and Reischmann submitted). The detailed field study along several cross sections in the Eastern Rhodope Massif provides evidence that the contact zone of the two terranes in Eastern and Central Rhodope is characterized by a mélange of metapelites, migmatitic amphibolites/eclogites (with oceanic-affinity, see e.g. Liati 1986, Barr et al. 1999), strongly sheared orthogneisses and marbles. The systematical occurrence of this characteristic rock association between the terranes implies that the Nestos suture is a continuous belt throughout the Greek Rhodope Massif. The rocks within this mélange zone experienced HP and locally UHP metamorphism in Jurassic times at ~ 150 Ma (Reischmann and Kostopoulos 2002, Liati 2005, Bauer et al. 2007).

In this study, a new UHP locality could be established and for the first time in the Greek Rhodope, metamorphic microdiamonds were identified in situ in their host zircons using Laser-Raman spectroscopy. The presence of diamond inclusions in the metamorphic zircon rims documents UHP metamorphic conditions of at least 4 GPa for the metapelitic samples of the Paterma-Ada section. The absence of Y and Yb from the metamorphic rims of the zircons, as indicated by TOF-SIMS ion maps, is explained by a partition of these elements into garnet in the presence of a melt phase at temperatures above 1000°C. The enrichment of Li in the same zircon domain suggests phengite melting, again during subduction, at temperatures in excess of 1000°C. Morphology and mineralogy of multiphase albite and K-feldspar inclusion pockets in the metamorphic rims of the zircons are interpreted to have precipitated from this melt. TOF-SIMS ion maps imply diamond precipitation from C-O-H-S-Cl-fluids.

U-Pb zircon dating of orthogneisses revealed that the structurally lower Thracia Terrane of the Eastern Rhodope Massif is of Permo-Carboniferous age. According to major and trace element geochemical data, it originated in a magmatic-arc environment related to the subduction of the Paleotethys below the European continental margin (Fig. 7.1a). Inherited zircons in the orthogneisses from the Thracia Terrane of the Eastern Rhodope Massif indicate the presence of a pre-existing Neoproterozoic and Ordovician-Silurian basement in this region. The Sr-Nd isotope

data for the Permo-Carboniferous basement of the Eastern and Central Rhodope Massif suggest a mixed crust-mantle source with variable contribution of older crustal material.

Triassic magmatism is witnessed by the zircons of few orthogneisses from the easternmost Rhodope Massif and is interpreted to be related to rifting of the Thracia Terrane during the formation of the Nestos Ocean, a branch of the Meliata-Maliac ocean system (Fig. 7.1b). In this context, the Sr-Nd isotopic similarity of the Thracia Terrane and the Pelagonian Zone documented here implies that the Pelagonian is a possible equivalent of the Thracia Terrane, which rifted off in Triassic times and moved southward during the formation of the Maliac/Meliata ocean.

In the Middle Jurassic (180 Ma) the northward movement of the African plate led to the formation of a northward directed subduction zone in the northern part of the Maliac-Meliata ocean system, south of the Thracia Terrane (Fig. 7.1c, d). According to Koglin (2007), this subduction zone gave rise to an intra-oceanic arc, which is related to the Evros ophiolite (Fig. 7.1e).

Jurassic subduction-related magmatism is recorded by zircons of orthogneisses from the Kimi area and east of Sidiro in the Eastern Rhodope Massif. U-Pb zircon analyses of the orthogneisses yield ages of ~ 150 Ma, indicating that the subduction-related magmatism and the HP/UHP metamorphism occurred during the same subduction event. This event corresponds to the northward subduction of the Nestos Ocean in Late Jurassic times, which built up the Late Jurassic/Early Cretaceous Rhodope magmatic arc on remnants of the Thracia Terrane as indicated by inherited Permo-Carboniferous zircons (Fig. 7.1e). The Sr-Nd isotopic data for the Rhodope Terrane of the Eastern and Central Rhodope Massif argue for a mixed crust-mantle source for the magma, similar to the Thracia Terrane.

The exhumation of the metapelitic UHP rocks can be explained by a magmatic scenario (Jolivet et al. 2003, Kostopoulos et al. 2003, Massone 2005). Partial melting at UHP conditions leads to the formation of a restite-melt mush with the preservation of prograde textures in garnet and kyanite. The first stage of exhumation is characterized by a quick rise of this restite-melt-mush to lower-crustal levels due to density contrast and buoyancy forces. At ca. 800°C and less the crystallization of a mica phase hampers further ascent. The second stage of exhumation is attributed to extensional shear zones and erosion.

Due to the final closure of the Nestos Ocean in the Late Jurassic/Early Cretaceous, the two terranes collided and the Permo-Carboniferous Thracia Terrane was overthusted by the Late

Jurassic/Early Cretaceous Rhodope Terrane (Fig. 7.1.f). The post-Jurassic evolution of the Rhodope Massif is characterized by the exhumation of the core complex due to extensional tectonics, which is associated with the intrusion of granites in the Tertiary.

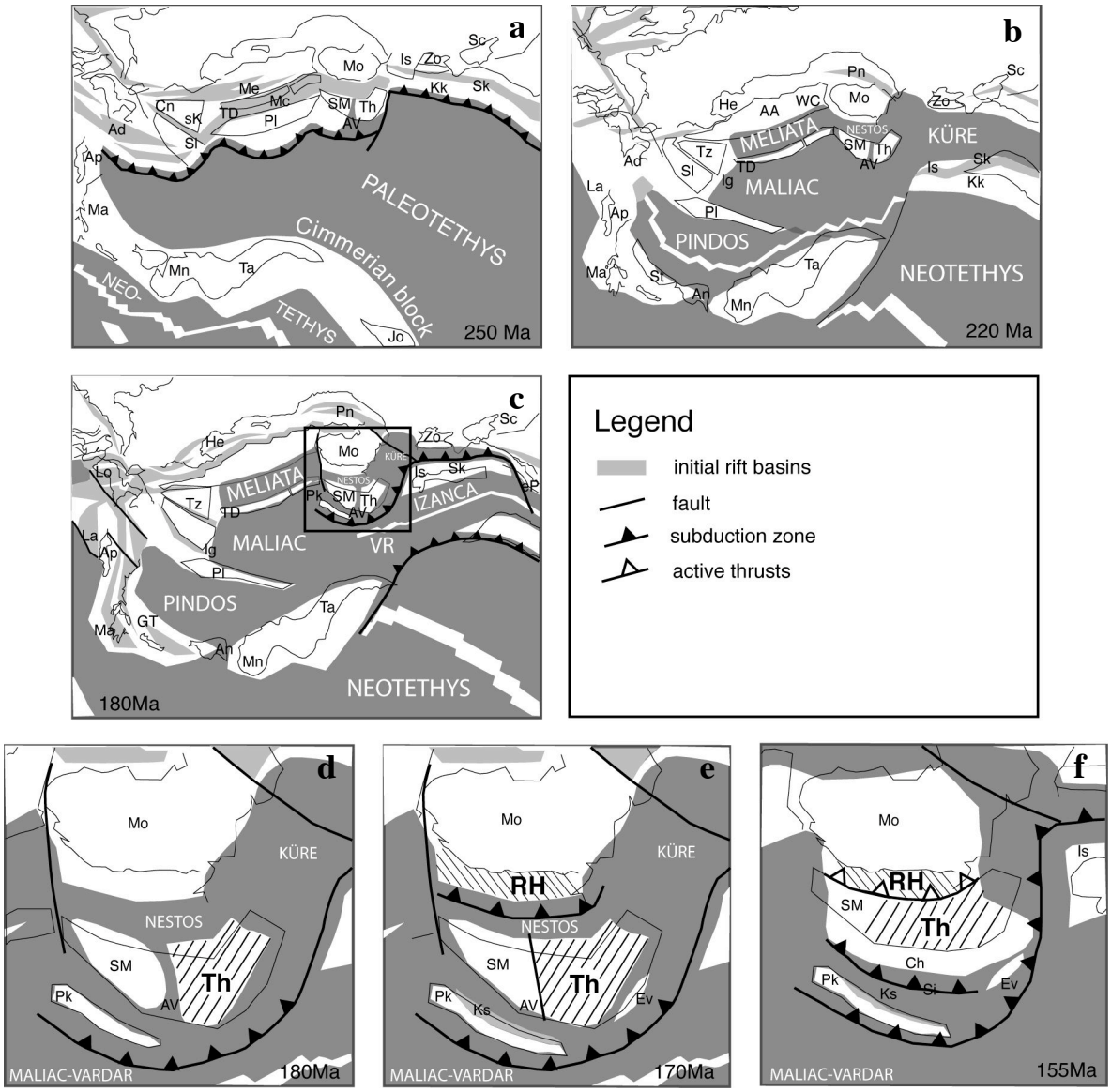

Figs: 7.1a-f: Palaeogeographic reconstructions of the Mediterranean area from Permian to Late Jurassic modified after Stampfli and Borel (2002) and Koglin (2007).

AA, Austroalpin; Ad, Adria; An, Antalya Alakir Cay; Ap, Apulia; AV, Athos-Volvi Zone; Ch, Chortiatis Arc; Cn, Carnic-Julian; eP, east Pontides; Ev, Evros island arc and rift; GT, Gavrovo-Tripolitza; He, Helvetic rim basin; Ig, Igal trough; Is, Istanbul; Jo, Jolfa; Kk, Karakaya complex; Ks, Kassandra rift basin; La, Lagonegro; Le, Lesvos rift; Lo, Lombardian; Ma, Mani; Mc, Maliac rift and ocean; Me, Meliata rift and ocean; Mn, Menderes; Mo, Moesia; NE, Nestos Ocean; Pk, Paikon Arc; Pl, Pelagonian; Pn, Pienniny rift; RH, Rhodope island arc and terrane; Sc, Scythian

platform; Si, Sithonia spreading ridge; Sk, Sakarya; sK, south-Karawanken fore arc; Sl, Slavonia; SM, Serbo-Macedonian; St, Sitia-E-Crete; Ta, Taurus; TD, Transdanubian; Th, Thracia Terrane; Tz, Tizia; VR, Vardar Ocean; WC, West-Carpathian; Zo, Zonguldak.

References

Aftalion, M., Bowes, D.R., Vrana, S. 1989. Early Carboniferous U-Pb zircon ages for garnetiferous perpotassic granulits, Blansky Les Massif, Czechoslovakia. Neues Jahrbuch für Mineralogie, Monatshefte, 4, 145-152.

Akaishi, M., Shaji Kumar, M.D., Kanda, H., Yamaoka, S., 2000. Formation process of diamond from supercritical H_2O-CO_2 fluid under high pressure and temperature conditions. Diamond and Related Materials, 9, 1945–1950.

Armstrong, J.T., 1993. Citzaf Version 3.03. California Instiute of Technology, JEOL implement by Paul Carpenter.

Anders, B., 2005a. The Pre-Alpine Evolution of the Basement of the Pelagonian Zone and the Vardar Zone, Greece. PhD Thesis, University of Mainz, Germany.

Anders, B., Reischmann, T., Poller, U., Kostopoulos, D., 2005b. Age and origin of granitic rocks from the Eastern Vardar Zone: new constraints on the evolution of the Internal Hellenides. Journal of the Geological Society, London, 162, 857–870.

Anders, B., Reischmann, T., Kostopoulos, D., 2007. Zircon geochronology of basement rocks of the Pelagonian Zone, Greece: constraints on the pre-Alpine evolution of the westernmost Internal Hellindes. International Journal of Earth Sciences, 96, 639–661.

Anders, B., Reischmann, T., Kostopoulos, D., Poller, U., 2006. The oldest rocks of Greece: first evidence for a Precambrian terrane within the Pelagonian Zone. Geological Magazine, 143, 41–58.

Barr, S.R., Temperley, S.T., Tarney, J., 1999. Lateral growth of the continental crust through deep level subduction-accretion: a re-evaluation of central Greek Rhodope. Lithos 46, 69–94.

Bauer, C., Rubatto, D., Krenn, K., Proyer, A., Hoinkes, G., 2007. A zircon study from the Rhodope metamorphic complex, N-Greece: time record of a multistage evolution. Lithos, 99, 207–228.

Black, L.P., Kamo, S.L., Allen, C.M., Aleinikoff, J.N., Davis, D.W., Korsch, R.J., Foudoulis, C., 2003. TEMORA 1: a new zircon standard for Phanerozoic U–Pb geochronology. Chemical Geology, 200, 155–170.

Bohlen, S.R., Montana, A., Kerrick, D.M., 1991. Precise determination of the equilibria kyanite-sillimanite and kyanite-andalusite and a revisited triple point for Al_2SiO_5 polymorphs. American Mineralogist, 76, 677–680.

Boncev, E., 1971. Problems of Bulgarian geotectonics. Sofia, D´rzhavno Izvestija Tekhnika, 204 p.

Bonev, N., Burg, J.P., Ivanov, Z., 2006. Mesozoic-Tertiary structural evolution of an extensional gneiss dome – the Kesebir-Kardamos dome, eastern Rhodope (Bulgaria – Greece). International Journal of Earth Sciences, 95, 318–340.

Boynton, W.V., 1984. Geochemistry of the rare earth elements: meteorite studies. In: Henderson, P. (ed), Rare Earth Element Geochemistry, Elsevier, Amsterdam, 63–114.

Brown, S.A.M., Robertson, A.H.F., 2004. Evidence for Neotethys rooted within the Vardar suture zone from the Voras Massif, nothernmost Greece. Tectonophysics, 381, 143–173.

Burg, J.P., Ivanov, Z., Ricou, L.E., Dimov, D., Klain, L., 1990. Implications of shear-sense criteria for the tectonic evolution of the Central Rhodope Massif, southern Bulgaria. Geology, 18, 451–454.

Burg, J.P., Ricou, L.E., Ivanov, Z., Godfriaux, I., Dimov, D., Klain, L., 1996. Syn-metamorphic nappe complex in the Rhodope Massif, Structure and kinematics. Terra Nova, 8, 6–15.

Carrigan, C.W., Mukasa, S.B., Haydoutov, I., Kolcheva, K., 2005. Age of Variscan magmatism from the Balkan sector of the orogen, central Bulgaria. Lithos, 82, 125–147.

Carrigan, C.W., Mukasa, S.B., Haydoutov, I., Kolcheva, K., 2006. Neoproterozoic magmatism and Carboniferous high-grade metamorphism in the Sredna Gora Zone, Bulgaria: An extension of the Gondwana-derived Avalonian-Cadomian belt?. Precambrian Research 147, 404–416.

Chakraborty, S., Ganguly, J., 1991. Compositional zoning and cation diffusion in aluminosilicate garnets. In: Ganguly, J. (ed), Diffusion, Atomic ordering and Mass Transport – selected problems in Geochemistry, Advances in Physical geochemistry, 8, Springer Verlag, New York.

Chatterjee, N.D., Krüger, R., Haller, G., Olbricht, W., 1998. The Bayesian approach to an internally consistent thermodynamic database: theory, database, and generation of phase diagrams. Contributions to Mineralogy and Petrology, 133, 149–168.

Chatzitheodoridis, E., Lyon, I., Vgenopoulos, A., 2005. IMA05, 4th International Conference on Instrumental Methods of Analysis, Modern Trends and Applications, Heraklion, Crete, Greece.

Chen, F., Siebel, W., Satir, M., Terzioglu, M., Saka, K., 2002. Geochronology of the Karadere basement (NW Turkey) and implications for the geological evolution of the Istanbul zone. International Journal of Earth Sciences, 91, 469–481.

Chopin, C., 1984. Coesite and pure pyrope in high-grade blueschists of the western Alps: a first record and some consequences. Contributions to Mineralogy and Petrology, 86, 107–118.

Chopin, C., Sobolev, N.V., 1995. Principal mineralogical indicators of UHP in crustal rocks. In: Coleman, R.G., Wang, X.M. (eds), Ultrahigh-Pressure Metamorphism, Cambridge University Press, Cambridge, UK, 96–133.

Corfu, F., Hanchar, J.M., Hoskin, P.W.O., Kinny, P., 2003. Atlas of zircon textures. In: Hanchar, J.M., Hoskin, P.W.O. (eds), Zircon, Reviews in Mineralogy and Geochemistry, 53, 469–500.

Cox, K.G., Bell, J.D., Pankhurst, R.J., 1979. The Interpretation of Igneous Rocks, George Allen and Unwin, London, 450 pp.

De La Roche, H., Leterrier, J., Grande Claude, P., Marchal, M., 1980. A classification of volcanic and plutonic rocks using R1-R2 diagrams and major element analysis – its relationship and current nomenclature. Chemical Geology, 29, 183–210.

Dimitriadis, S., Avesta, A., 1993. Sedimentation and magmatism related to the Triassic rifing and later events in the Vardar-Axios Zone. Bulletin of the Geological Society of Greece, 18, 149–168.

Dinter, D.A., Royden, L., 1993. Late Cenozoic extension in northeastern Greece: Strimon Valley detachment system and Rhodope metamorphic core complex. Geology, 21, 45–48.

Dinter, D.A., Macfarlane, A., Hames, W., Isachen, C., Bowring, S., Royden, L., 1995. U-Pb and $^{40}Ar/^{39}Ar$ geochronology of the Symvolon granodiorite: Implications for the thermal and structural evolution of the Rhodope metamorphic core complex , northeastern Greece. Tectonics, 14, 886–908.

Dobrzhinetskaya, L.F., Renfro, A.P., Green, H.W., 2004. Synthesis of skeletal diamonds: Implications for microdiamond formation in orogenic belts. Geology, 32, 869–872.

Dobrzhinetskaya, L.F., Green, H.W.,Bozhilov, K.N., Mitchell, T.E., Dickerson, R.M., 2003a. Crystallization environment of Kazakhstan microdiamond: evidence from nanometric inclusions and mineral associations. Journal of Metamorphic Geology, 21, 425–437.

Dobrzhinetskaya, L.F., Green, H.W., Weschler, M., Darus, M., Wang, Y.C., Massone, H.J., Stöckhert, B., 2003b. Focused ion beam technique and transmission electron microscope studies of microdiamonds from the Saxonian Erzgebirge. Germany, Earth and Planetary Science Letters, 10, 399–410.

Ellis, D.J., Thompson, A.B., 1986. Subsolidus and partial melting reactions in the quartz-excess $CaO + MgO + Al_2O_3 + SiO_2 + H_2O$ system under water-excess and water-deficient conditions to 10 kb: some implications for the origin of peraluminous melts from mafic rocks. Journal of Petrology, 27, 91–121.

Engel, M., 2006, Geochemie, Geochronologie und Isotopie der Grundgebirgsgneise und ausgewählter Marmore der zentralen Kykladen, Griechenland. PhD Thesis, University of Mainz, Germany.

Ernst, W.G., 2006. Preservation/exhumation of ultrahigh-pressure subduction complexes. Lithos, 92, 321–335.

Förster, H.J., Tischendorf, G., Trumbull, R.B., 1997. An evaluation of the Rb vs. (Y + Nb) discrimination diagram to infer tectonic setting of silicic igneous rocks. Lithos, 40, 261–293.

Frei, D., Hollis, J.A., Gerdes, A., Harlov, D., Karlsson, C., Vasquez, P., Franz, G., Johansson, L., Knudsen, C., 2006. Advanced in-situ trace element and geochronological microanalysis of geomaterials by laser ablation techniques. Geological Survey of Denmark and Greenland Bulletin, 10, 25–28.

Frost, B.R., Barnes, C.G., Collins, W.J., Arculus, R.J., Ellis, D.J., Frost, C.D., 2001. A geochemical classification for granitic rocks. Journal of Petrology, 42, 2033–2048.

Gebauer, D., Liati, A., 1997. Geochronological evidence for Mesozoic rifting and oceanization followed by Eocene subduction in the Rhodope Complex (Northern Greece). Terra Nova, 9, 10.

Georgieva, M., Mogessie, A., Cherneva, Z., 2005. Mineral needles and melt inclusions in garnet from the Chepelare area, Central Rhodope, Bulgaria. Mitteilungen der Österreichischen Mineralogischen Gesellschaft, 150, 40.

Gerdes, A., Zeh, A., 2006. Combined U-Pb and Hf isotope LA-(MC)-ICP-MS analyses of detrital zircons: Comparison with SHRIMP and new constraints for the provenance and age of an Armorican metasediment in Central Germany. Earth and Planetary Science Letters, 249, 47–61.

Goldstein, S.J., O`Nions, R.K., Hamilton, P.J., 1984. A Sm-Nd isotopc study of atmospheric dust and particulates from major river systems. Earth and Planetary Science Letters, 70, 221–236.

Gradstein, F.M., Ogg, J.G., Smith, A.G., 2004. A Geologic Time Scale 2004. Cambridge University Press, Cambridge.

Graf, J., 2001. Alpine Tectonics in western Bulgaria: Cretaceous compression of the Kraiste region and Cenozoic exhumation of the crystalline Osogovo-Lisec complex. PhD Thesis, ETH Zürich, Switzerland.

Hafkenscheid, E., Wortel, M.J.R., Spakman, W., 2006. Subduction history of the Tethyan region derived from seismic tomography and tectonic reconstructions. Journal of Geophysical Research, 11, B08401, doi:10.1029/2005JB003791.

Harris, N.B.W., Pearce, J.A., Tindle, A.G., 1986. Geochemical characteristics of collision-zone magmatism. In: Coward, M.P., Ries, A.C. (eds), Collision Tectonics, Geological Society, London, Special Publications, 19, 67–81.

Hemingway, B.S., Bohlen, S.R., Hankins, W.B., Westrum, E.F., Kuskov, O.L., 1998. Heat capacity and thermodynamic properties for coesite and jadeite, reexamination of the quartz-coesite equilibrium boundary. American Mineralogist, 83, 409–418.

Hermann, J., Green, D.H., 2001. Experimental constraints on high pressure melting of subducted crust. Earth and Planetary Science Letters, 188, 149–168.

Herron, M.M., 1988. Geochemical classification of terrigenous sands and shales from core or log data. Journal of Sedimentary Petrology, 58, 820–829.

Hetzel, R., Reischmann, T., 1996. Intrusion age of Pan-African augengneisses in the southern Menderes massif and the age of cooling after Alpine ductile extensional deformation. Geological Magazine, 133, 565–572.

Himmerkus, F., Reischmann, T., Kostopoulos, D., 2006a. Late Proterozoic and Silurian basement units within the Serbo-Macedonian Massif, northern Greece: the significance of terrane accretion in the Hellenides. In: Robertson, AHF., Mountrakis, D. (eds), Tectonic Development of the Mediterranean Region, Geological Society, London, Special Publications, 260, 35–50.

Himmerkus, F., Reischmann, T., Kostopoulos, D., 2006b. Permo-Carboniferous and upper Jurassic basement ages in the Kerdillion Unit, eastern Serbo-Macedonian Massif, northern Greece. Geophysical Research Abstracts, 8, 05758.

Himmerkus, F., Reischmann, T., Kostopoulos, D., 2008, submitted. Serbo-Macedonian revisited: a Silurian basement terrane from northern Gondwana in the Internal Hellinides, Greece.

Himmerkus, F., Zachariadis, P., Reischmann, T., Kostopoulos, D., 2005. The mafic complexes of the Athos-Volvi-Zone – a suture zone between the Serbo-Macedonian Massif and the Rhodope Massif?. Geophysical Research Abstracts, 7, 10240.

Holtz, F., Johannes, W., 1991. Genesis of peraluminous granites I. Experimental investigation of melt compositions at 3 and 5 kb and various H_2O activities. Journal of Petrology, 32, 959–978.

Horstwood, M., Foster, G.L., Parrish R.R., Noble, S.R., 2003. Common-Pb corrected in situ U–Pb accessory mineral geochronology by LA-MC-ICP-MS. Journal of Analytical Atomic Spectrometry, 18, 837–846.

Huang, W.L., Wyllie, P.J., 1981. Phase relationships of S-type granite with H_2O to 35 kbar: Muscovite granite from Harney Peak, South Dakota. Journal of Geophysical Research, 86, 10515–10529.

Ivanov, Z., 1988. Apercu général sur l´évolution géologique et structurale du massif des Rhodopes dans le cadre des Balkanides. Bulletin de la sociétée géologique de France, 8, 227–240.

Jackson, S., Pearson, N.J., Griffin, W.L., Belousova, E.A., 2004. The application of laser ablation – inductively coupled plasma – mass spectrometry to in situ U-Pb zircon geochronology. Chemical Geology, 211, 47–69.

Jacobshagen, V., 1986. Geologie von Griechenland. Beiträge zur Regionalen Geologie der Erde, 19, 1–363.

Janousek, V., Gerdes, A., Vrána, S., Finger, F., Erban, V., Friedl, G., Braithwaite, C.J.R., 2006. Low-pressure Granulites of the Lisoc Massif, Southern Bohemia: Visean Metamorphism of Late Devonian Plutonic Arc Rocks. Journal of Petrology, 47, 705–744.

Jolivet, L., Faccenna, C., Goffé, B., Burov, E., Agard, P., 2003. Subduction tectonics and exhumation of high-pressure metamorphic rocks in the Mediterranean Orogens. American Journal of Science, 505, 353–409.

Jones, C.E., Tarney, J., Baker, J.H., Gerouki, F., 1992. Tertiary granitoids of Rhodope, northern Greece: magmatism related extensional collapse of the Hellenic Orogen? Tectonophysics, 219, 295–314.

Kockel, F., Mollat, H., Walther, H.F., 1971. Geologie des Serbo-Mazedonischen Massivs und seines Mesozoischen Rahmens (Nordgriechenland). Geologisches Jahrbuch, 89, 529–551.

Kockel, F., Mollat, H., Walter, H.W., 1977. Erläuterungen zur Geologischen Karte der Chalkidiki und angrenzender Gebiete 1:100 000, Nordgriechenland. Bundesanstalt für Geowissenschaften und Rohstoffe, Hannover, 1–119.

Koglin, N., 2007. Geochemistry, petrogenesis and tectonic setting of ophiolites and ultra-mafic complexes in the Northeastern Aegean Region: New trace element, isotopic and age constraints. PhD Thesis, University of Mainz, Germany.

Kolcheva, K., Zeljaskova-Panajotova, M., Dobrecov, N.L., Stojanova, V., 1986. Eclogites in the Central Rhodope metamorphic group and their retrograde metamorphism. Geochemistry, Mineralogy and Petrology, 20–21, 130–144.

Kostopoulos, D.K., Ioannidis, N.M., Sklavounos, S.A., 2000. A new Occurence of Ultrahigh-Pressure Metamorphism, Central Macedonia, Northern Greece: Evidence from Graphitized Diamonds?. International Geology Reviews, 42, 545–554.

Kostopoulos, D., Gerdjikov, I., Gautier, P., Reischmann, T., Cherneva, Z., 2003. First Evidence for UHP Metamorphism in the Central Rhodope Massif of Southern Bulgaria. Geophysical Research Abstracts, 5, 08327.

Kostopoulos, D., Chatzitheodoridis, E., Cornelius, N., Baltatzis, E., Reischmann, T., 2007. Environment of diamond formation in UHPM rocks from the Greek Rhodope: A Raman study of inclusions in zircon. Geochimica et Cosmochimica Acta, A517.

Kurz, W., Froitzheim, N., 2002. The exhumation of eclogite-facies metamorphic rocks; a review of models confronted with examples from the Alps. International Geology Review, 44, 702–743.

Le Bas, M. J., Le Maitre, R. W., Streckeisen, A., Zanettin, B. A., 1986. Chemical classification of volcanic rocks based on the Total-Alkali-Silica diagram. Journal of Petrology, 27, 745–750.

Liati, A., 1986. Regional metamorphism and overprinting contact metamorphism of the Rhodope zone near Xanthi (N. Greece). PhD Thesis, Technische Universität Braunschweig, Germany.

Liati, A., 2005. Identification of repeated Alpine (ultra) high pressure metamorphic events by U-Pb SHRIMP geochronology and REE geochemistry of zircon: the Rhodope zone of northern Greece. Contributions to Mineralogy and Petrology, 150, 608–630.

Liati, A., Seidel, E., 1996. Metamorphic evolution and geochemistry of kyanite eclogites in central Rhodope, northern Greece. Contributions to Mineralogy and Petrology, 123, 293–307.

Liati, A., Gebauer, D., 1999. Constraining the prograde and retrograde P-T-t path of Eocene HP rocks by SHRIMP dating of different zircon domains: inferred rates of heating, burial, cooling and exhumation for central Rhodope, northern Greece. Contributions to Mineralogy and Petrology, 135, 340–354.

Liati, A., Fanning, C.M., 2005. Eclogites and their country rock orthogneisses in the East Rhodope representing Upper Permian gabbros and Upper Carboniferous granitoids: Geochronological constraints. Mitteilungen der Österreichischen Mineralogischen Gesellschaft, 150, 88.

Liati, A., Gebauer, D., Wysoczanski, R., 2002. U-Pb SHRIMP dating of zircon domains of UHP garnet-rich mafic rocks and late pegmatoids in the Rhodope zone (N Greece); evidence for Early Cretaceous crystallization and Late Cretaceous metamorphism. Chemical Geology, 184, 281–299.

Liew, T.C, Hofmann, A.W., 1988. Precambrian crustal components, plutonic associations, plate environment of the Hercynian Fold Belt of central Europe: Indications from a Nd and Sr isotopic study. Contributions to Mineralogy and Petrology, 98, 129–138.

Lips, A.L.W., White, S.H., Wijbrans, J.R., 2000. Middle-Late Alpine thermotectonic evolution of the southern Rhodope Massif, Greece. Geodinamica Acta, 13, 281–292.

Loos, S., Reischmann, T., 1999. The evolution of the southern Menderes massif in SW Turkey as revealed by zircon dating. Journal of the Geological Society, London, 156, 1021–1030.

Ludwig, K.R., 2001. SQUID 1.02. Berkeley Geochronological Centre, Special Publications, 2.

Ludwig, K.R., 2003. Isoplot/Ex vs. 3.0. A Geochronological Toolkit for Microsoft Excel. Berkeley Geochronological Centre, Special Publications, 4.

Macheva, L., Titorenkova, R., Zidarov, N., 2005. Kyanite-staurolite-garnet-bearing schists from Ograzhden Mountain, SW Bulgaria – metapelites or orthoschists?. Proceedings of the Jubilee International Conference „80 years BGS“, Sofia, 138–141.

Mahoney, J.B., Weis, D., Kieffer, B., Friedman, R., Pretorius, W., Scoates, J., Goolaerts, A., Maerschalk, C., 2003. Ongoing isotopic characterization og USGS standards: MC-ICPMS and TIMS data from the Pacific Centre for Isotopic and Geochemical Research, University of British Columbia. Geological Society of America, Abstracts with Programs, 35, 243.

Massone, H.J., 2003. A comparison of the evolution of diamondiferous quartz-rich rocks from the Saxinian Erzgebirge and the Kokchetav Massif: are so-called diamondiferous gneisses magmatic rocks?. Earth and Planetary Science Letters, 216, 347–346.

Massone, H.J., 2005. Ultra High Pressure Metamorphism. In: Selley, R.C., Cocks, L.R.M., Plimer, I.R. (eds), Encyclopedia of Geology, Elsevier Ltd., 533–541.

McKay, G.A., 1989. Partitioning of rare earth elements between major silicate minerals and basaltic melts. In: B.R. Lipin, G.A. McKay (eds), Geochemistry and mineralogy of rare earth elements. Reviews in Mineralogy, The Mineralogical Society of America, Washington D.C., 45-77.

Meinhold, G., 2007. Sedimentary rocks of the Internal Hellenides, Greece: age, source and depositional setting. PhD thesis, University of Mainz, Germany.

Meinhold, G., Reischmann, T., Kostopoulos, D., Lehnert, O., Matukov, D., Sergeev, S., 2008. Provenance of sediments during subduction of Palaeotethys: Detrital zircons ages and olistolith analysis in Palaeozoic sediments from Chios Island, Greece. Palaeogeography, Palaeoclimatology, Palaeoecology, 263, 71–91.

Mercier, J., Vergély, P., Bébien, J., 1975. Les ophiolites hélliniques „obducteés“ au Jurassique supérieur sont-elles les vestiges d´un Océan thétysien ou d´une mer marginale péri-européenne?. Comptes Rendues sommaires de la Sociètè Gèologique de France, 17, 108–112.

Mposkos, E., 1989. High-pressure metamorphism in gneisses and pelitic schists in Eastern Rhodope zone (N Greece). Mineralogy and Petrology, 41, 337–351.

Mposkos, E., Liati, A., 1993. Metamorphic evolution of metapelites in the high pressure terrane of the Rhodope Zone, northern Greece. Canadian Mineralogist, 31, 401–424.

Mposkos, E., Wawrzenitz, N., 1995. Metapegmatites and pegmatites bracketing the time of HP-metamorphism in polymetamorphic rocks of the E-Rhodope, N. Greece: petrological and geochronological constraints. Geological Society of Greece, Special Publications, 4, 602–608.

Mposkos, E., Krohe, A., 2000. Petrological and structural evolution of the continental high-pressure (HP) metamorphic rocks in the Alpine Rhodope domain. In: Panaydes, I., Xenophontos, C., Malpas, J. (eds), Proceedings of the 3rd international conference on the Geology of the Eastern Mediterranean, Geological Survey, Nicosia, Cyprus, 1, 221–232.

Mposkos, E.D., Kostopoulos, D.K., 2001. Diamond, former coesite and supersilicic garnet in metasedimentary rocks from the Greek Rhodope: a new ultrahigh-pressure metamorphic province established. Earth and Planetary Science Letters, 192, 497–506.

Nance, R.D., Murphy, J.B., 1994. Contrasting basement isotopic signatures and the palinspatic restoration of peripheral orogens; example from the Neoproterozoic Avalonian-Cadomian Belt. Geology, 22, 617–620.

Nehring, F., Jacob, D.E., Barth, M.G., Foley, S.F., 2007. Laser-ablation ICP-MS, analysis of siliceous rock glasses fused on an Iridium strip heater using MgO dilution. Microchmimica Acta, doi:10.1007/s00604-007-08197.

Nesbitt, H.W., Young, G.M., 1982. Early Proterozoic climates and plate motions inferred from major element chemistry of lutites. Nature, 299, 717–717.

Nesbitt, H.W., Young, G.M., 1984. Prediction of some weathering trends of plutonic and volcanic rocks based on thermodynamic and kinematic considerations. Geochimica et Cosmochimica Acta, 48, 1523–1543.

Nesbitt, H.W., Young, G.M., 1989. Formation and diagenesis of weathering profiles. Journal of Geology, 97, 129–147.

Okay, A.I., Satir, M., Tüysüz, O., Akyüz, S., Chen, F., 2001. The tectonics of the Strandja Massif: late-Variscan and mid-Mesozoic deformation and metamorphism in the northern Aegean. International Journal of Earth Sciences, 90, 217–233.

Ovtcharova, M., Cherneva, Z., von Quadt, A., Peytcheva, I., 2002. Migmatitic geochronology and geochemistry - a key to understand the exhumation of the Madan Dome (Bulgaria). Geochimica and Cosmochimica Acta, 66, A573.

Ovtcharova, M., von Quadt, A.V., Peytcheva, I., Neubauer, F., Heinrich, C.A., Kaiser, M., 2003. Time and Duration of Metamorphism and Exhumation of the Central Rhodopian Core Complex, Bulgaria. Geophysical Research Abstracts, 5, 10121.

Ovtcharova, M., von Quadt, A., Cherneva, Z., Sarov, S., Heinrich, C.A., Peytcheva, I., 2004. U–Pb dating of zircon and monazite from granitoids and migmatites in the core and eastern periphery of the Central Rhodopean Dome, Bulgaria. Geochimica and Cosmochimica Acta, 68, A664.

Özmen, F., Reischmann, T., 1999. The age of the Sakarya continent in W Anatolia: implications for the evolution of the Aegean region. Journal of Conference Abstracts, 4, 805.

Papanikolaou, D., Panagopoulos, A., 1981. On the structural style of the Southern Rhodope, Greece. Geologica Balcanica, 11, 13–22.

Pearce, J.A., Harris, N.B.W., Tindle, A.G., 1984. Trace element discrimination diagrams for the tectonic interpretation of granitic rocks. Journal of Petrology, 25, 956–983.

Perraki, M., Proyer, A., Mposkos E., Kaindl, R., Hoinkes, G., 2006. Raman micro-spectroscopy on diamond, graphite and other carbon polymorphs from the ultra-high-pressure metamorphic Kimi Complex of the Rhodope Metamorphic Province, NE Greece. Earth and Planetary Science Letters, 241, 672–685.

Peytcheva, I., von Quadt, A., 1995. U–Pb zircon dating of metagranites from Byala Reka region in the Eastern Rhodopes, Bulgaria. Geological Society of Greece Special Publications, 4, 637–642.

Peytcheva, I., von Quadt, A., Ovtcharova, M., Handler, M., Neubauer, F., Salnikova, E., Kostitsyn, Y., Sarov, S., Locheva, K., 2004. Metagranitoids from the eastern part of the Central Rhodopean Dome (Bulgaria): U–Pb, Rb–Sr and $^{40}Ar/^{39}Ar$ timing of emplacement and exhumation and isotope-geochemical features. Mineralogy and Petrology, 82, 1–31.

Planck, T., Langmuir, C.H., 1998. The chemical composition of subducting sediment and its consequences for the crust and mantle. In: Albarede, F., Blichert, T.J., Staudigel, H., White, W.M. (eds), Geochemical Earth Reference Model (GERM). Chemical Geology, 145, 325–394.

Pupin, J.P., 1980. Zircon and Granite Petrology. Contributons to Mineralogy and Petrology, 73, 207–220.

Pupin, J.P., Turco, G., 1972. Une typologie originale du zircon accessoire. Bulletin de la Societe Francaise de Minèralogie et de Cristallographie, 95, 348–359.

Reischmann, T., Kostopoulos, D., 2002. Timing of UHPM in metasediments of the Rhodope Massif, N Greece. Geochimica and Cosmochimica Acta, 66, A633.

Reischmann, T., Kostopoulos, D., 2007. Terrane accretion in the internal Hellenides. Geophysical Research Abstracts, 9, 05337.

Reischmann, T., Kostopoulos, D., Loos, S., Anders, B., Avgerinas, A., Sklavounos, S., 2001. Late Palaeozoic magmatism in the basement rocks southwest of the Mt. Olympos, Central Pelagonian Zone, Greece: Remnants of a Permo-Carboniferous Magmatic Arc. Bulletin of the Geological Society of Greece, 34, 985–993.

Ricou, L.E., Burg, J.P., Godfriaux, I., Ivanov, Z., 1998. Rhodope and Vardar: the metamorphic and olistostromic paired belts related to the Cretaceous subduction under Europe, Geodinamica Acta, 11, 285–309.

Robertson, A.H.F., Ustaömer, T., Pickett, E.A., Collins, A.S., Andrew, T., Dixon, J.E., 2004. Testing models of Late Palaeozoic–Early Mesozoic orogeny in Western Turkey: support for an evolving open-Tethys model. Journal of the Geological Society, London, 161, 501–511.

Robinson, P., 1991. The eye of the petrographer, the mind of the petrologist. American Mineralogist, 6, 1781–1810.

Rohrmeier, M., von Quadt, A., Handler, R., Ovtcharova, M., Ivanov, Z., Heinrich, C.A., 2002. The geodynamic evolution of hydrothermal vein deposits in the Madan metamorphic core complex, Bulgaria. Geochimica and Cosmochimica Acta, 66, A645.

Rubatto, D., Hermann, J., 2007. Experimental zircon/melt and zircon/garnet trace element partitioning and implications for the geochronology of crustal rocks. Chemical Geology, 241, 38–61.

Salters, V.J.M., Stracke, A., 2004. Composition of the depleted mantle. Geochemistry, Geophysics, Geosystems, 5, Q05004, doi:10.1029/2003GC000597.

Sato, K., Akaishi, M., Yamaoka, S., 1999. Spontaneous nucleation of diamond in the system $MgCO_3$-$CaCO_3$-C at 7.7 GPa. Diamond and Related Materials, 8, 1900–1905.

Schmidt, M.W., Vielseuf, D., Auzanneau, E., 2004. Melting and dissolution of subducting crust at high pressures: the key role of white mica. Earth and Planetary Science Letters, 228, 65–84.

Shand, S.J., 1943. Eruptive Rocks. Their Genesis, Composition, Classification and Their Relation to Ore-Deposits with a Chapter on Meteorite. John Wiley & Sons, New York.

Shatsky, V.S., Pal´yanov, Y.N., Sokol, A.G., Timolenko, A.A., Sobolev, N.V., 2001. Diamond formation in UPH metamorphic rocks: Natural and experimental evidence. In: Proceedings, UHPM Workshop 2001, Tokyo, Japan, Waseda University, 6–10.

Sircombe, K.N., 2004. AgeDisplay: an EXCEL workbook to evaluate and display univariate geochronological data using binned frequency histograms and probability density distributions. Computers & Geosciences, 30, 21–31.

Smith, D.C., 1984. Coesite in clinopyroxene in the Caledonides and its implications for geodynamics. Nature, 310, 641–644.

Sobolev, N.V., Shatsky, V.S., 1990. Diamond inclusions in garnets from metamorphic rocks: a new environment for diamond formation. Nature, 343, 742–746.

Sokol, A.G., Pal´yanov, Y.N., 2008. Diamond formation in the system MgO-SiO-HO-C at 7.5 GPa and 1600°C. Contributions to Mineralogy and Petrology, 155, 33–43.

Spear, F.S., 1993. Metamorphic phase equiblibria and pressure-temperature-time paths. Mineralogical Society of Amrica, Monographic Series, 779 p.

Stacey, J.S., Kramers, D.J., 1975. Approximation of terrestrial lead-isotope evolution by a two stage model. Earth and Planetary Science Letters, 26, 359–362.

Stampfli, G.M., 2000. Tethyan oceans. In: Bozkurt, E., Winchester, J.A., Piper, J.D.A. (eds) Tectonics and magmatism in Turkey and the surrounding area. Geological Society, London, Special Publications, 173, 1–23.

Stampfli, G.M., Borel, G.D., 2002. A plate tectonic model for the Paleozoic and Mesozoic constrained by dynamic plate boundaries and restored synthetic ocean isochrones. Earth and Planetary Science Letters, 196, 17–33.

Stampfli, G.M., Mosar, J., De Bono, A., Vavassis, L., 1998. Late Paleozoic, Early Mesozoic Plate Tectonics of the western Tethys. In: 8th International Congress of the Geological Society of Greece, Patras, Greece, XXXII/1, 113–120.

Stöckert, B., Duyster, J., Trpemann, C., Massonne, H.J., 2001. Microdiamond dauther crystals precipitated from supercritical COH + silicate fluids included in garnet, Erzgebirge, Germany. Geology, 29, 391–394.

Sunal, G., Natal´in, B.A., Muharrem, S., Toraman, E., 2006. Paleozoic magmatic events in the Strandja Massif, NW Turkey. Geodinimica Acta, 19, 282–300.

Tabata, H., Yamauchi, K., Maruyaman, S., Liou, J.G., 1998. Tracing the extent of a UHP metamorphic terrane: Mineral-inclusions study of zircons in gneisses from the Dabie Shan. In: Hacker, B.R., Liou, J.G. (eds), When continents collide: Geodynamics and Geochemistry of Ultra-high-Pressure Rocks, Kluwer Academic Publishers, Amsterdam, 261–273.

Taylor, S.R., McLennan,S.M., 1985. The continental crust: its Composition and Evolution, Blackwell, Oxford, 312 pp.

Turpaud, P., 2006. Characterisation of igneous terranes by zircon dating: implications for UHP relicts occurrences and suture identification in the Central Rhodope, Northern Greece. PhD Thesis, University of Mainz, Germany.

Turpaud, P., Reischmann, T., 2005. Relationships between crustal blocks and UHP relicts, an example from Northern Greece. Geophysical Research Abstracts, 8, 04353.

Turpaud, P., Reischmann, T., 2008, submitted. Characterisation of igneous terranes by zircon dating: implications for the UHP relicts occurrences and suture identification in the Central Rhodope, Northern Greece.

Tracy, R.J., 1982. Compositional zoning and inclusions in metamorphic minerals. In: Ferry, J.M. (ed), Characterization of Metamorhpism Through Mineral Equilibria, Reviews in Mineralogy, 10, 355–397.

Van Hinsbergen, D.J.J., Hafkenscheid, E., Spakman, W., Meulenkamp, J.E., Wortel, R., 2005. Nappe stacking resulting from subduction of oceanic and continental lithosphere below Greece. Geology, 33, 325–328.

Vavassis, I., De Bono, A., Stampfli, G.M., Giorgis, D., Valloton, A., Amelin, Y., 2000. U-Pb and Ar-Ar geochronological data from the Pelagonian Basement in Evia (Greece): geodynamic implications for the evolution of Paleotethys. Schweizerische Mineralogische und Petrographische Mitteilungen, 80, 21–43.

Warren, C.J., Beaumont, C., Jamieson, R.A., 2008. Modelling tectonic styles and ultra-high pressure (UHP) rock exhumation during the transition from oceanic subduction to continental collision. Earth and Planetary Science Letters, doi:10.1016/j.eps1.2007.11.025.

Wawrzenitz, N., 1997. Mikrostrukturell unterstützte Datierung von Deformationsinkrementen in Myloniten: Dauer der Exhumierung und Aufdomung des metamorphen Kernkomplexes der Insel Thassos (Süd-Rhodope, Nordgriechenland). PhD Thesis, University of Erlangen, Germany.

Wawrzenitz, N., Mposkos, E., 1997. First evidence for Lower Cretaceous HP/HT-metamorphism in the Eastern Rhodope, North Aegean Region, North-East Greece. European Journal of Mineralogy, 9, 659–664.

Wawrzenitz, N., Krohe, A., 1998. Exhumation and doming of the Thasos metamorphic core complex (S Rhodope, Greece): structural and geochronological constraints. Tectonophysics, 285, 301–332.

Wiedenbek, M., Allé, P., Corfu, F., Griffin, W.L., Meier, M., Oberli, F., von Quadt, A., Roddick, J.C., Spiegel, W., 1995. Three natural zircon standards for U-Th-Pb, Lu-Hf, trace element and REE analyses. Geostandard Newsletter, 19, 1–23.

Winchester, J.A., Floyd, P.A., 1977. Geochemical discrimination of different magma series and their differentiation products using immobile elements. Chemical Geology 20, 325–343.

Ye, K., Cong, B., Ye, D., 2000. The possible subduction of continental material to depths greater than 200 km. Nature, 407, 734–736.

Zachariadis, P., 2007. Ophiolites of the eastern Vardar Zone, N. Greece. PhD Thesis, University of Mainz, Germany.

Zang, J., Li, B., Utsumi, W., Liebermann, R.C., 1996. In-situ x-ray observation of the coesite-stishovite transition: reversed phase boundary and kinetics. Physics and Chemistry of Minerals, 23, 1–10.

Appendix

Appendix A - Sample localities and GPS coordinates: metapelites and orthogneisses

Chapter	Sample	Rock type	Locality	Latitude	Longitude
4	RH350	Metapelite	Paterma-Ada	41°15.006	25°29.128
4	RH352	Metapelite	Paterma-Ada	41°15.006	25°29.128
4	RH362	Metapelite	Paterma-Ada	41°14.643	25°30.632
4	RH363	Metapelite	Paterma-Ada	41°14.643	25°30.632
4	RH364	Metapelite	Paterma-Ada	41°14.643	25°30.632
3, 4	RH388	Metapelite	Mega Derio-Sidiro	41°14`56.5``	25°04`09.3``
4	RH391	Metapelite	Mega Derio-Sidiro	41°14`56.5``	25°04`09.3``
3, 4	RH412	Metapelite	Drania-Organi	41°14`56.6``	25°38`17.0``
3, 4	RH414	Metapelite	Organi-Smidaga	41°15`19.7``	25°41`43.1``
4	RH422	Metapelite	Smigada-Mirtiski	41°16`38.8``	25°45`59.1``
4	RH433	Metapelite	Kissari	41°16.464``	25°24.776``
3, 4	F157	Metapelite	Paterma-Ada	41°15`02.6``	25°29`06.0``
4	F162	Metapelite	Paterma-Ada	41°14`38.3``	25°30`37.5``
4	F163	Metapelite	Paterma-Ada	41°14`38.3``	25°30`37.5``
4	F166	Metapelite	Paterma-Ada	41°14.643	25°30.612

Chapter	Sample	Rock type	Locality	Latitude	Longitude
5	RH344	Orthogneiss	Paterma-Ada	41°13.551	25°30.270
3, 5	RH345	Orthogneiss	Paterma-Ada	41°13.607	25°30.125
5	RH346	Orthogneiss	Paterma-Ada	41°13.632	25°30.122
5	RH358	Orthogneiss	Paterma-Ada	41°12.787	25°30.620
5	RH360	Orthogneiss	Paterma-Ada	41°15.565	25°28.448
3, 5	RH361	Orthogneiss	Paterma-Ada	41°15.183	25°28.372
5	RH367	Orthogneiss	Paterma-Ada	41°15.434	25°30.530
5	RH369	Orthogneiss	Dadia-Kotronia	41°06.270	26°03.207
5	RH370	Orthogneiss	Dadia-Kotronia	41°06.881	26°00.608
5	RH371	Orthogneiss	Essimi-Leptokaria	41°07.844	25°55.573
5	RH373	Orthogneiss	Essimi-Leptokaria	41°04.879	25°54.747

5	RH375	Orthogneiss	Leptokaria-Dadia	41°05.171	25°54.582
5	RH376	Orthogneiss	Leptokaria-Dadia	41°05.424	25°54.567
5	RH382	Orthogneiss	Dadia-Kotronia	41°07.873	26°03.118
5	RH383	Orthogneiss	Dadia-Kotronia	41°09.365	26°03.321
3, 5	RH387	Orthogneiss	Mega Derio-Sidiro	41°14`00.8``	25°02`56.7``
3, 5	RH389	Orthogneiss	Mega Derio-Sidiro	41°13`42.9``	25°03`49.7``
3, 5	RH390	Orthogneiss	Mega Derio-Sidiro	41°13`35.7``	25°03`50.0``
3, 5	RH413	Orthogneiss	Drania-Organi	41°15`18.8``	25°41`39.2``
5	RH418	Orthogneiss	Organi-Smigada	41°16`53.2``	25°45`29.5``
3, 5	RH423	Orthogneiss	Smigada-Kimi	41°16`51.3``	25°43`19.4``
3, 5	RH429	Orthogneiss	Smigada-Mirtiski	41°15`44.7``	25°42`35.3``
5	RH434	Orthogneiss	Leptokaria-N. Sanda	41°06`29.5``	25°51`07.3``
5	RH441	Orthogneiss	Nymphea	41°13.013`	25°27.607`
5	RH447	Orthogneiss	Sidiro-Gianulli	41°14`01.8``	26°09´22.0``
3, 5	RH455	Orthogneiss	Sidiro	41°14.315`	26°08.346`

Appendix B – Analytical procedures and techniques

EMP analyses

Mineral chemical analyses were performed on polished thin sections using the Jeol JXA 8900 RL electron-microprobe, equipped with five wavelength-dispersive spectrometers, at the University of Mainz, Germany. The instrument was operated at 15 kV acceleration voltage with a beam current of 12 nA and a beam diameter of 2 μm for garnet, biotite, muscovite, paragonite, amphibole and staurolite. Operating conditions for feldspars were 15 kV/8nA with a beam diameter of 2 – 5 μm. Calibration of the instrument was carried out on natural and synthetical standards. The analyses were corrected using Citzaf (Armstrong 1993).

Whole-rock major and trace element analysis using XRF and LA-ICPMS

For whole-rock major and trace element analyses, the samples were crushed and milled to a grain size less than 50 μm. For major element analysis, the sample powder was mixed with $LiBO_4$ (1:7)

and fused in platinum crucibles. For trace element analysis, 6 g of sample powder were mixed with resin and hardener to prepare pressed pellets.

Routine analyses of major and trace elements in whole rocks were carried out on fused Li-tetraborate pellets and pressed powder pellets using the Philips PW1404 XRF instrument at the University of Mainz, Germany. Geochemical reference materials comprise AGV-1, BCR-1, BHVO-1 and JP-1. Errors on major and trace elements are in the range of 2 – 5 %.

The sample preparation for LA-ICPMS analyses of rare-earth elements, Hf, Ta, Th and U followed the method of Nehring et al. (2007). The samples were milled to a grain size less than 50 μm using an agate-mill. All samples were characterized by a silica content of >55 wt % SiO_2. High purity MgO powder was added to achieve a SiO_2 content of ≈55 wt % and the mixture was homogenized in an agate mortar. 40 mg of this sample powder were fused for 30 seconds at 1800 °C in an Iridium strip heater.

Whole-rock LA-ICPMS measurements of REE on fused glass droplets were performed on a Thermo-Finnigan Element II sector field ICP-MS equipped with a NewWave UP-213 laser system at the Max-Planck Institut für Chemie in Mainz. The ND-YAG Laser was operated at 10 Hz and the energy output was about 7 J/cm^2 with a spotsize of 120 μm. The LA-ICPMS analyses were carried out in low mass resolution mode. The mass spectrometer was tuned to keep oxide production low (ThO/Th < 1 %) for trace element analyses.

Typically, each analysis consisted of three runs, but to check homogenity, four spots were set on some samples. Each run comprised 20 blank and 70 ablation measurements for the trace elements. Abundance ratios of elements and isotopes were used for the data reduction. The blank corrected count rates of the trace elements were calculated to the internal standard element Ca. Generally, accuracy was better than 10% for the REE but in some cases less accuracy measurements were obtained for the low abundance REE Holmium and Thulium. Geochemical reference materials comprise NIST612, NIST610, GSE-1G and GSP-2.

U-Pb zircon dating using SHRIMP-II and LA-ICPMS

Zircon separation followed conventional procedures. The samples were crushed with a hydraulic press and a rotary mill. Zircons were extracted using the Wilfley table, magnetic and heavy-liquid separation and finally hand-picking. Selected zircon grains were mounted together with zircon

standard grains 91500 (U-calibration; ID-TIMS age = 1065.4 ± 0.3 Ma; Wiedenbek et al., 1995) and TEMORA 1 (calibration of U-Pb-ratios; ID-TIMS age = 416.75 ± 0.24 Ma; Black et al., 2003) in epoxy, polished, gold-coated and investigated by cathodoluminescence imaging. Analyses were performed by Guido Meinhold on the SHRIMP-II mass spectrometer using a secondary electron multiplier operated in a mass-scanning mode at the Centre of Isotopic Research (VSEGEI) in St. Petersburg, Russia. The spot size of the primary ion beam was ca. 25 μm with an intensity of 4 nA. Data reduction was processed using the SQUID and Isoplot/Ex add-in v. 3.0 for Excel (Ludwig 2001, 2003). Common lead correction followed the model of Stacey and Kramers (1975).

Prior to LA-ICPMS U–Pb geochronology, CL imaging was carried out on the the Jeol JXA 8900 RL microprobe at University of Mainz. LA-ICPMS analysis were performed on a Thermo-Finnigan Element II sector field ICP-MS equipped with a NewWave/Merchantek UP213 laser ablation system at the Geological Survey of Denmark and Greenland (GEUS) Copenhagen. The sample mount was rigorously cleaned before introduction into the sample cell to remove surface Pb contamination.

The methodology applied at GEUS essentially follows that described by Gerdes and Zeh (2006) and Frei et al. (2006). The nominal pulse width of the laser is 5 ns with a pulse-to-pulse stability of 2 % RSD. The laser was operated at a repetition rate of 10 Hz and a nominal energy output of 40 %, corresponding to a laser energy of ~0.006 mJ and a laser fluency of ~0.8 J cm^{-2}. All data were acquired with a single spot analysis on each individual zircon grain with a beam diameter of 30 μm. Samples and standards were held in a low-volume ablation cell specially developed for U-Pb-dating (Horstwood et al. 2003). Helium gas was used to flush the sample cell and was mixed downstream with the Ar sample gas of the mass-spectrometer. The washout time for this configuration was < 15 s. The ablated material was analyzed with an Element2 (ThermoFinnigan, Bremen) single-collector double focusing magnetic sector ICPMS equipped with a fast fieldregulator for increased scanning speed. The total acquisition time for each analysis was 60 s with the first 30 s used to measure the gas blank. The instrument was tuned to give large, stable signals for the ^{206}Pb and ^{238}U peaks, low background count rates (typically around 150 counts per second for ^{207}Pb) and low oxide production rates ($^{238}U^{16}O/^{238}U$ generally below < 0.2 %). All measurements were performed in low resolution mode using electrostatic scanning (E-scan) with the magnetic field resting at mass ^{202}Hg. The following masses were measured: ^{202}Hg, ^{204}(Pb +

Hg), ^{206}Pb, ^{207}Pb, ^{208}Pb, ^{232}Th, ^{235}U, and ^{238}U. All Data were acquired on four samples per peak with a sampling and a settling time of 1 ms for each isotope. Mass ^{202}Hg was measured to monitor the ^{204}Hg interference on ^{204}Pb (using a ^{202}Hg/^{204}Hg-ratio of 4.36). Only if the net intensities for mass ^{204}Pb, corrected for ^{204}Hg, were significantly above the limit of detection a common Pb-correction was performed. The laser induced elemental fractionation and the instrumental mass bias on measured isotopic ratios were corrected by matrix-matched external standardisation using the GJ-1 zircon standard (Jackson et al. 2004). Samples were analysed in sequences were three standards are analysed initially, followed by ten samples, again three standards, and so on. The raw data were exported in ASCII format and processed using in-house data reduction spreadsheets. The Plisovice zircon standard (Aftalion et al. 1989; provided by Jan Kosler, University of Bergen, Norway) was analysed as an unknown regularly. Long-term precision (2σ) based on 109 analyses of the Plesovice zircon by two different operators was 2 %, 2.3 % and 1.1 % for the ^{206}Pb/^{238}U, ^{207}Pb/^{235}U and ^{207}Pb/^{206}Pb ratios, respectively (Frei et al. 2006). Instrumental mass bias, laser-induced U-Pb fractionation as well as final age and error calculations were done using in-house developed age-calculation spreadsheets integrating the computer program IsoplotEx v. 3.0 (Ludwig 2003) for the final computation of ages. Probability density plots were generated using AgeDisplay (Sircombe 2004).

Sr- and Nd-whole-rock isotope composition analysis using TIMS

Sample preparation and TIMS analyses were performed at the Max-Planck Institute for Chemsitry in Mainz. To extract the isotopes, sample ca. 300 mg of sample powder was dissolved in 24M HF/ 14 M HNO3 solution and kept in teflon bombs at 200 °C for five days. The sample amount was 300 mg to represent the whole rock homogeniously. The HF/HNO3 mixture was fumed off and the relics were dissolved in HCl. For the separation of Sr and REE, 5 ml cation-exchange resin colums (AG50W-X12, 200-400 mesh), 2.5M HCl for Sr and 6M HCl for the REE were used. In order not to overload the colums, the samples were splitted. In a second step, the REE were further separated using Teflon powder colums coated with di-2-ethylhexyl phosphoric acid using 0.18mol/l HCl.

The Sr- and Nd-isotopes were analysed with a Finnigan MAT261 thermal ionization mass spectrometer (TIMS), equipped with a multicollector, in static mode. Sr-isotopes of the samples RH418, RH447, RH455, RH60, RH78, RH89, F180-2, F181 and F190 were analysed on a

ThermoFinnigan Triton. Sr was loaded on W filaments together with TaF2 for better ionization, whereas Nd was measured on doubly arranged Re filaments. Typically, twenty blocks of ten ratios were measured on each sample. La Jolla (for Nd) and NBS 987 (for Sr) standards were measured regularly.

The La Jolla standard yielded a mean of $^{143}Nd/^{144}Nd = 0.511845 \pm 12$ (2σ) on the MAT 261 instrument. Because Nd-isotopic ratios were measured over a time span of a year, all $^{143}Nd/^{144}/Nd$ ratios were corrected to a $^{143}Nd/^{144}/Nd$ ratio of 0.511850 for the La Jolla standard (Mahoney et al. 2003). The NBS 987 standard measured on the MAT 261 instrument gave a mean $^{87}Sr/^{88}Sr$ ratio of 0.710273 ± 10 (2σ) and on the Triton 0.710259 ± 7 (2σ). Mass fractionations were corrected to $^{146}Nd/^{144}Nd = 0.7219$ and $^{86}Sr/^{88}Sr = 0.1194$, respectively.

Appendix C – Abbreviations and mineral chemistry of the metapelites

Mineral chemical data are compiled as excel-files on a data CD attached to the thesis.

Abbreviations:

qtz = quartz, kfs = K-feldspar, pl = plagioclase, grt = garnet, amph = amphibolite, bt = biotite, ms = muscovite, par = paragonite, chl = chlorite, ky = kyanite, st = staurolite, ep = epidote, zoi = zoisite, ru = rutile, tur = turmaline, sph = sphene, cc = calcite, alm = almadine, grs = grossular, prp = pyrope, sps = spessartine, ab = albite, an = anorthite

Appendix D - Whole-rock major and trace elements of orthogneisses and metapelites

XRF orthogneisses

Sample	RH344	RH345	RH346	RH358	RH360	RH361	RH 369	RH 370	RH 375
location	Ada	Ada	Ada	Ada	Ada	Ada	Dadia-Kotronia	Dadia-Kotronia	Leptokaria-Dadia
SiO2	71.68	71.95	74.21	59.27	71.85	69.45	73.11	69.95	71.78
TiO2	0.26	0.24	0.23	0.26	0.17	0.32	0.16	0.34	0.28
Al2O3	14.77	12.96	13.05	10.72	14.26	14.87	14.96	15.66	14.78
Fe2O3	2.27	1.59	1.67	1.87	1.71	2.55	1.43	2.63	2.34
MnO	0.05	0.02	0.03	0.03	0.05	0.09	0.02	0.03	0.06
MgO	0.86	0.55	0.53	1.35	0.41	0.68	0.48	0.82	0.82
CaO	2.04	1.2	0.97	11.22	1.57	1.93	1.51	2.49	1.36
Na2O	3.31	3.58	3.39	2.48	3.4	3.54	4.87	4.05	3.83
K2O	3.7	3.31	4.61	2.78	3.88	4.36	2.49	3.1	2.96
P2O5	0.09	0.07	0.05	0.08	0.12	0.18	0.05	0.11	0.09
LOI	0.73	0.84	0.6	9.02	0.8	0.9	0.58	0.92	1.21
Sum	99.03	95.47	98.74	99.09	97.42	97.97	99.08	99.18	98.3
Sc	7	4	3	14	2	3	4	8	4
V	38	26	14	42	19	8	20	28	22
Cr	17	12	6	20	3	2	7	14	13
Co	3	3	5	5	2	4	1	2	1
Ni	6	6	4	7	6	2	2	6	4
Cu	3	1	0	12	1	2	2	3	8
Zn	45	28	25	39	31	50	40	40	67
Ga	15	15	13	12	20	19	17	19	18
Rb	129	97	117	84	187	158	60	106	93
Sr	167	105	124	117	96	211	411	262	188
Y	11	22	53	18	14	14	14	13	19
Zr	100	149	174	100	101	110	58	118	110
Nb	8	7	6	7	21	11	6	11	11
Ba	549	504	769	345	342	769	1120	578	449
Pb	31	20	24	14	11	29	18	43	33
Th	8	16.5	23.6	11	12.6	11.7	3.1	10.6	10.8
U	9.8	3.5	2.9	1.3	3.4	4.4	1.5	2.6	2
La	21	34	50	25	27	34	n.d.	22	19
Ce	27	63	97	41	41	53	n.d.	38	31
Pr	2	6	13	5	4	3	n.d.	1	1
Nd	14	29	45	23	23	27	n.d.	17	16
Sm	6	7	10	5	3	6	n.d.	4	7
A/NK	2.75	2.24	2.39	0	2.59	2.6	1.89	2.38	2.38
A/CNK	1.17	1.14	1.08	0	1.16	1.1	1.14	1.12	1.27
Nb/Y	0.73	0.32	0.11	0	1.5	0.79	0.43	0.85	0.58
Zr/TiO2	385	621	757	0	594	344	363	347	393
Fe*	0.73	0.74	0.76	0	0.81	0.79	0.75	0.76	0.74
Mali	4.97	5.69	7.03	0	5.71	5.97	5.85	4.66	5.43
ASI	1.13	1.1	0.99	0	1.11	1.05	1.18	1.14	1.26
CIA	52.88	52.65	51.41	0.00	52.99	51.41	52.65	51.84	55.23

Loi: loss on ignition; n.d.: not determined; A/NK: molecular Al2O3/(K2O+Na2O); A/CNK: molecular Al2O3/(CaO+K2O+Na2O); Fe*: FeOtot/(FeOtot+MgO); Mali: Na2O+K2O-CaO; ASI: Al/(Ca-1.67*P+Na+K); CIA: molecular [Al2O3/(Al2O3+CaO+Na2O+K2O)]*100.

XRF orthogneisses – continued

Sample	RH 376	RH 383	RH387	RH389	RH390	RH413	RH418	RH423
location	Leptokaria-Dadia	Dadia-Kotronia	Mega Derio-Sidiro	Mega Derio-Sidiro	Mega Derio-Sidiro	Drania-Organi	Organi-Smigada	Smigada-Kimi
SiO2	69.96	74.38	74.27	73.94	73.6	68.17	67.96	76.62
TiO2	0.37	0.29	0.09	0.22	0.14	0.4	0.49	0.13
Al2O3	14.46	12.73	14.62	13.85	14.78	15.61	15.89	12.95
Fe2O3	2.49	2.07	0.74	1.72	1.16	3.4	3.5	0.95
MnO	0.05	0.03	0.01	0.03	0.02	0.05	0.03	0.02
MgO	0.55	0.38	0.38	0.38	0.32	0.98	1.49	0.29
CaO	1.65	1.18	0.32	0.98	0.62	2.8	2.03	0.94
Na2O	3.2	2.98	4.21	3.89	4.16	3.7	3.65	3.41
K2O	5.46	4.69	4.89	4.38	4.77	3.34	3.24	4.61
P2O5	0.09	0.06	0.13	0.12	0.13	0.19	0.12	0.03
LOI	0.34	0.63	1.11	0.89	1.17	1.41	1.27	0.82
Sum	98.28	98.79	99.66	99.51	99.7	98.64	98.4	99.95
Sc	8	5	1	7	3	6	9	0
V	22	19	5	16	8	47	53	8
Cr	3	6	6	8	8	5	41	6
Co	1	1	b.d.	2	1	4	5	b.d.
Ni	6	5	0	3	2	3	12	1
Cu	3	6	3	5	5	20	31	5
Zn	42	35	26	38	30	65	57	16
Ga	15	15	20	19	19	20	19	13
Rb	102	159	187	192	187	140	137	135
Sr	155	84	66	89	90	250	207	252
Y	12	30	7	23	8	28	13	10
Zr	254	178	55	120	87	166	151	91
Nb	8	9	9	17	11	11	11	4
Ba	626	645	473	319	518	819	567	742
Pb	23	28	34	32	44	17	20	30
Th	10.9	15.3	5.4	16.8	9.1	13.6	13.3	39.4
U	2.9	2.7	1.7	5.5	3.8	4.9	2.6	3.7
La	73	58	1	34	9	41	28	25
Ce	125	119	9	50	29	80	48	41
Pr	11	13	1	4	2	6	8	2
Nd	41	51	8	29	13	37	23	17
Sm	7	9	2	8	3	6	4	6
A/NK	2.81	2.65	2.16	2.21	2.21	2.6	2.68	2.36
A/CNK	1.05	1.08	1.15	1.09	1.14	1.11	1.25	1.07
Nb/Y	0.67	0.3	1.29	0.74	1.38	0.39	0.85	0.4
Zr/TiO2	686	614	611	545	621	415	308	700
Fe*	0.82	0.84	0.66	0.82	0.78	0.78	0.7	0.77
Mali	7.01	6.49	8.78	7.29	8.31	4.24	4.86	7.08
ASI	0.95	0.98	1.06	1.03	1.06	1.12	1.24	0.98
CIA	50.49	51.21	53.31	51.73	52.94	51.34	54.62	51.27

Loi: loss on ignition; n.d.: not determined; b.d.: below detection limit; A/NK: molecular Al2O3/(K2O+Na2O); A/CNK: molecular Al2O3/(CaO+K2O+Na2O); Fe*: FeOtot/(FeOtot+MgO); Mali: Na2O+K2O-CaO; ASI: Al/(Ca-1.67*P+Na+K); CIA: molecular [Al2O3/(Al2O3+CaO+Na2O+K2O)]*100.

XRF orthogneisses – continued

Sample	RH429	RH434	RH441	RH447	RH455
location	Smigada-Mirtiski	Leptokaria-N.Sanda	Nymphea	Sidiro-Gianulli	Sidiro
SiO2	71.36	72.49	71,63	72.17	72.33
TiO2	0.33	0.2	0,26	0.18	0.24
Al2O3	14.86	13.97	14,48	14.6	13.84
Fe2O3	2.38	1.96	2,1	1.46	1.41
MnO	0.03	0.03	0,05	0.03	0.02
MgO	0.59	0.44	0,67	0.38	0.88
CaO	1.76	1.11	1,49	1.22	0.18
Na2O	3.37	3.55	4,41	3.5	2.64
K2O	3.75	4.47	3,25	4.11	3.62
P2O5	0.16	0.09	0,07	0.11	0.07
LOI	1.13	1.44	0,74	1.33	1.95
Sum	98.59	99.754	99,14	97.76	95.23
Sc	6	5	11	16	7
V	30	16	88	50	29
Cr	3	8	6	1	2
Co	b.d.	2	6	4	5
Ni	2	4	3	4	5
Cu	3	1	6	4	1
Zn	63	50	73	91	56
Ga	20	17	22	19	18
Rb	122	124	122	42	190
Sr	234	120	239	202	165
Y	13	8	17	36	16
Zr	144	145	135	164	112
Nb	9	13	18	11	14
Ba	894	543	231	212	566
Pb	25	31	22	5	25
Th	11.6	19.9	10,3	5	9.6
U	3.2	3	2,3	2.2	9.6
La	33	36	20	22	26
Ce	50	62	32	40	35
Pr	3	3	0	7	4
Nd	29	28	14	25	21
Sm	5	5	6	1	5
A/NK	2.72	n.d.	2.03	2.58	3.23
A/CNK	1.2	n.d.	1.1	1.2	1.62
Nb/Y	0.69	n.d.	0.69	0.88	0.31
Zr/TiO2	436	n.d.	348	467	911
Fe*	0.8	n.d.	0.76	0.79	0.62
Mali	5.36	n.d.	6.17	6.39	6.08
ASI	1.16	n.d.	1.1	1.14	1.45
CIA	53.71	n.d.	51.78	54.02	61.70

Loi: loss on ignition; n.d.: not determined; b.d.: below detection limit; A/NK: molecular Al2O3/(K2O+Na2O); A/CNK: molecular Al2O3/(CaO+K2O+Na2O); Fe*: FeOtot/(FeOtot+MgO); Mali: Na2O+K2O-CaO; ASI: Al/(Ca-1.67*P+Na+K); CIA: molecular [Al2O3/(Al2O3+CaO+Na2O+K2O)]*100.

LA-ICPMS orthogneisses, Eastern Rhodope

	RH344	RH345	RH346	RH358	RH360	RH 369	RH 370	RH 375	RH 376	RH 383	RH389	RH434	RH413	RH418	RH423	RH429	RH447
Rb	133.54	76.63	112.22	86.35	155.29	60.93	108.26	88.28	106.10	160.57	177.14	124.84	141.13	128.23	124.46	122.88	122.72
Sr	161.17	76.29	108.13	122.92	197.84	380.30	253.58	177.14	147.75	72.75	78.78	109.12	246.51	203.76	216.43	221.28	106.92
Y	9.28	14.49	43.75	17.80	12.30	8.86	9.43	14.56	9.70	23.51	17.95	6.44	24.35	11.61	7.31	11.04	13.47
Zr	82.38	96.93	159.25	148.98	88.26	36.36	120.36	129.91	279.61	125.31	93.27	113.03	164.91	121.79	90.92	136.81	84.92
Nb	6.46	4.52	5.62	6.36	9.93	3.76	9.13	9.23	6.14	7.31	14.40	9.55	11.13	10.24	2.78	8.17	13.95
Cs	2.19	1.62	1.71	3.43	5.43	1.15	2.90	1.51	3.77	2.38	4.24	2.37	6.53	5.48	0.61	6.62	0.85
Ba	512.70	374.12	668.96	306.70	683.86	1023.50	528.24	439.55	590.64	557.48	276.59	494.73	785.92	528.25	624.09	827.77	453.12
La	18.74	24.36	42.46	21.52	29.21	9.81	21.87	19.84	88.73	60.45	27.70	32.47	38.43	24.35	21.42	29.39	10.90
Ce	37.51	50.31	88.53	40.35	53.82	20.30	41.49	36.03	151.86	128.70	47.02	64.67	75.81	45.36	41.34	55.96	24.60
Pr	4.12	5.42	9.52	4.89	6.65	2.41	4.57	4.26	14.71	13.68	6.02	6.95	8.50	5.40	4.21	6.92	3.49
Nd	14.49	19.89	35.46	18.54	24.16	9.17	17.02	15.65	48.46	49.15	21.83	24.79	32.59	19.68	14.18	25.98	12.62
Sm	3.01	3.86	7.29	3.90	4.74	2.07	3.46	3.28	6.16	8.37	4.54	4.52	6.28	3.74	2.67	5.18	3.29
Eu	0.71	0.76	0.96	0.74	0.97	0.58	0.93	0.62	1.32	0.67	0.49	0.58	1.13	0.72	0.27	1.10	0.50
Gd	2.37	3.17	6.70	3.34	3.46	1.83	2.77	2.79	3.68	5.96	3.78	3.13	4.98	2.85	1.87	3.83	2.69
Tb	0.41	0.47	1.12	0.54	0.56	0.32	0.45	0.45	0.45	0.85	0.59	0.39	0.78	0.40	0.28	0.53	0.53
Dy	1.93	2.71	7.37	3.09	2.59	1.58	2.08	2.59	2.15	4.69	3.25	1.59	4.49	2.31	1.40	2.42	2.85
Ho	0.39	0.53	1.59	0.65	0.52	0.38	0.43	0.57	0.40	0.92	0.63	0.29	0.86	0.44	0.26	0.51	0.63
Er	0.95	1.40	4.29	1.77	1.21	0.90	0.96	1.70	0.97	2.27	1.61	0.66	2.21	1.20	0.71	1.01	1.61
Tm	0.16	0.21	0.66	0.37	0.25	0.19	0.18	0.31	0.19	0.35	0.26	0.12	0.28	0.19	0.12	0.25	0.34
Yb	0.88	1.27	4.21	1.86	1.14	0.82	0.84	2.14	0.90	2.14	1.61	0.69	1.57	1.20	0.84	0.94	1.96
Lu	0.16	0.19	0.61	0.35	0.23	0.15	0.15	0.36	0.17	0.31	0.26	0.14	0.22	0.19	0.14	0.19	0.33
Hf	2.50	2.86	4.69	4.52	2.70	1.15	3.36	3.52	6.35	3.51	2.94	3.23	4.46	3.46	3.11	3.85	2.78
Ta	0.89	0.37	0.44	0.94	1.59	0.53	0.90	0.92	0.40	0.56	1.89	0.59	1.20	0.99	0.38	0.74	0.92
Pb	19.67	6.99	18.81	13.15	19.13	9.73	20.43	15.64	24.50	17.77	10.49	16.66	11.22	10.05	16.83	21.50	16.43
Th	9.28	11.90	19.73	11.71	10.30	3.19	12.49	12.01	10.02	14.35	14.33	16.75	13.67	12.69	33.24	10.54	17.41
U	9.26	1.92	2.51	2.31	4.57	1.34	2.38	2.62	2.53	3.03	4.23	2.49	4.60	2.73	3.14	3.19	7.22

LA-ICPMS metapelites, Eastern Rhodope;

	F157	RH388B	RH412
Rb	99.5	117.9	57.8
Sr	131.5	88.5	67.0
Y	23.8	25.8	39.3
Zr	281.7	240.8	381.9
Nb	9.9	14.3	24.0
Cs	3.3	2.8	0.9
Ba	429.0	442.5	1525.3
La	26.7	31.5	41.7
Ce	53.1	68.8	86.9
Pr	6.2	7.2	9.2
Nd	23.5	27.1	34.7
Sm	4.6	5.1	6.6
Eu	1.0	1.0	1.4
Gd	3.9	4.4	6.4
Tb	0.6	0.7	1.1
Dy	3.8	4.5	7.0
Ho	0.8	0.9	1.4
Er	2.8	2.8	4.2
Tm	0.4	0.4	0.6
Yb	3.1	3.0	4.2
Lu	0.5	0.4	0.6
Hf	7.1	6.3	9.7
Ta	0.7	1.0	2.0
Pb	9.5	5.8	2.4
Th	10.3	12.3	13.2
U	2.0	2.5	1.1

LA-ICPMS orthogneisses, Central Rhodope

	RH11-1	RH60-1	RH78-1	RH89-1	RH330-1	F34-1	F180-2-1	F181-1	F190-1	F216-1
Rb	97.70	139.62	99.46	101.18	78.99	99.87	116.63	114.93	103.00	122.66
Sr	64.82	433.25	607.77	231.77	345.31	363.84	406.75	267.06	338.60	210.98
Y	9.56	17.77	37.41	10.03	19.00	9.13	25.84	5.19	23.66	19.79
Zr	47.75	163.85	141.71	136.74	55.26	174.59	264.85	104.43	226.53	144.96
Nb	3.47	15.08	18.80	6.70	7.67	8.28	9.01	9.76	5.75	9.41
Cs	1.14	1.84	2.10	2.58	1.98	1.18	2.28	2.78	3.75	3.79
Ba	360.07	877.98	1126.44	1036.93	709.08	749.19	709.56	427.70	568.29	484.95
La	22.40	44.53	46.44	35.67	13.48	41.78	15.93	31.65	34.20	23.79
Ce	42.69	83.73	101.73	69.77	28.67	78.71	36.33	63.83	68.52	48.30
Pr	4.67	9.61	12.07	7.57	3.52	8.35	4.22	6.96	7.49	5.50
Nd	16.42	36.14	47.16	28.31	13.74	30.22	21.11	26.65	28.66	21.42
Sm	2.95	6.48	8.92	5.09	3.67	5.08	4.92	4.59	5.48	4.48
Eu	0.53	1.24	1.90	0.92	0.85	1.23	1.29	1.08	1.07	0.91
Gd	1.50	4.65	7.01	3.42	3.35	3.37	3.47	3.24	4.78	4.06
Tb	0.32	0.63	1.04	0.43	0.57	0.39	0.69	0.34	0.73	0.63
Dy	1.73	3.47	6.28	2.08	3.47	1.96	4.11	1.46	4.44	3.73
Ho	0.36	0.64	1.30	0.35	0.72	0.32	0.81	0.23	0.88	0.75
Er	0.88	1.73	3.86	0.85	2.01	0.77	2.14	0.46	2.33	1.92
Tm	0.15	0.25	0.59	0.12	0.30	0.13	0.33	0.07	0.31	0.27
Yb	1.03	1.58	3.97	0.76	1.87	0.79	2.03	0.46	1.88	1.69
Lu	0.12	0.23	0.59	0.11	0.28	0.12	0.31	0.10	0.27	0.26
Hf	1.46	4.16	3.93	3.91	1.49	4.69	5.28	2.98	5.63	4.12
Ta	0.61	1.49	2.21	0.63	0.61	0.62	0.60	0.70	0.47	0.84
Pb	10.12	14.44	12.74	19.13	24.26	9.24	14.48	8.99	18.32	13.74
Th	11.97	15.41	16.63	12.31	5.68	18.66	5.87	11.65	8.70	10.52
U	1.19	3.48	5.07	1.59	1.53	2.06	1.39	3.06	2.32	5.69

Appendix E – U-Pb LA-ICPMS zircon data of metapelite F157, Eastern Rhodope

						Isotopic ratios						Apparent ages (Ma)							
Analysis No.	^{207}Pb (cps)	U[a] (ppm)	Pb[a] (ppm)	Th (ppm)	Th[c] U	^{207}Pb[e] ^{235}U	2 s %	^{206}Pb[e] ^{238}U	2 s %	rho	^{207}Pb[e] ^{206}Pb	2 s %	^{207}Pb ^{235}U	2 s (Ma)	^{206}Pb ^{238}U	2 s (Ma)	^{207}Pb ^{206}Pb	2 s (Ma)	Conc (%)
33	1442	64	2	51	0.78	0.1944	5.9	0.0240	3.6	0.61	0.0588	4.7	180	11	153	6	558	51	85
34	1823	76	3	89	1.17	0.2733	7.8	0.0387	6.3	0.80	0.0512	4.7	245	19	245	15	252	54	100
35	2584	212	5	67	0.31	0.1527	3.4	0.0216	2.1	0.61	0.0512	2.7	144	5	138	3	251	31	96
36	4967	345	5	12	0.04	0.0927	17.2	0.0146	2.8	0.17	0.0461	16.9	90	15	93	3	2	204	104
37	2330	64	4	207	3.21	0.3135	5.0	0.0394	3.1	0.61	0.0578	3.9	277	14	249	8	520	43	90
38	2444	149	3	123	0.82	0.1438	3.9	0.0180	2.7	0.68	0.0579	2.9	136	5	115	3	526	32	84
39	4455	324	6	10	0.03	0.1365	5.5	0.0178	2.5	0.46	0.0557	4.9	130	7	114	3	440	54	87
40	2610	99	5	354	3.59	0.9997	22.6	0.0434	11.1	0.49	0.1671	19.7	704	159	274	30	2529	165	39
41	4196	68	5	128	1.87	0.5916	41.1	0.0444	6.6	0.16	0.0967	40.6	472	194	280	19	1561	381	59
46	3179	73	4	139	1.91	0.2560	4.4	0.0355	1.8	0.42	0.0523	4.0	231	10	225	4	301	45	97
47	2327	389	3	41	0.11	0.0504	5.2	0.0074	2.6	0.50	0.0493	4.5	50	3	48	1	164	53	95
48	2555	249	3	22	0.09	0.1091	8.3	0.0139	4.9	0.59	0.0567	6.7	105	9	89	4	481	74	85
49	4742	61	3	116	1.88	0.1986	4.7	0.0272	3.4	0.73	0.0530	3.2	184	9	173	6	327	37	94
50	5155	344	6	107	0.31	0.1391	6.3	0.0177	2.1	0.33	0.0570	6.0	132	8	113	2	490	66	86
51	4415	18	1	41	2.24	0.1490	4.4	0.0228	2.3	0.53	0.0474	3.7	141	6	145	3	69	44	103
54	1793	224	2	168	0.75	0.0623	7.0	0.0093	6.3	0.90	0.0487	3.1	61	4	60	4	133	36	97
55	1787	71	3	89	1.26	0.2090	6.9	0.0290	5.8	0.84	0.0523	3.7	193	13	184	11	297	42	96
59	3543	312	5	21	0.07	0.1055	4.3	0.0147	2.6	0.61	0.0521	3.4	102	4	94	2	291	39	92
60	2571	179	4	75	0.42	0.1412	5.0	0.0194	2.1	0.41	0.0528	4.6	134	7	124	3	321	52	92
61	4358	385	7	75	0.20	0.1088	11.6	0.0168	2.2	0.19	0.0471	11.4	105	12	107	2	53	136	102
62	3376	155	4	62	0.40	0.1479	6.6	0.0214	1.9	0.29	0.0501	6.3	140	9	137	3	200	73	97
63	1150	79	2	14	0.18	0.1828	8.7	0.0259	2.2	0.25	0.0511	8.4	170	15	165	4	247	97	97
64	1735	399	2	8	0.02	0.0454	4.5	0.0066	2.9	0.64	0.0500	3.4	45	2	42	1	193	40	94
65	1831	91	3	81	0.89	0.2277	4.2	0.0322	1.9	0.45	0.0513	3.7	208	9	204	4	255	43	98
66	1359	43	1	42	0.98	0.2102	6.0	0.0270	2.8	0.46	0.0564	5.4	194	12	172	5	469	59	89
67	3806	449	6	20	0.04	0.0959	3.1	0.0141	1.9	0.61	0.0494	2.4	93	3	90	2	165	29	97
72	4626	92	4	203	2.19	0.2635	4.8	0.0359	3.5	0.74	0.0532	3.2	238	11	228	8	337	37	96
73	4202	215	8	233	1.09	0.2220	3.6	0.0299	2.0	0.56	0.0539	3.0	204	7	190	4	367	34	93
74	959	21	1	33	1.54	0.2671	7.4	0.0370	3.5	0.47	0.0524	6.5	240	18	234	8	301	74	97
75	2223	83	4	125	1.51	0.2578	4.5	0.0359	2.6	0.58	0.0521	3.7	233	10	227	6	289	42	98
76	701	5	0	12	2.52	0.2640	26.2	0.0368	7.3	0.28	0.0520	25.1	238	62	233	17	284	287	98
77	3318	81	4	111	1.38	0.2398	6.0	0.0331	3.1	0.51	0.0526	5.2	218	13	210	6	311	59	96

Appendix E continued – U-Pb LA-ICPMS zircon data of metapelite F157, Eastern Rhodope

						Isotopic ratios						Apparent ages (Ma)							
Analysis No.	^{207}Pb (cps)	U^{a} (ppm)	Pb^{a} (ppm)	Th (ppm)	Th^{c} U	^{207}Pb^{e} ^{235}U	2 s %	^{206}Pb^{e} ^{238}U	2 s %	rho	^{207}Pb^{e} ^{206}Pb	2 s %	^{207}Pb ^{235}U	2 s (Ma)	^{206}Pb ^{238}U	2 s (Ma)	^{207}Pb ^{206}Pb	2 s (Ma)	Conc (%)
78	2493	180	5	101	0.56	0.1771	4.5	0.0244	2.8	0.62	0.0526	3.5	166	7	156	4	310	40	94
79	3254	376	4	24	0.06	0.0719	7.6	0.0114	2.5	0.32	0.0459	7.2	71	5	73	2	-7	87	103
80	1212	20	1	37	1.89	0.3360	6.0	0.0440	3.8	0.63	0.0554	4.6	294	18	278	10	427	52	94
81	2362	127	3	125	0.98	0.1388	5.6	0.0198	2.3	0.41	0.0508	5.1	132	7	126	3	233	59	96
85	1962	429	3	28	0.07	0.0425	4.9	0.0064	2.1	0.43	0.0479	4.4	42	2	41	1	92	52	98
86	2628	152	5	75	0.50	0.2442	4.5	0.0314	2.7	0.61	0.0565	3.6	222	10	199	5	471	39	90

U-Pb SHRIMP-II zircon data

Orthogneisses RH373, RH346 Isotopic rations Apparent ages (Ma)

Spot name	% comm 206	ppm U	ppm Th	232Th /238U	ppm rad 206Pb	total 207 /206	% err	207r /235	% err	206r /238	% err	206Pb /238U	1s err	207Pb /206Pb	1s err
RH373.1.1	-0.13	1339	258	0.20	60.1	.0536	0.8	0.39	1.9	.0523	1.4	328.6	4.5	400	29
RH373.2.1	0.08	1558	308	0.20	68.5	.0528	1.1	0.37	1.9	.0512	1.4	321.6	4.4	290	28
RH373.3.1	0.36	370	159	0.44	15.8	.0549	2.2	0.35	3.8	.0494	1.6	310.8	4.7	288	78
RH373.4.1	0.08	2151	185	0.09	95.8	.0534	0.9	0.38	1.8	.0518	1.4	325.6	4.4	317	27
RH373.5.1	-0.13	1388	360	0.27	62.4	.0528	1.0	0.39	1.9	.0524	1.4	329.1	4.5	365	30
RH346.1.1	0.31	318	240	0.78	29.3	.0629	1.3	0.89	2.6	.1068	1.5	654.0	9.2	615	45
RH346.1.2	0.29	141	64	0.47	12.9	.0624	1.9	0.88	3.7	.1063	1.7	651.1	10.5	604	71
RH346.1.3	0.04	993	162	0.17	58.6	.0559	0.9	0.53	1.8	.0687	1.4	428.1	5.9	435	23
RH346.2.1	0.05	765	348	0.47	44.4	.0567	1.1	0.52	1.8	.0675	1.4	420.9	5.8	464	26
RH346.3.1	0.03	1175	328	0.29	78.8	.0567	1.0	0.61	1.8	.0781	1.4	484.8	6.5	469	25
RH346.4.1	0.00	105	65	0.64	6.8	.0576	2.7	0.60	3.2	.0757	1.7	470.2	7.9	514	60
RH346.5.1	0.09	360	99	0.28	23.9	.0560	1.5	0.59	2.3	.0770	1.5	478.3	6.8	424	39
RH346.5.2	0.12	907	18	0.02	43.5	.0547	1.3	0.41	2.3	.0557	1.4	349.6	4.9	359	40
RH346.6.1	0.27	729	70	0.10	38.4	.0558	1.2	0.45	2.4	.0611	1.4	382.5	5.3	355	43
RH346.7.1	0.35	680	31	0.05	28.9	.0548	1.4	0.35	3.7	.0492	1.5	309.9	4.5	283	78

Appendix E continued– U-Pb LA-ICPMS zircon data orthogneisses

					Isotopic ratios							Apparent ages						
	Ua	Pba	Tha	Thc	207Pbb	1 s	206Pbb	1 s	rho	207Pbb	1 s	207Pb	2 s	206Pb	2 s	207Pb	2 s	Concc
	(ppm)	(ppm)	(ppm)	U	235U	%	238U	%		206Pb	%	235U	(Ma)	238U	(Ma)	206Pb	(Ma)	(%)
RH344	237	9	29	0.12	0.238	5.6	0.0329	5.4	0.97	0.0525	1.5	217	24	209	23	309	33	96
	105	5	107	1.02	0.301	2.8	0.0415	2.5	0.89	0.0526	1.3	267	15	262	13	310	29	98
	86	5	81	0.95	0.325	2.1	0.0459	1.6	0.75	0.0513	1.4	285	12	289	9	256	32	101
	130	7	83	0.64	0.389	1.7	0.0535	1.4	0.80	0.0528	1.0	334	11	336	9	320	24	101
	143	8	127	0.89	0.357	2.4	0.0473	1.9	0.76	0.0548	1.6	310	15	298	11	406	35	96
	1111	45	409	0.37	0.292	2.7	0.0399	2.5	0.92	0.0531	1.1	260	14	252	13	333	25	97
	135	7	102	0.75	0.329	3.1	0.0452	2.1	0.68	0.0528	2.2	289	18	285	12	322	51	99
	102	6	119	1.17	0.347	3.1	0.0469	2.3	0.75	0.0536	2.0	302	18	296	14	355	46	98
	101	6	87	0.86	0.360	3.6	0.0491	2.4	0.67	0.0532	2.7	313	23	309	15	337	61	99
	78	4	87	1.11	0.339	3.0	0.0463	2.2	0.75	0.0531	2.0	296	18	292	13	331	45	99
	131	7	112	0.86	0.328	2.6	0.0452	1.7	0.67	0.0526	1.9	288	15	285	10	313	44	99
	114	7	121	1.07	0.371	2.3	0.0494	1.6	0.70	0.0545	1.6	321	15	311	10	391	37	97
	169	9	177	1.05	0.340	2.8	0.0466	1.9	0.66	0.0529	2.1	297	17	293	11	324	49	99
	173	8	83	0.48	0.324	2.9	0.0445	2.2	0.77	0.0528	1.9	285	17	281	13	319	43	99
	83	5	98	1.18	0.350	2.9	0.0480	2.2	0.75	0.0530	1.9	305	18	302	13	328	44	99
	87	5	105	1.20	0.357	2.5	0.0492	1.3	0.54	0.0526	2.1	310	15	309	8	312	47	100
	85	5	113	1.32	0.377	2.0	0.0473	1.4	0.68	0.0578	1.5	325	13	298	8	521	32	92
	103	5	76	0.74	0.322	2.6	0.0453	2.1	0.82	0.0517	1.5	284	15	285	12	270	34	101
	133	7	107	0.80	0.357	2.4	0.0489	1.7	0.73	0.0530	1.7	310	15	308	11	327	37	99
	194	10	117	0.61	0.350	1.8	0.0485	1.3	0.73	0.0524	1.2	305	11	305	8	303	27	100
	432	17	136	0.31	0.287	2.1	0.0387	1.7	0.80	0.0538	1.3	256	11	245	8	362	28	96
	333	17	210	0.63	0.394	2.0	0.0481	1.3	0.62	0.0595	1.6	338	14	303	8	585	35	90
	2159	99	339	0.16	0.352	1.8	0.0466	1.1	0.62	0.0548	1.4	306	11	293	7	403	32	96
	101	5	80	0.79	0.404	3.0	0.0412	2.3	0.76	0.0712	2.0	345	21	260	12	962	40	75
	116	7	134	1.15	0.348	2.0	0.0475	1.6	0.79	0.0531	1.3	303	12	299	10	334	29	99
	1443	70	112	0.08	0.382	1.4	0.0525	1.2	0.87	0.0528	0.7	329	9	330	8	320	16	100
	966	45	300	0.31	0.345	1.6	0.0471	1.2	0.76	0.0531	1.0	301	10	297	7	331	23	99

Appendix E continued– U-Pb LA-ICPMS zircon data orthogneisses

					Isotopic ratios							Apparent ages						
	Ua	Pba	Tha	Thc	207Pbb	1 s	206Pbb	1 s	rho	207Pbb	1 s	207Pb	2 s	206Pb	2 s	207Pb	2 s	Concc
	(ppm)	(ppm)	(ppm)	U	235U	%	238U	%		206Pb	%	235U	(Ma)	238U	(Ma)	206Pb	(Ma)	(%)
RH344	966	45	300	0.31	0.345	1.6	0.0471	1.2	0.76	0.0531	1.0	301	10	297	7	331	23	99
	80	5	124	1.56	0.342	2.2	0.0461	1.5	0.69	0.0538	1.6	299	13	291	9	363	37	97
	541	27	350	0.65	0.349	2.5	0.0478	2.0	0.79	0.0529	1.6	304	15	301	12	325	36	99
	192	10	120	0.62	0.339	2.7	0.0467	2.2	0.80	0.0527	1.6	297	16	294	13	318	37	99
RH345	162	11	111	0.69	0.549	5.6	0.0622	3.7	0.65	0.0640	4.3	444	50	389	28	741	90	88
	96	8	78	0.81	0.534	2.6	0.0693	2.0	0.74	0.0559	1.8	435	23	432	17	449	39	99
	609	25	91	0.15	0.318	2.5	0.0440	2.1	0.83	0.0525	1.4	281	14	278	12	305	32	99
	185	14	109	0.59	0.593	2.9	0.0736	2.2	0.77	0.0584	1.8	472	27	458	20	545	40	97
	348	32	338	0.97	0.580	2.4	0.0754	2.0	0.84	0.0558	1.3	465	22	469	19	445	29	101
	284	16	56	0.20	0.449	2.3	0.0581	2.0	0.88	0.0561	1.1	377	17	364	15	455	24	97
	383	26	114	0.30	0.544	2.2	0.0700	1.7	0.78	0.0564	1.4	441	19	436	15	469	30	99
	121	12	174	1.44	0.644	2.0	0.0830	1.2	0.60	0.0563	1.6	505	20	514	12	463	35	102
	120	9	72	0.60	0.534	2.0	0.0681	1.6	0.82	0.0568	1.1	434	17	425	14	485	25	98
	276	46	167	0.61	1.565	1.8	0.1589	1.5	0.82	0.0714	1.0	957	35	951	29	970	21	99
	329	25	187	0.57	0.590	3.9	0.0723	2.1	0.53	0.0592	3.3	471	37	450	19	575	72	96
	462	35	362	0.78	0.511	1.7	0.0680	1.1	0.67	0.0545	1.3	419	14	424	10	392	29	101
	137	11	64	0.46	0.625	4.1	0.0745	3.1	0.75	0.0609	2.7	493	40	463	28	634	58	94
	184	52	88	0.48	4.762	2.8	0.2655	2.0	0.72	0.1301	1.9	1778	98	1518	61	2099	33	85
	483	22	85	0.18	0.336	2.7	0.0465	2.1	0.79	0.0524	1.6	294	16	293	13	303	38	100
	815	60	245	0.30	0.593	3.2	0.0763	2.5	0.78	0.0563	2.0	473	30	474	23	465	44	100
	397	20	18	0.05	0.487	3.2	0.0515	1.4	0.45	0.0687	2.8	403	26	324	9	889	59	80

Appendix E continued– U-Pb LA-ICPMS zircon data orthogneisses

					Isotopic ratios						Apparent ages						
	Ua (ppm)	Pba (ppm)	Tha (ppm)	Thc U	207Pbb 235U	1 s %	206Pbb 238U	1 s %	rho	207Pbb 206Pb	1 s %	207Pb 235U	2 s (Ma)	206Pb 238U	2 s (Ma)	207Pb 206Pb	2 s (Ma)	Concc (%)
RH345	715	33	66	0.09	0.357	1.9	0.0486	1.4	0.74	0.0532	1.3	310	12	306	9	337	29	99
	427	32	149	0.35	0.570	2.2	0.0748	1.6	0.74	0.0553	1.5	458	20	465	15	423	32	102
	115	10	179	1.56	0.569	2.6	0.0730	2.0	0.77	0.0566	1.7	457	24	454	18	475	37	99
	998	78	371	0.37	0.648	1.9	0.0758	1.4	0.74	0.0620	1.3	507	20	471	14	674	28	93
	141	11	41	0.29	0.598	2.1	0.0771	1.6	0.75	0.0563	1.4	476	20	479	15	464	31	101
	406	29	364	0.89	0.506	3.1	0.0658	2.7	0.87	0.0558	1.5	416	26	411	22	443	34	99
	646	46	308	0.48	0.510	3.3	0.0657	3.0	0.92	0.0563	1.2	418	27	410	25	464	28	98
	626	28	571	0.91	0.334	2.0	0.0462	1.8	0.90	0.0524	0.9	292	12	291	11	303	21	100
	298	23	122	0.41	0.600	1.9	0.0771	1.7	0.89	0.0565	0.9	477	18	479	16	471	19	100
	215	17	156	0.72	0.600	2.7	0.0746	1.9	0.69	0.0583	2.0	477	26	464	18	541	43	97

	Ua (ppm)	Pba (ppm)	Tha (ppm)	Thc U	207Pbb 235U	1 s %	206Pbb 238U	1 s %	rho	207Pbb 206Pb	1 s %	207Pb 235U	2 s (Ma)	206Pb 238U	2 s (Ma)	207Pb 206Pb	2 s (Ma)	Concc (%)
RH346	239	22	132	0.55	0.700	1.4	0.0859	1.2	0.87	0.0592	0.7	539	15	531	13	573	15	99
	291	21	80	0.28	0.581	1.3	0.0747	1.2	0.89	0.0564	0.6	465	13	464	11	469	14	100
	420	27	141	0.34	0.499	3.8	0.0636	3.6	0.97	0.0569	0.9	411	31	397	29	488	20	97
	141	11	69	0.49	0.613	1.9	0.0782	1.6	0.87	0.0568	0.9	485	18	486	16	484	20	100
	188	14	69	0.37	0.582	1.8	0.0736	1.5	0.88	0.0574	0.8	466	16	458	14	508	18	98
	234	23	140	0.60	0.728	1.7	0.0877	1.5	0.85	0.0602	0.9	555	19	542	16	611	19	98
	134	16	113	0.85	0.871	2.0	0.1011	1.7	0.85	0.0624	1.1	636	25	621	21	690	23	98
	323	24	90	0.28	0.583	2.1	0.0742	1.7	0.83	0.0570	1.1	466	19	461	16	491	25	99
	397	32	136	0.34	0.487	2.4	0.0614	1.9	0.81	0.0575	1.4	403	19	384	15	513	31	95
	268	15	77	0.29	0.419	2.0	0.0558	1.5	0.77	0.0544	1.3	355	14	350	11	390	29	99

Appendix E continued– U-Pb LA-ICPMS zircon data orthogneisses

					Isotopic ratios						Apparent ages						
	Ua	Pba	Tha	Thc	207Pbb	1 s	206Pbb	1 s	rho	207Pbb	1 s	207Pb	2 s	206Pb	2 s	207Pb	2 s	Concc
	(ppm)	(ppm)	(ppm)	U	235U	%	238U	%		206Pb	%	235U	(Ma)	238U	(Ma)	206Pb	(Ma)	(%)
RH360	951	48	348	0.37	0.352	3.0	0.0472	2.4	0.79	0.0540	1.8	306	18	298	14	373	41	97
	2183	94	48	0.02	0.342	2.2	0.0469	1.8	0.85	0.0529	1.1	299	13	295	11	325	26	99
	851	42	357	0.42	0.351	2.5	0.0486	2.0	0.80	0.0523	1.5	305	15	306	12	299	34	100
	1239	59	199	0.16	0.368	2.3	0.0494	2.0	0.85	0.0540	1.2	318	15	311	12	372	28	98
	33	3	79	2.38	0.312	4.1	0.0421	3.1	0.76	0.0538	2.7	276	23	266	17	362	60	96
	119	17	65	0.55	1.241	2.9	0.1375	2.3	0.78	0.0655	1.8	819	48	831	38	789	39	101
	1819	69	65	0.04	0.314	4.8	0.0404	4.5	0.93	0.0564	1.8	277	27	255	23	470	39	92
	728	31	380	0.52	0.287	4.8	0.0399	4.5	0.94	0.0521	1.7	256	25	252	23	289	38	99
	195	12	234	1.20	0.367	2.5	0.0502	1.9	0.75	0.0531	1.7	318	16	316	12	332	38	99
	148	8	201	1.35	0.340	5.0	0.0435	4.6	0.91	0.0567	2.0	297	30	274	25	479	45	92
	30	2	53	1.73	0.356	2.9	0.0466	2.4	0.80	0.0554	1.8	309	18	294	14	428	39	95
	110	8	70	0.63	0.473	2.4	0.0627	1.7	0.71	0.0547	1.7	393	19	392	14	401	38	100
	16	2	57	3.46	0.314	4.4	0.0418	2.3	0.53	0.0545	3.7	277	24	264	12	394	84	95
	246	17	116	0.47	0.543	3.8	0.0661	3.4	0.88	0.0596	1.8	440	34	413	28	588	39	94
	138	7	106	0.77	0.330	3.3	0.0454	2.4	0.75	0.0527	2.2	289	19	286	14	317	49	99
	470	24	210	0.45	0.351	2.1	0.0477	1.4	0.70	0.0534	1.5	306	13	300	9	346	34	98
	844	41	293	0.35	0.354	2.0	0.0491	1.7	0.83	0.0523	1.1	308	13	309	10	298	26	100
	334	18	72	0.22	0.390	2.8	0.0526	2.1	0.75	0.0537	1.8	334	19	331	14	360	41	99
	371	18	229	0.62	0.340	2.6	0.0467	1.9	0.73	0.0529	1.8	298	16	294	11	323	41	99
	2830	87	585	0.21	0.258	3.2	0.0322	2.7	0.85	0.0581	1.7	233	15	204	11	532	37	88
	800	35	266	0.33	0.320	2.6	0.0435	2.2	0.84	0.0532	1.4	282	15	275	12	339	32	98
	729	36	213	0.29	0.366	2.8	0.0503	2.2	0.79	0.0528	1.7	317	18	316	14	319	40	100
	329	16	154	0.47	0.347	2.5	0.0480	2.0	0.79	0.0524	1.5	302	15	302	12	303	35	100
	991	45	154	0.16	0.353	2.3	0.0477	1.6	0.70	0.0537	1.6	307	14	301	10	359	36	98

Appendix E continued– U-Pb LA-ICPMS zircon data orthogneisses

					Isotopic ratios						Apparent ages						
	Ua	Pba	Tha	Thc	207Pbb	1 s	206Pbb	1 s	rho	207Pbb	1 s	207Pb	2 s	206Pb	2 s	207Pb	2 s	Concc
	(ppm)	(ppm)	(ppm)	U	235U	%	238U	%		206Pb	%	235U	(Ma)	238U	(Ma)	206Pb	(Ma)	(%)
RH360	319	15	178	0.56	0.350	4.0	0.0409	2.4	0.60	0.0621	3.2	305	24	258	12	676	68	85
	221	9	87	0.39	0.307	6.2	0.0384	4.9	0.79	0.0580	3.8	272	34	243	24	529	83	89
	786	47	253	0.32	0.402	4.7	0.0545	4.5	0.95	0.0535	1.5	343	33	342	31	350	34	100
	63	4	15	0.23	0.491	4.9	0.0544	2.3	0.47	0.0655	4.3	406	40	341	16	790	91	84
RH367	577	33	222	0.38	0.430	3.9	0.0590	3.6	0.94	0.0529	1.3	363	28	369	27	323	30	102
	991	44	249	0.25	0.328	2.2	0.0456	1.9	0.88	0.0522	1.0	288	13	288	11	293	23	100
	2415	114	163	0.07	0.327	1.7	0.0451	1.5	0.91	0.0525	0.7	287	10	284	9	308	16	99
	227	9	67	0.30	0.310	1.9	0.0408	1.5	0.80	0.0551	1.1	274	10	258	8	415	25	94
	1264	57	338	0.27	0.335	1.6	0.0465	1.4	0.87	0.0522	0.8	293	10	293	8	295	18	100
	1615	77	281	0.17	0.347	1.4	0.0480	1.3	0.91	0.0524	0.6	302	8	302	8	302	13	100
	1132	51	142	0.13	0.346	1.3	0.0480	1.2	0.92	0.0523	0.5	302	8	302	7	300	11	100
	116	6	131	1.13	0.344	1.7	0.0474	1.4	0.81	0.0526	1.0	300	10	299	8	312	23	99
	1402	65	413	0.29	0.343	1.3	0.0475	1.1	0.83	0.0524	0.7	300	8	299	6	305	16	100
	865	42	595	0.69	0.342	1.4	0.0478	1.3	0.88	0.0520	0.7	299	9	301	8	284	16	101
	331	18	264	0.80	0.367	1.9	0.0502	1.4	0.70	0.0530	1.4	317	12	316	9	329	31	100
	324	15	94	0.29	0.404	6.9	0.0489	6.1	0.88	0.0599	3.2	345	48	308	38	601	70	89
	122	7	182	1.49	0.343	1.7	0.0475	1.3	0.74	0.0524	1.2	300	10	299	8	303	27	100
	104	6	129	1.25	0.331	1.9	0.0461	1.5	0.76	0.0521	1.3	290	11	290	9	290	29	100
	310	15	224	0.72	0.338	1.6	0.0467	1.3	0.85	0.0525	0.8	296	9	294	8	307	19	100
	1066	51	294	0.28	0.353	1.2	0.0493	1.1	0.92	0.0519	0.5	307	7	310	7	283	11	101
	499	25	409	0.82	0.335	1.4	0.0467	1.1	0.81	0.0520	0.8	293	8	294	6	285	18	100
	1001	46	232	0.23	0.350	1.7	0.0483	1.2	0.74	0.0525	1.1	304	10	304	7	306	26	100

Appendix E continued– U-Pb LA-ICPMS zircon data orthogneisses

					Isotopic ratios						Apparent ages						
	Ua	Pba	Tha	Thc	207Pbb	1 s	206Pbb	1 s	rho	207Pbb	1 s	207Pb	2 s	206Pb	2 s	207Pb	2 s	Concc
	(ppm)	(ppm)	(ppm)	U	235U	%	238U	%		206Pb	%	235U	(Ma)	238U	(Ma)	206Pb	(Ma)	(%)
RH367	1623	74	507	0.31	0.333	1.6	0.0464	1.4	0.87	0.0520	0.8	292	9	292	8	287	18	100
	1370	67	401	0.29	0.366	1.3	0.0504	1.2	0.91	0.0527	0.6	317	8	317	8	317	13	100
	225	12	248	1.10	0.335	1.5	0.0465	1.2	0.78	0.0523	0.9	293	9	293	7	296	21	100
	3021	151	138	0.05	0.364	1.6	0.0513	1.4	0.93	0.0514	0.6	315	10	322	9	259	14	102
	407	17	82	0.20	0.330	1.6	0.0450	1.4	0.85	0.0531	0.9	289	9	284	8	334	20	98
	1599	77	471	0.29	0.367	1.5	0.0503	1.2	0.81	0.0530	0.9	318	9	316	8	327	20	100
	1163	56	314	0.27	0.330	1.4	0.0457	1.2	0.88	0.0523	0.6	289	8	288	7	299	15	100
RH369	457	31	81	0.18	0.542	1.4	0.0713	1.2	0.84	0.0552	0.8	440	13	444	11	419	17	101
	50	3	62	1.23	0.418	1.7	0.0570	1.1	0.61	0.0532	1.4	355	12	357	8	338	31	101
	224	11	50	0.22	0.372	1.6	0.0493	1.2	0.74	0.0547	1.1	321	11	310	8	398	25	97
	117	7	22	0.19	0.448	1.7	0.0582	1.2	0.74	0.0558	1.1	376	12	365	9	445	25	97
	118	6	32	0.27	0.355	3.5	0.0459	1.6	0.45	0.0562	3.1	309	22	289	9	459	70	94
	128	7	40	0.31	0.447	1.6	0.0582	1.1	0.68	0.0558	1.2	376	12	364	8	444	27	97
	488	25	139	0.29	0.392	1.8	0.0521	1.6	0.89	0.0546	0.8	336	12	328	11	395	18	97
	1490	74	175	0.12	0.396	1.3	0.0533	1.1	0.88	0.0539	0.6	339	9	335	7	369	13	99
	193	15	104	0.54	0.575	2.0	0.0737	1.9	0.94	0.0565	0.7	461	19	459	17	472	15	99
	107	6	112	1.04	0.415	2.3	0.0560	1.4	0.60	0.0537	1.8	352	16	351	10	358	41	100
	109	16	50	0.46	1.694	3.0	0.1350	1.8	0.60	0.0910	2.4	1006	59	816	29	1447	45	81
	612	29	177	0.29	0.361	2.0	0.0494	1.8	0.90	0.0531	0.9	313	12	311	11	331	19	99
	568	29	28	0.05	0.406	2.6	0.0543	2.5	0.94	0.0542	0.9	346	18	341	17	380	20	99
	70	6	62	0.89	0.619	1.9	0.0779	1.4	0.72	0.0577	1.3	489	19	483	13	518	29	99
	1126	53	78	0.07	0.384	1.9	0.0496	1.5	0.82	0.0561	1.1	330	12	312	10	456	24	95
	689	68	325	0.47	0.799	2.1	0.0973	1.9	0.91	0.0595	0.9	596	25	599	23	586	19	100
	1078	49	67	0.06	0.361	1.4	0.0495	1.3	0.93	0.0529	0.5	313	9	311	8	326	12	99

Appendix E continued– U-Pb LA-ICPMS zircon data orthogneisses

					Isotopic ratios							Apparent ages						
	Ua	Pba	Tha	Thc	207Pbb	1 s	206Pbb	1 s	rho	207Pbb	1 s	207Pb	2 s	206Pb	2 s	207Pb	2 s	Concc
	(ppm)	(ppm)	(ppm)	U	235U	%	238U	%		206Pb	%	235U	(Ma)	238U	(Ma)	206Pb	(Ma)	(%)
RH369	115	6	41	0.36	0.407	2.0	0.0554	1.5	0.76	0.0533	1.3	346	14	347	10	340	29	100
	123	7	86	0.69	0.413	1.9	0.0552	1.2	0.66	0.0543	1.4	351	13	346	9	382	31	99
	49	3	48	0.98	0.379	2.0	0.0501	1.4	0.73	0.0549	1.4	326	13	315	9	406	30	97
	57	35	99	1.74	13.695	1.9	0.4349	1.7	0.88	0.2284	0.9	2729	104	2328	78	3041	15	85
	494	24	47	0.09	0.378	1.5	0.0517	1.2	0.80	0.0530	0.9	325	10	325	8	330	20	100
	309	17	120	0.39	0.420	1.7	0.0554	1.5	0.84	0.0549	0.9	356	12	348	10	408	21	98
	54	3	62	1.15	0.408	2.6	0.0513	1.9	0.73	0.0576	1.8	347	18	323	12	516	39	93
	425	22	63	0.15	0.409	1.4	0.0552	1.2	0.82	0.0538	0.8	348	10	346	8	363	18	99
RH370	43	17	39	0.89	5.611	1.6	0.3309	1.3	0.83	0.1230	0.9	1918	62	1843	50	2000	16	96
	2033	96	115	0.06	0.331	1.7	0.0456	1.4	0.84	0.0528	0.9	291	10	287	8	318	21	99
	318	16	165	0.52	0.346	1.4	0.0475	1.2	0.84	0.0528	0.7	301	8	299	7	320	17	99
	337	17	188	0.56	0.374	1.4	0.0495	1.1	0.81	0.0548	0.8	323	9	311	7	405	18	97
	815	40	246	0.30	0.368	1.2	0.0505	1.1	0.85	0.0528	0.7	318	8	317	7	322	15	100
	894	45	218	0.24	0.380	1.6	0.0522	1.4	0.87	0.0527	0.8	327	10	328	9	316	18	100
	1123	59	376	0.33	0.383	1.6	0.0530	1.4	0.88	0.0524	0.8	329	10	333	9	303	17	101
	2375	114	809	0.34	0.367	1.3	0.0507	1.2	0.94	0.0524	0.4	317	8	319	8	305	10	101
	785	38	235	0.30	0.357	1.5	0.0494	1.3	0.88	0.0524	0.7	310	9	311	8	302	16	100
	389	19	153	0.39	0.377	1.7	0.0498	1.3	0.78	0.0549	1.1	325	11	313	8	410	24	96
RH373	656	31	154	0.24	0.350	1.4	0.0477	1.2	0.89	0.0532	0.6	305	8	300	7	337	14	99
	969	48	117	0.12	0.338	2.2	0.0440	2.1	0.94	0.0558	0.7	296	13	277	12	444	16	94
	413	20	112	0.27	0.352	1.4	0.0484	1.1	0.82	0.0528	0.8	307	8	304	7	322	18	99
	582	31	183	0.32	0.362	1.4	0.0494	1.2	0.86	0.0530	0.7	313	9	311	7	330	16	99
	442	22	111	0.25	0.378	1.5	0.0512	1.2	0.79	0.0536	0.9	326	10	322	8	354	21	99
	82	5	62	0.75	0.364	1.5	0.0501	1.2	0.74	0.0527	1.0	315	10	315	7	315	24	100
	488	18	104	0.21	0.307	5.4	0.0349	5.0	0.92	0.0639	2.1	272	30	221	22	737	45	81
	313	16	93	0.30	0.369	1.4	0.0510	1.2	0.81	0.0525	0.8	319	9	321	7	306	19	101

Appendix E continued– U-Pb LA-ICPMS zircon data orthogneisses

					Isotopic ratios						Apparent ages						
	Ua	Pba	Tha	Thc	207Pbb	1 s	206Pbb	1 s	rho	207Pbb	1 s	207Pb	2 s	206Pb	2 s	207Pb	2 s	Concc
	(ppm)	(ppm)	(ppm)	U	235U	%	238U	%		206Pb	%	235U	(Ma)	238U	(Ma)	206Pb	(Ma)	(%)
RH373	313	16	93	0.30	0.369	1.4	0.0510	1.2	0.81	0.0525	0.8	319	9	321	7	306	19	101
	551	26	106	0.19	0.354	1.3	0.0484	1.1	0.87	0.0530	0.6	308	8	305	7	330	14	99
	356	18	114	0.32	0.358	1.5	0.0488	1.2	0.83	0.0532	0.8	311	9	307	8	338	18	99
RH383	324	13	962	2.97	0.272	1.5	0.0380	1.2	0.81	0.0519	0.9	244	8	240	6	281	21	98
	253	11	188	0.74	0.265	1.6	0.0378	1.2	0.70	0.0509	1.2	239	8	239	6	238	27	100
	300	38	308	1.03	0.280	1.6	0.0393	1.2	0.72	0.0517	1.1	251	8	249	6	272	26	99
	192	36	121	0.63	1.664	1.8	0.1753	1.2	0.63	0.0688	1.4	995	37	1041	24	894	29	105
	533	23	336	0.63	0.262	2.4	0.0361	2.1	0.86	0.0526	1.2	236	11	228	10	311	28	97
	153	7	122	0.80	0.285	1.9	0.0402	1.4	0.74	0.0514	1.3	255	9	254	7	261	29	100
	163	9	42	0.26	0.420	1.6	0.0577	1.2	0.76	0.0528	1.0	356	11	362	9	319	23	102
	226	11	42	0.19	0.375	1.4	0.0512	1.1	0.76	0.0530	0.9	323	9	322	7	329	21	100
	2445	100	145	0.06	0.286	1.2	0.0406	1.1	0.94	0.0511	0.4	255	6	256	6	245	9	100
	1674	71	135	0.08	0.292	2.7	0.0415	2.6	0.95	0.0511	0.8	260	14	262	14	245	19	101
	188	20	145	0.77	0.805	1.8	0.0954	1.4	0.74	0.0612	1.2	600	22	587	16	648	27	98
	97	4	62	0.64	0.283	1.7	0.0399	1.2	0.67	0.0514	1.3	253	9	252	6	261	29	100
	190	8	114	0.60	0.239	2.4	0.0344	2.0	0.82	0.0503	1.4	217	11	218	9	210	32	100
	267	26	220	0.83	0.640	2.5	0.0815	1.9	0.77	0.0569	1.6	502	25	505	19	488	35	101
	858	40	221	0.26	0.364	2.5	0.0457	1.4	0.54	0.0578	2.1	315	16	288	8	521	47	91
	290	17	271	0.93	0.368	2.0	0.0505	1.5	0.78	0.0529	1.2	318	13	318	10	322	28	100
	68	4	56	0.82	0.741	3.0	0.0503	1.6	0.53	0.1067	2.6	563	34	317	10	1744	47	56
	774	31	-151	-0.20	0.276	1.4	0.0383	1.2	0.82	0.0523	0.8	248	7	242	6	298	18	98
	175	8	131	0.75	0.288	2.1	0.0403	1.4	0.66	0.0518	1.6	257	11	255	7	276	36	99
	512	22	284	0.55	0.364	3.7	0.0384	1.4	0.38	0.0689	3.4	316	23	243	7	895	70	77
	170	8	137	0.81	0.293	2.1	0.0408	1.6	0.75	0.0520	1.4	261	11	258	8	287	31	99

Appendix E continued– U-Pb LA-ICPMS zircon data orthogneisses

					Isotopic ratios						Apparent ages							
	Ua	Pba	Tha	Thc	207Pbb	1 s	206Pbb	1 s	rho	207Pbb	1 s	207Pb	2 s	206Pb	2 s	207Pb	2 s	Concc
	(ppm)	(ppm)	(ppm)	U	235U	%	238U	%		206Pb	%	235U	(Ma)	238U	(Ma)	206Pb	(Ma)	(%)
RH383	594	27	447	0.75	0.289	1.3	0.0407	1.1	0.85	0.0516	0.7	258	7	257	6	267	15	100
	368	17	357	0.97	0.296	1.7	0.0417	1.4	0.83	0.0515	0.9	263	9	263	7	265	21	100
	529	27	552	1.04	0.363	2.2	0.0441	1.4	0.65	0.0598	1.6	315	14	278	8	596	36	88
	413	17	281	0.68	0.265	2.7	0.0372	2.1	0.78	0.0517	1.7	239	13	235	10	271	38	99
	402	17	301	0.75	0.287	2.1	0.0404	1.8	0.85	0.0516	1.1	256	11	255	9	266	26	100
	374	15	240	0.64	0.280	1.5	0.0383	1.2	0.77	0.0529	1.0	250	8	243	6	324	22	97
	1001	62	325	0.32	0.288	2.4	0.0371	1.2	0.49	0.0563	2.1	257	12	235	6	463	46	91
	277	14	320	1.16	0.309	1.5	0.0439	1.3	0.81	0.0511	0.9	274	8	277	7	245	21	101
	186	8	182	0.98	0.262	1.8	0.0370	1.4	0.81	0.0513	1.0	236	8	234	7	255	24	99
RH389	1898	74	191	0.10	0.303	2.5	0.0414	2.1	0.83	0.0530	1.4	269	14	262	11	329	33	97
	789	42	242	0.31	0.462	7.3	0.0534	5.9	0.82	0.0627	4.2	386	56	336	40	700	89	87
	672	28	167	0.25	0.325	2.1	0.0423	1.9	0.91	0.0557	0.9	286	12	267	10	442	19	93
	632	25	152	0.24	0.310	3.1	0.0385	2.4	0.78	0.0584	1.9	274	17	244	12	545	42	89
	496	22	186	0.37	0.329	4.0	0.0439	3.9	0.96	0.0543	1.1	288	23	277	21	384	24	96
	602	29	178	0.30	0.367	7.1	0.0488	6.9	0.97	0.0546	1.7	318	45	307	43	394	37	97
	465	23	184	0.40	0.402	4.3	0.0503	2.4	0.56	0.0580	3.6	343	30	316	15	530	79	92
	7080	193	285	0.04	0.346	2.8	0.0253	1.9	0.67	0.0993	2.1	302	17	161	6	1611	39	53
	2460	112	346	0.14	0.368	2.5	0.0481	2.0	0.79	0.0554	1.6	318	16	303	12	430	35	95
	612	34	189	0.31	0.420	4.6	0.0582	4.2	0.91	0.0523	1.9	356	33	365	31	301	43	102
RH429	162	9	50	0.31	0.405	3.1	0.0550	2.5	0.78	0.0534	2.0	345	22	345	17	346	44	100
	186	17	135	0.73	0.705	2.4	0.0869	1.9	0.79	0.0588	1.4	542	26	537	20	559	31	99
	439	28	13	0.03	0.572	4.7	0.0679	3.6	0.78	0.0612	3.0	460	43	423	31	646	64	92
	229	11	104	0.45	0.351	2.8	0.0487	2.6	0.92	0.0522	1.1	305	17	307	16	294	26	100
	354	36	198	0.56	0.828	1.8	0.0999	1.6	0.87	0.0601	0.9	612	22	614	20	606	20	100

Appendix E continued– U-Pb LA-ICPMS zircon data orthogneisses

					Isotopic ratios						Apparent ages						
	Ua	Pba	Tha	Thc	207Pbb	1 s	206Pbb	1 s	rho	207Pbb	1 s	207Pb	2 s	206Pb	2 s	207Pb	2 s	Concc
	(ppm)	(ppm)	(ppm)	U	235U	%	238U	%		206Pb	%	235U	(Ma)	238U	(Ma)	206Pb	(Ma)	(%)
RH429	342	37	364	1.06	0.806	1.4	0.0967	1.2	0.88	0.0605	0.7	600	17	595	15	621	14	99
	550	27	80	0.15	0.380	3.6	0.0528	3.5	0.98	0.0521	0.7	327	23	332	23	291	15	102
	81	4	55	0.68	0.352	1.7	0.0488	1.3	0.72	0.0523	1.2	306	11	307	8	297	27	100
	30	2	60	1.98	0.350	3.0	0.0465	1.6	0.53	0.0545	2.6	304	19	293	9	392	58	96
	67	4	91	1.35	0.353	1.9	0.0487	1.0	0.53	0.0526	1.6	307	12	306	6	314	37	100
	409	41	127	0.31	0.847	1.4	0.1025	1.1	0.73	0.0599	1.0	623	18	629	13	601	21	101
	129	14	101	0.78	0.807	1.8	0.1030	1.4	0.80	0.0568	1.1	601	21	632	18	485	23	105
	69	4	78	1.13	0.340	1.8	0.0465	1.3	0.71	0.0530	1.3	297	11	293	7	327	29	99
	111	7	89	0.80	0.407	1.9	0.0547	1.4	0.76	0.0540	1.2	347	13	343	10	370	28	99
	215	22	130	0.61	0.832	3.2	0.0953	1.4	0.43	0.0633	2.9	615	39	587	16	719	61	95
	383	22	111	0.29	0.502	4.3	0.0578	3.0	0.68	0.0629	3.2	413	36	362	21	704	68	88
	284	13	55	0.19	0.349	1.5	0.0477	1.3	0.85	0.0530	0.8	304	9	300	8	330	18	99
	147	6	45	0.31	0.317	2.9	0.0426	2.2	0.76	0.0539	1.8	279	16	269	12	369	41	96
	495	23	204	0.41	0.331	1.9	0.0458	1.6	0.87	0.0525	0.9	290	11	288	10	306	21	99
	198	22	260	1.31	0.784	2.7	0.0944	1.8	0.68	0.0602	2.0	588	32	581	21	612	43	99
	213	23	149	0.70	0.844	2.7	0.1018	2.2	0.82	0.0602	1.6	622	34	625	28	609	34	101
	32	4	30	0.96	0.802	2.8	0.1005	1.8	0.65	0.0579	2.1	598	33	617	22	526	46	103
	132	7	91	0.69	0.432	5.8	0.0504	4.5	0.78	0.0621	3.6	365	42	317	28	679	77	87
	60	4	104	1.72	0.335	2.6	0.0465	1.8	0.70	0.0522	1.9	293	15	293	11	293	43	100
	159	7	53	0.33	0.328	2.9	0.0458	2.1	0.74	0.0519	1.9	288	17	289	12	282	44	100
	125	12	153	1.22	0.681	2.4	0.0854	1.7	0.70	0.0578	1.7	527	25	528	18	523	38	100
	158	9	89	0.56	0.483	3.9	0.0577	2.3	0.60	0.0607	3.1	400	31	362	17	630	67	90
	178	17	61	0.34	0.873	2.0	0.1010	1.5	0.76	0.0627	1.3	637	25	620	19	698	27	97
	683	30	149	0.22	0.351	1.8	0.0459	1.5	0.85	0.0555	0.9	306	11	289	9	434	21	95

Appendix E continued– U-Pb LA-ICPMS zircon data orthogneisses

					Isotopic ratios						Apparent ages							
	Ua (ppm)	Pba (ppm)	Tha (ppm)	Thc U	207Pbb 235U	1 s %	206Pbb 238U	1 s %	rho	207Pbb 206Pb	1 s %	207Pb 235U	2 s (Ma)	206Pb 238U	2 s (Ma)	207Pb 206Pb	2 s (Ma)	Concc (%)
RH429	445	38	267	0.60	0.654	1.7	0.0823	1.6	0.91	0.0577	0.7	511	17	510	16	517	16	100
RH441	683	32	207	0.30	0.341	1.3	0.0472	1.2	0.90	0.0524	0.6	298	8	298	7	302	13	100
	272	13	164	0.60	0.322	2.6	0.0438	2.4	0.93	0.0533	1.0	284	15	277	13	342	22	98
	136	7	78	0.58	0.442	4.4	0.0471	2.5	0.57	0.0680	3.6	371	32	297	15	869	74	80
	1268	59	315	0.25	0.362	1.5	0.0481	1.2	0.78	0.0546	0.9	314	9	303	7	396	21	97
	516	20	187	0.36	0.286	1.7	0.0389	1.3	0.78	0.0534	1.1	255	9	246	6	344	24	96
	204	9	177	0.87	0.308	4.6	0.0405	4.2	0.92	0.0551	1.8	272	25	256	22	418	40	94
	195	9	131	0.67	0.333	1.6	0.0453	1.3	0.81	0.0533	0.9	292	9	285	7	343	21	98
	327	17	184	0.56	0.372	2.7	0.0498	2.4	0.86	0.0542	1.4	321	18	313	15	380	31	97
	349	11	249	0.71	0.216	2.1	0.0288	1.4	0.67	0.0544	1.6	199	8	183	5	388	35	92
	550	23	152	0.28	0.310	2.2	0.0427	1.8	0.82	0.0527	1.2	274	12	270	10	315	28	98
	358	15	179	0.50	0.281	1.8	0.0390	1.5	0.85	0.0522	1.0	251	9	247	8	294	22	98
	393	21	362	0.92	0.358	1.8	0.0489	1.6	0.89	0.0531	0.8	311	11	308	10	333	19	99
	360	10	119	0.33	0.208	4.5	0.0291	4.0	0.89	0.0519	2.1	192	17	185	15	283	48	96
	341	17	186	0.54	0.341	1.5	0.0470	1.2	0.80	0.0526	0.9	298	9	296	7	313	21	99
	452	23	285	0.63	0.349	1.5	0.0482	1.2	0.81	0.0525	0.9	304	9	303	7	309	20	100
	361	15	345	0.96	0.280	1.5	0.0381	1.2	0.80	0.0532	0.9	250	8	241	6	338	21	96
	515	25	228	0.44	0.361	2.0	0.0489	1.6	0.79	0.0535	1.3	313	13	308	10	349	29	98
	384	5	14	0.04	0.112	3.3	0.0129	1.7	0.52	0.0627	2.9	108	7	83	3	697	61	77
	176	9	156	0.88	0.358	2.2	0.0478	1.8	0.83	0.0543	1.2	311	13	301	11	385	27	97
	523	24	199	0.38	0.344	2.4	0.0461	2.3	0.93	0.0541	0.9	300	15	291	13	377	20	97
	340	20	131	0.39	0.442	2.6	0.0592	2.5	0.93	0.0541	1.0	372	20	371	18	377	22	100
	248	12	177	0.71	0.323	1.5	0.0436	1.1	0.70	0.0538	1.1	284	9	275	6	363	24	97
	559	24	147	0.26	0.326	1.5	0.0446	1.3	0.83	0.0530	0.8	286	9	281	7	328	19	98

Appendix E continued– U-Pb LA-ICPMS zircon data orthogneisses

					Isotopic ratios						Apparent ages						
	Ua	Pba	Tha	Thc	207Pbb	1 s	206Pbb	1 s	rho	207Pbb	1 s	207Pb	2 s	206Pb	2 s	207Pb	2 s	Concc
	(ppm)	(ppm)	(ppm)	U	235U	%	238U	%		206Pb	%	235U	(Ma)	238U	(Ma)	206Pb	(Ma)	(%)
RH441	324	14	165	0.51	0.308	1.3	0.0418	1.1	0.84	0.0534	0.7	272	7	264	6	346	16	97
	2722	121	323	0.12	0.337	1.4	0.0476	1.3	0.90	0.0514	0.6	295	9	300	8	260	15	102
	1569	68	311	0.20	0.342	1.9	0.0456	1.1	0.60	0.0544	1.5	299	11	287	6	389	33	96
	267	14	149	0.56	0.369	1.9	0.0508	1.7	0.89	0.0527	0.9	319	12	319	11	315	20	100
	220	12	198	0.90	0.374	1.8	0.0516	1.5	0.81	0.0526	1.1	323	12	324	10	312	24	100
	493	22	172	0.35	0.329	1.7	0.0460	1.5	0.87	0.0518	0.8	289	10	290	9	279	19	100
RH423	1174	31	132	0.11	0.158	2.4	0.0229	1.9	0.78	0.0501	1.5	149	7	146	5	198	35	98
	1372	34	197	0.14	0.166	2.5	0.0236	1.9	0.75	0.0510	1.6	156	8	150	6	239	38	97
	5235	113	378	0.07	0.139	2.1	0.0202	1.6	0.76	0.0500	1.4	132	6	129	4	195	32	97
	4707	111	391	0.08	0.139	2.0	0.0203	1.9	0.92	0.0496	0.8	132	5	130	5	175	18	98
	686	20	235	0.34	0.166	2.0	0.0242	1.7	0.84	0.0497	1.1	156	6	154	5	183	25	99
	1147	57	213	0.19	0.330	1.6	0.0459	1.3	0.83	0.0522	0.9	290	9	290	8	292	21	100
	713	17	451	0.63	0.153	1.7	0.0215	1.3	0.80	0.0516	1.0	144	5	137	4	267	23	95
	5956	123	392	0.07	0.134	1.7	0.0188	1.4	0.85	0.0519	0.9	128	4	120	3	281	20	94
	1965	53	225	0.11	0.167	2.0	0.0247	1.9	0.93	0.0491	0.7	157	6	157	6	153	17	100
	3498	96	379	0.11	0.156	1.2	0.0230	1.1	0.88	0.0493	0.6	147	4	147	3	160	14	99
	520	16	157	0.30	0.172	1.3	0.0255	1.0	0.75	0.0491	0.9	162	4	162	3	150	20	100
	2420	62	191	0.08	0.162	1.3	0.0240	1.2	0.89	0.0491	0.6	153	4	153	4	152	14	100
	3121	63	315	0.10	0.116	3.8	0.0163	3.5	0.91	0.0515	1.5	111	8	104	7	264	35	94
	526	14	447	0.85	0.160	1.6	0.0229	1.3	0.78	0.0508	1.0	151	5	146	4	231	23	97
	603	15	468	0.78	0.151	2.4	0.0212	1.6	0.67	0.0514	1.8	142	7	135	4	259	41	95
	684	19	156	0.23	0.157	1.5	0.0230	1.1	0.77	0.0497	1.0	148	4	146	3	182	22	99
	964	27	129	0.13	0.162	1.2	0.0239	1.0	0.78	0.0492	0.8	152	4	152	3	155	18	100
	692	22	167	0.24	0.163	1.2	0.0242	0.9	0.76	0.0487	0.8	153	4	154	3	135	19	101

Appendix E continued– U-Pb LA-ICPMS zircon data orthogneisses

					Isotopic ratios							Apparent ages						
	Ua	Pba	Tha	Thc	207Pbb	1 s	206Pbb	1 s	rho	207Pbb	1 s	207Pb	2 s	206Pb	2 s	207Pb	2 s	Concc
	(ppm)	(ppm)	(ppm)	U	235U	%	238U	%		206Pb	%	235U	(Ma)	238U	(Ma)	206Pb	(Ma)	(%)
RH423	2563	65	270	0.11	0.155	1.2	0.0228	1.0	0.87	0.0492	0.6	146	3	145	3	158	14	99
	1707	42	154	0.09	0.159	1.9	0.0230	1.8	0.92	0.0502	0.8	150	6	146	5	203	18	98
	4959	106	412	0.08	0.132	1.8	0.0191	1.6	0.87	0.0500	0.9	126	5	122	4	195	21	97
	1385	36	190	0.14	0.154	1.6	0.0226	1.4	0.83	0.0494	0.9	145	5	144	4	166	22	99
	3062	85	318	0.10	0.166	1.4	0.0245	1.1	0.82	0.0491	0.8	156	4	156	4	153	19	100
	5334	117	405	0.08	0.143	4.1	0.0206	4.0	0.97	0.0504	1.0	136	11	131	10	215	23	97
	18	1	24	1.31	0.092	7.6	0.0108	3.7	0.49	0.0615	6.6	89	14	69	5	656	141	78
	1569	67	815	0.52	0.176	4.8	0.0221	2.6	0.55	0.0577	4.0	164	16	141	7	519	88	86
	750	21	156	0.21	0.152	2.7	0.0225	2.1	0.77	0.0492	1.7	144	8	143	6	156	41	99
	930	23	309	0.33	0.154	2.4	0.0223	1.9	0.81	0.0501	1.4	146	7	142	5	201	32	98
	653	18	425	0.65	0.162	2.5	0.0241	1.8	0.73	0.0488	1.7	153	8	154	6	141	40	101
	4277	109	284	0.07	0.176	2.2	0.0244	1.5	0.70	0.0524	1.6	165	7	155	5	303	36	94
RH447	1277	26	229	0.18	0.1502	4.4	0.0212	3.5	0.79	0.0513	2.7	142	6	135	5	255	31	95
	1135	23	77	0.07	0.1549	3.6	0.0222	2.7	0.75	0.0506	2.4	146	5	142	4	223	27	97
	1859	30	209	0.11	0.1218	2.4	0.0175	1.5	0.63	0.0504	1.9	117	3	112	2	211	22	96
	1532	33	138	0.09	0.1637	2.5	0.0233	2.1	0.82	0.0509	1.5	154	4	149	3	236	17	97
	344	14	239	0.70	0.2747	2.5	0.0392	1.8	0.73	0.0508	1.7	246	6	248	4	234	20	101
	830	19	11	0.01	0.1640	3.1	0.0235	1.6	0.53	0.0506	2.6	154	5	150	2	221	31	97
	1217	23	113	0.09	0.1380	3.1	0.0205	2.7	0.85	0.0489	1.7	131	4	131	3	143	20	100
	189	12	56	0.30	0.4999	3.6	0.0634	2.6	0.73	0.0572	2.5	412	15	396	10	500	27	96
	975	14	138	0.14	0.1040	5.6	0.0154	4.0	0.72	0.0488	3.8	100	6	99	4	140	45	98
	1726	38	91	0.05	0.1614	2.5	0.0236	1.9	0.75	0.0495	1.6	152	4	151	3	173	19	99
	1638	39	518	0.32	0.1650	2.4	0.0243	2.1	0.87	0.0493	1.2	155	4	154	3	164	14	100
	1190	26	241	0.20	0.1539	2.3	0.0226	1.7	0.72	0.0493	1.6	145	3	144	2	162	19	99

Appendix E continued– U-Pb LA-ICPMS zircon data orthogneisses

					Isotopic ratios							Apparent ages						
	Ua	Pba	Tha	Thc	207Pbb	1 s	206Pbb	1 s	rho	207Pbb	1 s	207Pb	2 s	206Pb	2 s	207Pb	2 s	Concc
	(ppm)	(ppm)	(ppm)	U	235U	%	238U	%		206Pb	%	235U	(Ma)	238U	(Ma)	206Pb	(Ma)	(%)
RH447	733	19	126	0.17	0.1719	6.7	0.0258	6.5	0.98	0.0483	1.5	161	11	164	11	112	17	102
	280	9	86	0.31	0.2342	6.9	0.0325	1.5	0.21	0.0522	6.7	214	15	206	3	296	77	97
	379	15	205	0.54	0.2737	2.8	0.0371	1.8	0.64	0.0534	2.2	246	7	235	4	348	25	96
	1815	37	211	0.12	0.1522	3.8	0.0215	2.2	0.58	0.0512	3.1	144	5	137	3	252	36	96
	177	7	95	0.54	0.2625	2.9	0.0366	2.0	0.70	0.0521	2.1	237	7	231	5	289	24	98
	233	6	52	0.22	0.1876	3.3	0.0268	2.4	0.73	0.0508	2.2	175	6	170	4	231	26	98
	162	6	72	0.45	0.2589	3.3	0.0366	1.9	0.57	0.0513	2.7	234	8	232	4	255	31	99
	975	22	109	0.11	0.1667	3.1	0.0239	2.2	0.69	0.0507	2.3	157	5	152	3	226	26	97
	231	9	134	0.58	0.2632	3.1	0.0364	2.2	0.73	0.0524	2.1	237	7	231	5	302	24	97
	1566	36	352	0.22	0.1601	2.8	0.0237	2.4	0.88	0.0490	1.3	151	4	151	4	148	16	100
	1164	12	10	0.01	0.0752	2.7	0.0114	2.0	0.75	0.0479	1.8	74	2	73	1	96	21	99
	2197	48	271	0.12	0.1585	3.7	0.0232	3.3	0.87	0.0495	1.8	149	6	148	5	174	21	99
	515	26	7	0.01	0.4097	2.9	0.0551	2.5	0.89	0.0539	1.3	349	10	346	9	367	15	99
	178	6	80	0.45	0.2525	13.8	0.0353	2.0	0.14	0.0518	13.7	229	32	224	4	278	156	98
	2595	29	19	0.01	0.0798	2.7	0.0121	2.1	0.79	0.0478	1.6	78	2	78	2	88	19	100
	3721	39	32	0.01	0.0751	2.3	0.0115	2.0	0.88	0.0474	1.1	74	2	74	1	70	13	100
	534	12	78	0.15	0.1647	2.5	0.0237	1.7	0.68	0.0504	1.9	155	4	151	3	214	21	97
	637	25	404	0.63	0.2634	3.3	0.0381	2.6	0.79	0.0501	2.1	237	8	241	6	201	24	102
	442	13	92	0.21	0.2123	2.2	0.0307	1.4	0.62	0.0502	1.7	195	4	195	3	203	20	100
	210	8	152	0.72	0.2689	2.7	0.0373	1.4	0.53	0.0522	2.3	242	7	236	3	296	26	98
	1863	43	450	0.24	0.1704	2.6	0.0238	1.5	0.56	0.0520	2.2	160	4	151	2	284	25	95
	1129	21	174	0.15	0.1371	3.5	0.0198	2.9	0.84	0.0502	1.9	130	5	127	4	202	22	97
	299	8	91	0.30	0.1928	3.6	0.0266	2.9	0.81	0.0525	2.1	179	6	169	5	309	24	95
	1687	39	233	0.14	0.1622	3.9	0.0239	1.7	0.45	0.0492	3.4	153	6	152	3	159	40	100

Appendix E continued– U-Pb LA-ICPMS zircon data orthogneisses

					Isotopic ratios						Apparent ages							
	Ua	Pba	Tha	Thc	207Pbb	1 s	206Pbb	1 s	rho	207Pbb	1 s	207Pb	2 s	206Pb	2 s	207Pb	2 s	Concc
	(ppm)	(ppm)	(ppm)	U	235U	%	238U	%		206Pb	%	235U	(Ma)	238U	(Ma)	206Pb	(Ma)	(%)
RH447	226	17	74	0.33	0.6318	2.6	0.0786	1.7	0.65	0.0583	2.0	497	13	488	8	540	22	98
	1456	34	432	0.30	0.1620	2.1	0.0237	1.6	0.75	0.0496	1.4	152	3	151	2	178	17	99
	1195	10	16	0.01	0.0635	2.8	0.0095	2.2	0.79	0.0484	1.7	62	2	61	1	121	20	98
RH455	432	15	138	0.44	0.3188	15.4	0.0337	8.0	0.52	0.0686	13.1	281	43	214	17	888	136	76
	585	30	181	0.79	0.3104	3.3	0.0434	2.7	0.80	0.0519	2.0	274	9	274	7	280	23	100
	283	9	67	0.18	0.2361	8.2	0.0325	3.9	0.47	0.0527	7.2	215	18	206	8	316	82	96
	1095	31	228	0.10	0.2081	3.6	0.0304	3.1	0.86	0.0496	1.8	192	7	193	6	175	21	101
	1166	37	290	0.09	0.2484	3.3	0.0336	2.0	0.60	0.0537	2.6	225	7	213	4	357	29	95
	898	39	298	0.23	0.3318	2.9	0.0458	2.6	0.90	0.0525	1.3	291	8	289	8	308	14	99
	890	21	159	0.03	0.1788	4.4	0.0251	3.9	0.89	0.0516	2.0	167	7	160	6	268	23	96
	252	10	65	0.54	0.2594	3.7	0.0355	2.8	0.76	0.0531	2.4	234	9	225	6	331	27	96
	98	7	54	0.77	0.5553	5.2	0.0679	4.3	0.82	0.0593	3.0	448	23	423	18	579	32	94
	118	6	40	0.88	0.3388	3.8	0.0414	2.4	0.63	0.0593	2.9	296	11	262	6	578	32	88
	780	31	223	0.31	0.2865	4.6	0.0400	4.5	0.96	0.0519	1.2	256	12	253	11	282	14	99
	368	47	435	0.15	1.1831	3.4	0.1338	2.6	0.76	0.0641	2.2	793	27	809	21	746	23	102
	469	40	353	0.01	0.7536	3.6	0.0911	3.2	0.88	0.0600	1.7	570	21	562	18	604	18	99
	446	18	129	0.36	0.2891	5.2	0.0408	4.9	0.94	0.0514	1.8	258	13	258	13	257	21	100
	594	17	109	0.45	0.1831	10.1	0.0258	9.4	0.93	0.0515	3.7	171	17	164	15	264	42	96
	625	15	111	0.43	0.1770	5.0	0.0234	4.3	0.86	0.0549	2.5	165	8	149	6	409	28	90
	1941	42	335	0.05	0.1725	3.4	0.0234	3.1	0.90	0.0534	1.5	162	5	149	5	346	16	92
	268	11	89	0.16	0.3311	4.5	0.0438	3.8	0.84	0.0549	2.5	290	13	276	10	408	28	95
	332	13	90	0.53	0.2700	4.4	0.0369	4.0	0.91	0.0531	1.8	243	11	233	9	333	21	96
	2142	32	209	0.23	0.0975	7.0	0.0145	4.6	0.65	0.0489	5.4	94	7	93	4	141	63	98
	645	17	134	0.06	0.2071	3.7	0.0285	2.8	0.76	0.0527	2.4	191	7	181	5	317	27	95

Appendix E continued– U-Pb LA-ICPMS zircon data orthogneisses

					Isotopic ratios						Apparent ages						
	Ua	Pba	Tha	Thc	207Pbb	1 s	206Pbb	1 s	rho	207Pbb	1 s	207Pb	2 s	206Pb	2 s	207Pb	2 s	Concc
	(ppm)	(ppm)	(ppm)	U	235U	%	238U	%		206Pb	%	235U	(Ma)	238U	(Ma)	206Pb	(Ma)	(%)
RH455	404	14	101	0.47	0.2491	4.4	0.0344	4.1	0.94	0.0525	1.5	226	10	218	9	309	18	96
	921	28	222	0.15	0.2407	6.7	0.0323	6.1	0.91	0.0540	2.7	219	15	205	13	373	31	94
	442	23	165	0.66	0.3737	3.7	0.0516	2.9	0.79	0.0525	2.3	322	12	324	9	309	26	101
	755	15	101	0.24	0.1335	9.0	0.0187	7.3	0.81	0.0518	5.2	127	11	119	9	276	60	94
	760	22	162	0.15	0.2124	3.6	0.0299	3.1	0.86	0.0516	1.9	196	7	190	6	268	21	97
	774	31	229	0.32	0.2957	2.8	0.0411	2.3	0.81	0.0522	1.6	263	7	259	6	296	19	99
	672	26	198	0.14	0.2940	4.3	0.0406	4.0	0.94	0.0526	1.5	262	11	256	10	310	17	98
	1000	20	138	0.14	0.1382	7.3	0.0193	6.8	0.94	0.0521	2.5	131	10	123	8	289	28	94
	1035	39	276	0.33	0.2670	6.2	0.0369	4.7	0.75	0.0525	4.1	240	15	233	11	308	46	97
	1281	32	236	0.06	0.1842	6.0	0.0265	3.2	0.54	0.0505	5.0	172	10	168	5	218	58	98
	740	22	160	0.15	0.2167	3.9	0.0303	2.9	0.74	0.0518	2.7	199	8	193	6	276	30	97
	543	12	95	0.13	0.1755	8.9	0.0216	4.2	0.47	0.0590	7.9	164	15	138	6	566	86	84
	87	5	37	0.14	0.4304	4.3	0.0561	2.7	0.64	0.0556	3.3	363	15	352	10	438	36	97
	577	24	174	0.35	0.3021	4.6	0.0424	3.1	0.67	0.0517	3.4	268	12	268	8	271	39	100
	736	26	200	0.19	0.2721	4.6	0.0371	3.5	0.77	0.0533	2.9	244	11	235	8	340	33	96

Appendix F– Sr- and Nd isotopic data of the orthogneisses

sample	location	Age (Ma)	$^{143}Nd/^{144}Nd_m$	2σ	$^{143}Nd/^{144}Nd_c$	$^{147}Sm/^{144}Nd^*$	$^{143}Nd/^{144}Nd_{ini}$	εNd_{ini}	T_{DM}	$^{87}Sr/^{86}Sr_m$	2σ	$^{87}Sr/^{86}Sr_{ini}$
RH345	Ada	295	0.512251	15	0.512258	0.1175	0.512027	-4.4	1.4	0.727318	20	0.714901
RH346	Ada	310	0.512287	10	0.512313	0.1245	0.512068	-3.6	1.3	0.729571	13	0.716742
RH358	Ada	300	0.512230	15	0.512252	0.1274	0.512001	-4.9	1.4	0.714986	12	0.706302
RH360	Ada	303	0.512102	17	0.512126	0.1188	0.511892	-7.0	1.6	0.718249	16	0.708546
RH370	Dadia-Kotronia	315	0.512304	14	0.512328	0.1218	0.512089	-3.2	1.3	0.714119	9	0.708842
RH375	Essimi-Leptokaria	312	0.512299	12	0.512313	0.1269	0.512064	-3.7	1.3	0.714924	14	0.708763
RH376	Essimi-Leptokaria	300	0.512358	13	0.512334	0.0826	0.512172	-1.6	1.1	0.713439	13	0.704562
RH383	Kotronia	254	0.512170	13	0.512146	0.1031	0.511977	-6.6	1.3	0.729658	12	0.706930
RH434	N.Sanda	300	0.512288	20	0.512320	0.1104	0.512103	-2.9	1.5	0.719236	4	0.705094
RH389	westl. Sidiro	300	0.512290	14	0.512322	0.1260	0.512108	-3.8	1.3	0.733596	8	0.705801
RH413	Drania-Organi	300	0.512165	11	0.512197	0.1167	0.511968	-5.5	1.5	0.714764	10	0.707687
RH418	Organi-Smigada	300	0.512164	17	0.512196	0.1151	0.511970	-5.5	1.5	0.714503	5	0.706723
Rh429	Smigada-Mirtiski	300	0.512156	12	0.512188	0.1208	0.511951	-5.9	1.5	0.713730	10	0.706865
RH423	Smigada-Kimi	150	0.512417	14	0.512440	0.1140	0.512328	-2.3	1.1	0.710434	10	0.706883
RH447	westl. Sidiro	150	0.512426	14	0.512402	0.1583	0.512247	-3.9	1.2	0.716072	5	0.708985
RH455*	Sidiro	150	0.512317	5	0.512307	0.1442	0.512166	-5.4	1.3	0.720002	9	0.712893
RH11†	N-Xanthi	300	0.512172	13	0.512152	0.1088	0.511938	-6.1	1.5	0.723418	11	0.710971
RH60†	W-Paranesti	276	0.512252	13	0.512266	0.1086	0.512053	-3.9	1.3	0.711521	6	0.707537
RH78†	N-Drama	283	0.512410	11	0.512424	0.1146	0.512199	-1.0	1.1	0.707088	15	0.705065
RH89†	Thassos	283	0.512133	11	0.512113	0.1089	0.511899	-6.9	1.6	0.714507	6	0.709110
F34†	N-Xanthi	291	0.512190	9	0.512206	0.1018	0.512006	-4.8	1.1	0.713592	11	0.710199
RH330#	Thermes	159	0.512281	13	0.512281	0.1618	0.512122	-6.3	1.4	0.710032	11	0.708620
F180-2†	N-Xanthi	149	0.512251	12	0.512235	0.1411	0.512097	-6.8	1.4	0.710138	7	0.708376
F181†	Thermes	138	0.512306	15	0.512330	0.1044	0.512228	-4.2	1.3	0.711344	8	0.708687
F190†	W-Paranesti	137	0.512293	15	0.512309	0.1159	0.512195	-4.9	1.3	0.709732	6	0.707836
F216#	N-Drama	163	0.512358	15	0.512390	0.1267	0.512266	-3.5	1.2	0.713269	8	0.709679
F220†	N-Sminthi	164	0.512480	5	0.512470	0.0969	0.512375	-1.4	1.1	0.716532	4	0.711842

Sr- and Nd concentrations obtained from LA-ICPMS; * = Sr- and Nd concentrations obtained from XRF; † = ages obtained from single zircon evaporation (Turpaud 2006); # = ages obtained by SHRIMP-II.